SINGLE CRYSTAL STUDIES OF HYDRATED TRANSITION METAL IONS BY ELECTRON PARAMAGNETIC RESONANCE

Akira Jindo
(Ph.D. Thesis)

January 1971

AEC Contract No. W-7405-eng-48

TWO-WEEK LOAN COPY

This is a Library Circulating Copy which may be borrowed for two weeks. For a personal retention copy, call Tech. Info. Division, Ext. 5545

UCRL-20386 c.2

LAWRENCE RADIATION LABORATORY
UNIVERSITY of CALIFORNIA BERKELEY

DISCLAIMER

This document was prepared as an account of work sponsored by the United States Government. While this document is believed to contain correct information, neither the United States Government nor any agency thereof, nor the Regents of the University of California, nor any of their employees, makes any warranty, express or implied, or assumes any legal responsibility for the accuracy, completeness, or usefulness of any information, apparatus, product, or process disclosed, or represents that its use would not infringe privately owned rights. Reference herein to any specific commercial product, process, or service by its trade name, trademark, manufacturer, or otherwise, does not necessarily constitute or imply its endorsement, recommendation, or favoring by the United States Government or any agency thereof, or the Regents of the University of California. The views and opinions of authors expressed herein do not necessarily state or reflect those of the United States Government or any agency thereof or the Regents of the University of California.

TABLE OF CONTENTS

ABSTRACT

I. INTRODUCTION ---------- 1

II. EXPERIMENTAL ---------- 6

A. Spectrometer ---------- 6

B. Computer ---------- 8

C. Chemicals and Crystal Growth ---------- 9

1. Metal Selenates ---------- 10

2. α-$NiSO_4 \cdot 6H_2O$ ---------- 13

3. $La_2Mg_3(NO_3)_{12} \cdot 24H_2O$ ---------- 14

4. Metal Bromates ---------- 15

III. HOST LATTICES ---------- 16

A. α-$NiSO_4 \cdot 6H_2O$ and $ZnSeO_4 \cdot 6H_2O$ ---------- 16

1. Crystal Structure ---------- 16

2. Magnetic Axes ---------- 19

B. $La_2Mg_3(NO_3)_{12} \cdot 24H_2O$ ---------- 24

1. Crystal Structure ---------- 24

2. Paramagnetic Ion Impurities ---------- 25

C. $Zn(BrO_3)_2 \cdot 6H_2O$ ---------- 27

1. Crystal Structure ---------- 27

2. Magnetic Axes ---------- 28

IV. Ni^{2+} in DIAMAGNETIC HOSTS ---------- 31

A. Theory ---------- 31

1. Crystal Field Model for $3d^8$ ---------- 31

2. Spin Hamiltonian ---------- 37

IV. B. Spectral Assignment ---------- 45

C. Ni^{2+} in $ZnSeO_4 \cdot 6H_2O$ ---------- 47

1. γc Plane Spectra ---------- 47

2. ac Plane Spectra ---------- 49

3. ab Plane Spectra ---------- 52

4. Discussion of Results ---------- 53

5. Summary ---------- 56

D. Ni^{2+} in LMN ---------- 58

1. Type 1 Ion ---------- 58

2. Type 2 Ion ---------- 69

E. Ni^{2+} in $Zn(BrO_3)_2 \cdot 6H_2O$ ---------- 71

1. Undiluted $Ni(BrO_3)_2 \cdot 6H_2O$ ---------- 71

2. Ni^{2+} Doped in $Zn(BrO_3)_2 \cdot 6H_2O$ ---------- 72

F. The Sign of D ---------- 75

1. Review of Past Work ---------- 75

2. Discrepancy and Discussion ---------- 83

V. Cu^{2+} in $ZnSeO_4 \cdot 6H_2O$ ---------- 89

A. Theory of Cu^{2+} ($3d^9$) ---------- 89

B. Results ---------- 95

C. Discussion ---------- 99

VI. Co^{2+} in $ZnSeO_4 \cdot 6H_2O$ ---------- 106

A. Theory for Co^{2+} ($3d^7$) ---------- 106

B. Results ---------- 108

C. Discussion ---------- 111

1. Analysis of the g Factor and the Axial Splitting --- 111

2. Second Order Hyperfine Shift ---------- 114

VII. PARAMAGNETIC IONS IN NICKEL SULFATE AND NICKEL SELENATE ---- 117

A. Co^{2+} in $NiSeO_4 \cdot 6H_2O$ ---------- 117

B. Co^{2+} in α-$NiSO_4 \cdot 6H_2O$ ---------- 122

C. Cu^{2+} in α-$NiSO_4 \cdot 6H_2O$ ---------- 125

D. Cu^{2+} in $NiSeO_4 \cdot 6H_2O$ and Mixed Crystals ---------- 133

E. α-$NiSO_4 \cdot 6H_2O$ ---------- 135

1. High-Field Transition ---------- 135

2. Coupled-Pair Transition ---------- 138

APPENDIX I Determination of ϕ ---------- 141

APPENDIX II Direction Cosines in $ZnSeO_4 \cdot 6H_2O$ ---------- 143

APPENDIX III Jahn-Teller Interaction ---------- 146

A. Cu^{2+} in LMN ---------- 147

B. Cu^{2+} in $Zn(BrO_3)_2 \cdot 6H_2O$ ---------- 151

C. VCl_4 in Various Host Lattices ---------- 152

APPENDIX IV Tables of Experimental Data ---------- 154

APPENDIX V Computer Programs ---------- 158

A. Field Positions of Ni^{2+} EPR Spectra ---------- 158

B. Hermitian Matrix Diagonalization ---------- 161

ACKNOWLEDGEMENTS ---------- 165

REFERENCES ---------- 166

FIGURE LIST ---------- 172

FIGURES ---------- 180

SINGLE CRYSTAL STUDIES OF HYDRATED TRANSITION METAL IONS BY ELECTRON PARAMAGNETIC RESONANCE

Akira Jindo

Inorganic Materials Research Division, Lawrence Radiation Laboratory
and Department of Chemistry
University of California, Berkeley, California

ABSTRACT

We have undertaken an electron paramagnetic resonance (EPR) study of certain transition metal ions in hydrated single crystals at temperatures ranging from 300 to 1.2°K.

We studied the EPR spectra of Co^{2+}, Ni^{2+} and Cu^{2+} doped into single crystals of $ZnSeO_4 \cdot 6H_2O$. This diamagnetic crystal is isostructural with the tetragonal α-$NiSO_4 \cdot 6H_2O$. The relationship between the principal spin Hamiltonian axes (x,y,z) and the crystallographic axes (a,b,c) has been established. The spin Hamiltonian parameters found for Cu^{2+} are $g_{\parallel} = 2.4295$, $g_{\perp} = 2.0965$, $A_{\parallel} = 115.6$ G, $A_{\perp} = 9.5$ G, $\phi = 43.3°$ and $\beta = 3°$, where ϕ is the angle that the z axis forms with the c axis and β is the angle by which the x axis is rotated from the ab bisector. For Ni^{2+} $g_{\parallel} = 2.219$, $g_{\perp} = 2.238$, $D = +4.20$ cm^{-1}, $E = 0$, $\phi = 35.5°$ and $\beta = 2.0°$. Finally, for Co^{2+} $g_{\parallel} = 5.975$, $g_{\perp} = 3.45$, $A = 77.0$ G, $A = 20$ G, $\phi = 58.5°$ and $\beta = 4.5°$. These parameters agree well with crystal field calculations for an elongated tetragonal symmetry, if some covalency is included.

The EPR spectra of Ni^{2+} were also investigated in the trigonal host lattices, $La_2Mg_3(NO_3)_{12} \cdot 24H_2O$(LMN) and $Zn(BrO_3)_2 \cdot 6H_2O$. In LMN two types of Ni^{2+} spectra were observed. Our results have confirmed the assignments previously reported by Hoskins et al. and by Culvahouse. The sign of D is negative for the type 2 Ni^{2+} ion and positive for the type 1 ion. The results for Ni^{2+} in $Zn(BrO_3)_2 \cdot 6H_2O$ were explained by

$g_{\parallel} = g_{\perp} = 2.235$, $D = -1.79\ cm^{-1}$ and $E = 0.001\ cm^{-1}$ at 1.7°K.

From a study of the results on Ni^{2+} in a variety of crystals we conclude that the sign of D can be correctly predicted by crystal field theory for Ni^{2+} only with tetragonal symmetry. For a trigonal symmetry simple crystal theory cannot explain the sign of D and other important effects must be taken into account.

We have re-examined the EPR spectra of pure α-$NiSO_4 \cdot 6H_2O$. We have detected a new type of spectrum which involves simultaneous transitions of two neighboring Ni^{2+} ions.

Cu^{2+} doped in α-$NiSO_4 \cdot 6H_2O$ showed a tetragonal symmetry with unusually high g values that were slightly dependent upon the crystal sahpe, temperature and resonance frequency. The observed parameters were $g_{\parallel} = 2.900$, $g_{\perp} = 2.482$, $A_{\parallel} = 93.9$ G, $A_{\perp} = 10$ G and $\phi = 61.8°$. Similarly high g values for Cu^{2+} were also detected in tetragonal $NiSeO_4 \cdot 6H_2O$. Exchange interaction between Ni^{2+} and Cu^{2+} are responsible for the anomalous g factors, but neither a simple molecular field correction nor an isotropic exchange between a Ni^{2+}-Cu^{2+} pair could give a quantitative agreement with the observed g values.

The presence of Ni^{2+} ions in the nearest neighbor sites had little effect upon the EPR of Co^{2+}. The spin Hamiltonian parameters of Co^{2+} in $ZnSeO_4 \cdot 6H_2O$, $NiSeO_4 \cdot 6H_2O$ and α-$NiSO_4 \cdot 6H_2O$ were all very similar.

We also report the EPR results of three systems with Jahn-Teller interactions: Cu^{2+} in LMN, Cu^{2+} in $Zn(BrO_3)_2 \cdot 6H_2O$ and VCl_4 in various host lattices.

I. INTRODUCTION

Since the discovery of electron paramagnetic resonance (EPR) the paramagnetic ions in single crystals have been the subject of an intense inquiry. The single crystal samples have been continuously used in the EPR work, mainly because more accurate characterization of the paramagnetic ions is possible from single crystals than from polycrystalline samples.

We limited the scope of this work to the first-row transition metal ions. In particular, we considered Co^{2+}, Ni^{2+} and Cu^{2+} ions incorporated in hydrated single crystals of both diamagnetic and paramagnetic hosts. We have prepared sulfates, selenates, bromates and double nitrates of transition metal ions in plus-two oxidation states. Single crystals of these hydrated compounds are easily grown from aqueous solutions by slow evaporation. In these crystals the paramagnetic ions are surrounded by six water molecules arranged in nearly octahedral symmetry with small tetragonal or trigonal distortions. The EPR of Co^{2+}, Ni^{2+} and Cu^{2+} ions are known to be very sensitive to the local symmetries around them.

We need to distinguish the two types of symmetries frequently referred to in the EPR studies of single crystals. These are the symmetry of the crystal lattice and the symmetry of the crystal field. The former is determined by all the atoms in the crystal, whereas the latter is determined largely by nearest neighbor atoms or molecules. It is the latter symmetry, called the site symmetry, that plays an important role in determining the EPR spectrum of single crystals.

When the site symmetry of a crystal under study is known, one can usually predict the behavior of the EPR spectra of paramagnetic ions substituted in that site. This is the case of lanthanum magnesium nitrate, $La_2Mg_3(NO_3)_{12}\cdot 24H_2O$, (abbreviated as LMN), and zinc bromate, $Zn(BrO_3)_2\cdot 6H_2O$, whose crystal structures are known in detail. Conversely, the results of the EPR studies can often reveal the site symmetry, even when it is unknown from the crystallographic study. The cupric ion can be used to resolve an axial symmetry into trigonal or tetragonal symmetry. For instance, when Cu^{2+} is substituted into a trigonal site, the resulting EPR spectra will consist of an anisotropic spectrum at very low temperature and an isotropic spectrum at higher temperature. Two such examples are given in Appendix IV. But when Cu^{2+} is introduced into a tetragonal site, only an anisotropic spectrum will result at all temperatures. By use of this technique we have determined the site symmetries of the metal ions in zinc selenate, $ZnSeO_4\cdot 6H_2O$. Of course, one cannot always hope to expect the ions of different size to maintain the same site symmetry around them. But in practice this expectation is well founded in many single crystals.

The theoretical apparatus developed to interpret the observed EPR spectra is called the spin Hamiltonian, which deals with the ground state of the magnetic ions located in a given crystalline field. A careful study of the spectra under various experimental conditions yields a set of spin Hamiltonian parameters such as the spectroscopic splitting factor g, the initial (or zero-field) splittings and hyperfine structure (hfs) constants. These parameters in turn furnish some

information as to the nature of the interactions involving the magnetic electrons with their environment. The information derived from the EPR spectra can, in favorable cases, provide estimates of the crystal field parameters. This is illustrated in the results of the Co^{2+}, Ni^{2+} and Cu^{2+} ions doped in $ZnSeO_4 \cdot 6H_2O$.

Throughout this work we use the intermediate crystal field theory (CFT), in which the crystal field is smaller than the coulombic repulsive energy of electrons but larger than the spin-orbit interaction. This is the case for the plus-two oxidation states of the iron group ions. In this scheme one can characterize the energy levels of a paramagnetic ion by the orbital and spin angular momentum of the unpaired electrons. The ground state of the free ion is determined by Hund's rules. In solids the crystal field generated by the nearest ligands modifies the energy levels of the ground and the excited states. Other weak interactions are considered as perturbations. These include the spin-orbit interaction, the Zeeman interaction, the hyperfine interaction, the exchange and electron dipole-dipole interactions. Concrete examples of the crystal field calculations are given in the theories of Ni^{2+} and Cu^{2+}.

First we will examine the EPR spectra of Co^{2+}, Ni^{2+} and Cu^{2+} in diamagnetic host lattices in order to establish their basic features as isolated systems. Then, by increasing the concentration of the paramagnetic ions or by using the paramagnetic host lattices we hope to elucidate the nature of additional interactions involving two or more adjacent magnetic ions. The effects of the neighboring magnetic ions are manifested in EPR as line broadening, line shifts and additional

transitions. Qualitative descriptions of these effects are shown in relatively concentrated samples of Ni^{2+} in $Zn(BrO_3)_2 \cdot 6H_2O$ and in LMN. Other examples are seen in the Co^{2+}, Ni^{2+} and Cu^{2+} ions in the paramagnetic host lattices of nickel sulfate, α-$NiSO_4 \cdot 6H_2O$ and nickel selenate, $NiSeO_4 \cdot 6H_2O$.

The EPR of α-$NiSO_4 \cdot 6H_2O$ has already been reported by Batchelder of this laboratory. His Ph.D. thesis (1970), which is the forerunner of this work, gives the references to the early work on the magnetic properties of α-$NiSO_4 \cdot 6H_2O$. We find considerable differences in the spin Hamiltonian parameters that have been reported by various authors. For example, the axial and the rhombic components of the zero-field splitting, D and E, vary from 2.74 to 4.77 cm^{-1} and from 0 to 0.28 cm^{-1}, respectively. The most comprehensive work carried out on this compound is the magneto-thermodynamic studies of Fisher et al. (1967, 1968 a, b) and of Fisher and Hornung (1968). They introduced a molecular field correction of the form γM, where γ is the molecular field constant and M is the magnetization. With this they could explain the magnetization and heat capacity of a spherical sample of α-$NiSO_4 \cdot 6H_2O$ in a magnetic field of 0 to 90 kG at liquid helium temperatures. Their least-square adjusted parameters are $g_{\parallel} = 2.216$, $g_{\perp} = 2.250$, $D = 4.741 \pm 0.001$ cm^{-1}, $E = 0.01 \pm 0.06$ cm^{-1}, $\phi = 39.0°$, and $\gamma = 0.266$ $mole.cm^{-3}$ in the ab plane and $\gamma = 0.272$ $mole.cm^{-3}$ along the c axis. But since the magnetization and the heat capacity measurements deal with the bulk properties of a single crystal, different contributions from non-equivalent ions could not be separated by this method. This could, however, be done by EPR.

Batchelder observed an anisotropic EPR spectrum corresponding to the transition between the two excited states of the Ni^{2+} spin triplets. His EPR results could be qualitatively explained by an isolated Ni^{2+} system, if an E of 0.032 cm^{-1} was used along with the parameters given by Fisher et al. But Batchelder's observations on the temperature dependence of the EPR line-widths and line positions could not be explained by the isolated Ni^{2+} model even if the molecular field correction was introduced. By use of a far-infrared spectrum Batchelder estimated the nearest neighbor exchange interaction to be approximately equal to 0.12 cm^{-1}. His studies of Mn^{2+}, Co^{2+} and Cu^{2+} in α-$NiSO_4 \cdot 6H_2O$ also indicated the importance of the exchange interactions with the neighboring Ni^{2+} ions. We will review his EPR work and report a new type of transition observed in α-$NiSO_4 \cdot 6H_2O$.

II. EXPERIMENTAL

A. Spectrometer

The EPR spectrometer used for the low temperature experiments on single crystals was essentially identical to that of previous investigators in this laboratory (Pratt, 1967; Batchelder, 1970). It was described in detail by Pratt. A few minor modifications were made. The first modification was to replace the magic tee with a three-port circulator and to change the bridge arrangement. Secondly, we modified the V4502 amplifier by the addition of a twin T filter in the external position. The 825 Hz modulation was provided by a HP200CD wide range oscillator followed by a power amplifier. A frequency of 825 Hz fed into the Varian V4250B sweep unit made the spectrometer less susceptible to microphonic noise coming from the bubbling of the liquid nitrogen in the Dewar and other laboratory vibrations. The third change was the use of a variable microwave coupler constructed from a length of 6 mm diameter quartz rod, a teflon circular disk (1 in. dia. x 0.4 in. high), and a 30 gauge copper wire helix imbedded in the teflon disk. Upon rotation of the quartz rod, the helical copper wire moved in front of a 5/16 in. coupling window. This enabled the incoming microwaves to vary their coupling with the cavity. The entire waveguide unit is shown in Fig.1. The quartz rod was held tightly to minimize its vibration. Several styroform pieces were inserted along the waveguide as shown in Fig.1. Although this variable coupler introduced an additional microphonic noise from the vibration of the quartz rod, it allowed an adjustment of coupling at

all temperatures.

The crystal mounting was accomplished by holding the crystals down with Scotch Brand Magic Tape in grooves machined in teflon disks. The three most frequently used mounters are sketched in Fig.2. For well cleaved single crystals the mounting was excellent.

A few experiments were conducted on powdered samples with a conventional Varian spectrometer and 100 kHz modulation. Cold N_2 was passed over the sample and it lowered the temperature to about -180°C.

The X-band microwave frequency was measured by a Hewlett-Packard electronic counter, model HP5245L, and a frequency converter unit, model HP5255A 3 to 12.4 GHz. When the HP5255A did not function well, a HP2590A microwave frequency converter and HP5253B (50 to 500 MHz) plug-in unit were substituted. The measurement of magnetic field was accomplished by detecting proton NMR with a Harvey-Wells FC-50 oscillator. The NMR probe was mounted outside of the Dewar on a pole face of the magnet. The NMR frequency, ν_p, was converted to a field by

$$H = 2.3487 \times 10^{-4} \nu_p$$

The electron g factor was calculated directly from the ratio of the electron and proton resonance frequencies by

$$g = \frac{h \nu_e}{\beta \nu_p} = 3.04208 \times 10^{-3} \frac{\nu_e}{\nu_p}$$

or from the magnetic field by

$$g = 7.1557 \times 10^{-7} \frac{\nu_e}{H}$$

where ν_e is the electron resonance frequency and β is the Bohr magneton which is equal to 9.2732×10^{-21} erg.gauss^{-1}.

B. Computer

In this work three digital computers were employed. Large scale numerical calculations and matrix diagonalization were performed with the XDS 910 of the College of Chemistry and with the CDC 6600 of the Lawrence Radiation Laboratory, Berkeley. We have also extensively used a PDP-8/I computer (Digital Equipment Corporation) equipped with 8K word memory, 32K Disk Monitor System, High Speed Reader and AX08 Laboratory Peripheral. This system, purchased primarily for the purpose of signal averaging and data processing, was extremely useful for various numerical calculations programmed in the easy Focal language. Spectral simulations were readily carried out on this computer by the addition of a 10.5 inch oscilloscope (Tektronix, Type 611) and a point plotter (HP 7004A X-Y recorder with a 17173A null detector). We will list two sample programs in Appendix V. One is a Focal program for the computation of the theoretical field positions of Ni^{2+} ion in $ZnSeO_4.6H_2O$ by solving the cubic equation and by successive iteration. The other is a Fortran IV diagonalization program of any symmetric hermitian matrix to give its eigenvalues and eigenvectors.

C. Chemicals And Crystal Growth

Most of the chemicals used in this work were commercially available, but some selenates, bromates and carbonates were prepared in the manner described below.

Single crystals of most metal hydrates are readily grown by slow evaporation from aqueous solution. An introductory book by Holden and Singer (1960) may prove useful for a beginner. All syntheses and crystal growing were done on a one-tenth to one-hundredth of a mole scale.

A desired compound is weighed in a beaker and dissolved in a minimum amount of distilled water. A magnetic stirrer and a hot plate, adjusted below boiling, often quicken the dissolution. The solution is filtered and cooled to room temperature. Occasionally many small crystals precipitate out in this rapid cooling process. They are kept for later use as seed crystals. Alternatively, seed crystals may be grown by placing a few drops of a saturated solution on a watch glass and allowing it to evaporate. Daily check of the slowly evaporating solutions is almost necessary, especially for the growth at elevated temperatures. The solutions are stirred and the crystals are moved or turned over to ensure uniform growth. Constant decantation or filtration may be necessary to allow only a few crystals to grow to large size. Where more than one form of hydrate is possible, careful control of temperature is imperative. An ample supply of small beakers (15 to 25 ml), forcepts, spatulas and vials is desirable. Experience helps a great deal, but it is the power of Nature that one

has to rely upon to produce good single crystals. Luck can and does play a large part in crystal growing.

Identification of crystal axes were usually unambiguous from their well developed tetragonal or trigonal shapes. However, when the identification seemed uncertain, particularly in some selenates, a cross-polaroid optical technique was employed (Gibb, 1942).

1. Metal Selenates

Selenates of divalent metallic elements are easily synthesized by reacting metal carbonates with a small excess of selenic acid (Klein, 1940). The reaction rapidly proceeds with vigorous effervescence and generation of heat. All the selenate crystals, except $NiSeO_4 \cdot 6H_2O$, were stored in a refrigerator at 5°C, for they dehydrate slowly to become white solids if left in dry air at room temperature. Table I lists the stable forms of metal selenates investigated by Klein.

(a) $ZnSeO_4 \cdot 6H_2O$

Fourteen grams of basic zinc carbonate (Mallinckrodt) were reacted with 35 ml of 40% selenic acid (H_2SeO_4, Alfa Inorganic). Slow evaporation of the colorless solution produced large transparent single crystals of tetragonal prismatic habit at room temperature, but with tetragonal bipyramidal habit at 5°C in a refrigerator. These two habits were reported for α-$NiSO_4 \cdot 6H_2O$ by Groth (1908) and are sketched in Fig. 3a and b. The tetragonal prism (a) has its crystal axis perpen-

Table I. Stable forms of metal selenates (Klein, 1940)

Metal	$n \cdot H_2O$	Crystal structure	Color	Stable temperature range in soln (°C)	Stable temperature range in room air (°C)
Mg	6	monoclinic		3.6~89.5	< 50
Mg	7			-7.1~ 3.6	
Mn	5*	triclinic	light garnet		< 55
Mn	2	orthorhombic			
Co	7	monoclinic	ruby red	-6.4~11.4	
Co	6*	monoclinic	dark pink	11.4~33.5	< 25
Co	5	triclinic		30~60	
Cu	5*	triclinic	blue	-1~40	
Ni	6*	tetragonal	deep green	-3~82	
Zn	6*	tetragonal	colorless	-7~35	< 25
Zn	5	triclinic		35~44	

*Synthesized in the present work.

dicular to the tetragonal base, while the tetragonal bipyramid (b) has its unique axis along the line connecting the two apexes. Both forms are easily cleaved by a razor blade along a plane perpendicular to their unique axes. No paramagnetic impurity was found by EPR from 300° to 1.3°K.

(b) $NiSeO_4 \cdot 6H_2O$

Since the commercially available $NiSeO_4 \cdot 6H_2O$ (Alfa Inorganic) contained large amounts of Co^{2+} impurity, a synthesis of $NiSeO_4$ was done by the carbonate method. Large crystals of tetragonal prism or plate, and never of bipyramid, crystallized at room temperature. No dehydration takes place in air at room temperature. $NiSeO_4 \cdot 6H_2O$ prepared from nickelous carbonate (Mallinckrodt) was found to contain traces of Co^{2+} and Mn^{2+} by EPR at 1.3°K.

The synthesis of pure nickelous carbonate was tried from $NiSO_4$ after the manner described by Brauer (1963). Fifteen grams of $KHCO_3$ (Baker and Adamson) was dissolved in 150 ml of water and CO_2 was bubbled through the solution kept at 0°C for about 15 minutes. 9.2 gram of $NiSO_4 \cdot 6H_2O$ (Alfa Inorganic, labeled "Ultra-pure") was dissolved in 350 ml of water and cooled to 0°C. Then the two solutions were mixed, stirred, and kept in a refrigerator. After three days dry N_2 gas was bubbled through the green solution to drive off excess CO_2. A thin film on the surface and white flocculent precipitate disappeared in this process. Fine crystalline particles deposited, leaving a clear supernate solution. After two days of sitting at room temperature,

the supernate liquid was decanted. The light green precipitate was washed several times with 5 ml of water. The product was dried in an oven at 105°C for a day. Starting with this $NiCO_3$, pure $NiSeO_4$ was prepared by the carbonate method.

(c) $CuSeO_4$, $MnSeO_4$ and $CoSeO_4$

Solutions of above selenates were synthesized by the carbonate method from basic cupric carbonate (Baker and Adamson), manganous carbonate (Merek & Co.) and cobaltous carbonate (Baker's Analyzed). According to Klein, $CuSeO_4 \cdot 5H_2O$ is least water soluble of all the metal selenates and decomposes in solution above 50°C.

2. α-$NiSO_4 \cdot 6H_2O$

Thin plates of α-$NiSO_4 \cdot 6H_2O$ single crystals were available from Semi-Elements Corporation. But these crystals contained a large amount of Co^{2+} impurity and traces of Cu^{2+} and Mn^{2+} (Batchelder, 1970). $NiSO_4$ was commercially available from several companies--Baker and Adamson, Mallinckrodt, Alfa Inorganic, to name a few-- all of which contained only a trace of Co^{2+}. Repeated crystallization near 0°C reduced the amount of impurity ions beyond our detection by EPR. "Ultra-pure" $NiSO_4 \cdot 6H_2O$ from Alfa Inorganic was indeed pure and free from Co^{2+} impurity.

When a saturated solution of $NiSO_4$ is kept at room temperature,

most likely $NiSO_4 \cdot 7H_2O$ precipitates. The heptahydrate that grows in a long monoclinic slab easily dehydrates to develop white marks on the surface. The hexahydrate forms a prism, similar to type (a) of $ZnSeO_4 \cdot 6H_2O$, and is stable in air. Some observers claim that the hexahydrate has deeper green than the heptahydrate.

In order to grow α-$NiSO_4 \cdot 6H_2O$ the solution must be kept well above 30.5°C, the temperature at which hexa- and hepta-hydrates exist in equilibrium (Gmelin, 1966). A simple thermostat bath was constructed, which was equipped with two single-blade heaters of 250 watts, stirrer, relay switch and a mercury thermo-switch thermometer. The bath temperature was controlled at 38.5±0.1°C. A large crystal (5x5x3 mm^3) of square prismatic shape can be grown within a few days in this apparatus. Impurity ions were introduced by adding a few drops of corresponding sulfate solutions.

3. $La_2Mg_3(NO_3)_{12} \cdot 24H_2O$ (LMN)

Lanthanum nitrate ($La(NO_3)_3 \cdot 5H_2O$, Alfa Inorganic) and magnesium nitrate ($Mg(NO_3)_2 \cdot 6H_2O$, Baker and Adamson) are mixed by the mole ratio of 2:3 and dissolved in water. Slow evaporation of water brings forth large transparent hexagonal plates. The crystals are relatively free from crystal imperfections and from paramagnetic impurities.

Deuteration of LMN was carried out by repeated crystallization from D_2O solution in a vacuum desiccator. $Ni(NO_3)_2 \cdot 6H_2O$ (Baker and Adamson, "low cobalt") was doped in LMN. For Cu^{2+} in LMN Cu^{63} isotope was used ($Cu^{63}O$, Union Carbide, Oak Ridge National Laboratory).

4. Metal Bromates

(a) $Zn(BrO_3)_2 \cdot 6H_2O$

This chemical is available from Alfa Inorganic or from Atomergic Chemicals. A large crystal of cubic habit with pronounced {111} faces, shown on the left, is readily grown by slow evaporation. A rectangular prism, though rarely grown, may prove very useful for orientational dependence of impurity spectra. A trace of Ni^{2+} ion is found by EPR.

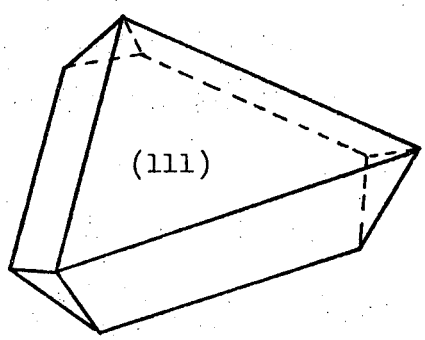

(b) Bromates of Ni^{2+}, Co^{2+}, and Cu^{2+}

Metal bromates are synthesized by reacting metal sulfates with barium bromates. Weigh out 10.5 gm of $Ba(BrO_3)_2 \cdot H_2O$ (Mallinckrodt) in a beaker and add 10 ml of water. Barium bromate is not very soluble in water. Dissolve equal mole of metal sulfate in water and add the solution dropwise to barium bromate from a separatory funnel. Maintain the mixture warm on a hot plate and keep stirring. A clear solution is obtained by filtering white $BaSO_4$ powder. Hexagonal prisms are crystallized both at room temperature and at 5°C. The colors of metal bromates are colorless, green, dark pink and blue for Zn^{2+}, Ni^{2+}, Co^{2+} and Cu^{2+}, respectively.

III. HOST LATTICES

A. α-$NiSO_4 \cdot 6H_2O$ and $ZnSeO_4 \cdot 6H_2O$

1. Crystal Structure

The crystal structure of $ZnSeO_4 \cdot 6H_2O$ has not been examined in detail. But it is structural with the tetragonal α-$NiSO_4 \cdot 6H_2O$ and its lattice dimension ratio is $a_o : c_o = 1 : 1.8949$ (Klein, 1940). Here we will discuss the crystal structure of α-$NiSO_4 \cdot 6H_2O$, for a complete structure has been established for it. The X-ray analysis of α-$NiSO_4 \cdot 6H_2O$ was first made by Beevers and Lipson (1932) and discussed by Beevers and Schwartz (1935). O'Connor and Dale (1966) investigated the arrangement of the hydrogen bonds in α-$NiSO_4 \cdot 6H_2O$ by neutron diffraction.

The crystal is tetragonal with a space group of either $P4_12_12$ or $P4_32_12$ depending upon its enantiomorphic form. There are four molecules in a unit cell whose dimensions are $a_o = b_o = 6.790 \pm 0.003$ A and $c_o = 18.305 \pm 0.004$ A. Fig. 4 is a three-dimensional model of α-$NiSO_4 \cdot 6H_2O$, depicting only Ni^{2+} and SO_4^{2-} ions for simplicity's sake. The large dark balls represent Ni^{2+} ions with six coordination axes. The small tetrahedral units are SO_4^{2-} ions. Four unit cells are shown here. The $Ni(H_2O)_6^{2+}$ and SO_4^{2-} groups form a layer lying in the (001) plane at positions of 0, 1/4, 1/2 and 3/4 in units of c_o. Fig. 5 shows a projection of one-half of a unit cell on (001) plane along the c axis. The two layers at z=0 and z= $c_o/4$ are depicted here with the relative positions of Ni, S and O atoms. The numbers within circles represent the coordinates in units of c_o along the c axis as determined by Beevers

and Lipson. The numbers in parentheses indicate the five nonequivalent oxygen atoms as denoted by O'Connor and Dale.

In each layer the $Ni(H_2O)_6^{2+}$ is located between two SO_4^{2-} units; one sulfate having the horizontal oxygen, O(5), closer to Ni^{2+} and the other having the vertical oxygen, O(4), closer to Ni^{2+}. For a given layer there is a two-fold symmetry about the ab bisector which we will hereafter call the γ axis. Adjacent layers are generated by the three successive operations of a four-fold rotation about the c axis, a translation of $c_o/4$ along the c axis and a translation of $a_o/\sqrt{2}$ units along the γ axis. The sense of the four-fold rotation may be right or left-handed, corresponding to the two enantiomorphic forms of α-$NiSO_4 \cdot 6H_2O$. Fig.5 corresponds to the left-handed enantiomorph. Each layer is linked to another by the hydrogen bonds between O(1') and O(3) and between O(3') and O(4). The Ni-O bond distances as determined by O'Connor and Dale and by Beevers and Lipson are listed below.

	O & D ($6H_2O$)	B & L ($6D_2O$)
Ni-O(1)	2.02±0.01 A	2.04 A
Ni-O(2)	2.07±0.01	2.04
Ni-O(3)	2.10±0.01	2.02

O'Connor and Dale made no correction for the thermal vibration effects. The actual uncertainty in the values of these bond distances may probably be much greater than the standard deviation given above. O'Connor and Dale concluded "Individual Ni-O bond distances do not show significant departures from their mean value, 2.06±0.02 A." We should

be careful not to place an undue significance upon the reported variation in the three Ni-O bond distances. All the bond angles of O-Ni-O within a $Ni(D_2O)_6^{2+}$ group are close to 90°, forming nearly a perfect octahedron. The crystallographic data alone will not unambiguiously support any distortion of an octahedron at the Ni^{2+} site.

The major difference among the six water molecules about Ni^{2+} is in that O(1) and O(2) have two hydrogen bonds, while O(3) has three. The O(3) acts as a proton acceptor and its negative charge should be diminished by the additional hydrogen bonding. This point becomes clear in the Pauling diagram of electrostatic valency given by Beevers and Schwartz. Lines of force start from cations (or more positively

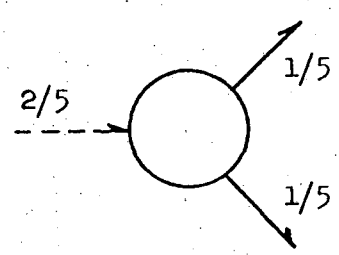

Type 1 and 2

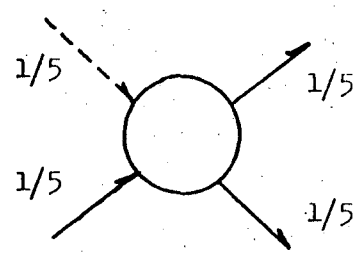

Type 3

charged atoms) and end on anions (or more negative atoms). Here the dotted arrows indicate the Ni-O bonds. The numbers refer to the strength of their electrostatic bonds. The sum of both incoming and outgoing lines about an atom must be equal to the electric charge on it. For example, the O(1) has one incoming bond of 2/5 from Ni^{2+}, one outgoing bond of 1/5 to O(3') and one outgoing bond of 1/5 to O(5), resulting in the net charge of zero. Similarly, O(2) has 2/5 from Ni^{2+},

1/5 to O(4) and 1/5 to O(5). O(3) has 1/5 from Ni^{2+}, 1/5 from O(1'), 1/5 to O(4) and 1/5 to O(5). Therefore, these purely electrostatic arguments predict that the oxygen atoms of type 1 and 2 are more strongly bonded to Ni^{2+} than that of type 3. This is equivalent to saying that the bond distance of Ni-O(3) should be longer than Ni-O(1) and Ni-O(2). We would assume the Ni-O(3) axis as the z axis of the crystalline electric field affecting the central metal ion. A more detailed argument will be given later in IV-A-1, since the nature of this bonding is important in predicting the properties of the paramagnetic ions in this crystal.

2. Magnetic Axes

The angle between the c axis and the magnetic z axis, hereafter called ϕ, is of special interest to us. The Zeeman interaction is primarily determined by the relative orientation of the z axis and the magnetic field. The crystallographic value for the angle ϕ is determined under the assumption that the axial crystal field is aligned along the Ni-O(3) bond. The magnetically determined value, however, refers to the principal axis of the spin Hamiltonians. The values of ϕ are tabulated in Table II along with the methods of determination and authors.

All the previous workers have assumed that one of the principal magnetic axes of a single crystal was parallel to the γ axis. This is the axis of the easiest magnetization and the largest magnetic susceptibility. This axis should also be a principal axis of the spin-Hamiltonian of the individual Ni^{2+} ions. One-half of the Ni^{2+} ions

Table II. Values of ϕ in α-$NiSO_4 \cdot 6H_2O$

ϕ	Methods of determination	Authors
33°	magnetic susceptibility	Watanabe (1962)
42°	neutron diffraction and X-ray analysis	O'Connor and Dale (1966)[a]
39°	heat capacity in strong magnetic field	Fisher and Hornung (1968)[b]
39.8°	EPR at 4.2°K	This work

a. See also Beevers and Schwartz (1935).

b. See also Stout and Hadley (1964).

have two-fold symmetry about one of the γ axes, [110], and one-half have two-fold symmetry about the other, [$\bar{1}$10]. If we denote this axis of each $Ni(H_2O)_6^{2+}$ by x, then y and z axes are contained in the γc plane, (1$\bar{1}$0) or ($\bar{1}$10). Fig. 6 shows the projection of the magnetic axes of one unit cell on the γc planes.

In our EPR experiments the sample orientation is fixed in a cavity and the magnetic field direction is rotated in a horizontal plane that coincides with one of the crystal ab, ac and γc planes. We can write down the direction cosines of the magnetic field with respect to the principal magnetic axes, (x,y,z). These direction cosines are tabulated in Table III a,b,c. The following abbreviations are used in the table: K1= sinϕ, K2= cosϕ, K3= sinα , K4= cosα , and RT= $1/\sqrt{2}$, where α is the direction of the magnetic field measured from the c axis in the ac and the γc planes and from the γ axis in the ab plane.

In the ab plane there are only two magnetically nonequivalent ions. In this plane the angle α is measured from the x axis of ion 4. Transformation of α to 90- α generates the direction cosines of ion 2 from those of ion 1. Ion 3 is equivalent to ion 1, save for the opposite signs in the direction cosines. Similarly, ion 4 is equivalent to ion 2. When the magnetic field, H, is oriented along the a or b axes, all four ions become identical. At $\alpha = 0°$ the spectra of the two ions are farthest apart, with ions 2 and 4 showing a perpendicular spectrum.

The ac plane spectra will exhibit a similar behavior. We will denote by α the angle that H is rotated from the c axis toward the a axis in the ac plane. Ions 1 and 4 are equivalent, while ions 2 and 3 are equivalent. The direction cosines of ion 3 are obtained by substitution of -α for α in those of ion 1. A similar change yields

Table III. Direction cosines (ℓ,m,n) in α-$NiSO_4 \cdot 6H_2O$

Ions	ℓ	m	n
	a. Magnetic field in ab plane		
1	K3	-K2×K4	K1×K4
2	-K2	-K2×K3	K1×K3
	$H_{3i} = -H_{1i}$, $H_{4i} = -H_{2i}$, ($i = \ell,m,n$)		
	b. H in ac plane		
1	K3×RT	K1×K4-K2×K3×RT	K2×K4+K1×K3×RT
2	-K3×RT	K1×K4-K2×K3×RT	K2×K4+K1×K3×RT
	For ion 3 (or 4) replace α by $-\alpha$ in ion 1 (or 2)		
	$RT \equiv 1/\sqrt{2}$		
	c. H in γc plane		
1	0	$-\sin(\alpha-\phi)$	$\cos(\alpha-\phi)$
2	-K3	K1×K4	K2×K4
3	0	$-\sin(\alpha+\phi)$	$\cos(\alpha+\phi)$
4	K3	K1×K4	K2×K4

the direction cosines of ion 4 from ion 2. At $\alpha=0°$, H along the c axis, the four ions are equivalent. So are they at $\alpha = 90°$, or along the a axis. Therefore, we will observe at most two types of spectra, except at the a and c axes where we will expect only one kind.

The most interesting spectrum will be seen in the γc plane. Here α is measured from the c axis toward [110] axis. Ions 2 and 4 are equivalent, while ions 1 and 3 are not. Three kinds of spectra will be observed at all angles except along the c axis and along the γ axis. Rotation of the magnet in this plane will encounter all three principal axes. When $\alpha = +\Phi$, ion 1 will have the magnetic field totally along its z axis. At $\alpha=90-\Phi$ the y axis of ion 3 is met, and at $\alpha = 90°$ the x axes of ions 2 and 4 are encountered. Thus, the γc plane data will contain the richest information, notwithstanding the most complex spectra.

It turns out that the direction cosines of Table III are too simple to account for the experimental results for ions substituted in the $ZnSeO_4.6H_2O$ lattice. The necessary correction in the direction cosines is different for each substituted paramagnetic ion and will be discussed in sections IV, V and VI.

B. $La_2Mg_3(NO_3)_{12}\cdot 24H_2O$

1. Crystal Structure

Zalkin, Forrester and Templeton (1963) studied in detail by X-ray diffraction the crystal structure of cerium magnesium nitrate, $Ce_2Mg_3(NO_3)_{12}\cdot 24H_2O$, CeMgN. There exists several isostructural double nitrates known with the general formula $T_2D_3(NO_3)_{12}\cdot 24H_2O$, where T is a trivalent ion such as Bi^{3+} and lanthanide ions and D is a divalent ion like Mg^{2+} and Zn^{2+}. They are rhombohedral crystals whose space group belongs to $R\bar{3}$. The hexagonal unit cell contains three formula units: six T ions and nine D ions. The cation D is surrounded by six water molecules in nearly octahedral symmetry, while the cation T is surrounded by twelve oxygen atoms of four nitrate ions arranged approximately in icosahedral symmetry.

While there is only one type of trivalent ion, there are two different types of divalent ions. Three Mg^{2+} ions per unit cell belong to the first kind and six Mg^{2+} ions belong to the second kind. Fig. 7 shows the positions of Mg^{2+} ions relative to the Ce^{3+} ion in CeMgN. The distances are in nanometers. The Mg(1) is surrounded by six Ce^{3+} ions at a distance of 6.98 A, and its site symmetry is C_{3i}. The nearest Mg^{2+} ions surrounding the Mg(1) are six Mg(2) ions at a distance of 7.15 A. The Mg(2) ion has as its nearest neighbors another Mg(2) on the trigonal axis at 4.99 A away, one Ce^{3+} ion at 6.17 A, three Ce^{3+} ions at 6.36 A and six Mg(1) at 7.15 A. The site symmetry of the Mg(2) ion is C_3. This difference in the site symmetry of the Mg^{2+} ions will manifest itself in their different degrees of distortion in the EPR of paramagnetic ions substituted in the Mg^{2+} sites; site 1 is nearly isotropic and site 2 is more anisotropic.

2. Paramagnetic Ion Impurities

Many paramagnetic ions doped in double nitrates have already been investigated by EPR. Two types of divalent ions have been observed for Co^{2+}, Mn^{2+} and Ni^{2+} but only one type of Cu^{2+} is reported. The magnetic z axis coincides with the [111] direction of the crystal. For the site 1 the trigonal distortion of an octahedral symmetry is small. The EPR spectra of the paramagnetic ions at site 1 are characterized by nearly isotropic g factors and hyperfine splitting constants A. For site 2 the trigonal distortion is fairly large and the g and A values show greater anisotropy. Since the type 2 ion can have another type 2 ion only at a distance of 4.99 A, the probability of a spin-spin exchange interaction is high in a relatively concentrated sample.

We need to clarify our distinction between the type 1 ions and the type 2 ions. Trenam (1953) and Gager et al. (1958) observed two types of Co^{2+} in BiMgN, long before the X-ray analysis of Zalkin et al. was reported. They called the less isotropic ion type I and nearly isotropic ion type II. Trenam (1953) also reported two types of Mn^{2+} in the same host lattice, and said that the type II ion, which had a smaller zero-field splitting or D value, was twice as intense as the more anisotropic type I. His conclusion contradicts the assignment of the Mg^{2+} ions by Zalkin et al. Accordingly to the latter authors the three Mg^{2+} ions in site 1 have a higher site symmetry than the six Mg^{2+} ions in site 2. Zalkin et al. showed that the oxygen atoms of the six water molecules surrounding the Mg^{2+} ions are at the corners of an octahedron which would be regular if bond angles were changed by less than 1° for site 1 and by 5° for site 2.

Culvahouse (1962) listed the D values of Ni^{2+} and the g values of Co^{2+} in several double nitrates. The ions in the "X-site" always had smaller D values and more nearly isotropic g values than the ions in the "Y-site". Thus, his X-ion should correspond to site 1 of Zalkin et al. and the Y-ion to site 2. And yet his diagram of the divalent X-ion shows another X-ion on the trigonal axis as the nearest neighbor, exactly opposite to the assignment of Zalkin et al. (Culvahouse et al., 1969). In this report we will follow the assignment of Zalkin et al. We will also abbreviate $La_2Mg_3(NO_3)_{12}\cdot 24H_2O$ as LMN.

Since the z axes of the divalent sites are all identically parallel to the trigonal axis of the crystal, there is only one set of direction cosines to be specified for each kind of ion. When the magnetic field lies in the hexagonal plane, (111), the line positions will correspond to the perpendicular spectra and will not vary with the field direction. If we assume that the x axes of the divalent ions lie parallel to the hexagonal edge of the single crystal, the direction cosines in the xz plane are given simply by ($\sin\alpha$, 0, $\cos\alpha$), where α is the angle between the [111] axis and the magnetic field.

C. $Zn(BrO_3)_2 \cdot 6H_2O$

1. Crystal Structure

The structure of this crystal was studied by Wyckoff (1922), Bradley and Jay (1932) and Yü and Beevers (1935). We will summarize the work of Yü and Beevers.

$Zn(BrO_3)_2 \cdot 6H_2O$ forms a cubic crystal of space group Pa3 (T_h^6) with four molecules per unit cell of a_o = 10.316 A. The unit cell consists of the octahedral $Zn(H_2O)_6^{2+}$ and the pyramidal BrO_3^- groups arranged on the four body diagonals of a cube. The zinc atoms occupy the positions at (000), (0 1/2 1/2), (1/2 0 1/2) and (1/2 1/2 0), forming a face-centered cubic sub-lattice. The bromine atoms lie on the corners of a simple cubic sub-lattice of nearly one half the cell edge of the actual crystal lattice; i.e., at (0.259, 0.259, 0.259).

Each Zn atom has a coordination of six water molecules and forms a regular octahedron. The distance $Zn-OH_2$ equals 2.12 A. Each Br atom is situated at the vertex of a trigonal pyramid whose base consists of three oxygen atoms at 1.54 A from the bromine atom. The $Zn(H_2O)_6^{2+}$ unit is surrounded by eight BrO_3^- units, and the hydrogen bonds bridge the two groups. Fig. 8 shows the bonding structures and the coordinates of the atoms in units of a_o along the [001] axis.

Each water molecule has two outgoing bonds (-1/6 each in a Pauling diagram) to oxygen atoms of a BrO_3^- group and one incoming (+1/3) bond from Zn^{2+}. Out of the twelve hydrogen bonds six are attached to two BrO_3^- groups on the same body-diagonal of the $Zn(H_2O)_6^{2+}$ group, and the remaining six hydrogen bonds are attached to six BrO_3^- units on the three neighboring body-diagonals. The distances of the two types of hydrogen bonds, H_2O-O, are very similar, 2.72 and 2.74 A, and the

angle between the two bonds, O-H_2O-O, is 121°. Thus, each zinc ion is surrounded by six water molecules arranged in nearly octahedral symmetry with a small trigonal distortion along its body-diagonal. The overall symmetry of the crystal is cubic, however, because of the symmetrical arrangement of the four such distorted octahedra.

2. Magnetic Axes

Despite its simple crystallographic structure, $Zn(BrO_3)_2 \cdot 6H_2O$ has previously been used as a diamagnetic host only for Cu^{2+} ion; even in this system, only the high temperature spectrum was studied. The EPR of undiluted $Ni(BrO_3)_2 \cdot 6H_2O$ was investigated by Owen but not published (quoted by Bowers and Owen, 1955). The reason for this apparent unpopularity seems due to the complications arising from the four sets of spectra.

The divalent ion at the Zn site is subject to a small trigonal distortion from a regular octahedral crystal field along the body diagonal. There are four such ions which are denoted as ions 1,2,3 and 4. We assume that each magnetic z axis is parallel to the three-fold axis. If the crystal field is exactly trigonal or of higher symmetry, the assignment of the z axis alone is sufficient to describe the EPR spectra. The x and y axes can be placed anywhere in the plane normal to the z axes, as long as the three-fold symmetry is kept intact. We will take the triangular edge of the single crystal as the x axis for the sake of convenience. Fig. 9 shows both a projection of the magnetic axes onto the (111) plane and its side view.

The angles that the z axes of ions 1, 2 and 3 form with respect to the (111) plane are called ϕ and are equal to -19°28'. This is because each of the (111) planes intersect with the three other {111} planes forming an angle of 109°28' (the tetrahedral angle). In the present EPR work the magnetic field is rotated both in the (111) plane and in the yz plane of ion 4 (see Fig. 9). The direction cosines are given in Table IV a and b, in which the same abbreviations are used an in Table III. The magnetic field direction, α, is measured counterclockwise from x_1 in the (111) plane, and from the (111) plane toward the [111] axis in the yz plane of ion 4. When H is in the (111) plane, ion 4 will show a perpendicular spectrum at all angles and ions 1, 2 and 3 will exhibit similar spectra, phase shifted by 120°. When H is rotated in the yz plane of ion 4, four kinds of strongly angularly dependent spectra will be observed. Along the z_4 axis ion 4 will display a parallel spectrum and ions 1, 2 and 3 will all be equivalent. Along the y_4 axis two sets of spectra will be seen; one perpendicular spectrum of ions 1 and 4, and the other a superposition of ions 2 and 4.

Table IV. Direction cosines (ℓ,m,n) in $Zn(BrO_3)_2 \cdot 6H_2O$

Ions	ℓ	m	n
	a. H in (111) plane		
1	K4	K1×K3	K2×K3
2	cos(α-120°)	sin(α-120°)×K1	sin(α-120°)×K2
3	cos(α+120°)	sin(α+120°)×K1	sin(α+120°)×K2
4	-K3	K4	0
	b. H in the yz plane of ion 4		
1	-K4	-K2×K3	K1×K3
2	-K4×sin30°	-K2×K4×cos30° -K1×K3	-K1×K4×cos30° +K2×K3
3	K4×sin30°	K2×K4×cos30° -K1×K3	K1×K4×cos30° +K2×K3
4	0	K4	K3

IV. Ni^{2+} IN DIAMAGNETIC HOSTS

A. Theory

1. Crystal Field Model for $3d^8$

Crystal field calculations are traditionally carried out by use of operator equivalent method developed by Stevens (1952). We will follow closely the approach of Abragam and Bleaney (1970, Chap. 7; henceforth abbreviated as A & B).

Here we are employing an intermediate field treatment in which the energy levels are characterized by given values of the total orbital and spin angular momentum quantum numbers L and S. There exists a set of essentially empirical rules, called Hund's rules, that dictate which state will be the ground state in the L-S coupling approximation. These rules are: 1) The ground state will have the maximum value of S consistent with the Pauli exclusion principle. 2) If several state have the same highest spin degeneracy, the most stable one will be the state of the highest L. Hence, the lowest term of the free Ni^{2+} ion, ($3d^8$), is ^3F (L=3, S=1). In the hydrated salts the Ni^{2+} ion is influenced by the electrostatic field of the surrounding water molecules. The effect of a predominantly octahedral crystal (or ligand) field is to split the seven-fold orbital degeneracy (2L+1) of ^3F into a lowest singlet ($^3A_{2g}$) and two excited triplets ($^3T_{2g}$, $^3T_{1g}$), the $^3T_{1g}$ lying higher in energy than $^3T_{2g}$. The overall splitting amounts to about 15,000 cm^{-1} in many hydrates of Ni^{2+}.

In the presence of a small tetragonal distortion from an octahedral crystal field, the crystal field potential is expressed as

$$\mathcal{H} = B_4 \left(O_4^0 + 5O_4^4\right) + \left(B_2^0 O_2^0 + B_4^0 O_4^0\right) \qquad (1)$$

where B's are the magnitude of crystal fields and O's are the "spin-operators" that can be expressed in terms of several orbital angular momentum operators.

If the distortion is trigonal, the Hamiltonian is

$$\mathcal{H} = -(2/3)B_4(O_4^\circ + 20\sqrt{2}\, O_4^3) + (B_2^\circ O_2^\circ + B_4^\circ O_4^\circ) \qquad (2)$$

The matrix elements of each spin operator operating upon orbital wave-functions are already listed in several places (Low, 1960, Table V-IX; A & B, Table 15-19; Hutchings, 1964, Table VIII-XII). Fig. 10 a and b are schematic energy diagrams of octahedral plus axial fields acting upon an F state ion. These calculations are valid for d^2, d^3, d^7 and d^8 systems in a nearly octahedral symmetry (O_h), provided that the energy levels are all inverted for d^2 and d^7. The parameters 10Dq, and B_2° and B_4° in favorable cases, are experimentally determined from optical absorption spectra. The typical value of 10Dq is of the order of 10^4 cm^{-1} (see Table V). Both B_2° and B_4° are much smaller than 10Dq, and B_4° is in general some fifty times smaller than B_2°.

With the point-charge model Orton (1968) expresses B_2° and B_4° as

$$\left.\begin{aligned} B_2^\circ &= -\frac{3ee'\delta}{a^4}\alpha\langle r^2\rangle \\ B_4^\circ &= -\frac{ee'\delta}{a^6}\beta\langle r^4\rangle \end{aligned}\right\} \qquad (3a)$$

where e; an electron charge, e': effective charge of a ligand, a: metal-ligand distance in a purely O_h symmetry, δ : distortion from an octahedron along the z axis of the crystal field and positive for elongation, α and β : crystal field parameters listed in Table V, and $\langle r^n\rangle$: mean value of r^n tabulated in Table 7.6 of A & B.

Table V. Crystal field parameters for 3d ions.

Ion	$(3d)^n$	α	β	Ground term	λ $(cm^{-1})^a$	10 Dq $(cm^{-1})^c$
V^{2+}	3	2/105	2/315	$^4A_2$	55	12 400 ($^4T_2$)
Cr^{3+}	3	2/105	2/315	$^4A_2$	91	15 000 (^2E)
Mn^{2+}	5	---	---	$^6A_1$	(60)[b]	18 800 ($^4T_1$)
Co^{2+}	7	-2/105	-2/315	$^4T_1$	-178	8 100 ($^4T_2$)
Ni^{2+}	8	2/105	2/315	$^3A_2$	-324	8 500 ($^3T_2$)
Cu^{2+}	9	2/21	-2/63	$^2B_2$	-830	12 600 ($^2T_2$)[d]

a. Abragam and Bleaney (1970, Table 7.6).
b. Dunn, (1961).
c. For hexahydrates in solution; Griffith (1961, Table A40).
d. Holmes and McClure (1957).

For d^3 (V^{2+}, Cr^{3+}, Mn^{4+}) and for d^8 (Ni^{2+}, Cu^{3+}), α and β are both positive. Hence,

$$\left.\begin{array}{l} B_2^\circ \propto -\delta \\ B_4^\circ \propto -\delta \end{array}\right\} \qquad (3b)$$

Therefore, an elongation along the z axis results in negative B_2° and B_4°.

An axial crystal field splits the two triply degenerate excited states, $^3T_{2g}$ and $^3T_{1g}$, into a doublet and a singlet. There is one very important difference in the trigonal and tetragonal distortions. In the former the doublet is lower in energy, if B_2° and B_4° are positive. On the other hand, the tetragonal distortion places the singlet below the doublet. If Δ_1 is the singlet energy level above the ground state, and if Δ_2 is the doublet energy level, then Δ_1-Δ_2 is positive for a trigonal symmetry but negative for a tetragonal symmetry. This difference will be reflected through the spin-orbit coupling in the sign of the zero-field splitting, D, of the ground state spin triplet. Table VI summarizes the effects of axial distortion upon the energy levels of d^8 system.

Let us see if the crystal structure of α-$NiSO_4 \cdot 6H_2O$ can make any prediction as to whether this distortion will be an elongation or a compression. As mentioned in III-A-1, the water molecule of the type 3 has one additional hydrogen bond which makes the charge on O(3) less negative. As far as the bonding characters are concerned, Ni-O(1) and Ni-O(2) are equivalent. Assuming that the Ni-O(3) direction coincides with the z axis of the crystal field and that the O(1)-Ni-O(2) plane forms the xy plane, we can employ either the crystal field theory (CFT)

Table VI. Effects of axial distortion in d^{8*}

		Elongation	Compression
Trigonal	B_2^0, B_4^0	Negative	Positive
	$\Delta_2 - \Delta_1$	Positive	Negative
	$g_{\parallel} - g_{\perp}$	Positive	Negative
	D	Negative	Positive
Tetragonal	B_2^0, B_4^0	Negative	Positive
	$\Delta_2 - \Delta_1$	Negative	Positive
	$g_{\parallel} - g_{\perp}$	Negative	Positive
	D	Positive	Negative

(*) For d^3 system only the sign of $g_{\parallel} - g_{\perp}$ is reversed owing to the opposite sign of λ.

or molecular orbital (MO) theory to predict the energy levels of Ni^{2+} ion.

In the CF treatment of Ni^{2+} ion, the ground state is an orbital singlet. The first excited state is a triplet $^3T_{2g}$ in O_h symmetry, which would be split into a doublet ^3E_g (xy, yz) and a singlet $^3B_{2g}$(xy) in the D_{4h} symmetry. The more positive character of O(3) over O(1) and O(2) reduces the electron-electron repulsion between the unpaired metallic electrons and the ligand electron cloud that is distributed along the Ni-O(3) direction. In other words, the xz and yz orbitals (E_g) are more stabilized than the xy (B_{2g}) orbital, since the latter has no electron distribution along the z axis. Hence, the E_g state will be lower than the B_{2g}.

In the MO theory the metal T_{2g} orbital transforms as p electrons do in O_h. In the first excited state of Ni^{2+}, ($t_{2g}^5 e_g^3$ in the strong field representation), the unpaired electron in T_{2g} can form a π bond with the p electrons of the ligand oxygen atoms. As before, the descent of symmetry to D_{4h} breaks T_{2g} into E_g and B_{2g}, the latter transforming as the xy orbital. The two hydrogen bonds of O(1 or 2) plus the Ni-O(1 or 2) bond form approximately the sp^2 hybridization, leaving the third p orbital of O(1) and O(2) capable of forming a π bond with the Ni^{2+} ion. However, because O(3) has already four bonds of the sp^3 type, it is incapable of forming a π bond. Thus, the ligand electrons of O(1) and O(2) can be transferred to the metallic π orbital with its electron density distributed in the xy plane. Consequently, π(xy) is more destabilized owing to the greater electron-electron repulsion and hence higher in energy than the π(xz)

and π(yz) orbitals. Although both the CFT and MOT predict the orbital doublet below the singlet in D_{4h}, we prefer the CFT to MOT, because the water molecules are known to be essentially of non-π bonding character (Gray, 1965).

Let us see if the above argument can predict the crystal field symmetry of Cu^{2+} substituted in the Ni^{2+} site of α-$NiSO_4 \cdot 6H_2O$. In Cu^{2+} the ground state is a hole in either x^2-y^2 or z^2. Since the x^2-y^2 orbital has no electron distribution along the z axis, it is relatively unaffected by the more positive charge on O(3) caused by the additional hydrogen bond. The z^2 orbital, on the other hand, has its greatest electron density along the z axis. Hence, the electron in the z^2 orbital is stabilized, while the hole in the x^2-y^2 orbital is stabilized. Therefore, the ground state of Cu^{2+} in D_{4h} is expected to be x^2-y^2, as will be proved in section V.

2. Spin Hamiltonian

The concept of spin-Hamiltonian was developed mainly by the Oxford group (Pryce, 1950; Abragam and Pryce, 1951a; Bleaney et.al, 1950). It is mostly concerned with the ground states of magnetic ions alone, the effects of excited states being incorporated into a small set of adjustable parameters. It offers a simple theory to relate experimental observations in terms of these parameters. We will see how this can be achieved.

First, we will start with the energy levels determined by the crystal field as in Fig. 10. Next, we will introduce spin-orbit and electronic Zeeman interactions as perturbations to these energy levels.

The perturbing Hamiltonian is written as

$$\mathcal{H} = \lambda \vec{L}\cdot\vec{S} + \beta \vec{H}\cdot(\vec{L} + 2\vec{S}) \qquad (4)$$

where $\vec{L}$ is the orbital angular momentum operator in units of $\hbar$, $\vec{S}$ is the electron spin angular momentum operator, $\vec{H}$ is the external magnetic field, λ is the spin-orbit coupling constant, and β is the Bohr magneton which is equal to 4.6689×10^{-5} cm^{-1} $gauss^{-1}$. Here 2 is used for the free electron g factor which is actually equal to 2.0023. Using the second order perturbation theory (Ballhausen, 1961, section 6-f,g), we obtain the ground state energy

$$W = (2\delta_{ij} - \lambda \Lambda_{ij})S_i H_j - \lambda^2 \Lambda_{ij} S_i S_j - \beta^2 \Lambda_{ij} H_i H_j \qquad (5)$$

with $(i,j = x,y,z)$, $\delta_{ij} = 1$ if $i = j$, otherwise 0, and

$$\Lambda_{ij} = \sum_{n \neq 0} \frac{\langle 0 | L_i | n \rangle \langle n | L_j | 0 \rangle}{W_n - W_0} \qquad (6)$$

Here $|0\rangle$ is the orbital ground state of energy W_0 and $|n\rangle$ is the excited orbital state of energy W_n. The matrix elements Λ_{ij} are easily calculated with the help of Ballhausen's Appendix I . The first term in Eq.(5) corresponds to the electron Zeeman interaction, the second is responsible for the zero-field splitting of the spin multiplet, and the third term contributes to the "temperature independent" paramagnetic susceptibility. We will ignore the last term, because it only shifts the energy levels of spin multiplet by equal amounts and bears no effect on EPR measurements.

We introduce two second-rank tensors whose components are related to Λ_{ij} by

$$g_{ij} = (2\delta_{ij} - \lambda \Lambda_{ij}) \tag{7}$$

$$D_{ij} = -\lambda^2 \Lambda_{ij} \tag{8}$$

Since any tensor composed of linearly independent vectors can be diagonalized by a suitable transformation, the spin Hamiltonian is now expressed in the more familiar way,

$$\mathcal{H}_{spin} = \beta(g_x H_x S_x + g_y H_y S_y + g_z H_z S_z) + D\left[S_z^2 - S(S+1)/3\right] + E(S_x^2 - S_y^2) \tag{9}$$

The (x,y,z) axes are the principal magnetic axes of a paramagnetic ion, determined by the crystalline electric field. D and E are axial and rhombic components of the zero-field splitting constants and are determined as

$$D = -3D_{zz}/2 = 3\lambda^2 \Lambda_{zz}/2 \tag{10a}$$

$$E = -(D_{xx} - D_{yy})/2 = \lambda^2(\Lambda_{xx} - \Lambda_{yy})/2 \tag{10b}$$

These spin Hamiltonian parameters are closely related to the crystal field parameters:

$$\left.\begin{aligned} g_{\parallel} &= g_z = 2(1-4\lambda/\Delta_1) \\ g_{\perp} &= (g_x+g_y)/2 = 2(1-4\lambda/\Delta_2) \end{aligned}\right\} \tag{11}$$

$$g_{\parallel} - g_{\perp} = 8\lambda\frac{(\Delta_1 - \Delta_2)}{\Delta_1 \Delta_2} \tag{12}$$

$$D = \lambda(g_{\parallel} - g_{\perp})/2 \tag{13}$$

$$E = \lambda(g_x - g_y)/4 \tag{14}$$

Thus, the crystal field parameters can be indirectly determined by EPR,

which measures g, D and E.

If the local crystal symmetry is a tetragonal compression, then $\Delta_2 > \Delta_1$, as in Fig. 10b. Then, from Eq. (12), $g_{\parallel} > g_{\perp}$ for d^8, and $g_{\parallel} < g_{\perp}$ for d^3. Similarly, from Eq. (13), D is negative for a tetragonal compression, and from Eq. (3b) B_4^0 is positive. The results are summarized in Table VI.

Our next task is to calculate the eigenvalues of Eq.(9) for S=1. Choosing M = 1, 0, -1 for our basis functions, we obtain the energy matrix.

M \ M	1	0	-1
1	$D+G_1n$	$G_2(\ell-im)$	E
0	$G_2(\ell+im)$	0	$G_2(\ell-im)$
-1	E	$G_2(\ell+im)$	$D-G_1n$

(15)

where (ℓ,m,n) are the direction cosines of the magnetic field with respect to (x,y,z) axes, $G_1 = g_{\parallel}\beta H$, and $G_2 = g_{\perp}\beta H/\sqrt{2}$. The eigenvalues of the matrix (15) are the roots of the following cubic equation:

$$W^3 - 2DW^2 - W\left[E^2 - D^2 + (G_1n)^2 + G_2^2(\ell^2 + m^2)\right]$$

$$+ D\left[G_2^2(\ell^2 + m^2)\right] - E\left[G_2^2(\ell^2 - m^2)\right] = 0 \qquad (16)$$

which is usually solved using numerical approximation and a high-speed computer. Alternatively we have developed a computer diagonalization program for complex Hermitian matrices of any size to give both eigenvalues and eigenvectors, whereby the matrix (15) is directly diagonalized. The two methods have given identical results.

When H is applied along (x,y,z) axes, the solutions of Eq.(16)

are reduced to simple forms. Table VIIa,b tabulates the energy quanta necessary for the three resonant transitions and their relative intensities. The transitions 2, 3 and 1 refer to those from the first excited state to the second excited state, from the ground state to the first excited state and from the ground state to the second excited state, respectively, for positive D. The transitions and relative intensities for $H \parallel y$ are easily obtained by a change in the sign of E and by an interchange of x and y in Table VIIb. Fig. 11a,b depicts the energy levels of the ground state spin triplet and the three transitions for $D/h\nu \sim 2/3$, which is suitable for Ni^{2+} in $La_2Mg_3(NO_3)_{12} \cdot 24H_2O$ (LMN) at X-band. The solid arrows are the fully allowed transitions and the broken arrows indicate the forbidden transitions.

Depending upon the relative size of the zero-field splitting and the Zeeman energy, the number of observable transitions of a given Ni^{2+} ion varies from three to zero. When $|D|$, $|E| \ll g\beta H$, three transitions, two anisotropic and one nearly isotropic, are observable. If $|D| \gg g\beta H$ and $|E| \ll g\beta H$, only transition 2 is possible at all orientations. The intensity and line positions of this transition are strong functions of field directions. Ni^{2+} : $ZnSeO_4 \cdot 6H_2O$ provides an example of this type. In the extreme case, where $|D|, |E| \gg g\beta H$, no resonance transition is observable. Incidentally, the maximum E is D/3, since for values greater than this a coordinate transformation can be chosen to bring $0 \leq E/D \leq 1/3$.

Perturbation theory can be used successfully for two limiting cases, $|D| \gg g\beta H$ and $|D| \ll g\beta H$. When $|D| \gg g\beta H$, the z axis of the D tensor is taken to be the quantization axis. Culvahouse (1962) plots

Table VII. Transitions and relative intensities.

a. When H along z axis ($n = 1, \ell = m = 0$):

Transition	$h\nu$	Intensity $H_1 \parallel x$	$H_1 \parallel y$	$H_1 \parallel z$
1	$D + K$	$\frac{1}{2}g_x^2(1 + \sin 2\theta)$	$\frac{1}{2}g_y^2(1 - \sin 2\theta)$	0
3	$-D + K$	$\frac{1}{2}g_x^2(1 - \sin 2\theta)$	$\frac{1}{2}g_y^2(1 + \sin 2\theta)$	0
2	$2K$	0	0	$(g_z \sin 2\theta)^2$

where $\tan 2\theta = E/G_1$ and $K = (G_1^2 + E^2)^{1/2}$

b. When H along x axis ($\ell = 1, m = n = 0$)

Transition	$h\nu$	Intensity $H_1 \parallel x$	$H_1 \parallel y$	$H_1 \parallel z$
2	$\frac{(-D + 3E)}{2} + K$	0	$g_y^2 \sin^2\theta$	$g_z^2 \cos^2\theta$
3	$\frac{(D - 3E)}{2} + K$	0	$g_y^2 \cos^2\theta$	$g_z^2 \sin^2\theta$
1	$2K$	$g_x^2 \cos 2\theta$	0	0

where $K = \left[\left(\frac{D+E}{2}\right)^2 + G_2^2\right]^{1/2}$ and $\tan 2\theta = G_2/2K$

the observed field positions of Ni^{2+} spectra versus $1/\cos\theta$, where θ is the angle between the magnetic field and the z axis. In our direction cosine representation $\cos\theta = n$. A calculated field position is approximated by

$$H^2 = 2(D/g\beta)^2 \{[(\cot\theta \csc\theta)^4 + (h\nu/2D)^2(\csc\theta)^4]^{1/2} - (\cot\theta \csc\theta)^2\} \qquad (18)$$

When θ is small, Eq.(18) reduces to a straight line of

$$H = h\nu/(2g\beta\cos\theta) \qquad (19)^*$$

This method turns out to be a good beginning for determing the values of Φ and D, though it is not sensitive enough for accurate analysis. Notice that this method has assumed an axial symmetry (E = 0) and an isotropic g value.

Rearranging and expanding the square roots of the equations for transition 2 in Table VII, we obtain the resonance conditions, to third-order in D, as

$$\left.\begin{array}{ll} H \parallel x & h\nu = 2E + (g_x\beta H)^2.(D+E)^{-1} - (g_x\beta H)^4.(D+E)^{-3} \\ H \parallel y & h\nu = -2E + (g_y\beta H)^2.(D-E)^{-1} - (g_y\beta H)^4.(D-E)^{-3} \\ H \parallel z & h\nu = 2g_z\beta H + E^2.(g_z\beta H)^{-1} - E^4.(g_z\beta H)^{-3}/4 \end{array}\right\} \qquad (20)$$

We will use Eq.(20) to determine the values of E and D from the resonance line positions.

---

* It must be mentioned that we failed to reproduce the derivations on page 2722 of Culvahouse (1962). Expansion of his secular determinant yielded Eq.(19) directly without ever reaching Eq.(18).

In the case of $|D| \ll g\beta H$, a formula derived by Bleaney (1951) can be safely applied. For the transition $M \leftrightarrow M-1$ in $S = 1$, the resonance condition is given by

$$h\nu = g\beta H + D(M-1/2)[3(g_{\parallel}/g_{\perp})^2\cos^2\theta - 1]$$
$$+ (2g\beta H_o)^{-1}(Dg_{\parallel}g_{\perp}\cos\theta\sin\theta/g^2)^2 [1 + 24M(M-1)]$$
$$+ (8g\beta H_o)^{-1}(Dg_{\perp}^2\sin^2\theta/g^2)^2[1 - 6M(M-1)] \qquad (21)$$

with $H_o = (h\nu/g\beta)$ and

$$g^2 = g_{\parallel}^2\cos^2\theta + g_{\perp}^2\sin^2\theta$$

Again the direction cosine n can be substituted for $\cos\theta$. The two lines of $\Delta M = \pm 1$ are equally displaced about H_o by the second term, and slightly shifted by the third and the fourth term.

When $|D| \sim g\beta H$, a complete solution of Eq.(15) or (16) is necessary. This is the case for Ni^{2+} in LMN.

B. Spectral Assignment

In order to determine the spin Hamiltonian constants, D, E, g, and ϕ, the principal axes of the spin Hamiltonian must first be identified. A knowledge of the crystal structure of the host lattice is indispensable in this deduction. For a given crystal orientation in the microwave cavity the magnetic field direction is changed by 5 to 10° increments and all the observed line positions are plotted on a graph. The directions at which the resonance lines reach a maximum or a minimum are carefully determined. They often correspond to the principal axes of the spin Hamiltonian, or they are simply related to them. Also the directions at which the resonance lines cross are critically examined. Similar measurements in two (or three for lower than an axial symmetry) planes should be sufficient to relate the principal axes (x,y,z) to the crystallographic axes (a,b,c), whereby direction cosines of the magnetic field are determined.

After successful assignment of the observed spectra to the three possible transitions, the measured line positions with H along the (x,y,z) axes are substituted in the equations given in Table VII or in Eq.(20) for the evaluation of the parameters. Measurements at two different frequencies provide a good check on the assignments of the spin Hamiltonian constants. A final check is performed by comparing the experimental points with theoretical positions calculated by direct matrix diagonalization.

The EPR measurements of the line positions alone give no information as to the signs of D and E. They can be determined, at least

in principle, from an intensity study as a function of temperature. For example, when D is positive and of appreciable magnitude, lowering the temperature will enhance the intensity of the transition originating in the lowest level and diminish that of the transition between the excited states. A relative sign of D with respect to the hyperfine splitting constant can be determined from the second order shifts of the hyperfine lines. But since nickel has only one isotope of non-zero nuclear spin (Ni^{63}, 1.25% natural abundance, $I = 3/2$), whose hyperfine splitting is too weak and too small to be observed in hydrated salts, this method does not apply here. The sign of E is only relative, for it depends upon the assignment of x and y axes of the spin Hamiltonian. Once x and y axes are fixed from intensity measurements, the line positions of $H // x$ and y determine the size and sign of E in Eq.(20).

C. Ni^{2+} in $ZnSeO_4 \cdot 6H_2O$

1. Gamma-c Plane Spectra

A large single crystal of a bipyramidal shape (Fig.3b) was grown in a desiccator at room temperature. From it a thin rectangular plate was easily cleaved in a plane perpendicular to the crystal axis, which was located by two cross-polaroid films. The Ni^{2+} concentration was found to be 3 mole %, as determined by a colorimetric method (Skoog et. al., 1958).

This crystal was oriented in a cavity with its rectangular edge lying horizontally. We expected, from the crystal structure, the Ni^{2+} spectra of the ac plane in which ions 1 and 4 and ions 2 and 3 would be equivalent. However, when we lowered the temperature to 77°K, we discovered the crystal orientation was really the γc plane.

The signal was strong enough for derivative detection with the 825 Hz field modulation at this temperature. Four lines of large anisotropy was observed. The lines became broader and stronger in the higher field; the highest magnetic field needed was beyond our magnet's capability which was about 11 kG. The low field lines were sharper but much weaker in the integrated intensity. The line 1 became too weak to see near the z axis, where the direct determination of $g_{\parallel}$ was possible if it could have been observed, and where this transition was nearly forbidden owing to $|E/G_1 n| \ll 1$.

All four lines more or less merged, though not exactly due to a slight misorientation, at one angle, which we quickly assigned as the c axis. A rotation of the magnet by 90° brought ions 1 and 3 together.

This orientation corresponded to the γ axis. Ion 3 reached the maximum field near $\alpha = 55°$. Since this is the angle between the c axis and the y axis of ion 3, ϕ must be about 35°.

The EPR spectra at 4.2° and 1.3°K proved that the intensities of Ni^{2+} appreciably decreased while that of diphenyl picryl hydrazyl (DPPH) increased as the temperature was lowered. Thus, the sign of D is positive. The positive D value was expected, since α-$NiSO_4 \cdot 6H_2O$ and $ZnSeO_4 \cdot 6H_2O$ are isomorphous. The thermodynamic work on α-$NiSO_4 \cdot 6H_2O$ has clearly established its D value as being positive and 4.74 cm^{-1} in value.

In Fig. 12 the observed line positions are plotted as circles and the average positions of 2 and 4 as crosses. First a plot of H vs. $\sec\theta$, Eq.(19) was tried to determine the spin Hamiltonian parameters. D and g were strongly dependent on the choice of ϕ. The best fit was obtained by $\phi = 35°$, $D = 4.5\ cm^{-1}$ and $g = 2.23$, as shown in Fig. 13. The accuracy in Eq.(19) was not high and we abandoned this method. Instead we attempted to calculate the line positions by diagonalizing the 3 x 3 matrix of Eq.(15) for a given orientation. The result is shown as solid curves in Fig. 12. The parameters used are

$$\left.\begin{array}{lll} g_{\parallel} = 2.216, & g_{\perp} = 2.235, & \\ D = +4.20\ cm^{-1}, & E = 0, & \phi = 35.6° \end{array}\right\} \quad (22a)$$

The overall fit is satisfactory, if the splittings of 2 and 4 could be ignored. Because of a slight misorientation, which, nevertheless, caused a large splitting of ions 2 and 4, we did not fully analyze the γc plane data.

2. ac Plane Spectra

Next we placed the same crystal in a V slot of a teflon mounter (Fig. 2). This orientation normally gave a γc plane for other crystals of the prismatic shape, but for this particular crystal it was the ac plane. At 77°K two pairs of doublets were easily observed. Ions 1 and 4 and ions 2 and 3 moved together. All four collapsed into one line at the c axis. One pair reached the maximum field at $\alpha = 63°$, from which ϕ was calculated to be 35.7° (see Appendix I).

If Ni^{2+} : $ZnSeO_4 \cdot 6H_2O$ possesses exactly axial symmetry, the highest field position observed in the ac plane corresponds to the orientation of H in the xy plane. The relative magnitude of $g_\perp$ and D can be computed from this position. For instance, at ν_e = 8.601 GHz, the observed H = 10,864 G gives $g_\perp$ = 2.24 for D = 4.18 cm^{-1}, $g_\perp$ = 2.242 for D = 4.19 cm^{-1}, etc. A small E can make a large difference, for the resonance observed is due to the transition 2 between the two excited states of Table VIIb. For example, an E of 0.001 cm^{-1} can change $g_\perp$ to 2.239 for D = 4.21 cm^{-1}.

In order to explain the doublet structures, we modified the direction cosines of Table IIIb by tilting the x axes from the γ axes toward the c axis in the γc plane. The new direction cosines in the ab, γc, and ac planes are tabulated in Table A-2-a,b,c, respectively, of Appendix II. Introduction of a new angle β broke the equivalency of ions 1 and 4 and ions 2 and 3 in the ac plane, and of ions 2 and 4 in the γc plane. The result was satisfactory, as shown in Fig. 14. The open circles and crosses are the experimental points, while the solid

and broken curves are calculated from the following parameters.

$$\left.\begin{array}{lll} g_{\parallel} = 2.216, & g_{\perp} = 2.235, & D = 4.16\ \mathrm{cm}^{-1} \\ E = 0, & \Phi = 35.4°, & \beta = 1.5° \end{array}\right\} \quad (22b)$$

We recalculated the theoretical positions in the γc plane with the above set of parameters. The tilting angle of 1.5° did not produce enough splittings of ions 2 and 4; instead, $\beta = 4°$ was necessary. This large discrepancy was believed to be due to the poor mounting of the crystal in the γc plane.

A second crystal of a rectangular prism (Fig. 3a) gave the identical spectra. This crystal had the a and b axes along the rectangular edges. Dehydration at 225 to 250°C for 8 hours proved that both crystals contained six water molecules per Zn atom. The fractions of the weight loss were 0.3420 and 0.3413, as compared with the theoretical value of 0.3417 for the hexahydrate.

The signal-to-noise ratio improved considerably when the temperature was lowered from 77° to 4.2°K. Further lowering to 1.3°K diminished the absorption intensity of Ni^{2+}, while that of Co^{2+} impurity remained the same, supporting the positive D value. Contrary to many Ni^{2+} crystals that are known to change the magnitudes of g and D with temperature, Ni^{2+} in $ZnSeO_4 \cdot 6H_2O$ shows practically no temperature dependence. As seen from Table VIII, the line positions and widths of Ni^{2+} at 77° and 4.2°K are virtually the same.

Table VIII. Temperature effect on the line positions of $Ni^{2+}:ZnSeO_4 \cdot 6H_2O$, ac plane.

	77°K			4.2°K		
	8.601 GHz			8.596 GHz		
α	H (gauss)	Doublet splitting (gauss)	Line-width (gauss)	H (gauss)	Doublet splitting (gauss)	Line-width (gauss)
0°	1 706	0	15	1 695	~0*	(~30)*
90°	3 371	245	35	3 364	250	39
62.8°	10 864	0	61	10 844	0	69
-63°	10 871	0	72	10 847	0	72

*Uncertainty due to a poor overlap.

3. ab Plane Spectra

The spectra of Ni^{2+} in the ab plane were as expected, save for the doublet structures that could not be accounted for by the direction cosines of Table A-2 in Appendix II. We looked at two different crystals of Fig. 2a and b, and found that the doublet splittings were real. The separation of the doublet reached maximum near $\alpha = 20°$ from the γ axis, and zero near $\alpha = 0°$. Near $\alpha = 45°$, or a axis, the two sets were completely superimposed but the splitting of each set was not zero. This suggested that ions 1 and 3 and ions 2 and 4 became equivalent near the γ axis, and that ions 1 and 4 and ions 2 and 3 were equivalent near the a axis. Thus, we modified the direction cosines by tilting the x axes from the γ axis in the ab plane. With the new x axes, as shown on the left, we obtained the new direction cosines that are listed in Table A-3-a of Appendix II. The results are shown in Fig. 15, in which the dotted curves are calculated from

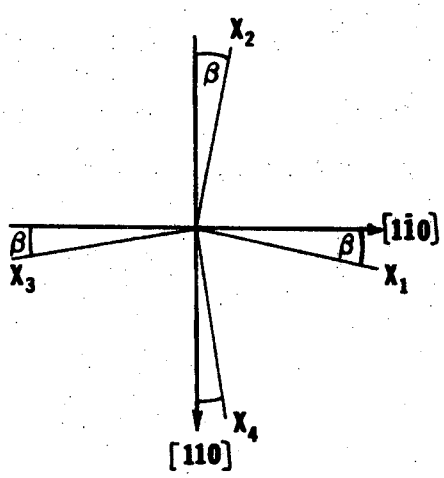

$$\left.\begin{array}{lll} g = 2.222, & g = 2.241, & D = 4.22\ \mathrm{cm}^{-1} \\ E = 0, & \Phi = 35.5°, & \beta = 2.0° \end{array}\right\} \quad (22c)$$

We see that a β of 2.0° is slightly too large and is more like 1.8°. The overall fit is satisfactory.

We find that the new arrangement of the x axes will also lift the equivalency of ions 1 and 4 and of ions 2 and 3 in the ac plane

but will not split ions 2 and 4 in the γc plane. Therefore, the real x axes are tilted from the γ axes by about 2°, lying neither in the ab plane nor in the γc plane. The ac plane data can be fitted well by taking $\beta = 2.1°$ in the direction cosines of Table A-3-c, as will be demonstrated in Table IX of the next section.

4. Discussion

Out of the six parameters ($g_{\parallel}$, $g_{\perp}$, D, E, ϕ, and β) two (ϕ and β) could be quickly determined by the method explained in Appendix I and from the size of the doublet splitting. The remaining four were determined by successive adjustments to give the best fit of the observed line positions in the three different planes. Our X-band klystron was capable of generating microwave frequencies from 8.48 to approximately 9.9 GHz. The highest magnetic field attainable by our magnet was about 11 kG, because of the wide pole gap needed to accommodate the double Dewar system. Hence the direct determinations of $g_{\perp}$, D and E were impossible with these limitations.

Table IX illustrates the kind of fitting we obtained for the ac plane data. The line positions were calculated from the following parameters with the direction cosines of Table A-3-c.

$$\left.\begin{array}{lll} g_{\parallel} = 2.222, & g_{\perp} = 2.241, & D = 4.23\ \mathrm{cm}^{-1} \\ E = 0, & \phi = 35.5°, & \beta = 2.1° \end{array}\right\} \quad (22d)$$

Table IX. Calculated and observed field positions of $Ni^{2+}:ZnSeO_4 \cdot 6H_2O$, ac plane. 8.596 GHz, 4.2°K.

α (deg)	Ion	H_{obs} (gauss)	H_{cal} (gauss)	$H_{cal}-H_{obs}$ (gauss)	Comments
0	3, 4	1 695	1 698	3	c axis
90	3	3 239	3 248	9	a axis
90	4	3 489	3 494	5	
62.8	3	10 869	10 866	-3	Highest field
62.8	4	10 819	10 810	-9	
58	3	10 108	10 095	-15	
58	4	9 537	9 490	-47	
53	3	7 905	7 915	10	
53	4	7 235	7 221	-14	
48	3	5 827	5 845	18	
48	4	5 399	5 388	-11	
43	3	4 481	4 490	9	
43	4	4 229	4 220	-9	
-27.1	3	1 507	1 504	-3	Lowest field
-27.1	4	1 532	1 528	-4	

Our accuracy in the field measurement was limited by three factors: (1) typical line width was 40 to 70 G, (2) the NMR probe with a shunt was not very sensitive above 10 kG, (3) the line positions shifted over 50 G at a change of 0.1° in orientation near H = 9 kG. The errors involved in (1) and (2) would not exceed a few gauss, but a slight misalignment of the crystal or magnetic field direction would lead a large error in (3). Thus, our fit to the experiment can be considered to be satisfactory.

Let us see how the simple CFT compares with our results. From Eq. (22d)

$$\langle g \rangle = (g_{\parallel} + 2g_{\perp})/3 = 2.232$$

$$\langle g \rangle - g_e = 0.229$$

$$g_{\parallel} - g_{\perp} = -0.019 \qquad (23)$$

Then, Eqs.(12) and (13) yield

$$\lambda = -(0.229 \times 8500)/8 \sim -245 \text{ cm}^{-1} \qquad (24)$$

$$D = -(245) \times (-0.019) \times (0.5) \sim +2.3 \text{ cm}^{-1} \qquad (25)$$

$$\Delta_1 - \Delta_2 = (4.20/4) \times (8500/245)^2 \sim 1200 \text{ cm}^{-1} \qquad (26)$$

The spin-orbit coupling constant of the free Ni^{2+} ion, -315 cm^{-1}, is about 20% too large to account for the g shift. This discrepancy is ascribed to bonding effects. And yet the free spin-orbit coupling constant is roughly 50% too small to explain the observed D value. This type of discrepancy is not uncommon and is found in many crystals cited in Table XIII. McGarvey (1964b) attributes the discrepancy to the neglect of the charge transfer states. The contribution of the charge transfer state, excited $^1T_{2g}$ state for example, is of the same sign

as that of lower lying states and will increase the magnitude of calculated D and E, but for g the effect is opposite to that of lower energy states so as to bring the calculated g closer to the free spin value. The tetragonal distortion is calculated to be about 1200 cm^{-1}, with the orbital doublet lying lower than the singlet. This result supports our assumption that the tetragonal distortion at the Ni^{2+} site is an elongation.

5. Summary of Ni^{2+} in $ZnSeO_4 \cdot 6H_2O$

The EPR spectra of Ni^{2+} in $ZnSeO_4 \cdot 6H_2O$ single crystal could be explained by a tetragonal crystal field with a large positive D value. Each of the four x axes is tilted from the ab bisector by about 2° and lies neither in the ab nor γc plane. This fact is different from α-$NiSO_4 \cdot 6H_2O$ whose x axes coincide with the γ axes. The tetragonal distortion is assumed to be an elongation in accord with the CFT prediction and with the result of Cu^{2+} in $ZnSeO_4 \cdot 6H_2O$ that will be treated in section V.

The EPR of Ni^{2+} in ab, ac and γc planes could be best fitted by the following set of spin Hamiltonian parameters.

$$\left.\begin{array}{ll} g_{/\!/} = 2.219 \pm 0.003, & g_{\perp} = 2.238 \pm 0.003 \\ D = +4.20 \pm 0.04\ cm^{-1}, & E = 0 \\ \phi = 35.5 \pm 0.1°, & \beta = 2.0 \pm 0.5° \end{array}\right\} \quad (22e)$$

The signs of $(g_{/\!/} - g_{\perp})$ and D are consistent with the CFT. The

spin-orbit coupling constant of the free Ni^{2+} ion must be reduced by about 20% to fit the observed g values and must be increased by about 50% to explain the observed D. The reason for this discrepancy is explained in terms of the neglect of charge-transfer states, as quoted in the previous section. The apparent temperature independence of these parameters presents an interesting contrast to Ni^{2+} ion in trigonally distorted diamagnetic crystals in which the magnitude of D is known to change appreciably with temperature.

The host crystal grows in two external habits, both hexa-hydrated. The EPR spectra of Ni^{2+} in these crystals behave identically, indicating that they must have the same lattice structure.

D. Ni^{2+} in LMN

1. Type 1 Ion

(a) Spectra at 77°K

The hexagonal plate of Ni^{2+}: LMN single crystal was oriented vertically so that the magnetic field was rotated in the xz plane. At 77°K three lines, originating from the three transitions among the Ni^{2+} ground state triplets, were easily detected at all angles. Fig. 16 shows the observed line positions of these three transitions as a function of angle. Line 1 was the least angularly dependent and it was due to the transition from the lowest to the highest level of the triplets. This transition is often called a half-field transition, or a $\Delta M = \pm 2$ transition or a forbidden transition. The last two names are a misnomer, because when the energy quanta is comparable to the zero-field splitting, the M values are not good quantum numbers and the transition is far from forbidden. The line was always sharp (~40 G) and fairly strong except when H was oriented nearly perpendicular to the z axis. At this orientation its transition probability is calculated to be zero.

In contrast, lines 2 and 3 were highly anisotropic, of which 3 was the more intense and the more anisotropic. When H was along the z axis, line 2 became weak but sharp. The line-shape was distinctly asymmetric and this will be discussed later. The position of line 2 at this angle gives in the first-order the value of $g_{//}$ from

$$g_{//} = h\nu/(2\beta H) = 2.226$$

and

$$D = (H_3 - H_1)/(2\beta H) = 0.1776 \text{ cm}^{-1}$$

Lines 2 and 3 crossed at $\alpha = 52.9°$ at $\nu_e = 9.2$ GHz. This angle served as a good marker for the crystal orientation, for the crossing angle did not vary more than 0.1° over a frequency change of 0.3 GHz. The energy diagram is shown in Fig. 17. Incidentally, when the second order effect of D can be neglected, the crossing angle is equal to 54°44', at which the lowest and the highest levels are equally disposed about the middle level. At the crossing angle an absorption of two quanta of $h\nu$ can cause a transition from the ground state to the highest excited state. This is called a double quantum transition (DQ) and has been observed in a number of triplet states such as Ni^{2+}: MgO (Orton et.al., 1960a; Smith et.al., 1969) and in many extended π systems (e.g., Wasserman et.al., 1964). The DQ transition is a very sharp line of about 2 G wide and its intensity varies roughly as the square of the microwave power.

The (111) plane data revealed a small angular dependence of lines 2 and 3. Line 1 was again very weak. When line 3 was at the maximum field, line 2 was at the minimum field. Rotation of H by 90° shifted line 3 to the lowest field and line 2 to the highest field. The line shifts for 2 and 3 were 17.1 and 17.7 G, respectively at $\nu_e = 9.813$ GHz. From this the size of E was estimated to be 0.0007 cm^{-1}. There was clearly 120° periodicity in the spectra of the (111) plane, indicating that each Ni^{2+} ion in the site 1 has its x axis along the hexagonal edge of the single crystal. Whether we call this axis x or y is immaterial, for the exchange of x with y merely changes the sign of E.

The best fit to the xz plane spectra was obtained by the following

parameters. The calculated field positions are drawn as solid curves in Fig. 16.

$$\left.\begin{aligned} & g_{\parallel} = 2.230\pm0.005, \quad g_{\perp} = 2.230\pm0.005 \\ & D = +0.1785\pm0.0005 \text{ cm}^{-1} \\ & E = 0.0007\pm0.0002 \text{ cm}^{-1} \\ & \phi = 0. \end{aligned}\right\} \quad (27)$$

The sign of D was determined at liquid helium temperatures, as explained in the next section.

(b) Spectra at liquid helium temperatures

At liquid helium temperatures the signal-to-noise ratio improved considerably so that we could observe straight absorption spectra of Ni^{2+} ion even at -30dB attenuation of the microwave power. This corresponds to about 0.3 mV at the crystal detector. When H lay in the (111) plane, two strong absorption peaks were observed. They corresponded to line 3 at 1822 G and to line 2 at 3802 G when $\nu_e = 9.3382$ GHz. There were two weaker lines; line 1 near 1300 G and a line near 8500 G that was arising from the second type of Ni^{2+} ion. At 1.7° and 1.3°K line 3 became definitely more intense than line 2. Their angular variations were about 15 G in this plane. The spectra observed in the xz plane at the liquid helium temperatures were essentially the same as at 77°K, except for the shifts in the line positions. The differences between the observed and the calculated field positions are better than a gauss for most angles, some of which are illustrated in Table X.

Table X. Calculated and observed line positions, Ni:LMN, Type 1, ac plane, 4.2°K.

α (deg)	Transition	H_{obs} (gauss)	H_{cal}* (gauss)	$H_{cal}-H_{obs}$
0	3	5 026.2	5 026.9	0.7
0	1	1 178.4	1 178.5	0.1
90	2	3 947.7	3 949.6	-1.9
90	3	1 914.1	1 917.9	3.8
52.9	2,3	2 896.1	2 896.1	0.0
52.9	1	1 095.1	1 095.5	0.4

*ν_e = 9.7057 GHz

$$\left.\begin{array}{l} g_{\parallel} = 2.235,\ g_{\perp} = 2.233 \\ D = +0.2005\ \mathrm{cm}^{-1},\ \ E = 0.0007\ \mathrm{cm}^{-1} \end{array}\right\} \quad (28)$$

At $\alpha = 52.9°$ the two transitions 2 and 3 coincided to give a single strong line. We varied the microwave power level to test if the double quantum transition could be observed. Even at about 200 mW no DQ line was detected. Nor could we detect a sharp line with a phase inverted (IN) over the power range of 200 mW to 200 μW. This IN line was observed in a powder sample of Ni^{2+}: LMN (see section IV-D-3).

Two crystals of different Ni^{2+} concentration were used. Their EPR spectra were identical except for the line widths of the site 1 ion and multiplet structures of the site 2 ion. The typical line widths of Ni^{2+} were 100~140 G for the more concentrated crystal and about 40 G for the more dilute one. The latter was about 15 times more dilute, as estimated from relative intensities.

In order to determine the sign of D a study of relative intensities at different temperatures was conducted on the dilute crystal. Straight absorption spectra were recorded at power levels low enough to prevent saturation and the intensities were calculated from the area under the curve. The result is shown in Table XI. The intensity of the transition 2 was diminished as those of 1 and 3 were enhanced. Therefore, it was concluded that D is positive.

The line shape of 2 at $H \parallel z$ has been seen in the half-field transition of non-Kramers ions (Fe^{2+}: MgO, Low and Weger, 1960) and is commonly attributed to the strain effect of the crystal lattice. While in Fe^{2+}: MgO the high-field side is sharply cut off and the low-field region tails off gradually, in our Ni^{2+}: LMN the low-field side

Table XI. Relative intensities vs. temperatures. Ni^{2+}:LMN, ac plane

T (°K)	α = 90° I_2/I_3	α = 44.6° I_2/I_1	α = 44.6° I_2/I_3
1.36	0.56	0.84	0.58
1.80	0.61	0.89	0.63
4.2	0.78	0.96	0.79

ν_e = 9.7057 GHz

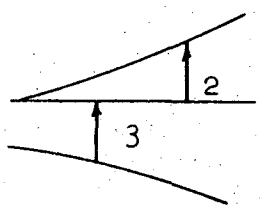

α = 90°

H_2 = 4.0 kG
H_3 = 1.9

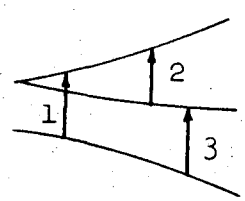

α = 44.6°

H_1 = 1.15 kG
H_2 = 2.7
H_3 = 3.3

is more sharply cut off as shown in Fig. 20a (absorption) and b (first derivative). A & B (section 3.14) explain this line shape in terms of rhombic strains that upset the axial symmetry. When the crystal field is exactly axial, this transition is strictly forbidden (see Table VIIb). The presence of a rhombic strain, equivalent to $E \neq 0$, gives rise to a small initial splitting and allows a weak transition to take place. If this strain is oriented randomly, the resonance line is broadened to the lower field side of $H_o = h\nu/(2g_{\parallel}\beta)$, when the frequency is fixed and the magnetic field is varied. For an oscillatory field H_1 along the z axis, the maximum peak occurs at

$$H = H_o - (\Delta_o^2)\cdot(4h\nu g_{\parallel}\beta)^{-1}$$

where Δ_o^2 is the most probable value of Δ^2. Thus, the smaller the average local strain is, the sharper the cut off on the high-field side. There is a greater shift of the maximum peak to the lower field in Ni^{2+}: LMN than in Fe^{2+}: MgO, whose site symmetry is octahedral.

(c) Powder spectra

The EPR of powdered samples with $S > 1/2$ has been investigated most actively for organic triplets and only to a smaller extent for the ground state orbital singlets of first row transition metal ions. Among the organic triplets are aromatic π systems whose powder spectra give almost as much information as do single crystal samples. The zero-field splitting of these aromatic compounds does not arise from the spin-orbit coupling, for it is much smaller than in the metal ion, but primarily from dipole-dipole interaction of the electron spins. The size of this splitting can be as large as 0.3 cm^{-1}. Although an S state ion, Mn^{2+} for example, can be seen easily in a powder sample, we will not be concerned with it here, because it requires a special treatment. Burns (1961) demonstrated the accuracy of the determination of g and D for the powder sample of Cr^{3+} in ammonium alum.

In a single crystal containing a spin triplet the transitions of $\Delta M = \pm 1$ are strong and highly anisotropic and that of $\Delta M = 2$ is weak and nearly isotropic. Since in a powder sample, on the other hand, all the angles between the spin axis of each micro-crystallite and the magnetic field are possible, the spectral region of $\Delta M = \pm 1$ spreads over 2D. The greater the angular dependence of a transtion is, the less intense it is in a powder spectrum. Therefore, a fairly strong $\Delta M = 2$ line is seen and only lines of $\Delta M = \pm 1$ occuring at maximum or minimum field ($H // x, y, z$) are observed in the powder sample. Fig.19 is a typical computed powder spectrum of an axially symmetric spin triplet. Here x_1 denotes the line position of the transition 1 at $H \parallel x$, etc.

We ground the concentrated single crystal of Ni^{2+} : LMN used in section IV-D-1. The powder spectra at -160°C are shown in Fig. 20a and b. Table XII lists the observed and calculated field positions. A reasonably good agreement supports our choice of the spin Hamiltonian parameters and the assignment of the powder spectra. The theoretical field positions are calculated from the successive iteration and diagonalization of the 3 × 3 matrices. Similar answers, though not exactly identical, can be obtained from the approximate equations given by Wasserman et al. (1964, Eq. 13).

Of special interest is the central line with a phase inverted (IN) at the position of the DQ. This IN line has also been observed for Ni^{2+} in MgO (Smith et al., 1969), Co^{2+} in MgO (Orton et al., 1960b) Ni^{2+} in $SrTiO_3$ (Rubins and Low, 1963) and Ni^{2+} in CaO (Low and Rubins, 1963). In Ni^{2+} : MgO the IN line was observed at low microwave power but was obscured by the strong DQ line at higher power level. We raised the power to the maximum level of our klystron, that is about 250 mW, but saw no DQ line.

The origin of the IN line is not clear to us. It may arise from a superposition of two assemblies of Lorentzian curves. Smith et al. show that the IN line is not a true EPR absorption line but represents a dip in the intensity of the two absorptions of $\Delta M = \pm 1$ lines. Each of the absorption bands is an aggregate of spin packets created by random strains in the crystal. When the local strain is small, they argue, the effect of the cross relaxation between the two transitions

Table XII. Powder Ni^{2+}: LMN at -160°C.

Transition	H_{obs} (gauss)	H_{cal} (gauss)	Line-width (gauss)
x_1	1 148.2	1 192.0	76
x_3	1 922.2	1 902.1	74
DQ, IN	2 775.8	2 773.7	43
x_2	3 682	3 687.2	
z_3	4 644.9	4 645.3	

*Calculated from

$g_{\parallel} = 2.230, \quad g_{\perp} = 2.230, \quad D = 0.1780\ cm^{-1}$

$E = 0.0007\ cm^{-1}$ at $\nu_e = 9.1625$ GHz

pushes intensity away from the center of the line, where the spin packets of the two transitions overlap. The result is a small dip in the absorption curve and an inverted phase in the derivative curve. They conclude that the width of the IN line is of the order of the width of the individual spin packet and that the height depends on the strength of the mechanism responsible for the cross relaxation between the $\Delta M = \pm 1$ lines. Note that the argument of Smith et.al. is aimed for a single crystal. As mentioned earlier, neither IN nor DQ line was observed in the single crystal of Ni^{2+}: LMN.

As the temperature of the powder sample was raised, the line widths rapidly increased. At -100°C a very weak sextet of equal spacing started appearing at g = 2 and gradually increased its intensity as the Ni^{2+} lines broadened. We assigned the sextet to the six hyperfine lines of Mn^{2+}, for which we estimated g = 1.996, D = 0.020 cm^{-1} and A = 92.3 x 10^{-4} cm^{-1}.

The temperature dependence of the Mn^{2+} spectra can be explained as a phenomenon of two paramagnetic species, one with a very short spin-lattice relaxation time, T_1, and the other with a long spin-spin relaxation time, T_2 (A & B, p.535). At room temperature a broad resonance due to the Ni^{2+} ion was observed because of its short T_1, while the Mn^{2+} resonance was observed with a line width of 8 G which is nearly the same as in a diamagnetic host lattice of hydrated salts. The local field at the Mn^{2+} ion due to the neighboring Ni^{2+} ions persisted only for a time of the order of T_1 for Ni^{2+}. This field was averaged out over a period longer than or comparable to

the period of the microwave frequency. At -160°C the T_1 of Ni^{2+} became long enough to broaden the Mn^{2+} lines. The T_1 measurements for Ni^{2+}: LMN at liquid helium temperatures were conducted by Chang of our laboratory and will be reported in his Ph.D. thesis (1971).

2. Type 2 Ion

We have detected a second type of Ni^{2+} spectrum that was formerly investigated by Culvahouse (1962). Because of a large D value, only one transition was seen at X-band. In the dilute sample the second type of spectrum appeared as a sharp singlet. Its intensity at 1.7°K was of similar magnitude to that of the first kind. From 4.2° to 1.3°K the intensity increased only slightly, indicative of a negative D. With H rotated in the (111) plane, the line changed its position only by some 40 G, showing that the E was small. The best fit to the xz plane data was given by

$$\left.\begin{aligned} g_{\parallel} &= g_{\perp} = 2.24 \\ D &= -2.232\ \mathrm{cm}^{-1} \\ E &= 0.0008\ \mathrm{cm}^{-1} \end{aligned}\right\} \qquad (29)$$

In a concentrated sample this line was about 100 times as weak as the first kind. When H was oriented perpendicular to the c axis, there appeared two shoulders on each side of the central line. At different orientations only one shoulder was seen either on the left

or on the right side. The origin of the shoulders was thought to be a dipole-dipole interaction of neighboring Ni^{2+} ions or an exchange interaction known to be present in the Mg(2) site due to its nearest neighbor at a close distance. We did not fully investigate the magnitude of the nearest neighbor interactions.

E. Ni^{2+} in $Zn(BrO_3)_2 \cdot 6H_2O$

1. Undiluted $Ni(BrO_3)_2 \cdot 6H_2O$

Owen studied the undiluted $Ni(BrO_3)_2 \cdot 6H_2O$ at room temperature and attained $g = 2.29$, $D = 1.93\ cm^{-1}$ and $E = 0$ (unpublished, quoted in Bowers and Owen, 1955). We investigated a large single crystal with H rotated in the (111) plane. At 4.2°K a strong broad band of about 2500 G width appeared near 8 kG. There was also observed a weak signal of large anisotropy in the low field. Below the lambda-point of the liquid helium (2.17°K) the signal became so intense that the microwave bridge could not be kept locked at resonance.

We looked more carefully at a small square prism. No absorption of Ni^{2+} could be seen at 77°K or above. At liquid helium temperatures two broad bands, one intense and the other weak, were observed. With H lying in the (100) plane there existed a 90° periodicity. The highest field position, corresponding to [110] direction, was located at 7975 G at $\nu_e = 9.0927$ GHz. At 45° from this angle, or [100], the signal became weak and reached the lowest field of 3003 G. The calculation with $g = 2.22$ and $D = -1.95\ cm^{-1}$ showed a good agreement near the highest field but 300 to 400 G lower than the observed position in the low field region. As the temperature was lowered, the signal intensity increased, indicating the negative D. The line position also shifted to a higher field, the amount of the shift depending on the field orientation. From 4.2° to 1.7°K, for example, the highest position moved by 700 G and the 3000 G line shifted only by 100 G, while the DPPH signal remained unmoved. This behavior is to be com-

pared with the temperature dependence of α-$NiSO_4 \cdot 6H_2O$ which is known to possess a positive D value and to shift to a lower field at lower temperatures. The band widths, however, narrowed with decreasing temperature, just as the undiluted α-$NiSO_4 \cdot 6H_2O$ did.

2. Ni^{2+} Doped in $Zn(BrO_3)_2 \cdot 6H_2O$

We examined the Ni^{2+} ion doped in $Zn(BrO_3)_2 \cdot 6H_2O$ at the liquid helium temperature. We detected four sets of triplets by orienting the magnetic field in the (111) and the yz planes of the ion 4 (see Fig. 9). Each triplet belonged to one of the four Ni^{2+} ions in the unit cell. The center line of the triplet was much more intense than the two side bands, which were separated about 400 G from the central line, as shown in Fig. 21. The highest field positions of the four sets were all equal at 7831 G when ν_e = 9.613 GHz.

In the (111) plane ion 4 was nearly isotropic with a small fluctuation of approximately 120 G over 100° rotation of the magnet. If this angular variation of line 4 arises strictly from the rhombic contribution, but not from the misorientation, then it requires an E value of about 0.001 cm^{-1}. The other three lines were very anisotropic and exhibited the sixty degrees periodicity (Fig. 22). The Ni^{2+} line width at the highest field was about 110 G. As the line moved toward upfield, the signal became stronger. The relative intensity of Ni^{2+} to DPPH increased with decreasing temperature; hence,

D is negative. The line positions of Ni^{2+} did not vary significantly over the temperature change of 77° to 1.7°K, which is quite different from the pure $Ni(BrO_3)_2 \cdot 6H_2O$.

The multiplet structures were dependent on the Ni^{2+} concentration. In a more dilute single crystal each set was a narrow singlet of roughly 60 G width, while in a more concentrated sample the multiplet appeared as a quintet or more. Therefore, the origin of the multiplet structure is believed to be the dipole-dipole or exchange interactions with neighboring Ni^{2+} ions. We have not studied carefully this interaction.

Fig. 23 shows the angular dependence of the main lines in the yz plane. Lines 2 and 3 merged at the [111] direction or $\alpha = 0°$. They reached the maximum positions at $\alpha = \pm 22.5°$, which is the angle between the c axis and the xy planes of ions 2 and 3 projected on the yz plane. From this the angle between [111] and the xy planes of ions 2 and 3 is calculated as

$$\tan\phi = \pm(\tan 22.5°).(\cos 30°) = \pm 0.3587$$

$$\phi = \pm 19°44' = \pm 19.73°$$

which agrees well with the theoretical value of $\phi = \pm 19.47°$. This supports our assumption that each z axis is aligned parallel to the body-diagonal of a cube. The most anisotropic line was 4, whose lowest field of 1550 G at 9.73 GHz corresponded to the $H \parallel z$, from which $g_{\parallel}$ was calculated in the first order to be 2.235. Line 1 was least angular dependent and yet most susceptible to a crystal misorientation. Two different experiments resulted in two widely different positions of line 1 near the [111] direction. The minimum field of

line 1 in Fig. 23 was 4558 G, about 100 G higher than the calculated field. The fits for lines 2,3 and 4 were generally better than 40 G. The spin Hamiltonian parameters are

$$g_{\parallel} = 2.235 \pm 0.005, \quad g_{\perp} = 2.235 \pm 0.005$$
$$D = -1.79 \pm 0.01 \text{ cm}^{-1}, \quad E = 0.001 \pm 0.001 \text{ cm}^{-1} \qquad (30)$$
$$\Phi = -19.73^{\circ} \text{ for ions } 1,2,3 \text{ and } \Phi = 0^{\circ} \text{ for ion } 4.$$

F. The Sign of D

The sign and magnitude of the zero-field splitting has been a subject of considerable controversy in the past decade. In this section we will first review all the EPR work carried out for $3d^3$ and $3d^8$ systems in "predominantly axial" fields. Next, we will make some generalizations about the spin Hamiltonian parameters. Lastly, we will give a few arguments why a simple crystal field theory does or does not predict correct values for g and D.

1. Review of Past Work

Table XIII lists the observed g and D values of $3d^3$ and $3d^8$ ions in axial or nearly axial crystal fields. We have limited the criterion of an axial field by imposing an arbitrary boundary of $|E/D|<0.03$.

A few remarks are in order. Since the D values are in general dependent upon the temperature and concentration of paramagnetic ion, undue emphasis should be placed not upon their values but on their magnitudes and signs. Secondly, accurate determination of g values is often difficult owing to broad absorption lines, and two separate investigators sometimes report widely separated g values. Thirdly, the signs of D have not been experimentally determined in very many cases. In spite of the incomplete accumulation of data, Table XIII suggests several general trends:

1) The crystal field symmetry at paramagnetic ions is more likely determined by the local crystal symmetry of the host lattice.
2) The sign of D is generally negative in a trigonal field and positive in a tetragonal field.

Table XIII. g and D in axial symmetry.

(1) Predominantly trigonal
(* sign not determined)

Ion	Host	$g_{\parallel}$	$g_{\perp}$	D (cm^{-1})	$\lvert E/D \rvert$	Ref.
V^{2+}	Al_2O_3	1.991		-0.1601	0	1
($3d^3$)	$CdCl_2$	1.9661	1.9704	-0.2077	0	2
	$ZnSiF_6 \cdot 6H_2O$	1.970	1.976	0.0804*	0	3
	$CsMgCl_3$	1.974	1.976	0.0858*	0	29
Cr^{3+}	Al_2O_3	1.982	1.979	-0.1912	0	4
($3d^3$)	Al_2O_3	1.984	1.987	-0.1908	0	1
	$AlCl_3 \cdot 6H_2O$	1.977		0.0327*	0	5
	$MgAl_2O_4$	1.985	1.980	0.925*	0	6
	$MgAl_2O_4$	1.986	1.989	0.495*	0	7
	Al_2SiO_5	1.982	1.977	0.637*	0.028	8
	Y_2O_3	1.97		+1.21	0	9
	Al (hfaca)$_3$	1.98		0.70*	0	10
	Co (aca)$_3$	1.9802		0.600*	0.014	11
	Al (aca)$_3$	1.9820		0.592*	0.016	11
	$Co(en)_3Cl_3 \cdot 3H_2O$	1.9900		0.036*	0	12
	NH_4 alum	1.977		0.049	0	13,14
	emerald	1.973	1.97	-0.895	0	15
Mn^{4+}	Al_2O_3	1.974		-0.1957	0	16
($3d^3$)	Al_2O_3	1.994		-0.1957	0	17
Ni^{2+}	Al_2O_3	2.1957	2.1859	-1.375	0	18
($3d^8$)	$CdCl_2$	2.28		1.410*	0	19
	$CdCl_2$	2.25	2.22	1.35*	0	20
	$ZnSiF_6 \cdot 6H_2O$	2.25		-0.129	0	21
	$NiSiF_6 \cdot 6H_2O$	2.30		-0.52	0	22
	$NaNi(aca)_3$	2.20		-2.19	0	23
	MgLaN					
	site 1	2.235	2.233	+0.2005	0	24,25
	site 2	2.24		-2.232		25,26

Table XIII. (Continued)

Ion	Host	$g_{\parallel}$	$g_{\perp}$	D (cm^{-1})	$\lvert E/D \rvert$	Ref.
	ZnLaN	2.235		0.043*	0	24
	$Ni(BrO_3)_2 \cdot 6H_2O$	2.22		-1.95		27
	$Zn(BrO_3)_2 \cdot 6H_2O$	2.235	2.235	-1.79	0.001	25
	$CsMgCl_3$	2.257	2.241	2.000*	0	29
Cu^{3+} ($3d^8$)	Al_2O_3	2.0788	2.0772	-0.1884	0	28

Abbreviations used in the above table:

hfaca = hexafluoro-acetylacetonate $[(CF_3CO)_2CH]^-$
aca = acetylacetonate $[(CH_3CO)_2CH]^-$
NH_4 alum = $NH_4Al(SO_4)_2 \cdot 12H_2O$
MgLaN = $Mg_3La_2(NO_3)_{12} \cdot 24H_2O$
ZnLaN = $Zn_3La_2(NO_3)_{12} \cdot 24H_2O$
emerald = beryl, $Be_3Al_2Si_6O_{18}$

References

1. Lawrence and Lambe (1963); 2. Chan et al. (1965); 3. Orton (1959); 4. as quoted in McGarvey (1966); 5. Wong (1960); 6. Atsarkin (1963); 7. Stahl-Brada and Low (1959); 8. Hutton and Troup (1964); 9. Carson et al (1961); 10. Jarret (1957); 11. McGarvey (1964a); 12. McGarvey (1964b); 13. Davis and Strandberg (1957); 14. Walsh (1959b); 15. Geusie et al. (1959); 16. Sierro and Lacroix (1959); 17. Geschwind et al. (1962); 18. Marshall et al (1962); 19. Orton (1959); 20. Iri and Kuwabara (1968); 21. Hoskins et al. (1959a); 22. Walsh (1959a); 23. Peter (1959); 24. Hoskins et al. (1959b); 25. This work; 26. Culvahouse (1962); 27. Bowers and Owen (1955); 28. Blumberg et al. (1963); 29. McPherson et al. (1970).

Table XIII. (Continued)

(2) Predominantly tetragonal, as suggested by authors

Ion	Host	$g_{\parallel}$	$g_{\perp}$	(cm^{-1})	$\lvert E/D \rvert$	Ref.
Cr^{3+} ($3d^3$)	$K_2Zn(SO_4)_2 \cdot 6H_2O$	1.977	1.979	0.332*	0.030	1
Ni^{2+}	$CdBr_2$ [a]	2.19	2.18	+0.220	0	2
	α-$NiSO_4 \cdot 6H_2O$	2.215	2.250	+4.741	0.007	3,4
	$ZnSeO_4 \cdot 6H_2O$	2.219	2.238	+4.20	0	5

References

1. Arkhangel'skaya et al. (1963).
2. Katsumata and Yokozawa (1970).
3. Fisher and Hornung (1968).
4. Batchelder (1970).
5. This work.

a. The tetragonal symmetry is uncertain. See the text.

3) On the basis of (2) alone the distortion is predicted as an elongation rather than a compression of an octahedron.

4) For a given ion, g is sensitive to the nature of the bonding but not to a distortion in the crystal. D, on the other hand, is very sensitive to crystal distortions.

These generalizations are in accord with the CFT. The only exceptions found so far are: to (2), the positive D's of Cr^{3+}:Y_2O_3, Cr^{3+}: ammonium alum, and Ni^{2+}: LMN, all in trigonal distortions, and to (1), a tetragonal crystalline field of Ni^{2+}: $CdBr_2$ with a hexagonal crystallographic structure.*

There is other experimental evidence that support the predictions of the CFT. Walsh conducted a study of pressure and temperature effects on D and g values of Cr^{3+} and Ni^{2+} in several host crystals (1959 a,b). The EPR spectra of $NiSiF_6 \cdot 6H_2O$ at room temperature with no hydrostatic pressure applied could be explained by D = -0.52 cm^{-1} and $g_{//} \sim g_{\perp} \sim 2.30$. Upon exerting pressure along the c axis of the crystal, which was the z axis of the trigonal electric field, Walsh observed D to become less negative and eventually change its sign at high pressure. The change in g could not be detected beyond the experimental uncertainty. The volume expansion with increasing temperature made D more negative. With a strain gauge technique he found that as the temperature was

---

*Katsumata and Yokozawa (1970) found two types of Ni^{2+} in $CdBr_2$, one in a cubic site and the other in a tetragonal site. The X-ray analysis concludes that both $NiBr_2$ and $CdBr_2$ form mixed hexagonal and cubic close-packing of the anions. In view of the fact that Ni^{2+}:$CdCl_2$ (isomorph of $CdBr_2$) was found in a trigonal field, the choice of the tetragonal symmetry for Ni^{2+}:$CdBr_2$ is not convincing.

raised, the crystal expanded along the c axis and contracted perpendicular to it. This high degree of anisotropy supported the large temperature dependence of the D value. His result suggested that the site symmetry in $NiSiF_6 \cdot 6H_2O$ was an elongation along the z axis, resulting in negative D and negative slope of $\partial D/\partial P$.

Another experiment by Walsh was carried out on Cr^{3+}: ammonium alum. The Cr^{3+} ion was located on the [111] axis of a cubic alum, where there was a small trigonal distortion along [111]. He found that D was positive and increased with increasing pressure applied along the trigonal axis. Increased pressure enhanced the compression along the z axis, making D more positive.

Table XIV illustrates the effects of covalency and crystal structure on the spin Hamiltonian parameters. As the metal-ligand bonding increases its covalency character, the crystal field splitting, $\Delta = 10$ Dq, increases; in fact, it was found that about two-thirds of Δ originates from the covalency effect, the remaining one-third from the ionic model (Owen and Thornley, 1966). Consequently, the g factor approaches the free spin value, and the hyperfine constant decreases with increasing covalency, this trend seemingly independent of the crystal structure. When the crystal field symmetry becomes lower, however, D and E increase, irrespective of the bonding nature.

The effect of crystal field environments of Ni^{2+} is seen in Table XV. D increases as the crystal lattice contracts at lower temperature. D also increases with the increasing size of trivalent ion and decreases

Table XIV. Effects of Covalency and Crystal Structure.[a]

Salt	Site symmetry	g	D (cm^{-1})	E (cm^{-1})	A ($\times 10^4$ cm^{-1})
Cr^{3+}:					
K alum[b]	trigonal	1.976	0.0900	0	18.5
Al_2O_3	trigonal	1.980	-0.1912	0	16.8
MgO	cubic	1.980	0	0	16.0
MgS	cubic	1.987	0	0	15.3
$K_3Co(CN)_6$	rhombic	1.992	+0.0831	+0.0108	14.7
V^{2+}:					
Tutton[c]	rhombic	1.973	-0.1561	-0.0228	83
MgO	cubic	1.980	0	0	74.2
MgS	cubic	1.990	0	0	70.7
KFeCN[d]	rhombic	1.992	-0.0264	-0.0072	55.5

a. Compiled from Low (1960), Table XXIII and XXIV, and from McGarvey (1966), Table X.

b. K alum = $KAl(SeO_4)_2 \cdot 12H_2O$

c. Tutton = $(NH_4)_2Zn(SO_4)_2 \cdot 6H_2O$

d. KFeCN = $K_4Fe(CN)_6 \cdot 3H_2O$

Table XV. Crystal field environment of Ni^{2+}.[a]

	$\|D\|$ (cm^{-1})	
Host lattice	77°K	4.2°K
ZnLaN[b]	0.043	0.065
MgLaN	0.177	0.200
ZnBiN	0.128	0.164
MgBiN	0.269	0.298

a. Hoskins et al. (1959).

b. Double nitrates of the form $D_3T_2(NO_3)_{12} \cdot 24H_2O$, where D is a divalent ion (Mg^{2+} or Zn^{2+}) and T is a trivalent ion (Bi^{3+} or La^{3+}).

with the increasing size of divalent host cation. These seem to indicate that a compression of the octahedron increases D. The positive value of Ni^{2+}: LMN supports this conjecture.

2. Discrepancy and Discussion

Controversy arises in the case of Al_2O_3, in which $3d^3$ and $3d^8$ ions all have negative D values. Sturge reports positive values of trigonal field splittings for $3d^3$ in Al_2O_3 (1963). The trigonal field splitting is often denoted by K or v which are related to our $\Delta_1 - \Delta_2$ in Fig.10a by

$$\Delta_1 - \Delta_2 = W(^4A_{1g}) - W(^4E_g) = -3K/2 = v/2$$

Ion	K (cm^{-1})	$\Delta_1 - \Delta_2$ (cm^{-1})	Reference
V^{2+}	-160	240	Sturge (1963)
Cr^{3+}	-330	500	Sugano and Peter (1961)
Mn^{4+}	-700	1050 (tentative)	Geschwind et.al. (1962)

The positive $\Delta_1 - \Delta_2$ corresponds to a compression which in simple CFT predicts positive D, contrary to the observed negative value.

As seen in Table XIII, the negative D and positive $(g_{\parallel} - g_{\perp})$ of Ni^{2+} and Cu^{3+} in Al_2O_3 led Blumberg et.al. (1963) to conclude that the trigonal field splitting was negative, as opposed to the case for $3d^3$ ions in Al_2O_3.

The site symmetry of Al^{3+} in emerald, $Be_3Al_2Si_6O_{18}$, is known to be D_3, owing to a small trigonal compression of a regular octahedron. The EPR of Cr^{3+} in this crystal is explained by $D = -0.87\ cm^{-1}$. The calculated trigonal field splitting is negative, which is contrary to the prediction of a compression (Lohr and Lipscomb, 1963). The observed negative D value, however, is consistent with the negative trigonal field splitting.

Several postulates have been put forth to account for these apparently wrong signs of D for $3d^3$ and $3d^8$ ions in some of the trigonally distorted host lattices. These are:

(a) A small displacement of the order of 0.1 A of the paramagnetic ions from the Al^{3+} site can change the sign of the trigonal field (McClure, 1962).

(b) A few percent of anisotropy in the spin-orbit coupling constant can reverse the sign of D with positive v (Kamimura, 1962).

(c) Configurational mixing of higher excited states and/or covalency effects of ligands can alter the energy levels of both the ground state and the excited states, which will modify the magnitude of D (Lacroix, 1961; Kamimura, 1962).

Because of lack of experimental evidence the validity of postulates (a) and (b) cannot be fully supported or repudiated. We will proceed our discussion along the line of (c).

The CFT, which in its simplest form deals with an ion in a static electric field, has been criticized for its inadequacy to explain certain experimental observations; viz., the presence of super-hyper-

fine structure of ligand nuclei, a reduction of the metal hyperfine splitting in complexes, a reduction of the orbital contribution to the g factor, and a reduction of crystal field splittings in solids.

Let us go back to section IV-A-1 to find out what tacit approximations were made to derive Eqs.(12) and (13). First we have considered only the spin-orbit interaction as the source of a zero-field splitting and ignored the dipole-dipole interaction of electron spins. Since the latter contributes no more than 5% of the spin-orbit interaction to the zero-field splitting in 3d ions, our assumption was valid. Secondly, we have assumed that only excited states of the same L.S configuration as the ground state would contribute to the zero-field splitting. It is this assumption that we need now to reexamine. In Fig. 10a the trigonal distortion splits T_{1g} into A_{2g} and E_g, T_{2g} into A_{1g} and E_g, while the ground state A_{2g} remains unchanged. Now the configuration interaction mixes A_{2g} of T_{1g} into the ground state A_{2g} and also E_g of T_{1g} into E_g of T_{2g}. Although these mixing coefficients are small, they are nevertheless very important, because there is a direct spin-orbit coupling between the T_{1g} and T_{2g} states in a trigonal symmetry. There is another T_{2g} state of a different L.S configuration, ^2G, at about 35,000 cm^{-1} that has a non-zero matrix element of the spin-orbit coupling with the ground state. An extensive MO calculation of Lohr and Lipscomb (1963) shows that for Cr^{3+} in trigonal symmetry about three-fourths of the contribution to D and E comes from a $^2T_{2g}$ term whose energy is slightly higher than $^4T_{2g}$. Sugano et.al (1970) show that the lowest-order perturbations giving

rise to the zero-field splitting are the third-order ones involving the spin-orbit interaction twice and the trigonal distortion once. They show at least three separate perturbations from $^4T_{2g}$, $^4T_{1g}$ and $^2T_{2g}$, all of which give comparable contributions to the splitting of the $^4A_{2g}$ term. Kamimura (1962) also suggests that under the trigonal distortion, which transforms like T_2 symmetry in an octahedral group, the t_2 molecular orbitals (xy, yz, xz) are distorted by covalent bonding, making the trigonal field splitting $\Delta_1-\Delta_2$ positive. Therefore, the excited states of other configurations and the covalent effect are very important in determining the zero-field splitting of the ground state in a trigonal distortion.

The g value, however, is influenced mainly by $^4T_{2g}$ which is the sole contributor to the first-order interaction of the ground state with an external magnetic field. This fact is illustrated by the observation of relatively small anisotropy in the g factor, even when D is large. Since covalent bonding can influence the $^4T_{2g}$ term, the g value is very sensitive to the nature of the molecular orbitals.

In summary, although there are several systems whose D values can be correctly predicted by the CFT, an accurate calculation of the zero-field splitting in a trigonal field requires consideration of all the excited states. For the calculation of the g factor the nature of covalent bonding should be taken into account.

Tetragonal distortion presents a more encouraging picture. First of all there is no excited state that is admixed to the ground state by configurational interaction. The two excited states, E_g of

T_{2g} and E_g of T_{1g}, are admixed by configurational interaction, which shifts the energy level of lower E_g relative to B_{2g}. This effect on the zero-field splitting will be small, however, because the T_{1g} and the T_{2g} states are not connected by the spin-orbit coupling. These states are relatively pure, apart from the small mixing arising from the configurational interaction. Therefore, the ground state B_{1g} is influenced mainly by T_{2g}, as we have assumed in the simple crystal field treatment. In spite of a small number of examples, the experimental results of Ni^{2+} in a tetragonal symmetry is well approximated by the CFT, provided a small adjustment in the spin-orbit coupling constant is made owing to the bonding effects. We should point out that the presence of a rhombic distortion can generate states of the same symmetry as the ground state, so that the configuration interaction, which was previously symmetry forbidden, is now possible between the excited states and the ground state.

McGarvey (1964b) gives an instructive energy diagram of $3d^3$ ions in O_h, D_{4h} and D_{2h} symmetries. His diagram shows which excited states can be mixed to the ground state by the configurational interaction in D_{2h} symmetry. In his calculation of the spin Hamiltonian parameters for $Cr(en)_3^{3+}$ complexes using the CFT and MO theory, McGarvey shows that a small distortion to D_{2h} can produce a large change in the direction of the principal axes of the D tensor and in its magnitude. He concludes that D and E are very sensitive to the lower crystal field symmetries but not to the nature of molecular orbitals. His crystal field approach gives good results of the calculated D with the free ion spin-orbit coupling constant. However, in calculating the g factor,

a reduced value of the spin-orbit coupling constant must be used, presumably because the g factor is very sensitive to the bonding character. We have seen a similar result in $Ni^{2+}:ZnSeO_4 \cdot 6H_2O$.

V. Cu^{2+} in $ZnSeO_4 \cdot 6H_2O$

A. Theory of Cu^{2+} ($3d^9$)

The cupric ion has been most extensively studied by EPR. It has nine 3d electrons, one of which is unpaired. In a free ion the unpaired d electron possesses two units of orbital angular momentum, constituting a ^2D term. For hexahydrates the highest symmetry that Cu^{2+} can have is octahedral,in which the five-fold degeneracy is split into a lower doublet and an excited triplet. The Jahn-Teller theorem, however, requires that the local symmetry of Cu^{2+} must be distorted in such a way that the orbital degeneracy is removed. Because this distortion into a lower symmetry can yield a state of lower energy, Cu^{2+} is known to prefer large distortions. In the present work we assume this distortion to be tetragonal D_{4h}, as discussed in IV-A-1. The trigonal case is discussed in Appendix III, because it creates a special problem.

The schematic energy diagram for Cu^{2+} is shown in Fig. 24. The designations of the spin-orbit states are obtained from the direct products of the tetragonal orbital states with the spin state $E_{1/2}$ (Herzberg, 1966, Table 56 and 57). Because the tetragonal distortion is fairly large in Cu^{2+}, and because there is no spin-orbit coupling within the E_g state, we can treat the ground state of Cu^{2+} effectively as an orbital singlet. The presence of an external magnetic field separates the ground state Kramer's doublet, between which paramagnetic resonance is observed. Whether the tetragonal distortion is an elongation or a compression becomes apparent in the g values of the Cu^{2+} ions,

as explained below. In almost all Cu^{2+} complexes, which have been studied by EPR, the tetragonal distortion is an elongation of an octahedron along the z axis relative to the xy plane. The only exception known is K_2CuF_2 , where a compressed octahedron was found (Knox, 1959).

An elongation of an octahedron along the x axis stabilizes electrons in a_{1g} (z^2) orbital state but holes in b_{1g} (x^2-y^2) state. Cu^{2+} is conveniently treated as one unpaired hole. The g values of Cu^{2+} can be calculated from Eq. (7), which is correct to order (λ/Δ). The matrix elements $\langle 0 | L_i | n \rangle^2$ and Λ_{ij} for the ground state of x^2-y^2 and z^2 are tabulated in Table XVIa, b, and c. The tensor components Λ_{ij} are substituted in Eq. (7). We assume again an axial spin Hamiltonian, in which

$$g_{/\!/} = g_z = g_e(1-\lambda\Lambda_{zz})$$

$$g_{\perp} = g_x = g_y = g_e(1-\lambda\Lambda_{xx})$$

The result is as follows:

	ground state x^2-y^2	z^2
$g_{/\!/}$	$g_e(1-4\lambda/\Delta_1)$	g_e
$g_{\perp}$	$g_e(1-\lambda/\Delta_2)$	$g_e(1-3\lambda/\Delta_3)$

(31)

Noting the negative value of λ for Cu^{2+}, we see

$$g_{/\!/} > g_{\perp} \text{ in } x^2-y^2 \text{ and } g_{/\!/} < g_{\perp} \text{ in } z^2.$$

An observation of $g_{/\!/} > g_{\perp}$ clearly indicates that the tetragonal distortion is an elongation rather than a compression along the z axis.

The spin Hamiltonian of Cu^{2+} in the D_{4h} symmetry is

$$\mathcal{H}_{spin} = g_{\parallel}\beta H_z S_z + g_{\perp}\beta(H_x S_x + H_y S_y) + A_{\parallel} S_z I_z + A_{\perp}(S_x I_x + S_y I_y) \qquad (32)$$

At X-band the quantization axis is taken along the direction of the magnetic field, for the Zeeman term is much greater than hfs. A coordinate transformation to a new set of axes will diagonalize the Zeeman term to a form $g\beta HS_z'$. The new principal axis of the g tensor has the direction cosines of $(\ell g_{\perp}/g,\ mg_{\perp}/g,\ ng_{\parallel}/g)$ with respect to the old axes, where the quantities $(\ell,\ m,\ n)$ are listed in Table A-2, The g is the observed value and can be calculated from

$$g^2 = g_{\perp}^2(\ell^2 + m^2) + g_{\parallel}^2 n^2$$

Since the normalization of direction cosines requires $\ell^2+m^2+n^2 = 1$,

$$g^2 = (g_{\parallel}^2 - g_{\perp}^2)n^2 + g_{\perp}^2 \qquad (33)$$

A plot of g^2 vs. n^2 will result in a straight line with a slope of $(g_{\parallel}^2 - g_{\perp}^2)$ and a y intercept of $g_{\perp}^2$. This turns out to be a good method to check the value of ϕ and to extrapolate $g_{\parallel}$ and $g_{\perp}$. It should be noted that the data from only one plane will not unambiguously determine the g and hfs constants. A good example of this error will be discussed in the section of Co^{2+} : α-$NiSO_4 \cdot 6H_2O$.

If the hf tensor has the same principal axes as the g tensor, a similar transformation of the nuclear spin components will diagonalize the hf tensor to the form of $AS_z'I_z'$. Here I_z' refers to the new principal axis whose direction cosines with respect to (x,y,z) are

$$(\ell g_{\perp} A_{\perp}/gA,\ mg_{\perp}A_{\perp}/gA,\ ng_{\parallel}A_{\parallel}/gA).$$

Table XVI. Matrix elements.

a. $|\langle x^2 - y^2 | Li | n \rangle|^2$

Li \ n	z^2	xy	yz	xz
Lz	0	4	0	0
Lx	0	0	1	0
Ly	0	0	0	1

b. $|\langle z^2 | Li | n \rangle|^2$

Li \ n	$x^2 - y^2$	xy	yz	xz
Lz	0	0	0	0
Lx	0	0	3	0
Ly	0	0	0	3

c. Non-zero matrix elements of Λ_{ij}

ij \ $\|0\rangle$	$x^2 - y^2$	z^2
zz	$4/\Delta_1$	0
xx	$1/\Delta_2$	$3/\Delta_3$
yy	$1/\Delta_2$	$3/\Delta_3$

Substituting $\lambda = -830\ cm^{-1}$ and $\Delta_1 \sim \Delta_2 \sim 12x10^3\ cm^{-1}$, we obtain $g_{\parallel} \sim 2.6$ and $g_{\perp} \sim 2.15$, which are about 20% greater than the commonly observed values of $g_{\parallel} \sim 2.4$ and $g_{\perp} \sim 2.1$. The discrepancy is attributed to the covalency effect that reduces the orbital contribution. For z^2 the calculated g values are $g_{\parallel} = 2.00$ and $g_{\perp} \sim 2.4$. More accurate formulae for g and hyperfine constants are given by Abragam and Pryce (1951b) and by Bleaney et.al. (1955).

In Eq.(9), for S = 1/2, the D term merely shifts all of the energy levels without causing a splitting and the E term is zero. This is another way of saying that the zero-field splitting exists only for ions with $S > 1/2$.

If the paramagnetic ion possesses a nuclear spin, it can have additional interactions. The electron-nuclear hyperfine (hfs) interaction is given rise to by the magnetic field, induced by an unpaired electron, interacting with the nuclear spin. There are two stable copper isotopes: Cu^{63} (69.09% natural abundance, I = 3/2, μ_n = 2.221 n.m.) and Cu^{65} (30.91%, I = 3/2, μ_n = 2.379 n.m.). Each isotope will exhibit 2I+1 or four hfs lines. If the nuclear spin is greater than 1/2, as in copper, it can interact with the quadrupole electric field gradient in the nucleus (NQ). Since NQ is usually smaller than hfs ($10^{-3} \sim 10^{-4}$ cm^{-1} of NQ vs. $10^{-2} \sim 10^{-4}$ cm^{-1} of hfs) in hydrated Cu^{2+}, we will ignore NQ at first and consider it in a more detailed analysis. We will neglect the nuclear Zeeman and ligand hyperfine (super hfs) interactions, since they are usually much smaller and are not observed in the EPR of hydrated Cu^{2+} salts, except as line broadening effects.

The hyperfine constant A, measured in units of energy, is given by

$$g^2A^2 = (g_{\parallel}^2A_{\parallel}^2 - g_{\perp}^2A_{\perp}^2)n^2 + g_{\perp}^2A_{\perp}^2 \qquad (34a)$$

or in units of gauss,

$$g^4A^2 = (g_{\parallel}^4A_{\parallel}^2 - g_{\perp}^4A_{\perp}^2)n^2 + g_{\perp}^4A_{\perp}^2 \qquad (34b)$$

In the first order approximation the measured separation of the central two hfs lines can be substituted for A in Eq.(34b). A plot of g^4A^2 vs. n^2 will again yield a straight line, provided that the principal axes of the g and hfs tensors coincide.

The transitions we observe in the EPR of Cu^{2+} are of the type $\Delta M = \pm 1$ and $\Delta m_I = 0$. Then, the spin Hamiltonian (32) gives

$$H = H_o - Am_I - \left(\frac{A_{\perp}^2g_{\perp}^2}{4H_og^2}\right)\left(\frac{A_{\parallel}^2g_{\parallel}^2 + A^2g^2}{A^2g^2}\right)\left[I(I+1) - m_I^2\right]$$

$$= \frac{1}{2H_o}\left(\frac{A_{\parallel}^2g_{\parallel}^2 - A_{\perp}^2g_{\perp}^2}{Ag^2}\right)^2\left(\frac{g_{\parallel}g_{\perp}}{g}\right)^4\left[n^2(1-n^2)m_I^2\right] \qquad (35)$$

where $A_{\parallel}$, $A_{\perp}$ and A are all in gauss and $H_o = h\nu/g\beta$. The deviation of H_o from the actual magnetic field is small enough to be ignored. In Eq.(35) the second term is responsible for 2I+1 equally spaced lines that are centered at H_o. The third and the fourth terms shift each line to lower field, disturb the equal spacings of the lines and give a progressive linear change in the spacing. When the magnetic field is either parallel or perpendicular to the z axis, the fourth term is zero and the third term makes the spacing successively smaller toward the high-field end. If $A_{\parallel} \gg A_{\perp}$, the second order effect becomes very important near the perpendicular direction (Rollman and Chan, 1969).

B. Results

A rectangular plate (6.5x6.5x2 mm^3) was cleaved from a large crystal of Cu^{2+} : $ZnSeO_4.6H_2O$ grown at 5°C in a refrigerator. The concentration of $CuSeO_4$ in the mother liquor, from which single crystals were grown, was about 2 mole %. We have not attempted to analyze the Cu^{2+} concentration in the crystal, but we think it to be less than 1%, judging from the narrow line widths of the Cu^{2+} EPR lines. The sample was mounted horizontally, or in the ab plane, in an X-band cylindrical cavity and cooled to liquid nitrogen temperature in the double Dewar.

Two sets of four lines, characteristic of Cu^{2+} hfs, were seen at all angles except at one orientation where the two sets became equivalent. The lines were strong, narrow (peak-to-peak width of a derivative spectrum ranging from 8.4 G to 12 G) and easily detectable at this temperature with the 825 Hz field modulation. The effect of the two copper isotopes were clearly seen in the splittings of outer lines. The ratio of the two hfs constants was 1 : 1.07, in close agreement with the ratio of their nuclear magnetic moments, 2.22 : 2.38 = 1 : 1.07.

Near the ab bisector, or the γ axis, one set was at the lowest field, and the other was at the highest field. The low field hf lines were clearly separated, the center of which gave g = 2.259 and A = 90.0 G.

The powdered sample of Cu^{2+} : $ZnSeO_4 \cdot 6H_2O$ was looked at over the temperature range of 20° to -160°C at X-band with the 100 kHz modulation. The spectra consisted of two groups: four evenly spaced, half-derivative parallel lines in the low field and extensively overlapped perpendicular lines in the high field. At -160°C the powder spectrum resulted in

$$g_{\parallel} = 2.4291, \quad g_{\perp} = 2.098$$
$$A_{\parallel} = 115.9 \text{ G}, \quad A_{\perp} < 21 \text{ G}$$

Next, the crystal was mounted vertically with the field in the γc plane. Fig. 25a shows a typical Cu^{2+} spectrum, exhibiting four sets of four hfs lines. Fig. 26 displays the angular dependence of the four Cu^{2+} ions in this plane. The points are the positions of the lowest field hf components ($m_I = -3/2$). Solid curves are drawn to connect these points. The two sets, 2 and 4, moved closely together as the magnetic field was rotated. All four sets merged perfectly at the c axis, as shown in Fig. 25b. As the magnetic field direction was moved away from the c axis, ion 1 went toward the lower field or higher g value, and ion 3 shifted to the higher field. At $\alpha = 43.3°$ ion 1 reached the lowest field with $g = 2.4293$ and $A = 115.7$ G. Rotating the magnet to $\alpha = -42.9°$ (the sign of the angle is only relative), we saw another minimum with the same g and A values. Thus, the Φ , the angle between the c and the z axes, must be close to 42°. At $\alpha = 90°$ ions 1 and 3 merged in the low field, while ions 2 and 4 overlapped in the high field.

In the following analysis we take the average field positions and hf splittings of ions 2 and 4, assuming that the splittings had resulted from a misorientation of the crystal. A computer plot of g^2 vs. n^2 is shown in Fig. 27. The data points are taken from the γc and ac planes. A straight line is made to fit to the experimental points by a least-squares method. The ϕ of 43.3° gives minimum variances in the slope and the intercept. An extrapolation yields $g_{\parallel} = 2.4289 \pm 0.0001$ and $g_{\perp} = 2.0963 \pm 0.0001$. Fig. 27b demonstrates the accuracy involved in the evaluation of ϕ. A change of ϕ to 40° places the experimental points (crosses) no longer in a straight line but in an ellipse. A similar plot of g^4A^2 vs. n^2 in Fig. 28 shows an essentially axial symmetry of the g and hf tensors. A best fit is obtained by $\phi = 43.0°$, resulting in $A_{\parallel} = 115.4$ G and $A_{\perp} = 9.9$ G. With these parameters the angular dependence of g and A values are calculated and compared with the experimental values in Fig. 29a and b. The fit is excellent for g and fairly good for A.

However, we have seen similar splittings of ions 2 and 4 in the γc plane of Co^{2+} and Ni^{2+} in $ZnSeO_4 \cdot 6H_2O$. We have looked at a few Cu^{2+} : $ZnSeO_4 \cdot 6H_2O$ crystals and found that the splitting was real. Now we need to modify the direction cosines of the magnetic axes. Judging from the good agreement in Fig. 29a and b, we can assume that this change will be small. We have detected no splitting in the ab plane, nor at the c axis. This requires a small rotation of the z and x axes about the second γ axis; i.e., the x axis is tilted by a small angle β in the γc plane.

The new sets of direction cosines are given in Table A-2 in Appendix II. The angular dependences of g and A are recalculated and shown in Fig. 30 and Fig. 31. The dotted curves are drawn by the computer with

$$g_{\parallel} = 2.4295, \quad g_{\perp} = 2.0965, \quad \phi = 43.2°$$
$$A_{\parallel} = 115.6 \text{ G}, \quad A_{\perp} = 9.5 \text{ G}, \quad \beta = 4.1°$$

Using new sets of direction cosines we next calculate the ab plane spectra. In this plane only two sets are seen. The maximum and minimum g values do not occur at the γ axes, neither do the two sets merge at the a axis. The modification of the direction cosines merely shifts the angle by 4.3°, as illustrated in Fig. 32.

A real test is in the ac plane. Here again the four ions are not equivalent except at the c axis. In Fig. 33 the dotted curves represent the predicted values from the result of the γc plane. The observed splittings, however, were not so large as calculated and varied with different runs. We could not differentiate how much of the splitting was due to a misorientation of the crystal and how much was due to the actual tilting of the x axes. The average g values of ions 1 and 4 and of ions 2 and 3 are plotted as open circles in Fig. 33.

In summary we list the best set of parameters for Cu^{2+}: $ZnSeO_4 \cdot 6H_2O$.

$$\left.\begin{array}{ll} g_{\parallel} = 2.4295 \pm 0.0005, & g_{\perp} = 2.0965 \pm 0.0005 \\ A_{\parallel} = 115.6 \pm 0.3 \text{ G}, & A_{\perp} = 9.5 \pm 1.0 \text{ G} \\ \phi = 43.3 \pm 0.1° & \beta = 3 \pm 1° \end{array}\right\} \quad (36)$$

C. Discussion

In Table XVII we list the results for Cu^{2+} from the three crystal planes of $ZnSeO_4 \cdot 6H_2O$. We feel that the assignments of the g values are quite certain but that of $A_\perp$ may contain a large uncertainty. The Cu^{2+} spectra can be explained by an axial spin Hamiltonian, if the magnetic x axis is tilted by a few degrees from the γ axis toward the c axis. The fact that the Cu^{2+} spectrum remained axial over the temperature range of 77° to 300°K suggests that the distortion of an octahedron is tetragonal rather than trigonal. Judging from the g values, we conclude that the ground state of Cu^{2+} is (x^2-y^2). This result is consistent with the nature of the hydrogen bondings in the host crystal and with the interpretation of the Ni^{2+} spectra in $ZnSeO_4 \cdot 6H_2O$.

From Eq.(31) the CFT predicts

$$\left.\begin{aligned} g_{\parallel} - g_e &= -8\lambda/\Delta_1 = 0.4272 \\ g_{\perp} - g_e &= -2\lambda/\Delta_2 = 0.0942 \end{aligned}\right\} \qquad (37)$$

The ratio of $\Delta_2/\Delta_1 = 1.1$ also supports the elongated octahedron model. Bleaney, Bowers and Pryce have calculated the effects of order $(\lambda/\Delta)^2$ on the spin Hamiltonian parameters. The theoretical g values given for the ground state (x^2-y^2) are

$$\left.\begin{aligned} g_{\parallel} &= g_e(1 + 4w - 3u^2/2 - 2uw) \\ g_{\perp} &= g_e(1 + u - 2w^2) \end{aligned}\right\} \qquad (38)$$

Table XVII. Observed and Calculated g and A of Cu^{2+}: $ZnSeO_4 \cdot 6H_2O$.

		Observed		Calculated		
Axis	Plane	g	A (gauss)	g	A (gauss)	Method of calculation[a]
a	ab	2.179	69.3	2.179	69.9	1
a	ac	2.179	68.6			
c	ac	2.278	97.2	2.279	96.1	1
c	γc	2.279	97.3			
γ_1[b]	ab	2.260	91.4	2.260	91.8	1
γ_1	γc	2.259	90.1	2.259	91.7	1
γ_2[c]	γc	2.098	≤15	2.097		1
x	ab	2.095		2.0963	7.6	2
x	Powder	2.098		2.0965	8.5	3
z	Powder	2.4291	115.9	2.4295	115.9	3
z	γc	2.4292	115.7	2.4289	115.6	2

a. 1: From Eqs. (33) and (34b).
2: From plot of g (or A) vs. α.
3: From extrapolation of the plots of Eqs. (33) and (34b).
b. γ_1 denotes the ab bisector at which the low field spectrum is observed.
c. γ_2 denotes the other ab bisector at which the high field spectrum is observed.

Here we distinguish 2.0023 for g_e from 2.000 and define the quantities u and w as

$$\left.\begin{aligned} u &= \lambda/\Delta_2 \\ w &= \lambda/\Delta_1 \end{aligned}\right\} \qquad (39)$$

The use of successive approximations in Eq.(38) yield the values of u and w.

	Eq.(37)	Eq.(38)
u	0.0471	0.0533
w	0.0534	0.0559

The optical spectra of $Cu(H_2O)_6^{2+}$ have been observed in solution and the cubic field splitting is found to be $\Delta = 12600\ cm^{-1}$ (Table V). If we assume that the average of Δ_1 and Δ_2 is close to this value, we obtain the spin-orbit coupling constant,

$$\lambda = -12600x(0.0546) = -690\ cm^{-1}$$

which is 83% of that of the free Cu^{2+} ion. This reduction is commonly ascribed to bonding effects.

The hfs constants can be treated in a similar fashion. Bleaney et.al (1955) give the following equations.

$$\left.\begin{aligned} A_{\parallel}/p &= -\kappa(1-u^2) - 4/7 + 6u/7 + 8w - 3u^2/7 - 40uw/7 \\ A_{\perp}/p &= -\kappa(1-u^2/2 - 2w^2) + 2/7 + 11u/7 + 9u^2/14 - 4w^2/7 \end{aligned}\right\} \qquad (40)$$

where $$p = g_e g_n \beta \beta_n \langle r^{-3} \rangle \qquad (41)$$

p will be calculated below. The constant κ is an empirical parameter, often called the core polarization parameter, which represents a measure of the admixture of excited configurations with unpaired s electrons.

There are two stable isotopes of copper, both with I = 3/2. Cu^{63} (69.1% abundance) has a nuclear magnetic moment, μ_n, of +2.226, while Cu^{65}(30.9% abundance) has μ_n = +2.385, in units of the nuclear magneton. We will take the weighted average of the two isotopes as μ_n = 2.275 n.m. 1 n.m. = 5.050×10^{-24} erg.gauss^{-1}. Then

$$g_e g_n \beta\beta_n = g_e \beta \mu_n / I = (2.0023)(9.273\times10^{-21})(2.275)(5.050\times10^{-24})/1.5$$
$$= 1.422\times10^{-43}\ \text{erg}^2.\text{gauss}^{-2}$$

Since gauss^2 = gm.cm^{-1}.sec^{-2} and erg = gm.cm^2.sec^{-2}, erg^2.gauss^{-2} = erg.cm^3. Changing erg into cm^{-1}, we obtain

$$g_e g_n \beta\beta_n = (5.035\times10^{15})(1.422\times10^{-43})$$
$$= 7.160\times10^{-27}\ \text{cm}^{-1}.\text{cm}^3 \qquad (42)$$

The quantity $\langle r^{-3} \rangle$ is listed in Table 7.6 of A & B and for a free Cu^{2+} ion is equal to 8.252 in atomic units. Therefore, for the free Cu^{2+} ion

$$p_o = (7.160\times10^{-27})(8.252)(0.529\times10^{-8})^{-3}$$
$$= 0.0399\ \text{cm}^{-1} \qquad (43)$$

in close agreement with the 0.036 cm^{-1} value of Abragam and Pryce, who used $\langle r^{-3} \rangle$ = 7.25 a.u. for the Cu^{2+} ion. Before we calculate the theoretical hfs constants of Eq.(40), a word about κ is in order.

The unpaired electron of Cu^{2+} is in the 3d orbital for which the electron density at the nucleus is zero. However, in practice it has been found necessary to assume a small admixture of s character into the d orbital in order to explain the observed hf of the iron-group ions. Since the s electron has a non-zero electron density at the nucleus, its hf interaction through the so called Fermi contact term

is very much stronger than that of the d electrons. Only a small admixture of excited s configurations is sufficient to modify the hf appreciably. All other properties of the ground state, however, remain unaffected by this small admixture. The sign of κ is found to be positive so that the electronic hf field at the nucleus is parallel to the electron spin S. It is customary to introduce another quantity, χ, which expresses the density of unpaired spins at the nucleus. χ is related to κ by

$$\chi = -3\kappa\langle r^{-3}\rangle /2 \tag{44}$$

Substitution of u and w into Eq.(40) results in

$$\left.\begin{aligned} 1.003\ A\ /p &= -\kappa - 0.0971 \\ 1.008\ A\ /p &= -\kappa + 0.372 \end{aligned}\right\} \tag{45}$$

A general equation of the form

$$A_i'/p = -\kappa + f_i \tag{46}$$

shows that a plot of A_i' vs. f_i will result in a straight line of slope p and of intercept κ with the abscissa. The sign of the hf constants is experimentally indeterminant, but Eq.(45) and the plot of Eq.(46) usually determine the sign. For example, in Cu^{2+}: $ZnSeO_4 \cdot 6H_2O$, $|A_{\parallel}| > |A_{\perp}|$, hence $\kappa > 0$ and $A_{\parallel} < 0$. We plot in Fig. 34 the results of Cu^{2+} in $ZnSeO_4 \cdot 6H_2O$ and also in LMN and in $Zn(BrO_3)_2 \cdot 6H_2O$. The last two systems possess a trigonal symmetry and will be discussed in Appendix III,

Table XVIII lists the parameters calculated for the three systems. The three straight lines of nearly equal slopes in Fig. 34 demonstrate

Table XVIII. Analysis of hf constants of Cu^{2+}.

	$ZnSeO_4 \cdot 6H_2O$	LMN		$Zn(BrO_3)_2 \cdot 6H_2O$	
	77°K	1.7°K	77°K	1.7°K	77°K
u	0.0533	0.0561	0.0593	0.0521	0.0575
w	0.0559	0.0605		0.0582	
$A_{\parallel}$ [b]	-131.5	-111.5	-26.7	-112.0	-25.9
$A_{\perp}$ [b]	+ 8.3	+ 16.8		+ 18.7	
$f_{\parallel}$	- 0.097	- 0.060	0.232	- 0.080	0.225
$f_{\perp}$	0.372	0.377		0.370	
κ	0.339	0.316		0.305	
p [b]	330	298		291	
p/p_o	82.7%	74.7%		72.9%	
λ [c]	-690	-730		-700	
λ/λ_{free}	83%	88%		84%	
$\langle r^{-3} \rangle$ [d]	6.82	6.16		6.02	
χ [d]	- 3.47	- 2.92		- 2.75	
He/S [e]	289	244		229	

a. Calculated for the isotropic spectra of the dynamic Jahn-Teller interaction discussed in Appendix III.

b. In units of 10^{-4} cm^{-1}.

c. In units of cm^{-1}.

d. In atomic units (a.u.)

e. In units of kG.

the correct signs of the hf constants and the soundness of the prediction of the CFT. The calculated value of p for Cu^{2+}: $ZnSeO_4 \cdot 6H_2O$ is 82.7% of the free ion value. The amount of reduction is quite similar to the reduction in the spin-orbit coupling. This indicates that both reductions are due to bonding effects. The degree of covalency in the three systems is expected to be similar, since all three are coordinated with six water molecules in nearly octahedral symmetry. This expectation is supported by the similar values of λ/λ_{free} in the three systems. However, the smaller values of p/p_o in Cu^{2+}: LMN and in Cu^{2+}: $Zn(BrO_3)_2 \cdot 6H_2O$ are surprising. We should probably not take too literally the parameters of Table XVIII as a measure of the degrees of covalency in the Cu^{2+} hydrated salts.

We may say, from Eq.(41), that in a solid $\langle r^{-3} \rangle$ is reduced to 6.49 a.u. Then χ is calculated to be

$$\chi = -(1.5)(0.339)(6.49) = -3.14 \text{ a.u.}$$

The value of χ has been fount to be nearly constant at about -3 a.u. for the ions of the iron-group. It depends on the nature of the ligand, and decreases a little with increasing covalency.

The hf field due to the core polarization alone can be computed from

$$H_e = -\beta \chi S = -83.4 \chi S \quad \text{kG} \tag{47}$$

when χ is in atomic units (A & B, Eq. 7.68). The fact that χ remains constant for all the $3d^n$ ions predicts the nearly identical core polarization field of 250 kG per unit of electron spin, which is in very good agreement with experimental results (see Table 7.21 of A & B, and the references given there).

VI. Co^{2+} : $ZnSeO_4 \cdot 6H_2O$

A. Theory for Co^{2+} ion ($3d^7$)

The lowest term of the free Co^{2+} ion is ^4F. The effect of a cubic crystal field is to split the seven-fold orbital degeneracy of the ^4F term into two triplets and a singlet, as in the case of Ni^{2+}. The order of these energy levels, however, is the exact reverse of those in the $3d^8$ system; the ground state is the orbital triplet $^4T_{1g}$ with $^4T_{2g}$ at 8Dq and $^4A_{2g}$ at 18Dq. The overall separation is of the order of 20,000 cm^{-1} for the water complex.

We can use the energy level diagrams of Fig. 10a and b for the $3d^7$ system, provided that all the energy levels are inverted and that the spin degeneracy is increased by one. We represent the ground state orbital triplet by a fictitious angular momentum $\tilde{\ell} = 1$. The relationship between the fictitious angular momentum and the real orbital angular momentum is defined as

$$\vec{L} = \alpha \tilde{\ell} \qquad (48)$$

where the proportionality constant α is sometimes called the effective orbital g factor. The value of α lies between -3/2 for the weak field limit and -1 for the strong field limit.

The spin-orbit coupling will remove the twelve-fold total degeneracy (3 x 4), leaving a Kramers doublet ($\tilde{J} = 1/2$, $W = -5\alpha\lambda/2$) lowest, a quartet ($\tilde{J} = 3/2$, $W = -\alpha\lambda$) and a sextet ($\tilde{J} = 5/2$, $W = 3\alpha\lambda/2$) at some several hundred wave numbers higher. Here $\tilde{J}$ is a fictitious total angular momentum that is obtained by coupling $\tilde{\ell}$ and $\vec{S}$.

The presence of an axial distortion further removes the degeneracy of the excited quartet and the sextet, so that $\tilde{J}$ is no longer a good quantum number. Instead $\tilde{J}_z = \tilde{\ell}_z + S_z$ must be used to describe a number of Kramers doublets with $\tilde{J}_z = \pm 1/2$, $\pm 3/2$ and $\pm 5/2$. Then the simple relationship between $\vec{L}$ and $\tilde{\ell}$ is modified to the form

$$L_x = a'\tilde{\ell}_x, \quad L_y = a'\tilde{\ell}_y, \quad L_z = a\,\tilde{\ell}_z \tag{49}$$

The perturbing Hamiltonian of Eq. (4) is now modified to

$$\begin{aligned} \mathcal{H} &= \Delta(\tilde{\ell}_z^2 - 2/3) + \lambda\left[a\tilde{\ell}_z S_z + a'(\tilde{\ell}_x S_x + \tilde{\ell}_y S_y)\right] \\ &\quad + \beta\left\{g_e(H\cdot S) + \left[a H_z \tilde{\ell}_z + a'(H_x\tilde{\ell}_x + H_y\tilde{\ell}_y)\right]\right\} \end{aligned} \tag{50}$$

where the first term represents the axial distortion, the second is the spin-orbit coupling and the last term refers to the Zeeman interaction of the total angular momentum. Equation (50) is found in A & B (section 19.4) and also in Griffith (sections 10-2-3 and 12-4-8). The magnitude of Δ in most hydrated Co^{2+} salts has been found to be several hundred cm^{-1}, which is comparable to the splitting due to the spin-orbit coupling. In Tutton salts the sign of Δ was found negative, placing the orbital doublet ($\tilde{\ell}_z = \pm 1$) lower than the singlet ($\tilde{\ell}_z = 0$).

Because the microwave quanta used for our EPR is much smaller than this splitting, we can consider only the transition between the lowest Kramers doublet ($\tilde{J}_z = \pm 1/2$). The spin Hamiltonian for this ground doublet is identical with Eq. (32),

$$\begin{aligned} \mathcal{H}_{spin} &= g_{\parallel}\beta H n S_z + g_{\perp}\beta H(\ell S_x + m S_y) \\ &\quad + A_{\parallel} S_z I_z + A_{\perp}(S_x I_x + S_y I_y) \end{aligned}$$

Cobalt has one stable isotope Co^{59} with 100% natural abundance, I = 7/2 and μ_n = 4.639 n.m. The analysis of the g and hf constants used for Cu^{2+} can be applied to the ground state doublet of Co^{2+} as well. The second order effect of the hf interaction in Eq.(35) can become very large for I = 7/2. In fact, this second order line shift is so large near the perpendicular direction that the hf lines of large m_I components cross over in some hydrated Co^{2+} ions (Bleaney and Ingram, 1951). This makes the accurate determination of $g_\perp$ and $A_\perp$ rather difficult.

Because of the presence of the low-lying excited states, which are connected to the ground state by the spin-orbit coupling, the spin-lattice relaxation time of Co^{2+} is so short that the EPR spectrun of Co^{2+} is observable only near liquid helium temperatures.

B. Results

A colorless rectangular plate was readily cleaved from a large single crystal of Co^{2+}: $ZnSeO_4 \cdot 6H_2O$ grown in a refrigerator. The Co^{2+} concentration was about 4% in the mother liquor but no chemical analysis of Co^{2+} contained in the single crystal was made.

We observed no EPR of Co^{2+} in this host lattice at 77°K or above. All the experiments were carried out at 1.7°K. The lines were strong at this temperature and slightly broader (9 ~ 10 G) than the Cu^{2+} lines.

The ab plane spectra showed only two groups of eight hf lines that merged near the a axis at g = 4.453 and A = 81.6 G. In the first

order the hf splitting constant was taken directly from the separation of the central hf lines ($m_I = \pm 1/2$). The validity of this method will be discussed in the next section. The hf spacings were found to decrease progressively toward the high field. Near the γ axis one set reached the maximum g of 5.424 with A = 78.3 G, and the other set of partially overlapping eight lines reached the minimum g of about 3.26 with A ~ 15 G. Unlike the spectra of other orientations the perpendicular lines showed progressively smaller hf spacings toward lower field. The lowest three hf components were superimposed on top of one another.

When the crystal was mounted vertical so that H was rotated in the γc plance, four sets of eight lines were detected. The general behavior of these four sets resembled closely that of Cu^{2+}:$ZnSeO_4$. $6H_2O$. The splittings of ions 2 and 4 were real in Co^{2+} : $ZnSeO_4 . 6H_2O$. The four sets merged perfectly at the c axis at g = 4.315 and A = 79.2G. The lowest field in the γc plane occured at $\alpha = 58°$ from the c axis. The results are shown in Figs.35 and 36. As before, the experimental points are drawn in as open circles. We assume that the x axes of the Co^{2+} ions are tilted from the γ axes toward the c axis. This assumption is made on the following considerations. First, there were only two types of Co^{2+} ions detected in the ab plane. Secondly, the four ions became identical at the c axis. Ions 2 and 4 and ions 1 and 3 became equivalent at the γ axis. These observations require both the x and z axes of the four ions to lie in the γc planes, as in Cu^{2+} in $ZnSeO_4 . 6H_2O$.

The plots of g^2 vs. n^2 and of g^4A^2 vs. n^2 showed nearly straight lines with $g_{\parallel} = 5.976$, $g_{\perp} = 3.454$, $A_{\parallel} = 76.6$ G, $A_{\perp} = 24.4$ G, $\phi = 58°$ and $\beta = 2.5°$. We varied the above parameters until we obtained the best fits to the experimental points. The theoretical curves are drawn by the PDP-8/I computer with the following set of parameters.

$$\left.\begin{array}{ll} g_{\parallel} = 5.975\pm0.010, & g_{\perp} = 3.45\pm0.1 \\ A_{\parallel} = 77.0\pm0.5 \text{ G}, & A_{\perp} = 20\pm4 \text{ G} \\ \phi = 58.5\pm0.5°, & \beta = 4.5\pm1.0° \end{array}\right\} \quad (51)$$

The agreement is not very good. The large uncertainties involved in the perpendicular components of the g and the hfs constants are due to the difficulty in determining the center position of the eight lines, which are shifted as much as thirty gauss by the second order effect. This point will be discussed in the next section.

We investigated the Co^{2+} ion impurity in a mixed solid solution of $(Ni^{2+}, Zn^{2+})\ SeO_4.6H_2O$ at liquid helium temperature. The concentration of Ni^{2+} was roughly estimated to be about 10 mole %. While the Co^{2+} signal remained unchanged from 4.2° to 1.7°K, the Ni^{2+} signals disappeared at the lower temperature, supporting the positive D of Ni^{2+} in $ZnSeO_4.6H_2O$. The line positions and the hf splittings of Co^{2+} were nearly identical to those of Co^{2+} in the absence of Ni^{2+} ions. This is to be contrasted to the Cu^{2+} spectra in the paramagnetic host lattices, as discussed later in VII-C.

C. Discussion

1. Analysis of the g Factor and the Axial Splitting

Abragam and Pryce (1951c) discussed the theory of $3d^7$ with a small axial distortion of an octahedral field. They chose the wave-functions of the ground state doublet ($\tilde{J}_z = \pm 1/2$) as the linear combinations of $|\tilde{\ell}_z, S_z\rangle$.

$$|1/2\rangle = a\,|-1,3/2\rangle + b\,|0,1/2\rangle + c\,|1,-1/2\rangle$$

$$|-1/2\rangle = a\,|1,-3/2\rangle + b\,|0,-1/2\rangle + c\,|-1,1/2\rangle$$

with $a^2+b^2+c^2 = 1$.

They expressed the g factor and the axial splitting in a parametric form of x:

$$\left.\begin{aligned} g_{\parallel} &= 2 + 4(2-\alpha)\left[\frac{3}{x^2} - \frac{4}{(x+2)^2}\right]\cdot\left[p + \frac{6}{x^2} + \frac{8}{(x+2)^2}\right]^{-1} \\ g_{\perp} &= 4\left[p - \frac{2\alpha}{(x+2)} + \frac{12}{x(x+2)}\right]\cdot\left[p + \frac{6}{x^2} + \frac{8}{(x+2)^2}\right]^{-1} \end{aligned}\right\} \quad (53)$$

$$\Delta = \lambda\frac{\alpha'^2}{\alpha}\left(\frac{3}{x} + \frac{4}{x+2}\right) - \alpha\lambda(x+3)/2 \quad (54)$$

with $p = (\alpha'/\alpha)^2$ (55)

$$a : b : c = \frac{\sqrt{6}}{x} : -\frac{\alpha}{\alpha'} : \frac{\sqrt{8}}{x+2} \quad (56)$$

and $\lambda = -180\ \mathrm{cm}^{-1}$ for the free Co^{2+} ion.

It is noted that the signs of α and α' here are opposite to those given in Abragam and Pryce. They also assumed $g_e = 2.00$. The x is a positive number and equals two in a cubic symmetry. As mentioned before, α is expected to lie between -1 and -3/2. First let us calculate the g factor of Co^{2+} in an octahedral symmetry to familiarize ourselves with the technique of Abragam and Pryce. From $\Delta = 0$ and $\alpha = \alpha'$ in Eq.(54), we obtain

$$x = 2, \quad a = -(2)^{-1/2}, \quad b = (3)^{-1/2}, \quad c = -(6)^{-1/2}$$

$$g_{\parallel} = g_{\perp} = (10-2\alpha)/3$$

For $\alpha = -3/2$, the weak field limit, we get

$$g_{\parallel} = g_{\perp} = 13/3 = 4.333$$

which is in good agreement with the experimental g factor of Co^{2+} in MgO, CaO and $KMgF_3$ (quoted by Orton, 1968, Table 11.5a).*

An introduction of a non-zero Δ will add one more parameter to be determined. Without an accurate knowledge of Δ, we will not be able to determine all the three unknown parameters, (α, p, x), from the two experimentally known values ($g_{\parallel}$, $g_{\perp}$). If we assume p = 1, or $\alpha = \alpha'$, we can eliminate x in Eq.(53) and determine α. More conveniently a graph of $g_{\parallel}$ vs. $g_{\perp}$ is plotted as a function of α and x, as shown in Fig. 37. A number of Co^{2+} salts that have been investigated in the past show g values lying between curves A and B (Orton, 1968, Fig. 11-2). The data of Co^{2+} in $ZnSeO_4.6H_2O$, α-$NiSO_4.6H_2O$, and $NiSeO_4.6H_2O$ are

---

* The g factor of the ground state doublet is known to be very sensitive to distortions in the crystal field. But it has been found that the average g value, defined as $(g_x+g_y+g_z)/3$, is very close to 4.3. In Co^{2+} : $ZnSeO_4.6H_2O$ the average g factor is equal to 4.27.

drawn in Fig.37. We find that α must be close to -1.5 for all three systems. From Eqs.(53) and (54) we find the following parameters for Co^{2+} : $ZnSeO_4 \cdot 6H_2O$.

	α	x	g	g	Δ
p = 1	1.5	1.21	5.96	3.42	440 cm^{-1}
	1.47	1.23	5.87	3.44	410
p = 0.7	1.45	1.27	5.97	3.46	380
	1.40	1.245	5.97	3.40	380
	1.35	1.22	5.97	3.34	390

Thus, we conclude that

$$\left.\begin{array}{l} \alpha = 1.4\sim1.5, \quad p = 0.7\sim1.0, \quad x = 1.21\sim1.25 \\ \Delta = 380\sim440\ cm^{-1} \end{array}\right\} \quad (57)$$

These values are comparable to those found for Co^{2+} in Tutton salts and in zinc fluorosilicate discussed in Abragam and Pryce. The positive Δ means that the orbital doublet is higher than the singlet in accord with a tetragonal elongation of an octahedron.

So far we have neglected the effect of the excited ^4P term, which lies at about 14000 cm^{-1} above ^4F, derived from the same $3d^7$ configuration. Since the ^4P term transforms as $^4T_{1g}$ in O_h symmetry, it can admix with the ground state $^4T_{1g}$ of ^4F. The amplitude of this admixture is of the order of 0.2 and the g factor is decreased by about 4%. Inclusion of covalent bonding is known to further reduce g. Our lack of knowledge of the crystal field parameters does not warrant any further analysis of the second order effect and covalency effect on the g factor and the hf constants.

2. Second Order Hyperfine Shift

In the analysis of the experimental data we have consistently made two assumptions. The first assumption was that the g value could be calculated from the average position of the two central hf lines. The second one was that the hf splitting was taken as the spacing of these two center lines. Here we examine the validity of these two assumptions.

In Table XIX we compare the observed line positions and spacings with those calculated from Eq.(35). For H along the c axis we find that the agreement is better than 0.1% for the parameters that are consistent with the values given in Eq.(51). The agreement is much worse for the perpendicular direction; we ought to use the parameters that have considerable departure from those of Eq.(51).

A point to note is the difference between H_o and H_{center}. H_o is the theoretical line center that determined the g value ($H_o = h\nu/g\beta$), while H_{center} is the average field position of the two central hf lines. The experimental g values in this work were calculated from H_{center}, which was always smaller than H_o. The difference between these two quantities are about 3 G for $H \parallel c$ and over 30 G for the perpendicular spectrum. These shifts make the observed g values larger by 0.2% (or $\Delta g = +0.008$) for $H \parallel c$ and by 1.5% (or $\Delta g = +0.05$) for $H \parallel x$. Hence, the error involved in the observed g factor becomes appreciable near the perpendicular direction. And yet the deviation of the $g_\perp$ in Eq.(51) from the observed $g_\perp$ is much greater than the uncertainty involved in the assumption that $H_o = H_{center}$. In fact, the second

Table XIX. Hyperfine field positions of Co^{2+} in $ZnSeO_4 \cdot 6H_2O$.[a] (in units of gauss)

	H ∥ c				H ∥ γ			
	Observed		Calculated[b]		Observed		Calculated[c]	
Lines	H	ΔH	H	ΔH	H	ΔH	H	ΔH
1	1342.1		1340.9				2124.5	
		86.5		87.7				7.8
2	1428.6		1428.6				2132.3	
		85.0		85.0				10.6
3	1513.6		1513.7				2142.9	
		82.2		82.4				13.4
4	1595.8		1596.0		2158		2156.3	
		79.2		79.7		14		16.2
5	1675.0		1675.7		2172		2172.5	
		76.9		77.1		19		19.0
6	1751.9		1752.8		2191		2191.5	
		75.6		74.4		22		21.8
7	1827.5		1827.2		2213		2213.3	
		73.2		71.7		25		24.6
8	1900.4		1898.9		2238		2237.9	
H_o			1638.7				2196.8	
H_{center}	1635.4		1635.9		2165		2164.4	

a. measured at 9.8615 GHz

b. Calculated from $g_{\parallel} = 5.96$, $g_{\perp} = 3.45$, $A_{\parallel} = 77.5$ G, $A_{\perp} = 24$ G, $\phi = 58°$, and $\beta = 5°$.

c. Calculated from $g_{\parallel} = 5.99$, $g_{\perp} = 3.21$, $A_{\parallel} = 77$G, $A_{\perp} = 16$G, $\phi = 58.8°$, and $\beta = 2.5°$.

order hf correction changes the g factors in the wrong direction. We have encountered this problem in other Co^{2+} systems (see section VII-A, B). We do not know the reason for this large discrepancy.

In Eq.(35) we find that the first, third and fourth terms make the same contribution to the line position of $+m_I$ as to that of $-m_I$. The separation of the $\pm m_I$ lines is equal to $2Am_I$. Therefore,

$$A = [H(m_I) - H(-m_I)]/(2m_I) \qquad (57)$$

Since the two central lines of Co^{2+} (and of Cu^{2+}) always correspond to $m_I = \pm 1/2$ lines, $A = H(1/2) - H(-1/2)$. Thus, we can safely take the separation of the two center lines as the true hf splitting. In Table XIX we see that experimental observation substantiates the above statement fairly well.

H // c	$\pm m_I$	ΔH (G)	$\Delta H/(2m_I)$ (G)
	1/2	79.2	79.2
	3/2	238.3	79.4
	5/2	398.9	79.8
	7/2	558.3	79.8

In conclusion, we say that the first assumption of $H_o = H_{center}$ may contain a considerable error near the perpendicular direction, but that the second assumption seems valid for all directions.

VII. PARAMAGNETIC IONS IN NICKEL SULFATE AND NICKEL SELENATE

In the course of his EPR study of α-$NiSO_4 \cdot 6H_2O$, Batchelder found traces of Co^{2+}, Cu^{2+} and Mn^{2+} impurities. The preliminary accounts of these impurity ions have already been given in his Ph.D. thesis (Batchelder, 1970). We intentionally increased the concentrations of the impurity ions and studied their EPR spectra at 4.2° and 1.3°K. We also imvestigated the EPR spectra of Co^{2+} and Cu^{2+} in $NiSeO_4 \cdot 6H_2O$. We extended the theory of the nearest neighbor exchange interactions of Batchelder to include both the possibility of more than two neighboring Ni^{2+} ions being in the excited states ($M = \pm 1$) and the next-nearest neighbor interactions. These modifications enlarged the 3x3 Hamiltonian matrix up to a 9x9 hermitian matrix. We used extensively the Fortran IV diagonalization program given in Appendix V, but we have not as yet come to a successful calculation of the exchange effects of Ni^{2+} on the neighboring paramagnetic ions.

In this section we will give only the experimental results and simple discussions on them. We also wish to describe a second kind of transition detected in α-$NiSO_4 \cdot 6H_2O$.

A. Co^{2+} in $NiSeO_4 \cdot 6H_2O$

We studied the EPR spectra of the Co^{2+} impurity in $NiSeO_4 \cdot 6H_2O$ at the liquid helium temperature. We found the general behavior of the Co^{2+} resonance spectra very similar to that of Co^{2+} in $ZnSeO_4 \cdot 6H_2O$, except for a few minor points.

First of all the signals were weak at 4.2°K but very strong at 1.3°K. This strong temperature dependence of the intensity is contrasted to virtually no temperature effect on Co^{2+}: $ZnSeO_4.6H_2O$. The spin-lattice relaxation time of Co^{2+} is shortened by the interaction with the Ni^{2+} neighbors. Secondly, the line widths of individual hf lines were approximately 17 G at 1.3°K, which was about twice as broad as those lines of Co^{2+} in $ZnSeO_4.6H_2O$. Lastly, the magnetic x axes of Co^{2+} in $NiSeO_4.6H_2O$ are not tilted from the γ axes, but exactly parallel to them. Therefore, we detected at most three sets of eight hf lines in all the three planes (ab, ac and γc) of the single crystal.

The four Co^{2+} ions became equivalent along the c and a axes. It seems that Co^{2+} can perfectly fit in the Ni^{2+} site as compared with a small lattice distortion of Co^{2+} doped in the Zn^{2+} site of $ZnSeO_4.6H_2O$.

In Table XX we list the principal g and A values of Co^{2+} in $NiSeO_4.6H_2O$. These values are the average of several different runs at 1.7°K. We see small shape effects on the g values but not on A. Over the temperature change from 4.2° to 1.3°K we detected a small but definite increase in g values. When H was along the γ axis, the g value of the low field set changed from 5.836 to 5.849, which was equivalent to 3 G shift in the center position of the hf lines. For H along the c axis the shift was only 1 G. We can attribute these shifts to a change in the local field induced by the magnetization of the neighboring Ni^{2+} ions, if we use a positive value for the molecular field constant. We do not have all the necessary magnetization data to calculate the change in the induced local field as a function of temperature. If we assume that the molecular field parameter available

Table XX. Principal g and A of Co^{2+}: $NiSeO_4 \cdot 6H_2O$.

Axes	Planes	Shape of crystal	g	A (gauss)
a	ab	Plate	4.776	79.2
a	ac	Plate	4.782	79.3
c	ac	Plate	4.313	78.5
c	γc	Prism	4.303	78.1
γ_1	ab	Plate	5.861	74.7
γ_1	γc	Prism	5.837	74.1
z	γc	Prism	6.317	72.8
z		Powder	6.350	72.9
x	ab	Plate	3.381	~25
x	γc	Prism	3.36	~25
x		Powder	3.34	

for the Ni^{2+}-Ni^{2+} interaction in the isomorphous α-$NiSO_4 \cdot 6H_2O$ can be used in this calculation, we would predict a 50 G change in the internal field from 4.2° to 1.75°K, and a 6 G change from 1.75° to 1.25°K for H along the γ axis. For H along the c axis the change will be only 3 G from 1.75° to 1.25°K. These calculated shifts are too large to account for the experimental variations. Thus, it seems that the Co^{2+}-Ni^{2+} interaction is fairly small.

When we plotted g^2 vs. n^2 for the three crystal planes, we found an interesting trend. In Fig. 38 we differentiated the points from the ab plane by triangles, those from the ac plane by crosses and those from the γc plane by circles. The slope of the resulting straight line was greatest for the ab plane data and least for the ac plane. This difference was also observed in Co^{2+} : α-$NiSO_4 \cdot 6H_2O$, the shape of which was spherical so that there should have been no shape effect on the g factor. We took the angle for ϕ to be 62°, which was the average of the ϕ from the γc plane (62.5°) and from the ac plane (61.5°). The extrapolation of the straight line in Fig. 38 yielded g = 6.25 and g = 3.54. These were appreciably different from the observed values. A similar plot of g^4A^2 vs. n^2 was drawn in Fig. 39. The choice of ϕ = 60.5° gave the least standard deviations for the γc and the ab plane data. The extrapolated hf constants were A = 73.8 G and A = 32.1 G if g = 6.25 and g = 3.54.

In Fig. 40 we plotted the experimental g values of the γc plane along with the calculated curves that were computed from g = 6.318, g = 3.38 and ϕ = 61.5°. Fig. 41 shows a similar plot for the ac plane

with a different set of parameters: $g_{\parallel} = 6.10$, $g_{\perp} = 3.68$ and $\phi = 62°$. We summarize the results of Co^{2+} in $NiSeO_4.6H_2O$ by the following spin Hamiltonian parameters;

$$\begin{aligned} g_{\parallel} &= 6.30\pm0.05, & g_{\perp} &= 3.45\pm0.1 \\ A_{\parallel} &= 72.8\pm0.5\ G, & A_{\perp} &= 25\pm4\ G \\ \phi &= 62\pm0.5°, & \beta &= 0° \end{aligned} \qquad (59)$$

The large uncertainties in Eq.(59) are due to the independent behavior of each of the three planes. For a given plane the uncertainty is much smaller.

The second order hf terms were equally large in Co^{2+}: $NiSeO_4.6H_2O$ as in $ZnSeO_4.6H_2O$. In the analysis of the g factors (see VI-C-1), we found

$$\alpha = 1.5, \quad p = 0.5, \quad x = 1.215, \quad \text{and} \quad \Delta = 430\ cm^{-1} \qquad (60)$$

The difference between the Co^{2+} in the paramagnetic $NiSeO_4.6H_2O$ and in the diamagnetic $ZnSeO_4.6H_2O$ is not large but definite beyond our experimental uncertainties.

B. Co^{2+} in α-$NiSO_4 \cdot 6H_2O$

This system had already been studied by Batchelder who had used a spherical sample. We investigated only rectangular plates and prisms. No Co^{2+} signal could be detected above 2.5°K. The signals were quite intense at 1.3°K. The individual hf line widths were about 17 G. There were at most three sets of eight hfs lines in all the three planes. The general feature was almost identical with the spectra of Co^{2+} in $NiSeO_4 \cdot 6H_2O$.

In Table XXI we list the principal g and A values of Co^{2+} in α-$NiSO_4 \cdot 6H_2O$. We see again the small but definite shape effects on the g values. The temperature effect on g was much smaller than the change in the bulk magnetization of α-$NiSO_4 \cdot 6H_2O$. For example, when the temperature was lowered from 2.2° to 1.3°K, the g value for H along the a axis changed less than 0.003, which was of the order of our experimental accuracy. It was then concluded that the magnetization of the paramagnetic crystal was not the main source of the shape effect on the g factor.

For the analysis described below we borrowed the data of Batchelder on the spherical sample of Co^{2+} : α-$NiSO_4 \cdot 6H_2O$. While we were plotting a graph of g^2 vs. n^2 in the ac plane, we accidentally switched the a and c axes. We found that ϕ must be 49.5° in order that the experimental points, with wrong angles, lie on a straight line. Using this ϕ and the extrapolated values of $g_{\parallel} = 6.06$ and $g_{\perp} = 3.41$, we found the calculated g factors agree very well with the experimental points, as shown in Fig. 42. This false agreement is a good example

Table XXI. Principal g and A of Co^{2+}:α-$NiSO_4 \cdot 6H_2O$. 1.3 ~ 1.7 °K.

Axes	Planes	Shape of crystal	g	A (gauss)
a	ab	Plate	4.744	88.5
a		Sphere*	4.688	90.9
γ_1	ab	Plate	5.953	78.2
γ_1	γc	Plate	5.933	78.7
c	γc	Plate	4.282	87.2
c		Sphere*	4.301	
c	ac	Plate*	4.246	
z	γc	Plate	6.457	76.4
z		Powder	6.444	76.2
x	ab	Plate	~3.051	
x		Powder	~3.3	~25

*Batchelder (1970).

of why the g factor with an axial symmetry cannot be unambiguously determined from the data of one plane alone. Correcting the angles of the ac plane, we replotted g^2 vs. n^2 in Fig. 43 for the ab plane (triangles) and for the ac plane (crosses) together. We observe the points taken from different planes fall on two different straight lines. The slope for the ab plane is again steeper than that for the ac plane. The value of 60.5° used in this plot agrees well with the experimental ϕ of 59.8° and 60.7° in the γc plane of a rectangular plate. Extrapolation yielded $g_{\parallel} = 6.45$ and $g_{\perp} = 3.27$. In Fig. 44 the experimental g vales of the ac plane were compared with the calculated values with $g_{\parallel} = 6.34$, $g_{\perp} = 3.40$ and $\phi = 60°$. Although the agreement in Fig.44 appears to be fairly good, the uncertainties in $g_{\parallel}$ and $g_{\perp}$ are large. In all the three Co^{2+} systems described in this work we found that each plane required a different set of spin Hamiltonian parameters with $g_{\parallel}$ largest in the ab plane and smallest in the ac plane. We list below the averaged parameters over the three planes of Co^{2+} : α-$NiSO_4.6H_2O$.

$$\left.\begin{array}{ll} g_{\parallel} = 6.44\pm0.10, & g_{\perp} = 3.25\pm0.15 \\ A_{\parallel} = 76.3\ G, & A_{\perp} = 25\ G \\ \phi = 60.2\pm0.5° & \end{array}\right\} \qquad (61)$$

The theory of Abragam and Pryce give

$$\alpha = 1.5, \quad p = 0.5, \quad x = 1.20, \quad \Delta = 440\ cm^{-1} \qquad (62)$$

These are very similar to the case of Co^{2+} in $NiSeO_4.6H_2O$.

C. Cu^{2+} in α-$NiSO_4 \cdot 6H_2O$

We employed both the X-band and K-band spectrometers to study the EPR spectra of Cu^{2+} in α-$NiSO_4 \cdot 6H_2O$. Single crystals of rectangular plate and prism were examined at the liquid helium temperature. We saw no Cu^{2+} signals above the lambda-point of helium (2.17°K). As the temperature was lowered, the signals gradually became stronger and sharper. The typical line width of individual hf lines were about 20 G at 1.25°K. At 1.17°K the effect of the two copper isotopes were clearly visible in the end hf lines in the derivative presentation. At 1.3°K this isotope effect was already obscured by the line broadening. The interactions with the neighboring Ni^{2+} ions drastically reduced the spin-lattice relaxation time of Cu^{2+} ion.

The four ions were all equivalent at the a and the c axes. The tilting angle β was zero. We found it necessary to switch off the electromagnet before we varied the magnetic field direction. Otherwise the crystals taped on the teflon mount rotated every time the magnet was rotated. This was due to the strong tendency of α-$NiSO_4 \cdot 6H_2O$ crystal to orient itself in such a way that the γ axis, the axis of the maximum magnetic susceptibility, be parallel to the external magnetic field.

While the experimental uncertainty in the g value measurement of the Co^{2+} lines was better than 0.1% (about 1 G) at the X-band, the uncertainty for Cu^{2+} is even less than that for Co^{2+} by a factor of 2.5 and 5 at the X-band and K-band, respectively. In Table XXII we list the observed g and A of Cu^{2+} : α-$NiSO_4 \cdot 6H_2O$ for H along the principal

Table XXII. Principal g and A of Cu^{2+} : α-$NiSO_4 \cdot 6H_2O$.

Axes	Plane	Frequency	g	A (gauss)
a	ab	X-band	2.679	59.1
	ab	K	2.669	59.4
	ac	X	2.681	60.6
c	ac	X	2.491	90.6
	γc	X	2.501	91.5
γ_1	ab	X	2.850	75.5
	ab	K	2.837	73.7
z	γc	X	2.905	93.9
	Powder	X	2.890	93.6
x	ab	X	2.489	
	ab	K	2.482	~10
	Powder	X	2.481	

magnetic and crystallographic axes. There we note three distinct features that were not present in Cu^{2+} in $ZnSeO_4.6H_2O$. First, we see that different crystal orientations in the cavity produce small changes in the observed g values, as was already seen in the Co^{2+} spectra in the previous sections. We do not know the reason for this. It could not be due to the shape effect, because a similar variation was observed in the sphere of Co^{2+}: α-$NiSO_4.6H_2O$. A possibility of misorientation is also ruled out, since the values listed are the average of several independent experiments.

The second feature is a small frequency dependence of the g factor. We notice the g values at K-band are smaller than at X-band for all the three axes studied. In other words, the greater the Zeeman interaction of Cu^{2+} is, the smaller the g value deviation from the free electron g factor. This is related to the third feature, which is most characteristic of Cu^{2+} in α-$NiSO_4.6H_2O$; the unusually high g values of Cu^{2+} in all orientations. We also detected the abnormally large g in the mixed crystals of $(Cu^{2+}, Ni^{2+}, Zn^{2+})SeO_4.6H_2O$ and <u>not</u> in $(Cu^{2+}, Zn^{2+})SeO_4.6H_2O$. We believe this anomaly is due to the effects of the surrounding Ni^{2+} ions.

First thing that comes to our mind is the effect of the magnetic field induced by the magnetization of the nearby Ni^{2+} ions. Fisher and Hornung (1968) and Fisher et.al.(1968b) were successful in explaining the magneto-thermodynamic properties of α-$NiSO_4.6H_2O$ by an introduction of the molecular field. If we write the effective magnetic field (H_{eff}) seen by the Cu^{2+} ion as the sum of the external field (H) plus

the induced field, ofter called a molecular field, then

$$H_{eff} = H + H_{mol} \tag{63}$$

where H_{mol} is the molecular field arising from the magnetic dipole-dipole interaction plus the elctrostatic exchange interaction of the neighboring Ni^{2+} ions. A simple formula for the molecular field is given by Fisher and Hornung (1968),

$$H_{mol} = \gamma M \tag{64}$$

where the constant γ is the molecular field factor and M is the magnetization in the applied field H. Fisher et.al. (1968b) give the values of γ that are 0.272 for the c axis and 0.266 for the ab plane. Using the magnetization data of Fisher et.al (1967, 1968a,b), we made the molecular field corrections for the observed g factors. The results are shown in Table XXIII. The correction appreciably reduced the g values. And yet the corrected g values are still higher than the "normal" g factor of Cu^{2+} by 0.1.

Before we question the validity of the molecular field correction, we wish to describe the temperature dependence of the Cu^{2+} line positions and line widths. The results we obtained at X-band and the K-band were very close and here we describe only the K-band result. We measured the peak-to-peak line width and the line center of the second hf line ($m_I = -1/2$) as a function of temperature. At the klystron frequency of about 21.13 GHz, which was stable better than 10^{-2}% (equivalent to about 0.5 G shift) over the temperature change of one degree, the field positions of the $m_I = -1/2$ line were 5639.4 G

Table XXIII. Molecular field correction to g values of Cu^{2+}: α-$NiSO_4 \cdot 6H_2O$.

Axes	T (°K)	Apparent g	Local H (gauss)	Corrected g
a	1.25	2.681	327	2.372
γ_1	1.25	2.850	339	2.520
x	1.25	2.489	354	2.200
c	1.34	2.491	178	2.337
z[a]	1.34	2.887	196[b]	2.561

a. Powdered sample.
b. Used the magnetization data of the γ axis. The error involved may not be greater than 10%, since the angle ϕ is 60° or more.

for the a axis and 5280.6 G for the γ axis at 1.18°K. For H along the γ axis the line width changed by 5.2 G and the line center shifted to the higher field by 3.8 G between 1.17° and 1.87°K. For H along the a axis the temperature was varied from 1.18° to 2.12°K, over which the line width broadened by 12 G and the line center shifted to the higher field by 9.5 G.

According to Fisher et.al (1968a,b) the magnetization at H = 5 kG decreases by 196 $G.cm^3.mole^{-1}$ for H// a, when the temperature is changed from 1.177° to 2.104°K. The resulting molecular field change is a decrease of 53.4 G. In order to see the Cu^{2+} resonance the external magnetic field must be increased by the same amount so that the effective field seen by Cu^{2+} remains constant. In actuality the observed line shift was a factor of 4 smaller than the calculated shift.

For H along the γ axis we must differentiate the magnetizations of the two nonequivalent Ni^{2+} ions. If we denote by type 1 the Ni^{2+} ion for which the applied field is parallel to its x axis, then the Cu^{2+} ion at the type 2 site sees the molecular field originating from the nearest neighbors of type 1 ions. The magnetization of Ni^{2+} of type 1 is 120% greater than the observed value, which was the averate of type 1 and type 2, at H = 5 kG (Fisher and Hornung, Table IV). When the temperature is raised from 1.252° to 1.806°K, the magnetization that Cu^{2+} would see changes by 117 $G.cm^3.mole^{-1}$. Then the molecular field decreases by 31.7 G. This expected change is again an order of magnitude too large. Therefore, the molecular field correction in the form of Eq.(64) is too simple to account for the anomalous g factor of Cu^{2+} in α-$NiSO_4.6H_2O$.

We have attempted to calculate the dipolar field induced by the neighboring Ni^{2+} ions at the site of Cu^{2+} ion. This field was only one-tenth to one-thirtieth of the local field necessary to account for the abnormally large g values of Cu^{2+} in α-$NiSO_4 \cdot 6H_2O$. The internal field then arises mainly from the exchange interaction of the neighboring ions. Batchelder gives a simple formula for the nearest neighbor exchange interaction of paramagnetic impurity ions with the Ni^{2+} ions. He assumes that the magnetic z axes of both ions are aligned parallel. To the second order perturbation theory, he derives a g value shift that is proportional to -J/D. He estimates J to be about -0.3 cm^{-1}, which is greater than 0.12 cm^{-1} of the Ni^{2+}-Ni^{2+} exchange interaction observed in the far-infrared spectra of α-$NiSO_4 \cdot 6H_2O$.

We made a similar calculation of the nearest neighbor exchange interaction of Cu^{2+} and Ni^{2+} with an isotropic exchange constant J. Our method did not employ the perturbation theory but used the hermitian diagonalization scheme. We found that J of about -1 cm^{-1} must be used in order to decrease the g factors to the "normal" values of $g_{\parallel} \sim 2.45$ and $g_{\perp} \sim 2.10$. We found that in addition to the isotropic exchange interaction a fairly large anisotropic exchange interaction need to be included. We have not yet solved this problem.

We list the observed line positions, apparent g and A values of the ab plane in Table A-6 of Appendix IV. The plot of g^2 vs. n^2 results in $g_{\parallel} = 2.954$ and $g_{\perp} = 2.496$ for $\phi = 61.8°$. These values are much greater than the observed g factors. In order to fit the apparent g values well we must use $\phi = 70°$, as shown in Fig. 45. However, we

feel the experimentally determined ϕ is quite accurate, for both the ac and the γc planes indicated $\phi = 61.8°$. Without the correct interpretation of the anomalous g factor, we do not expect to be able to account for the angular dependence of the g values of Cu^{2+} in α-$NiSO_4 \cdot 6H_2O$.

D. Cu^{2+} in $NiSeO_4 \cdot 6H_2O$ and Mixed Crystals

The study of this system is less complete than Cu^{2+} in α-$NiSO_4 \cdot 6H_2O$. In the pure $NiSeO_4 \cdot 6H_2O$ the Cu^{2+} lines were weak even at 1.3°K. Along the c axis there was only one set of four lines at g = 2.555 and A = 83.3 G. Comparing with Cu^{2+} in α-$NiSO_4 \cdot 6H_2O$, we find a larger g and a smaller A for H along the c aixs of Cu^{2+} : $NiSeO_4 \cdot 6H_2O$. Although we did not examine the spectra in other planes, we would have expected abnormally large g values of Cu^{2+} in $NiSeO_4 \cdot 6H_2O$.

We prepared a series of mixed solutions of nickel and zinc selenate whose proportion ranged from 10 to 30 mole % for Ni^{2+}. In order to minimize the Co^{2+} impurity we used the nickel selenate that had been synthesized from nickelous carbonate. To these mixed solutions we introduced a small amount of the saturated cupric selenate solution. Slow evaporation at room temperature precipitated large single crystals of pale green color with the prismatic form of Fig. 3a.

When a sample containing 10% Ni^{2+} was mounted in the γc plane, we observed at most three sets of four hf lines at 77°K. There was no splitting of ions 2 and 4 seen at all angles. The line width of Cu^{2+} in this crystal were somewhat broader (13 to 15 G wide) and a little more extensively overlapped than the Cu^{2+} lines in $ZnSeO_4 \cdot 6H_2O$. The g and A values of the former were exactly identical to those of the latter at 77°K. The g factors were 2.2788, 2.2595, 2.097, and 2.4294 for H along the c, γ, x, and z axes, respectively. The corresponding A were 97.8, 90.7, 18, and 115.7 G. Thus we conclude that 10% Ni^{2+} in $ZnSeO_4 \cdot 6H_2O$ has no effect on the g and A of Cu^{2+} at 77°K.

When the same sample was cooled to liquid helium temperature, the signals became very complex. There were some twenty lines of uneven intensities owing to extensive overlapping. Near the c axis strong but poorly superimposed four lines were observed at $g \sim 2.30$. Weaker lines were also seen at g very roughly equal to 2.5. We saw near the γ axis two weak sets of four lines at about $g \sim 2.63$, one strong single band at $g \sim 2.13$ and two intermediate sets of four lines in between. The complicated structure of overlapping lines prevented us from a systematic study of the anisotropic g values.

The transition from the high to the low temperature spectra was reversible. At low temperature we saw the spectra of Cu^{2+} surrounded by one or more Ni^{2+} ions in addition to the spectra of Cu^{2+} surrounded by Zn^{2+} ions alone. The interaction between Cu^{2+} and Ni^{2+} shifts the Cu^{2+} spectra toward lower field and shortens the spin-lattice relaxation time of the Cu^{2+} ion. At high temperature the spectra arising from the Cu^{2+}-Ni^{2+} interaction were broadened beyond our detection. We saw only the spectra of Cu^{2+} surrounded by the Zn^{2+} ions alone.

A second sample contained 25% of Ni^{2+} ions. We could observe no Cu^{2+} spectra at 77°K with the 825 Hz field modulation. At 1.7°K the spectra in the γc plane were consisted of 16 to 20 intense lines with excessive overlap. Even near the c axis the spectra were too complex to permit a definite assignment. Next we ground this crystal to a fine powder and observed its EPR at -160°C with 100 kHz modulation. Only a single band of about 100 G line width was detected at g 2.10. No parallel lines were observed at this temperature. We need further investigate the powdered spectra at liquid helium temperature.

E. α-$NiSO_4 \cdot 6H_2O$

1. "High-Field" Transition

This transition between the excited states was observed by Batchelder in both single crystal and powdered samples. In the present work we have used only rectangular plates or prisms.

The EPR spectrum was a superposition of at least two lines of uneven intensities. At the γ axis the line was strongest and sharpest. As H was oriented away from the γ axis, the intensities fell rapidly so that the transitions could be observed only in the narrow range of orientations. The line became broader and doublet structures began to appear. Batchelder reported temperature effects on the line widths, line positions and intensities; as the temperature was lowered, the line widths narrowed, the line positions shifted to lower fields, the doublet splitting reduced and the intensities diminished.

We plotted the observed line positions of the "high-field" transitions as open circles in Fig.46 and 47, taking the average positions, whenever the doublets appeared. In the γc plane lines 2 and 4 reached the maximum field of 10280 G at 8.6887 GHz, when H was aligned along the γ axis. Lines 1 and 3 appeared always as singlets and their intensities were much weaker. At $\pm 39.8°$ away from the γ axis lines 1 and 3 reached the maximum field of 10284 G. These orientations corresponded to the y axes of ions 1 and 3. We then know $\Phi = 39.8°$, in close agreement with Fisher et.al. (39.0°) and with Stout and Hadley (40.2°). The fact that the line positions of H along x and y axes were nearly the same indicated that E must be negligibly small

in contrast to Batchelder's $E = 0.032\ cm^{-1}$. If we force to fit the "high-field" transitions observed in the ab plane to the isolated Ni^{2+} system, we obtain a new set of parameters:

$$\left.\begin{array}{lll} g_{\parallel} = 2.22, & g_{\perp} = 2.25, & D = +3.75\ cm^{-1} \\ E = 0, & \Phi = 39.8^{\circ} & \end{array}\right\} \quad (65)$$

In Table XXIV we list the calculated positions from the above set of parameters. The agreement is good to about 100 G for 1.7°K but poorer for 4.2°K and for the data taken in the γc plane. We also list in the same table the line positions and the doublet splittings to illustrate their orientational and temperature dependence. Not listed in the table are the line widths of the high-field lines. At the half-maximum the half-widths of the absorption spectra of H along the γ axis were 3400, 2100 and 820 G at 77°, 4.2° and 1.7°K, respectively. The spectrum at 77°K was strong and exceedingly complex. There appeared at least three lines overlapping with one another, altogether shifted to higher fields.

The new D and E in Eq, (65) greatly disagree with the results of Fisher and Hornung and of Batchelder. In one of our experiments, the results of which are shown in Fig. 46, line positions of H along the x and y axes differred about 300 G, which was equivalent to an E of 0.004 cm^{-1}, but we never detected such a great difference between the x and y axes as the E of 0.032 cm^{-1} would require. If we were to continue to apply the isolated Ni^{2+} model to the EPR spectra of α-$NiSO_4.6H_2O$, we would have to use small D and E. We have detected similar anisotropic

transitions in $NiSeO_4.6H_2O$, whose line positions were higher than those of α-$NiSO_4.6H_2O$ at the same resonance frequency, indicating a smaller E or a larger D. We recall that the Ni^{2+} ions in the diamagnetic $ZnSeO_4.6H_2O$ lattice gave D = 4.20 cm^{-1} and E = 0. Thus, it is reasonable to assume smaller values of D and E for α-$NiSO_4.6H_2O$ than the reported values of 4.74 and 0.032 cm^{-1}. Although Fisher and Hornung found a good overall agreement in their magneto-thermodynamic experiments on α-$NiSO_4.6H_2O$, their value of E = 0.01±0.06 cm^{-1} contained a large uncertainty. We have seen in the above discussion that a small change in E can cause a large change in D when H is along x or y axes. Our EPR results do not allow such a large uncertainty in E.

We attempted to account for the doublet structures by introducing the second angle β as we had done in Ni^{2+}: $ZnSeO_4.6H_2O$. We found β to be 3 to 5°. D was found to depend strongly on the size of β; an increase of 2° in β increased D by 0.2 cm^{-1}. However, we had to abandon any further analysis of α-$NiSO_4.6H_2O$ as an isolated system, because the temperature dependence of the line positions and the doublet splittings could not be explained by the isolated Ni^{2+} model. We cannot argue with the far-infrared result of Batchelder, who observed D greater than 4.4 cm^{-1} with H = 0 at 4.2° and 1.3°K. Suffice it to say that the parameters in Eq.(65) are the most consistent, not necessarily the closest to the truth, values with the <u>isolated</u> Ni^{2+} system in the paramagnetic α-$NiSO_4.6H_2O$. We have not yet succeeded in solving the problem of the anisotropic exchange interaction between the nearest neighbor Ni^{2+} ions.

2. Coupled-pair Transitions

In this section we will discuss a new type of transitions observed in the undiluted single crystals of α-$NiSO_4 \cdot 6H_2O$ by our X-band spectrometer. The transitions were roughly two order of magnitude weaker than the "high-field" lines. They were detected at 4.2°K and the signals gained intensities at 1.7°K. Their angular dependence is illustrated in Figs.46 and 47, where the observed positions are indicated by crosses. We would like to call this new transition the "coupled-pair" transition for the reason that becomes obvious below.

We will consider two nearest neighboring Ni^{2+} ions. If there is an interaction between them, a transition occuring at one ion may cause a second transition to take place in the opposite direction analogous to the spin flip-flop mechanism. When these two ions are non-equivalent in the magnetic field, the net energy of the two simultaneous transitions will be different from zero. By sweeping the magnetic field at a constant frequency we can vary the Zeeman energy levels of the two spin triplets until when the energy difference of the two possible transitions become equal to the resonance energy. Then a simultaneous transition can take place.

Diagramatically this is shown in Fig. 48. On the left side are the energy levels of ion 1 plotted as a function of the magnetic field. On the right is a similar plot for ion 2. We use the notations of M = ±1 and 0 for the spin triplet states for the sake of simplicity. When ions 1 and 2 make the simultaneous transition, as indicated by arrows, the net energy change will be equal to

$$h\nu = W(-1') - W(0') - W(1) + W(0) \qquad (66)$$

where the shaded arrow correspond to the resonance energy $h\nu$. By calculating the energy difference of the two isolated ions* 1 and 2, we obtain the field positions of the coupled-pair transitions of Eq.(66) for the γc plane, as shown in Fig. 49. The points represent the experimental positions which are also tabulated in Table A-7 of Appendix IV. The solid curves correspond to the positions calculated from the parameters of Eq.(65). The computed positions are always higher than the observed values by 100 to 1500 G.

A few interesting features are to be noted. Near the c axis the coupled-pair transition occurs at an infinite field. This is because the two ions 1 and 2 become equivalent at the c axis. In order to satisfy Eq.(66) the magnetic field must be very large as H approaches the c axis. The 1-2 pair and the 2-3 pair cross at the γ axis, beyond which the positions of both pairs sharply rise. In our experiments we never detected any of the sharp rising lines in the region of the broken curves in Fig. 49. We could have chosen other combinations of the energy levels in Eq. (66) such as W(1)-W(0) of ion 1 and W(1')-W(0') of ion 2. This combination would have placed the calculated positions some 2 to 3 kG higher than our previous choice. What we observed was not such higher transitions but lower field lines some 2 kG below the ones shown in Fig. 49. This second transition is also tabulated in

* Although the nature of the exchange constant J must be specified and included in this calculation, we will continue to use the isolated Ni^{2+} system on account of the difficulty of the anisotropic exchange calculation.

Table A-7. Considering the crudeness of the model, we deem the qualitative agreement to be satisfactory.

In the ab plane the agreement is less satisfactory. While the observed coupled-pair transitions crossed at the γ axis (see Fig. 47), our computed positions of Eq.(66) reached the minimum field at the γ axis. This is shown in Fig. 50, in which the circles are experimental and the solid curve is theoretical. In order to fit the lower field positions we had to choose another energy combination of the form

$$h\nu = W(1') - W(0') - W(-1) + W(0) \qquad (67)$$

which is shown as the broken curve in Fig. 50. We may understand the qualitative picture of the coupled-pair transition in the ab plane by considering the actual curve to be a superposition of the solid and broken curves.

As often mentioned earlier, the exact agreement may have to wait for a complete analysis of the anisotropic exchange interaction of the nearest neighboring 1-2 pairs.

APPENDIX I

DETERMINATION OF Φ

For S = 1/2 the observed g factor is a simple function of the magnetic field:

$$g = h\nu/\beta H$$

where $g = [(g_{\parallel}^2 - g_{\perp}^2)n^2 + g_{\perp}^2]^{1/2}$

if the g tensor is axially symmetric.

Differentiating g with respect to α and setting it to zero, we obtain an angle at which the g factor becomes maximum or minimum. The angle α is measured from the c axis for H in the ac or in the γc plane. For the ac plane, if $g_{\parallel} > g_{\perp}$, then Φ is related to α_{max} simply by

$$\tan\Phi = (2)^{1/2}\mathrm{ctn}(\alpha_{max}) \qquad (1\text{-}1)$$

If $g_{\parallel} < g_{\perp}$,

$$\tan\Phi = (2)^{1/2}\mathrm{ctn}(90° - \alpha_{max})$$
$$= (2)^{1/2}\tan(\alpha_{max}) \qquad (1\text{-}2)$$

Although Ni^{2+} has a spin of 1, the above argument still holds, if we define an effective g value as

$$g_{eff} = h\nu/\beta H.$$

For example, in the ac plane of Ni^{2+}:$ZnSeO_4 \cdot 6H_2O$, one pair of the doublet reached the maximum field at $\alpha_{max} = 63°$. Substituting α_{max} into (1-2), for $g_{\parallel} < g_{\perp}$, we find $\Phi = 35.7°$

For the γc plane the method is more direct: locate the angle at which one set of lines reaches the lowest magnetic field (or highest

g value). Then, the difference between this angle and the c axis is equal to ϕ, provided that the z axis lies in the γc plane and that $g_{\parallel} > g_{\perp}$.

A comparison of g_c and g_γ will tell whether ϕ is greater or less than 45°. Because the z axis is assumed to lie in the γc plane, $g_c > g_\gamma$ requires $\phi < 45°$, provided again $g_{\parallel} > g_{\perp}$. The difference between g_c and g_γ indicates how much ϕ deviates from 45°, as shown in Table A-1.

The final check is made on ϕ by the analytical methods of Eqs. (19)-(21) and (33), (34), and by the best fit of the experimental spectra. All of these methods give a consistent value of ϕ for systems studied in this work.

Table A-1. Values of ϕ

Ion	Lattice	g_c	g_γ	$\phi \gtrless 45°$	obs'd ϕ
Cu^{2+}:	$ZnSeO_4 \cdot 6H_2O$	2.279	2.259	$<$	43.3°
Cu^{2+}:	$NiSO_4 \cdot 6H_2O$	2.491	2.850	$>$	61.8
Cu^{2+}:	$NiSeO_4 \cdot 6H_2O$	2.555	(incomplete)		
Co^{2+}:	$ZnSeO_4 \cdot 6H_2O$	4.259	5.423	$>$	58.5
Co^{2+}:	$NiSeO_4 \cdot 6H_2O$	4.31	5.86	$>$	60.7
Co^{2+}:	$NiSO_4 \cdot 6H_2O$	4.282	5.953	$>$	60.3
Ni^{2+}:	$ZnSeO_4 \cdot 6H_2O$	3.63	2.61	$<$	35.5

APPENDIX II

DIRECTION COSINES IN $ZnSeO_4 \cdot 6H_2O$

We define ϕ to be the angle between the magnetic z axis and the crystallographic c axis, β to be the angle between the x and γ axes, and α to be the direction of the magnetic field measured from the c axis in the ac and γc planes and from the γ axis in the ab plane. We also abbreviate the following cosine and sine functions as

$$K1 = \sin\phi, \quad K2 = \cos\phi, \quad K3 = \sin\alpha$$

$$K4 = \cos\alpha, \quad K5 = \sin\beta, \quad K6 = \cos\beta$$

$$K7 = \cos(45° + \beta), \quad K8 = \cos(45° - \beta)$$

and $RT = (2)^{-1/2}$.

Table A-2. Direction cosines (ℓ,m,n) for the x axis tilted in the γc plane.

Ions	ℓ	m	n
		a. H in ab plane	
1	K3*K6	-K1*K3*K5-K2*K4	-K2*K3*K5+K1*K4
2	-K3*K6	K1*K4*K5-K2*K3	K2*K4*K5+K1*K3
		$H_{3i} = -H_{1i}$, $H_{4i} = -H_{2i}$, ($i = \ell$,m,n)	
		b. H in γc plane	
1	K5	-sin(α-ϕ)*K6	cos(α-ϕ)*K6
2	-sin(α+β)	cos(α+β)*K1	cos(α+β)*K2
3	K5	-sin(α+ϕ)*K6	cos(α+ϕ)*K6
4	sin(α-β)	cos(α-β)*K1	cos(α-β)*K2
		c. H in ac plane	
1	K4*K5 +K3*K6*RT	K1*K4*K6+K2*K3*RT -K1*K3*K5*RT	K2*K4*K6-K1*K3*RT -K2*K3*K5*RT
2	K4*K5 -K3*K6*RT	K1*K4*K6-K2*K3*RT +K1*K3*K5*RT	K2*K4*K6+K1*K3*RT +K2*K3*K5*RT

From 1→3 and 2→4, replace α by $-\alpha$.

Table A-3. Direction cosines (ℓ,m,n) for the x axis tilted in the ab plane.

Ions	ℓ	m	n
		a. H in ab plane	
1	$\sin(\alpha+\beta)$	$-\cos(\alpha+\beta)$*K2	$\cos(\alpha+\beta)$*K1
2	$-\cos(\alpha+\beta)$	$-\sin(\alpha+\beta)$*K2	$\sin(\alpha+\beta)$*K1
3	$-\sin(\alpha-\beta)$	$\cos(\alpha-\beta)$*K2	$-\cos(\alpha-\beta)$*K1
4	$\cos(\alpha-\beta)$	$\sin(\alpha-\beta)$*K2	$-\sin(\alpha-\beta)$*K1
		b. H in γc plane	
1	K3*K5	K1*K4-K2*K3*K6	K2*K4+K1*K3*K6
2	-K3*K6	K1*K4-K2*K3*K5	K2*K4+K1*K3*K5
3	K3*K5	K1*K4+K2*K3*K6	K2*K4-K1*K3*K6
4	K3*K6	K1*K4-K2*K3*K5	K2*K4+K1*K3*K5
		c. H in ac plane	
1	K3*K7	K1*K4-K2*K3*K8	K2*K4+K1*K3*K8
2	-K3*K8	K1*K4-K2*K3*K7	K2*K4+K1*K3*K7
3	-K3*K8	K1*K4+K2*K3*K7	K2*K4-K1*K3*K7
4	K3*K7	K1*K4+K2*K3*K8	K2*K4-K1*K3*K8

APPENDIX III

JAHN-TELLER INTERACTION

Historically, it was the celebrated phenomenon of Jahn-Teller (J.T) distortions that prompted me to become engaged in the single crystal studies of transition metal ions by EPR. About the time of completion of my work on Cu^{2+}: LMN, almost identical results to mine, granted a more detailed analysis, were reported by Breen, Krupka and Williams (1969). The discovery of their paper obliged me to bury in my laboratory notebook the work on Cu^{2+}: LMN along with other unfinished work on J.T interactions. Now I would like to review the results again so that other workers in this field may have an access to our data.

The subject of the J.T interaction is rather complex and requires a thorough exposition of the theory. However, I will not review the theory, because a few good papers and review articles on this theory have already been published (O'Brien, 1964; Sturge, 1967; A & B, ch.21). Since the original group-theoretical treatment by Jahn and Teller (1937) many theoretical works have been published. And yet the understanding of the J.T interaction is far from complete. A few recent experimental works have proved the complicated (and beautiful) nature of the J.T interaction. The list of J.T ions studied by EPR is expanding. We will summarize the results of $3d^1$ and $3d^9$ ions studied in our laboratory.

A. Cu^{2+} in LMN

1. Low Temperature Spectrum

When the crystal field affecting a Cu^{2+} ion is either trigonal or octahedral, the ground state is an orbital doublet. Since the spin-orbit interaction has no matrix elements within this doublet, the ground state will be subject to a large J.T distortion. This distortion is of tetragonal form along one of the fourfold axes of an octahedron, so that the orbital doublet is split into two singlets (x^2-y^2 and z^2). In most instances the tetragonal distortion is an elongation, placing the x^2-y^2 orbital below the z^2 orbital.

There are three fourfold axes in a regular octahedron, [100], [010], and [001], which are the directions of the cube edges. Any one of the three could be the axis of the distortion, which we call the z axis. If, say, [100] is the z axis of a J.T ion, then [010] and [001] will correspond to the x and y axes. The diagram on the left shows a projection of these three axes on the (111) plane. In our LMN this (111) plane corresponds to the hexagonal crystal plane and the [111] axis is along the c axis of the crystal. Each axis is tilted from the [111] axis by an angle of 54°44'.

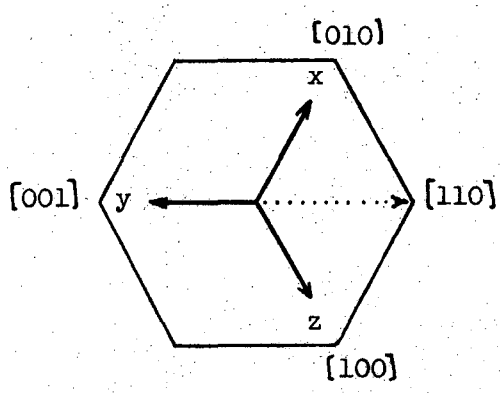

When the magnetic field was rotated in the (111) plane, we saw, at 4.2°K or lower, three sets of four hfs lines with 60° periodicity, as shown in Fig. 50. When H was along one of the hexagonal edges,

one set reached the maximum g of 2.349 with a spacing of A = 87.0 G and the other two sets crossed at g = 2.159 with A = 46.8 G. The former corresponded to $n^2 = 2/3$ in Eq.(33) and the latter two to $n^2 = 1/6$, verifying that the sum of the three n^2 adds up to 1. A rotation of 30° brought the two sets together at g = 2.286 ($n^2 = 1/2$, A = 79.5 G) and one set at the lowest g = 2.098 ($n^2 = 0$, A = 17 G).*

Next, the crystal was oriented vertically so that the magnetic field was rotated in the plane that contained the [001], [111] and [110] directions. We called this plane the (110) plane. Again three sets of four hf lines were observed in this plane. All three sets merged completely at g = 2.226 ($n^2 = 1/3$, A = 69.5 G), when H was along [111]. There was another direction at which all the three sets merged; this was 109.4° away from [111].

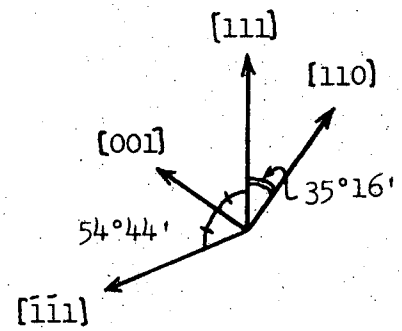

For H along [110] two sets merged at g = 2.286 ($n^2 = 1/2$, A = 79.5 G) and one set was at g = 2.098 ($n^2 = 0$, A ~ 18 G). When H was aligned in the direction of [001], we observed one set at the highest g of 2.465 ($n^2 = 1$, A = 97.1 G) and a superposition of two sets at g = 2.100.

The powdered sample of Cu^{2+} : LMN at liquid helium temperatures displayed a typical axial Cu^{2+} spectra with $g_{//} = 2{,}464$, $g_{\perp} = 2.10$, $A_{//} = 97.2$ G and $A_{\perp} \sim 19$ G. We then conclude that

---

* We saw a doubling of this set: two sets of four lines with unequal g and A. The g value given here is the average of 2.103 and 2.092.

$$\left.\begin{array}{l} g_{\parallel} = 2.465, \qquad g_{\perp} = 2.099 \\ A_{\parallel} = -97.1\ G = -111.8 \times 10^{-4}\ cm^{-1} \\ A_{\perp} = 17\ G = 16.8 \times 10^{-4}\ cm^{-1} \end{array}\right\} \qquad (68)$$

These parameters are almost identical to the results of Breen et. al. (1969). The signs of $A_{\parallel}$ and $A_{\perp}$ were determined by the plot of A_i' vs. f_i of Eq.(46) in section V-C. Our theoretical calculation agreed very well with the experimental points.

2. High Temperature Spectrum

When the single crystal of Cu^{2+} : LMN, oriented in the (110) plane, was warmed to 63°K (solid nitrogen temperature), one strong set of four lines was seen at g = 2.22, in addition to complicated weak spectrum on both sides. The strong middle set was slightly angularly dependent and at some orientations five lines, instead of four, were observed. The lowest set of the weak lines was at a g of about 2.45 with 45 G splitting and the highest set had a complicated structure near g of 2.05. As the temperature was further raised to 77°K (liquid nitrogen temperature), the weak spectra gradually disappeared and only the strong middle set remained at g = 2.222 with a spacing of 26.0 G. At -40°C the hf lines disappeared and a single broad band of about 110 G width was observed at g = 2.227. The powdered spectrum at 90°K showed four isotropic lines of g = 2.221 and A = 25.7 G. Thus, we have observed a gradual transition of the low temperature spectrum

to the high temperature spectrum in the temperature region of 60 to 75°K. The high temperature spectrum is characteristic of a dynamic J.T ion, for which all the anisotropies in the contributions to the g and hf constants from the spin-orbit interaction are averaged out owing to lattice vibration. The high temperature g and hf constants can be calculated from the low temperature values by

$$\left.\begin{aligned} \langle g \rangle &= (g_{\parallel} + 2g_{\perp})/3 = 2.221 \\ \langle A \rangle &= (A_{\parallel} + 2A_{\perp})/3 = -26.1 \times 10^{-4}\ \mathrm{cm}^{-1} \end{aligned}\right\} \quad (69)$$

which agree well with the observed values.

B. Cu^{2+} in $Zn(BrO_3)_2 \cdot 6H_2O$

The room temperature spectrum of Cu^{2+} : $Zn(BrO_3)_2 \cdot 6H_2O$ consisted of a single broad band about 160 G wide at g = 2.21. As the temperature was lowered, the four line hf began to appear. At 77°K these weak isotropic lines were centered at g = 2.217 with a 25 G splitting. The single crystal spectrum at liquid helium temperature was exceedingly complex. Because four to five sets of hfs were badly overlapped, we could not study the angular dependence of the line positions in either the (110) plane or the (111) plane. Instead, we used a powdered sample that gave at liquid helium temperature

$$\left.\begin{aligned} g_{\parallel} &= 2.448, \qquad g_{\perp} = 2.093 \\ A_{\parallel} &= -97.7\ \text{G} = -111.7 \times 10^{-4}\ \text{cm}^{-1} \\ A_{\perp} &= 19\ \text{G} = 18.6 \times 10^{-4}\ \text{cm}^{-1}. \end{aligned}\right\} \qquad (70)$$

C. VCl_4 in various host lattices

Vanadium tetrachloride, VCl_4, is tetrahedrally coordinated. The ground state of V^{4+} ($3d^1$) in this symmetry is identical to Cu^{2+} ($3d^9$) in the octahedral symmetry. Hence we should expect a similar J.T distortion in VCl_4. This problem was extensively investigated by Pratt (1967). Here we will merely list in Table A-4 the tentative assignments of glass spectra of VCl_4 in five host lattices.

As described in Pratt's thesis, we often found no EPR signal until several hours had passed following the liquid helium transfer. Then, very slowly the eight-line hfs began to show up. The V^{4+} signals were readily saturated. After saturation ample time (5 ~ 30 minutes) needed to elapse, with the magnetic field and the microwave power off, before the second spectra was taken.

Table A-4. Glass spectra of VCl_4

Host Lattices	Appearance[a] at R.T.	g_1	g_2	A_1 (gauss)	A_2
CCl_4[b]	yellow, L	1.942	1.914	98	113
mineral oil	yellow, L	1.940	1.910		103
$SiBr_4$[b]	orange, L	1.929	1.900	80	128
CBr_4	brown, S		1.919		113
$TiCl_4$[b]	yellow, L		1.898		119

a. L = liquid, S = solid

b. saturation readily occurred.

APPENDIX IV

TABLES OF EXPERIMENTAL DATA

Table A-5 Observed line positions and intensities of Ni^{2+} : LMN, ac plane.

Table A-6 Observed line positions, apparent g and A values of Cu^{2+} : α-$NiSO_4 \cdot 6H_2O$, ab plane, 1.37°K.

Table A-7 Observed line positions of the pair-wise transitions in the γc and the ab planes of α-$NiSO_4 \cdot 6H_2O$.

Table A-5. Observed line positions and intensities of Ni^{2+} : LMN, ac plane.[a]

angle (degree)	Line 1 H (G)	Line 1 Int.[b]	Line 2 H (G)	Line 2 Int.[b]	Line 3 H (G)	Line 3 Int.[b]
0.3	1193.4	6.9	1469.7	0.3	4611.5	8.3
15.3	1139.7	6.8	1610.3	1.7	4388.0	9.4
30.3	1082.8	6.1	1955.3	3.9	3807.1	10.2
45.3	1064.6	5.2	2448.0	5.4	3081.7	12.2
60.3	1088.3	3.9	3023.0	7.3	2434.5	13.2
75.3	1141.4	2.7	3483.3	5.5	2017.1	12.2
90.0	1188.3	0.0	3680.9	5.1	1852.8	11.8

a. At 77°K and ν_e = 9.08605 GHz.

b. Intensity measured at 1.7°K and expressed in arbitrary units.

Table A-6. Observed line positions, apparent g and A values of Cu^{2+} : α-$NiSO_4.6H_2O$, ab plane, 1.37°K

α (degree)	H (G)	g	A (G)
90	2430	2.850	74
85	2429	2.851	74
80	2433	2.846	73
75*	2446	2.831	72
70	2458	2.817	70
65	2476	2.797	71
60	2495	2.775	68
55	2512	2.757	68
50	2547	2.719	60
45*	2576	2.688	59
40	2607	2.656	59
35*	2641	2.622	54
30	2667	2.596	46
25*	2695	2.570	42
20	2723	2.543	35
15*	2743	2.525	
10	2773	2.497	
5	2778	2.493	
0	2785	2.486	

* frequency at 9.6766 GHz. All other points were taken at ν_e = 9.6777 GHz.

Table A-7. Observed line positions of the pair-wise transitions in α-$NiSO_4 \cdot 6H_2O$, 1.7°K.

	γc plane[a] (gauss)			ab plane[b] (gauss)
angle	transition 1	transition 2	angle	H
11.7°		9537	-15	5190
16.7	9406	6651	-10	4700
21.7	7635	5142	-5	4050
26.7	6618	4421	0	3630
31.7	5929	3896	5	3370
36.7	5405	3437	10	3180
41.7	4945	3273	20	2820
46.7	4683	3109	25	2720
51.7	4421	3043	30	2590
56.7	4224		35	2490
61.7	4027		40	2460
66.7	3961		45	2460
71.7	3896		50	2460
76.7	3908		55	2490
81.7	3975			
86.7	4172			
91.7	3929			
96.7	3961			
101.7	3896			

a. ν_e = 9.6936 GHz.

b. ν_e = 8.503 GHz.

APPENDIX V

COMPUTER PROGRAMS

A. Field Positions of Ni^{2+} EPR Spectra

This is a routine computation of the theoretical field positions of the Ni^{2+} EPR spectra in the three planes of $ZnSeO_4 \cdot 6H_2O$. The program is written in the simple Focal language, which is developed for the PDP-8/I computer system. The program solves the cubic equation (16) by the Newton-Raphson method. The magnetic field is successively varied until the computed energy separation of the two excited states becomes sufficiently close to the resonance energy $h\nu$. This field position is then plotted on an oscilloscope and/or on a X-Y plotter. The experimental points are also plotted on the same (or separate) graph.

C-8K FOCAL ©1969

```
01.01 C      COMPUTATION OF FIELD POSITIONS OF NI ESR SPECTRA
01.02 C      4 IONS IN 3 PLANES OF ZINC SELENATE
01.03 C      EIGENVALUES FROM CUBIC EQUATION OF THE FORM
01.04 C      E(X)=A(3)*X↑3+A(2)*X↑2+A(1)*X+A(0)
01.07 C
01.08 C      SET THE X-AXIS LIMITS IN THE X-Y PLOTTER
01.09 ASK "LOW LIMIT"SG,"  HIGH LIMIT"EG,!,"  INTERVAL",DG,!
01.10 C      SET THE Y-AXIS LIMITS
01.11 A "START",ST,"INCREMENT",IN,"END",END,!
01.12 S MT=500/(END-ST);S MT=500/(EG-SG)
01.20 C
01.21 ASK !?GZ GX?,!
01.22 ASK ?D?,
01.23 A "E"DE
01.24 A "PHI"PHI,"BETA"OMEGA,!
01.26 A "NU"NU;S NO=NU/29.9793;T ! "NU",%6.05,NO,!
01.27 T "WHICH PLANE?  AB =1, AC =2, B-C =3  ",!
01.28 ASK PL
01.30 S PI=3.14159;S RAD=PI/180
01.31 S BOHR=0.466887E-04
01.32 S G1=GZ*BOHR;S G2=GX*BOHR
01.34 S K1=FSIN(PHI*RAD);S K2=FCOS(PHI*RAD)
01.37 S K5=FSIN(OMEGA*RAD);S K6=FCOS(OMEGA*RAD)
01.41 S TP=1
01.42 S ANG=START
01.43 S HO=5000
01.47 S K3=FSIN(ANG*RAD);S K4=FCOS(ANG*RAD)
01.50 IF (PL-2) 1.55,1.6,1.65
01.55 DO 3
01.56 GOTO 1.9
01.60 DO 4
01.61 GOTO 1.9
01.65 DO 5
01.90 S A(3)=1;S A(2)=-2*D
01.91 S A(1)=D*D-DE*DE-(G1*HZ)↑2-(G2*G2)*(HX*HX+HY*HY)
01.92 S A(0)=(G2*G2)*(HX*HX+HY*HY)*D-(G2*G2)*(HX+HY)*(HX-HY)*DE
01.93 S NP=1
01.95 GOTO 6.1

03.10 S K3=FSIN((ANG+OMEGA)*RAD)
03.11 S K4=FCOS((ANG+OMEGA)*RAD)
03.12 S K5=FSIN((ANG-OMEGA)*RAD)
03.13 S K6=FCOS((ANG-OMEGA)*RAD)
03.20 IF (TP-3) 3.25,3.25,3.6
03.25 IF (TP-2) 3.3,3.4,3.5
03.30 S HX=HO*K3;S HY=-HO*K4*K2;S HZ=HO*K4*K1;RETURN
03.40 S HX=-HO*K4;S HY=-HO*K3*K2;S HZ=HO*K3*K1;RETURN
03.50 S HX=-HO*K5;S HY=HO*K6*K2;S HZ=-HO*K6*K1;RETURN
03.60 S HX=HO*K6;S HY=HO*K5*K2;S HZ=-HO*K5*K1;RETURN

04.10 S K5=FCOS((45+OMEGA)*RAD);S K6=FCOS((45-OMEGA)*RAD)
04.12 S U1=K1*K4;S U2=K2*K4;S U3=K3*K6;S U4=K3*K5
04.20 IF (TP-3) 4.25,4.25,4.6
04.25 IF (TP-2) 4.3,4.4,4.5
04.30 S HX=HO*U3;S HY=HO*(U1-U4*K2);S HZ=HO*(U2+U4*K1);RETURN
04.40 S HX=-HO*U4;S HY=HO*(U1-U3*K2);S HZ=HO*(U2+U3*K1);RETURN
04.50 S HX=-HO*U4;S HY=HO*(U1+U3*K2);S HZ=HO*(U2-U3*K1);RETURN
04.60 S HX=HO*U3;S HY=HO*(U1+U4*K2);S HZ=HO*(U2-U4*K1);RETURN
```

```
05.10 S U1=K1*K4;S U2=K2*K4;S U3=K3*K5;S U4=K3*K6
05.20 IF (TP-3) 5.25,5.25,5.6
05.25 IF (TP-2) 5.3,5.4,5.5
05.30 S HX=HO*U3;S HY=HO*(U1-U4*K2);S HZ=HO*(U2+U4*K1);RETURN
05.40 S HX=-HO*U4;S HY=HO*(U1-U3*K2);S HZ=HO*(U2+U3*K1);RETURN
05.50 S HX=HO*U3;S HY=HO*(U1+U4*K2);S HZ=HO*(U2-U4*K1);RETURN
05.60 S HX=HO*U4;S HY=HO*(U1-U3*K2);S HZ=HO*(U2+U3*K1);RETURN

06.10 S Y(1)=D+G1*HO;GOTO 6.2
06.15 S Y(1)=D-G1*HO;S NP=2
06.20 S M=1
06.22 S B1(4)=0;S C1(4)=0
06.30 F JJ=1,1,4;DO 10
06.40 S Y(M+1)=Y(M)-B1(0)/C1(1)
06.45 IF (FABS(Y(M+1)-Y(M))-0.0001) 6.7,6.7,6.5
06.50 S M=M+1;IF (M-15) 6.22,6.7,6.7
06.70 IF (NP-2) 6.75,6.9,6.9
06.75 S X1=Y(M+1);GOTO 6.15
06.90 S X2=Y(M+1);GOTO 9.2

09.20 S V2=X1-X2
09.21 S B=NO-V2
09.30 IF (FABS(B)-0.001) 9.8,9.8,9.4
09.40 IF (HO-4000) 9.41,9.41,9.43
09.41 S PP=0.7;GOTO 9.7
09.43 IF (HO-8000) 9.44,9.44,9.46
09.44 S PP=1.;GOTO 9.7
09.46 S PP=1.5
09.70 S HO=HO+PP*B/G1;GOTO 1.5
09.80 T ! "ANGLE",ANG,"   HO"HO,"   DIFF",B,!
09.81 DO 13
09.82 IF (ANG-END) 9.83,9.85,9.85
09.83 S ANG=ANG+INCR;GOTO 1.47
09.85 IF (TP-4) 9.86,9.9,9.9
09.86 S TP=TP+1;GOTO 1.42
09.90 DO 11
09.91 GOTO 12.1


10.10 S   II=4-JJ
10.20 S B1(II)=A(II)+Y(M)*B1(II+1);S C1(II)=B1(II)+Y(M)*C1(II+1)
10.30 RETURN

11.10 S XX=(EG-SG)/DG
11.20 F I=0,1,XX-1;DO 11.3
11.30 S Y=I*MT*DG-250;F J=0,1,5;S X=0+J;S Z=FDIS(X,Y);DO 13.8
11.40 S Z=FDIS(0,-250);DO 13.8;F I=-250,1,250;DO 13.8;S Z=FDIS(0,I)
11.50 F I=ST,10,END;S X=(I-ST)*TT+5;DO 11.6
11.60 F II=-250,1,-245;DO 13.8;S Z=FDIS(X,II)
11.70 F I=0,1,510;DO 13.8;S Z=FDIS(I,-250)

12.10 *
12.20 ASK ANG,HO
12.25 IF (HO) 12.5,12.5,1.23
12.30 IF (N-15) 12.32,12.32,12.4
12.32 DO 13
12.35 S N=N+1;GOTO 12.2
12.40 T !;S N=0;GOTO 12.2
12.50 QUIT

13.10 S X=(ANG-ST)*TT+5
13.20 S Y=(HO-SG)*MT-250
13.30 S Z=FDIS(X,Y);DO 13.8
13.40 RETURN
13.80 F JJ=0,15;S JJ=JJ
*
```

B. Hermitian Matrix Diagonalization

We have developed a Fortran IV program that diagonalizes any hermitian matrix to give both eigenvalues and eigenvectors. In a usual diagonalization scheme the order of the original hermitian matrix is doubled to form a real symmetric matrix which can then be diagonalized by a library subroutine, HDIAG. Our procedure does not require this doubling but instead uses matrix multiplications of two unitary matrices which can readily be formed from the original complex hermitian matrix.* It must be mentioned that the eigenvectors calculated by this program contain small errors; the sum of the squares of eigenvectors deviates slightly from 1.000 for a matrix containing nearly degenerate eigenvalues.

---

* See Kogbetliantz, E.G., Solution of Linear Equations by Diagonalization of Coefficients Matrix, Quart. Appl. Math. 13, 123 (1955).

```
                PROGRAM SHORI(INPUT,OUTPUT)
000041          REAL B(9,9),C(9,9),EIGV(9),VECT(9)
000041          REAL EGVRL(9,9),EGVIMA(9,9)
000041          COMPLEX EVEC(9,9)
000041       10 FORMAT(I2)
000041       20 FORMAT (2F10.0)
000041       25 FORMAT (1H ,9(F11.7,2X))
000041       30 FORMAT (1H1,10X,25HMATRIX TO BE DIAGONALIZED )
000041       31 FORMAT(4X,9HREAL PART )
000041       32 FORMAT(/,4X,15H IMAGINARY PART )
000041       35 FORMAT(//,24HSUM OF SQUARE OF VECTORS )
000041       85 CONTINUE
000041          READ 10,N
000046          IF(N)200,200,90
000050       90 CONTINUE
000050          MVEC=1
          C
          C   CLEAR MATRIX
000051          DO 100 J=1,N
000053          DO 100 I=1,N
000061          B(I,J)=0.
000062      100 C(I,J)=0.
          C
          C   MATRIX ELEMENTS ARE READ IN ROW BY ROW
000066          DO 110 I=1,N
000067          READ 20,(B(I,J),C(I,J),J=1,I)
000106      110 CONTINUE
          C
          C   SYMMETRY OF HERMITIAN MATRIX
000111          NN=N-1
000112          DO 120 J=1,NN
000114          JJ=J+1
000115          DO 120 I=JJ,N
000126          B(J,I)=B(I,J)
000127          C(J,I)=-C(I,J)
000130      120 CONTINUE
000134          PRINT 30
000137          PRINT 31
000142          DO 130 I=1,N
000144      130 PRINT 25, (B(I,J),J=1,N)
000162           PRINT 32
000165          DO 132 I=1,N
000167      132 PRINT 25,(C(I,J),J=1,N)
          C
000205          CALL HERMIT(B,C,N,MVEC,EIGV,EVEC)
          C
000211          PRINT 300,(EIGV(I),I=1,N)
000223      300 FORMAT(//,12HEIGEN-VALUES ,/,1H ,9(F11.7,2X))
          C
000223          DO 320 I=1,N
000225          DO 320 J=1,N
000236      320 EGVRL(I,J)=REAL(EVEC(I,J))
000243          DO 321 I=1,N
000244          DO 321 J=1,N
000255      321 EGVIMA(I,J)=AIMAG(EVEC(I,J))
000262          PRINT 305
000265      305 FORMAT(//,13HEIGEN-VECTORS ,/)
000265          PRINT 31
000270          DO 350 I=1,N
000272      350 PRINT 25,(EGVRL(I,J),J=1,N)
000310          PRINT 32


000313          DO 352 I=1,N
000315      352 PRINT 25, (EGVIMA(I,J),J=1,N)
000333          DO 355 I=1,N
000334          VECT(I)=0.
000335          DO 356 J=1,N
000337          VECT(I)=VECT(I)+(CABS(EVEC(I,J)))**2
000346      356 CONTINUE
000351      355 CONTINUE
000353          PRINT 35
000356          PRINT 25, (VECT(I),I=1,N)
000370          GO TO 85
000371      200 CONTINUE
000372          END
```

```
              SUBROUTINE HERMITIA,B,NUM,MVEC,EIGV,EVEC)
        C     FORTRAN IV DIAGONALIZATION OF A HERMITIAN MATRIX BY
        C     UNITARY MATRIX
        C     AUGUST 13, 1970
        C     CALLING  SEQUENCE FOR DIAGONALIIATION
        C                                  CALL HERMIT(A,B,NUM,MVEC,TR,TI)
        C                 WHERE A AND B ARE THE REAL AND IMAGINARY ARRAYS.
        C                 TO BE DIAGONALIZED.
        C     NUM IS THE ORDER OF THE MATRIX,A AND B
        C     IF YOU WANT THE EIGENVECTORS AS WELL,SET MVEC =1,
        C                 IF NOT, SET MVEC =0
        C     TR AND TI ARE THE REAL AND IMAGINARY TRANSFORMATION MATRICES.
001476        REAL A(9,9),B(9,9),C(9,9),EIGV(9)
001476        REAL TR(9,9),TI(9,9)
001476        COMPLEX STAND(9,9),PROD(9,9),EVEC(9,9)
001476        NN=NUM-1
001477        ROOT=SQRT(2.)
001502        CON=1.E-06
001503        MW=1
001504        INDEX=1
001510   100  IF (MVEC-1) 178, 165,165
        C          SET THE TRANSFORMATION MATRIX TO BE 0
001512   165  DO 170 J=1,NUM
001514        DO 170 I=1,NUM
001523        STAND(I,J)=(0.,0.)
001525   170  CONTINUE
        C          SET THE DIAGONAL ELEMENTS OF THE TRANSFORMATION MATRIX = 1
001534        DO 175 I=1,NUM
001544        STAND(I,I)=(1.,0.)
001546   175  CONTINUE
001553   178  SUM=0.
001554        DO 180 J=1,NUM
001556        DO 180 I= 1,NUM
001557        SUM=A(I,J)**2 + B(I,J)**2
001564        C(I,J)= SQRT(SUM)
001575   180  CONTINUE
        C          SELECT THE LARGEST OFF-DIAGONAL ELEMENT.
001601   190  XMAX=0.
001602        DO 200 I=1,NN
001604        JJ=I+1
001605        DO 200 J=JJ,NUM
001615        IF (XMAX-C(I,J))  210,210,200
001617   210  XMAX=C(I,J)
001620        K=I
001620        L=J
001621   200  CONTINUE
001630        IF(INDEX-75) 202,202,205
001633   205  PRINT 206,XMAX
001644   206  FORMAT(5X,4HXMAX,F12.7)
001644        GO TO 900
001644   202  CONTINUE
001644        IF (XMAX-CON)  800,800,220
001647   800  IF (MW-1) 520,520,900
001657   220  PM=0.5*(A(K,K)+A(L,L))
001662        Q=0.5*(A(K,K)-A(L,L))
001663        PMK=A(K,L)
001664        Q=B(K,L)
001665        W=SQRT(PMK**2+Q**2)
001672        R=SQRT(PMK**2+Q**2+Q**2)
        C          DETERMINATION OF COS AND SIN
        C            WHEN Q=0, ONLY REAL OFF DIAG. ELEMS. ARE NON-ZERO


        C            WHEN W=0, REAL DIAG. ELEMS. ARE EQUAL, AND OFF-DIAG. ELEMS=0
001703   230  IF (W-1.0E-08) 270,270,232
001706   232  IF (ABS(PMK)-CON) 280, 280, 235
001712   235  DEL=P/W
001714        GAMMA=W/R
001716        T=PMK
001717        X=T/ABS(T)
001721        IF (ABS(ABS(DEL)-1.)-1.E-08) 236,236,237
001726   236  IF (DEL) 238,238,239
001730   238  C1=0.
001731        S1=X
001733        GO TO 247
001733   239  C1=1.
001735        S1=0.
001736        GO TO 247
001736   237  C1=SQRT(0.5*(1.+DEL))
001744        S1= X*SQRT(0.5*(1.0-DEL))
001755   247  IF (ABS(Q)-1.E-08) 290,290,250
001761   250  T=-Q
001763        X=T/ABS(T)
001765        C2= SQRT(0.5*(1.+GAMMA))
001775   255  S2=X*SQRT(0.5*(1.0-GAMMA))
002004        GO TO 300
002020   270  C1=1.
002022        S1=0.
002023        C2=0.5*ROOT
002024        T=-Q
002026        X=T/ABS(T)
002030        S2=0.5*ROOT*X
002031        A(K,K)=   PM-   Q*X
002033        A(L,L)=   PM+   Q*X
002035        GO TO 310
002035   280  IF (ABS(P)-1.E-08) 270,270,281
002041   281  IF (ABS(Q)-1.0E-08) 700,700,282
002047   282  X=P/ABS(P)
002050        S1=0.5*(1.0-X)
002053        C1=0.5*(1.0+X)
002054        X=Q/ABS(Q)
002057        T=ABS(P)/R
002061        IF (T-1) 285,286,286
002064   286  C2=1.
002066        S2=0.
002067        GO TO 300
002067   285  C2=SQRT(0.5*(1.+T))
002075        S2=-X*SQRT(0.5*(1.0-T))
002103        GO TO 300
002107   290  S2=0.
002110        C2=1.0
002112        GO TO 300
        C          K-TH ROW AND L-TH COLUMN ELEMENTS AFTER A ROTATION
002120   300  A(K,K)=PM+R
002123        A(L,L)=PM-R
002131   310  A(K,L)=0.
002131        A(L,K)=0.
002131        B(K,L)=0.
002132        B(L,K)=0.
002135   330  DO 400 IC=1,NUM
002150        IF (IC-K)  340,400,340
002152   340  IF (IC-L)  350,400,350
002156   350  ALFA=C1*A(IC,K)+S1*A(IC,L)
002157        ALMD=C1*B(IC,K)+S1*B(IC,L)
002162        BETA=C1*A(IC,L)-S1*A(IC,K)
```

```
002164          BMU=C1*B(IC,L)-S1*B(IC,K)
002166          A(IC,K)=ALFA*C2-BMU*S2
002171          A(K,IC)=A(IC,K)
002172           A(IC,L)=BETA*C2-ALAMD*S2
002174          A(L,IC)=A(IC,L)
002175          B(IC,K)=ALAMD*C2+BETA*S2
002176          B(K,IC)=-B(IC,K)
002177          B(IC,L)=BMU*C2+ALFA*S2
002202          B(L,IC)=-B(IC,L)
002202      400 CONTINUE
          C         DO YOU WISH TO HAVE AN EIGENVECTOR
002213      410 IF (MVEC-1) 700,500,500
          C         TRANSFORMATION MATRIX AFTER ROTATION
002231      500  STAND(K,K)=CMPLX(C1*C2,-S1*S2)
002234           STAND(L,L)=STAND(K,K)
002237           STAND(K,L)=CMPLX(-S1*C2,-C1*S2)
002242           STAND(L,K)=CMPLX(S1*C2,C1*S2)
002250      510 IF (MW-1) 520,520,550
002253      520 DO 530 J=1,NUM
002255          DO 530 I=1,NUM
002265           EVEC(I,J)=STAND(I,J)
002267      530 CONTINUE
002277          MW=MW+1
002300          GO TO 700
002301      550 DO 570 J=1,NUM
002303          DO 570 I=1,NUM
002304           PROD(I,J)=(0.,0.)
002311          DO 560 JACK=1,NUM
002325           PROD(I,J)=PROD(I,J)+STAND(I,JACK)*EVEC(JACK,J)
002335      560 CONTINUE
002342      570 CONTINUE
002346      600 DO 610 J=1,NUM
002350          DO 610 I=1,NUM
002360           EVEC(I,J)=PROD(I,J)
002362      610 CONTINUE
          C         NOW TEST TO SEE IF THERE ARE ANY MORE OFF-DIAGONAL
          C         ELEMENTS LARGE ENOUGH TO REQUIRE FURTHER ROTATIONS
002372      700  INDEX=INDEX+1
002374           GO TO 100
002376      900  CONTINUE
002374           DO 905 I=1,NUM
002404      905  EIGV(I)=A(I,I)
          C
002406           DO 1200 I=1,NUM
002413           DO 1200 J=1,NUM
002424           TR(I,J)=REAL(EVEC(I,J))
002425     1200 TI(I,J)=AIMAG(EVEC(I,J))
002436           PRINT 1109
002445     1109  FORMAT(//,12HEIGEN-VALUES)
002445     1110  FORMAT(1H ,9(F11.6,2X))
002445           PRINT 1110,(EIGV(I),I=1,NUM)
002471           PRINT 1111
002500     1111  FORMAT(//,13HEIGEN-VECTORS)
002500           PRINT 1112
002507     1112  FORMAT(4HREAL)
002507           DO 1115 I=1,NUM
002510     1115  PRINT 1110,(TR(I,J),J=1,NUM)
002537           PRINT 1113
002546     1113  FORMAT(/,9HIMAGINARY)
002546           DO 1116 I=1,NUM
002547     1116  PRINT 1110,(TI(I,J),J=1,NUM)
          C


002576           DO 910 I=1,NN
002577           JJ=N-I
002600           DO 910 J=1,JJ
002602           IF (EIGV(J)-EIGV(JJ+1)) 920,910,910
002614      920  TEMPO=EIGV(JJ+1)
002615           EIGV(JJ+1)=EIGV(J)
002617           EIGV(J)=TEMPO
002620           IC=J
002621           JC=JJ+1
002622           DO 930 K=1,NUM
002624           DO 930 L=1,NUM
002625           IF(K-IC) 940,950,940
002627      940  IF(L-JC) 930,960,930
002632      950  IF(L-JC) 970,980,970
002645      980  EVEC(K,L)=EVEC(L,K)
002647           EVEC(L,K)=EVEC(K,L)
002651           EVEC(K,K)=EVEC(L,L)
002653           EVEC(L,L)=EVEC(K,K)
002655           GO TO 930
002661      960  EVEC(K,L)=EVEC(K,IC)
002671           GO TO 930
002672      970  EVEC(K,L)=EVEC(JC,L)
002701      930  CONTINUE
002706           DO 1210 I=1,NUM
002707           DO 1210 J=1,NUM
002720           TR(I,J)=REAL(EVEC(I,J))
002721     1210  TI(I,J)=AIMAG(EVEC(I,J))
002732           PRINT 1140,IC,JC
002745     1140  FORMAT(//,I2,5H AND  ,I2,17H ARE INTERCHANGED )
002745           PRINT 1109
002754           PRINT 1110,(EIGV(I),I=1,NUM)
003000           PRINT 1111
003007           PRINT 1112
003016           DO 1130 I=1,NUM
003017     1130  PRINT 1110,(TR(I,J),J=1,NUM)
003046           PRINT 1113
003055           DO 1135 I=1,NUM
003056     1135  PRINT 1110,(TI(I,J),J=1,NUM)
003105      910  CONTINUE
003112           RETURN
003113          END
```

ACKNOWLEDGEMENTS

I would like to express my sincere gratitude to Professor Rollie J. Myers for his counsel and encouragement during the course of this work. I also wish to acknowledge valuable contributions of my collegues: David Pratt, Tom Batchelder, Raymond Pao, James Chang, Joyce Tevebaugh and Tom Hynes.

In particular, I wish to thank Tom (B) for his critical comments on the first draft and for stimulating discussions on both physical and metaphysical problems, Jim for his invaluable assistance with experimental and computational problems, and Joyce for the proof-reading. Rich Mertins provided his EPR measurements on Ni^{2+} in zinc bromate.

I owe special appreciation to my wife, Esther Nijiko, for her patience and encouragement. The members of the Original Gospel Tabernacle have greatly enriched my spiritual life.

This work was conducted under the auspices of the United States Atomic Energy Commission.

REFERENCES

ABRAGAM, A. and BLEANEY, B. (1970) Electron Paramagnetic Resonance of Transition Ions. Clarendon Press, Oxford.

Most recent and most comprehensive book on EPR of transition metal ions and rare-earth ions in solids. This book is quite readable and should be consulted by every worker in the field.

ABRAGAM, A. and PRYCE, M. H. L. (1951a) Proc. Roy. Soc. (London) A205, 135

ABRAGAM, A. and PRYCE, M. H. L. (1951b) Proc. Roy. Soc. (London) A206, 164

ABRAGAM, A. and PRYCE, M. H. L. (1951c) Proc. Roy. Soc. (London) A206, 173

ARKHANGEL'SKAYA, E. D., ZARIPOV, M. M., POL'SKII, Y. E., STEPANOV, V. G., CHIRKIN, G. K., and SHEKUN, L. Y. (1963) Soviet Phys.--Solid State 4, 1855

ATSARKIN, V. A. (1963) Soviet Phys. (JETP) 16, 593

BALLHAUSEN, C. J. (1962) Introduction to Ligand Field Theory. McGraw-Hill, N. Y.

BATCHELDER, W. T. (1970) The Electron Paramagnetic Resonance Spectra of α-$NiSO_4 \cdot 6H_2O$ at Liquid Helium Temperature (Ph.D. thesis), University of California, Berkeley, UCRL-19157.

BEEVERS, C. A. and LIPSON, H. (1932) Z. Krist. 83, 123

BEEVERS, C. A. and SCHWARTZ, C. M. (1935) Z. Krist. 91, 157

BLEANEY, B. (1951) Phil. Mag. 7, 42, 441

BLEANEY, B., BOWERS, K. D. and PRYCE, M. H. L. (1955) Proc. Roy. Soc. (London) A228, 166

BLEANEY, B. and INGRAM, D. J. E. (1951) Proc. Roy. Soc. (London) A208, 143

BLUMBERG, W. E., EISINGER, J. and GESCHWIND, S. (1963) Phys. Rev. 130, 900

BOWERS, K. D. and OWEN, J. (1955) Rept. Progr. Phys. 18, 304

BRADLEY, A. J. and JAY, A. H. (1932) Proc. Physic. Soc. 44, 563

BRAUER, G. (1963) Handbook of Preparative Inorganic Chemistry. Editor, Academic Press, N. Y., Vol. 1, p. 433; Vol. 2, pp. 1074-1087

BREEN, D. P., KRUPKA, D. C. and WILLIAMS, F. I. B. (1969) Phys. Rev. 179, 241

BURNS, G. (1961) J. Appl. Phys. 32, 2048

CARSON, J. W., DEVOR, D. P. and HOSKINS, R. H. (1961) Phys. Rev. 122, 1141

CHAN, I. Y., DOETSCHMAN, D. C., HUTCHINSON, C. A., KOHLER, B. E., and STOUT, J. W. (1965) J. Chem. Phys. 42, 1048

CHANG, J. J. (1971) Relaxation Time Measurements in Electron Paramagnetic Resonance (Ph.D. thesis), University of California, Berkeley, UCRL-19691

CULVAHOUSE, J. W. (1962) J. Chem. Phys. 36, 2720

CULVAHOUSE, J. W., SCHINKE, D. P., and PFORTMILLER, L. G. (1969) Phys. Rev. 177, 454

DAVIS, C. F. and STRANDBERG, M. W. P. (1957) Phys. Rev. 105, 447

FISHER, R. A. and HORNUNG, E. W. (1968) J. Chem. Phys. 48, 4284

FISHER, R. A., HORNUNG, E. W., BRODALE, G. E., and GIAUQUE, W. F. (1967) J. Chem. Phys. 46, 4945

FISHER, R. A., BRODALE, G. E., HORNUNG, E. W., and GIAUQUE, W. F. (1968a) J. Chem. Phys. 48, 1769

FISHER, R. A., BRODALE, G. E. HORNUNG, E. W., and GIAUQUE, W. F. (1968b) J. Chem. Phys. 48, 4096

GERRISTEN, H. J. and SABISKY, E. S. (1962) Phys. Rev. 125, 1853

GESCHWIND, S., KISLIUK, P., KLEIN, M. P., REMEIKA, J. P., and WOOD, D. L. (1962) Phys. Rev. 126, 1684

GEUSIE, J. E., PETER, M., and SCHULZ-du-BOIS, E. O. (1959) Bell System Tech. J. 38, 291

GIBB, T. R. P. (1942) Optical Methods of Chemical Analysis. McGraw-Hill, N. Y., ch. 6

GMELIN, L. (1966) Gmelins Handbuch der Anorganischen Chemie, Verlag Chemie.GMBH. Weinheim, Bergstrasse, System No. 57, Vol. 8, Pt. B2, pp. 699, 752

GRAY, H. B. (1965) Electrons and Chemical Bonding. Benjamin, New York

GRIFFITH, J. S. (1961) The Theory of Transition-Metal Ions. University Press, Cambridge

GROTH, P. (1908) Chemische Krsytallographie (Leipzig) 2. Teil, p. 423

HERZBERG, G. (1966) Electronic Spectra and Electronic Structure of Polyatomic Molecules. D. Van Nostrand, Princeton, N. J.

HOLDEN, A. and SINGER, P. (1960) Crystals and Crystal Growing. Anchor Books (Doubleday), New York

HOLMES, O. G. and MCCLURE, D. S. (1957) J. Chem. Phys. 26, 1686

HOSKINS, R. H., PASTOR, R. C., and TRIGGER, K. R. (1959a) J. Chem. Phys. 30, 601

HOSKINS, R. H., PASTOR, R. C., and TRIGGER, K. R. (1959b) J. Chem. Phys. 30, 1630

HUTCHINGS, M. T. (1964) Solid State Physics, 16, 227

HUTTON, D. R. and TROUP, G. J. (1964) Brit. J. Appl. Phys. 15, 275

IRI, T. and KUWABARA, G. (1968) J. Phys. Soc. Japan, 24, 127

JAHN, H. A. and Teller, E. (1937) Proc. Roy. Soc. (London) A161, 220

JARRET, H. S. (1957) J. Chem. Phys. 27, 1298

KAMIMURA, H. (1962) Phys. Rev. 128, 1077

KATSUMATA, K. and YOKOZAWA, Y. (1970) J. Phys. Soc. Japan, 28, 1368

KLEIN, A. (1940) Annales de Chemie, 14, 263

KNOX, K. (1959) J. Chem. Phys. 30, 991

LACROIX, R. (1961) Compt. Rend. 12, 1768

LAURENCE, N. and LAMBE, J. (1963) Phys. Rev. 132, 1029

LOHR, L. L. and LIPSCOMB, W. N. (1963) J. Chem. Phys. 38, 1607

LOW, W. (1960) Paramagnetic Resonance in Solids. Academic Press, N. Y.
Useful tabulations of matrix elements for crystal field calculations

LOW, W. and RUBINS, R. S. (1963) in Paramagnetic Resonance, Low, W., Ed. Academic Press, Vol. 1, p. 79

LOW, W. and WEGER, M. (1960) Phys. Rev. 118, 1130

MARSHALL, S. A., KIKUCHI, T. T., and REINBERG, A. R. (1962) Phys. Rev. 125, 453

MCCLURE, B. R. (1962) J. Chem. Phys. 36, 2757

MCGARVEY, B. R. (1964a) J. Chem. Phys. 40, 809

MCGARVEY, B. R. (1964b) J. Chem. Phys. 41, 3743

MCGARVEY, B. R. (1966) ELectron Spin Resonance of Transition-Metal Complexes, in Transition Metal Chemistry, Vol. 3, ed. by Carlin, R. L. Marcel Dekker, New York
Useful tabulations of EPR results of transition metal ions in single crystals.

MCPHERSON, G. L., KISTENMACHER, T. J., and STUCKY, G. D. (1970) J. Chem. Phys. 52, 815

NORDAL, P. E. (1965) An Investigation on Paramagnetic Resonance in Some Nickel Salts (Master thesis), Institutt for Teknisk Fysikk, Almenavdelingen, Norway.

O'BRIEN, M. C. M. (1964) Proc. Roy. Soc. (London) A281, 323

O'CONNOR, B. H. and DALE, D. H. (1966) Acta. Cryst. 21, 705

ORTON, J. W. (1959) Rept. Prog. Phys. 22, 204

ORTON, J. W. (1968) Electron Paramagnetic Resonance, "An Introduction to Transition Group Ions in Crystals". Iliffe Books Ltd., London A good introductory treatment on EPR of solids. Particularly useful are the sample calculations of crystal field and spin-Hamiltonian for $3d^1$ and $3d^3$ systems. The book has one chapter devoted to a summary of EPR and spin-lattice relaxation experiments carried out between 1959 and 1966.

ORTON, J. W., AUZINS, P., and WERTZ, J. E. (1960a) Phys. Rev. Letters 4, 128

ORTON, J. W., AUZINS, P., and WERTZ, J. E. (1960b) Phys. Rev. 119, 1691

ORTON, J. W., AUZINS, P., GRIFFITHS, J. H. E., and WERTZ, J. E. (1961) Proc. Phys. Soc. 78, 554

OWEN, J. and THORNLEY, J. H. M. (1966) Rept. Progr. Phys. 26, [2], 675

PETER, M. (1959) Phys. Rev. 116, 1432

PRATT, D. W. (1967) Magnetic Resonance Spectra of VCl_4 and Other Paramagnetic Species (Ph.D. thesis), University of California, Berkeley, UCRL-17406

PRYCE, M. H. L. (1950) Proc. Phys. Soc. (London) A63, 25

ROLLMAN, L. D. and CHAN, S. I. (1969) J. Chem. Phys. 50, 3416

RUBINS, R. S. and LOW, W. (1963) in Paramagnetic Resonance. ed. by Low, W. Vol. 1, p. 59

SIERRO, J. and LACROIX, R. (1959) Helv. Phys. Acta. 32, 286

SKOOG, D. A., LAI, M. G., and FURST, A. (1958) Analytical Chem. 30, 365

SMITH, S. R. P., DRAVNIEKS, F., and WERTZ, J. E. (1969) Phys. Rev. 178, 471

STAHL-BRADA, R. and LOW, W. (1959) Phys. Rev. 116, 561

STEVENS, K. W. H. (1952) Proc. Phys. Soc. (London) A65, 209

STURGE, M. D. (1963) Phys. Rev. 130, 639

STURGE, M. D. (1967) Solid State Physics, 20, 91

SUGANO, S. and PETER, M. (1961) Phys. Rev. 122, 381

SUGANO, S., TANABE, Y., and KAMIMURA, H. (1970) Multiplets of Transition-Metal Ions in Crystals. Academic Press, N. Y.

STOUT, J. W. and HADLEY, W. B. (1964) J. Chem. Phys. 40, 55

WALSH, W. M. (1959a) Phys. Rev. 114, 1473

WALSH, W. M. (1959b) Phys. Rev. 114, 1485

WASSERMAN, E., SNYDER, L. C., and YAGER, W. A. (1964) J. Chem. Phys. 41, 1763

WATANABE, T. (1962) J. Phys. Soc. Japan, 17, 1856

WONG, E. Y. (1960) J. Chem. Phys. 32, 598

WYCKOFF, R. W. G. (1922) Amer. J. Sci. IV, 188

YU. S. H. and BEEVERS, C. A. (1936) Z. Krist. 95, 426

ZALKIN, A., FORRESTER, J. D., and TEMPLETON, D. H. (1963) J. Chem. Phys. 39, 2881

FIGURE LIST

1. Schematic diagram of an X-band waveguide and cavity unit with a variable coupler arrangement.

   A: 6 mm diameter quartz rod; B: Wilson seal;

   C: Brass X-band rectangular waveguide, broad face shown here;

   D: Styroform pieces inserted in several sections of the waveguide to prevent vibrations of the quartz rod;

   E: Stainless X-band rectangular waveguide;

   F: 3-1/2 in. long transition from a rectangular to circular waveguide;

   G: Circular teflon disk (1 in. dia. and 0.4 in. high) with a 30 gauge copper wire helix;

   H: A silver circular plate with a 5/16 in. coupling window;

   I: Brass X-band cylindrical cavity, silver plated inside, screwed to the waveguide. Frequency is 9.5 GHz when teflon is filled;

   J: Teflon cap supporting a silver plate K;

   K: Silver plate that forms the bottom of a cavity, electrically insulated from the cavity by mylar sheet;

   L: 30 gauge copper wire helix imbedded in a teflon disk.

2. The three most frequently used crystal mounters for X-band experiments at low temperatures.

3. Two forms of $ZnSeO_4 \cdot 6H_2O$ crystal habits grown in this work.

   (a) grown at room temperature (b) grown at 5°C, often half of this crystal is grown.

4. Photograph of crystal model of α-$NiSO_4 \cdot 6H_2O$ showing only Ni^{2+} and SO_4^{2-} ions. The four unit cells are viewed with the c axis vertical.
5. Projection of one-half of a unit cell of α-$NiSO_4 \cdot 6H_2O$ on the (001) plane. Two layers of $Ni(H_2O)_6^{2+}$ and SO_4^{2-} groups are depicted here with the relative positions of Ni, S and O atoms.
6. Projection of the magnetic axes of the four Ni^{2+} ions in a unit cell on the γc planes. A and B refer to the corners of the square base shown in Fig. 5.
7. The relative positions of the two types of Mg^{2+} ions in CeMgN. The distances are in nanometers, as determined by Zalkin et.al. (1963).
8. Projection of $Zn(BrO_3)_2 \cdot 6H_2O$ on the (001) plane. The numbers within the circles are the coordinates of the atoms in units of c_o along the c axis, as determined by Yü and Beevers (1935).
9. Projection of the magnetic axes on the (111) plane of $Zn(BrO_3)_2 \cdot 6H_2O$ and its side view.
10. Schematic energy diagrams of $3d^3$ and $3d^8$ ions in an octahedral plus axial crystal field. (a) trigonal and (b) tetragonal symmetry. When B_2^o and B_4^o are positive, the axial distortion is a compression, while negative B_2^o and B_4^o correspond to an elongation. The numbers in parentheses represent the orbital degeneracies.
11. The Zeeman energy levels of the Ni^{2+} spin triplets with a positive D. (a) H along the z axis, (b) H along the x axis. We assume $D/h\nu \sim 2/3$. The arrows represent three transitions and their relative intensities. The broken arrows indicate the forbidden transitions.

12. The line positions of the Ni^{2+} EPR spectrum in the γc plane of $ZnSeO_4.6H_2O$. The circles are the experimental positions, the crosses are the average positions of ions 2 and 4, and the solid curves are the theoretical values.

13. Plot of the line positions vs. $\sec\theta$ of Eq.(19) for Ni^{2+} : $ZnSeO_4.6H_2O$. The circles represent the observed field positions and the solid curves are calculated.

14. Observed and calculated field positions of Ni^{2+} : $ZnSeO_4.6H_2O$ in the ac plane.

15. Plot of the observed and calculated field positions of Ni^{2+} in $ZnSeO_4.6H_2O$ in the ab plane. The circles are as usual experimental and the dotted curves are computer drawn with the parameters given in the text.

16. Three transitions of the Ni^{2+} ion at the site 1 of LMN. The circles are the observed positions with H in the xz plane and the solid curves are theoretical. The angle α is measured from the [111] direction.

17. The Zeeman energy levels of Ni^{2+} in LMN, when H is oriented at an angle of 52.9° from the [111] axis in the xz plane and at the frequency of 9.2 GHz. The transitions 2 and 3 occur at the same field. A transition of two energy quanta (DQ line) may take place at the same field as 2 and 3.

18. The assymmetric line shape of transition 2 of the Ni^{2+} ion, type 1, in LMN, when H is along the z axis. Both presentations, (a) absorption spectrum and (b) first derivative spectrum, show a sharp cut off in the lower field side.

19. Computed powder spectrum of a spin triplet in an axial crystal field. (a) absorption and (b) first derivative spectra. The notations x_1, x_2 and x_3 mean the line positions of the three transitions for $H \parallel x$, z_2 and z_3 stand for the positions of the two transitions for $H \parallel z$, and DQ corresponds to the double quantum transition.

20. Observed powder spectrum of Ni^{2+}: LMN at -160°C. (a) absorption (b) derivative. From left to right we see x_1, x_3, IN, x_2, and z_3.

21. The derivative spectrum of Ni^{2+}: $Zn(BrO_3)_2 \cdot 6H_2O$ at 1.7°K, showing four Ni^{2+} ions of a unit cell. The side bands of each ion result from the electron dipole-dipole interaction or from the exchange interaction of adjacent Ni^{2+} ions. The magnetic field is oriented at an angle of 22° from the [111] direction in the yz plane.

22. The angular dependence of the Ni^{2+} absorption lines in the (111) plane of $Zn(BrO_3)_2 \cdot 6H_2O$. Ion 4 is nearly isotropic in this plane, while ions 1, 2, and 3 show 60° periodicity. The circles are the experimental points and the dotted curves are calculated from $g_{\parallel} = g_{\perp} = 2.235$, $D = -1.79\ cm^{-1}$ and $E = 0.001\ cm^{-1}$.

23. The angular dependence of the Ni^{2+} ions in $Zn(BrO_3)_2 \cdot 6H_2O$ in the yz plane.

24. The schematic energy diagram of $3d^9$ ion in a tetragonal elongation of an octahedral crystal field. The numbers in parentheses mean the orbital degeneracies.

25. The derivative spectra of Cu^{2+}: $ZnSeO_4 \cdot 6H_2O$. (a) H at $\alpha = 20°$ in the γc plane, (b) H along the c axis, four sets of four hf lines totally superimposed.

26. The observed positions of $m_I = -3/2$ lines in the γc plane of Cu^{2+}: $ZnSeO_4.6H_2O$.

27. (a) Plot of g^2 vs. n^2 for the γc plane (o) and for the ac plane (x) of Cu^{2+}: $ZnSeO_4.6H_2O$ at $\Phi \cong 43.3°$. A straight line is drawn from the least-squares analysis.

    (b) Same as (a) except at $\Phi = 40°$. A demonstration of the accuracy involved in the plot of g^2 vs. n^2.

28. Plot of g^4A^2 vs. n^2 for the γc and ac planes of Cu^{2+}: $ZnSeO_4.6H_2O$.

29. The angular dependence of (a) g and of (b) A values in the γc plane of Cu^{2+}: $ZnSeO_4.6H_2O$. The average values of ions 2 and 4 are taken.

30. The same as Fig. 29(a). New direction cosines are used to calculate the g values of ions 2 and 4.

31. The same as Fig. 29(b). The splittings of ions 2 and 4 are taken into account. The dotted curves are calculated from $g_{\parallel} = 2.4295$, $g_{\perp} = 2.0965$, $A_{\parallel} = 115.6$ G, $A_{\perp} = 9.5$ G, $\Phi = 43.2°$ and $\beta = 4.1°$.

32. The theoretical g values of Cu^{2+}: $ZnSeO_4.6H_2O$ in the ab plane, calculated from the parameters of Fig. 31. The circles and the numerical balues represent the observed g values.

33. The predicted and the observed g values of the Cu^{2+}: $ZnSeO_4.6H_2O$ in the ac plane. The averaged g values of ions 1 and 4 and of ions 2 and 3 are drawn in as circles.

34. Plot of A_i' vs. f_i for the three Cu^{2+} systems in $ZnSeO_4.6H_2O$, LMN, and $Zn(BrO_3)_2.6H_2O$. For explanation see the text.

35. The angular dependence of the g factors of Co^{2+}: $ZnSeO_4 \cdot 6H_2O$ in the γc plane.

36. The angular dependence of the hf constants of Co^{2+}: $ZnSeO_4 \cdot 6H_2O$ in the γc plane. The parameters used in the calculation are $g_{\parallel} = 5.975$, $g_{\perp} = 3.45$, $A_{\parallel} = 77.0$ G, $A_{\perp} = 20$ G, $\phi = 58.5°$ and $\beta = 4.5°$.

37. Plot of $g_{\perp}$ vs. $g_{\parallel}$ as a function of α and p.

	A	B	C	D	E
α	-1.0	-1.5	-1.0	-1.45	-1.5
p	1.0	1.0	0.7	0.7	0.5

The experimental points of the three Co^{2+} systems are found to lie in the region of the weak-field limit, $\alpha = -1.5$.

38. Plot of g^2 vs. n^2 for the three planes of Co^{2+}: $NiSeO_4 \cdot 6H_2O$. The points of different planes fall on different straight lines.

39. Plot of g^4A^2 vs. n^2 of Co^{2+}: $NiSeO_4 \cdot 6H_2O$ for the γc and ab planes.

40. The angular dependence of the g values of Co^{2+} in the γc plane of $NiSeO_4 \cdot 6H_2O$. The dotted curves are calculated from $g_{\parallel} = 6.318$, $g_{\perp} = 3.38$ and $\phi = 61.5°$.

41. The angular dependence of the g values of Co^{2+} in the ac plane of $NiSeO_4 \cdot 6H_2O$. The calculated curves are drawn from a set of parameters different from those of Fig. 40.

42. An illustration of a false assignment of axial g factors from the data of only one plane. The angle α is measured from the a axis, whereas the direction cosines use the α measured from the c axis. The ac plane data of spherical Co^{2+}: α-$NiSO_4 \cdot 6H_2O$ are used.

43. Plot of g^2 vs. n^2 for the ab and ac planes of Co^{2+}: α-$NiSO_4 \cdot 6H_2O$.

44. Observed and calculated g values of Co^{2+}: α-$NiSO_4 \cdot 6H_2O$ in the ac plane. The parameters used are $g_{/\!/} = 6.34$, $g_{\perp} = 3.40$, and $\phi = 60°$.

45. The angular dependence of the apparent g values in the ab plane of Cu^{2+}: α-$NiSO_4 \cdot 6H_2O$. The crosses are the observed values and the dotted curves are calculated from $g_{/\!/} = 2.905$, $g_{\perp} = 2.486$ and $\phi = 70°$.

46. The observed line positions of the Ni^{2+} spectra in the γc plane of α-$NiSO_4 \cdot 6H_2O$. The circles are those transitions between the excited states, "high-field" transition, and the crosses are the "coupled-pair" transition.

47. The same as Fig. 46 in the ab plane. The dots are the second kind of the "coupled-pair" transition.

48. A model of the "coupled-pair" transition. Two non-equivalent ions take part in the simultaneous transitions, the net energy of which is equal to the resonance energy. Here the magnetic field is oriented along the x axis of ion 2. Ion 1 undergoes a downward transition from W(-1) to W(0), while ion 2 undergoes an upward transition from W(0') to W(-1'). The shaded arrow represents the difference in the two transition energies.

49. Observed (dots) and calculated (solid and broken curves) field positions of the "coupled-pair" transitions of Eq. (66) in the γc plane of α-$NiSO_4 \cdot 6H_2O$. The 1-2 pair and the 2-3 pair cross at the γ axis.

50. The field positions of the coupled-pair transitions in the ab plane of α-$NiSO_4 \cdot 6H_2O$. The circles are the experimental positions, while the solid curve is calculated from Eq. (66) and the broken curve is from Eq. (67). Qualitatively the coupled-pair transitions in the ab

plane may be considered as the superposition of the solid and the broken curves.

51. The angular dependence of the g factors of Cu^{2+} in the (111) plane of LMN at 1.7°K.

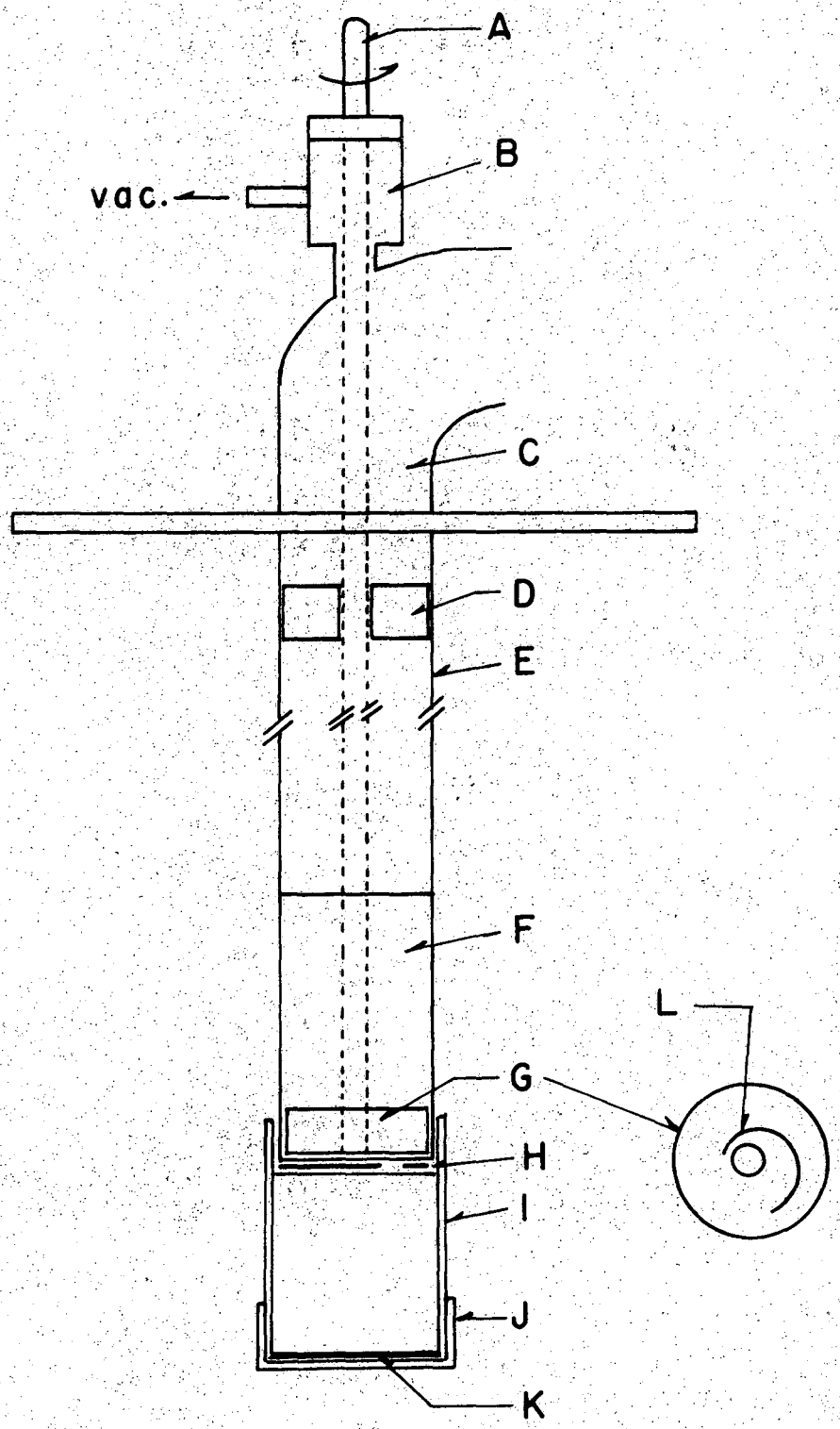

XBL 7012-7310

Fig. 1

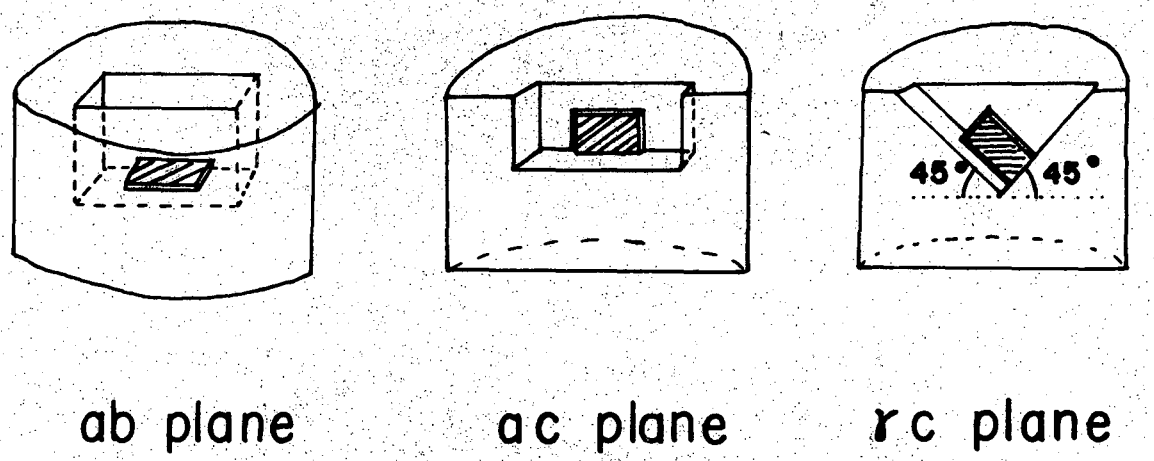

Fig. 2

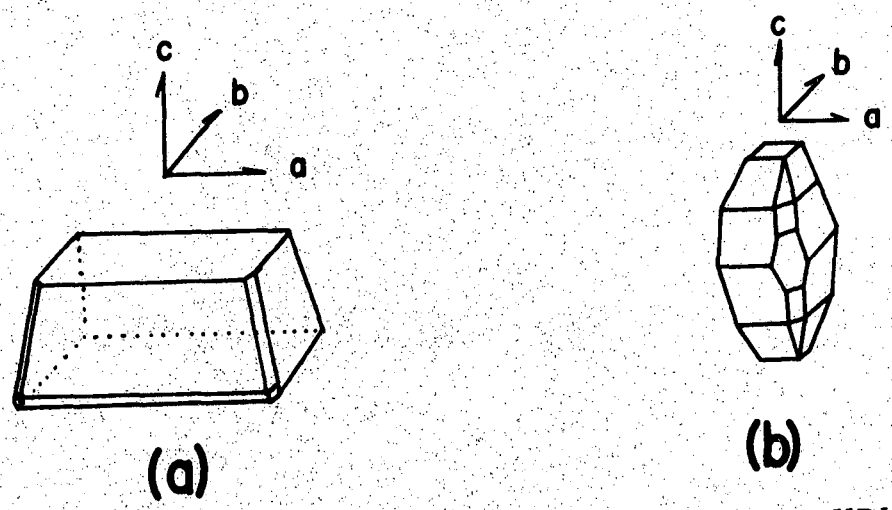

XBL 7012-7294

Fig. 3

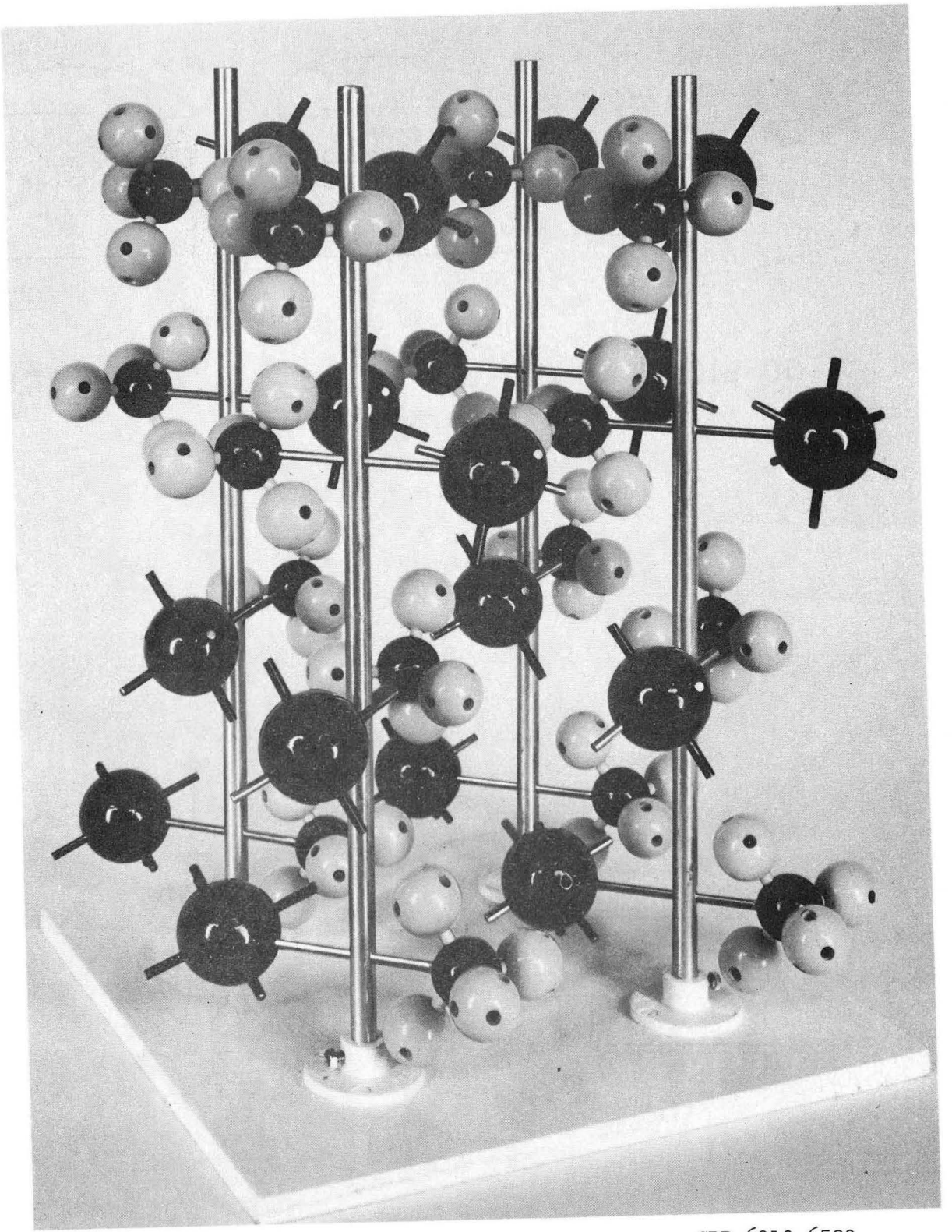

CBB 6910-6530

Fig. 4

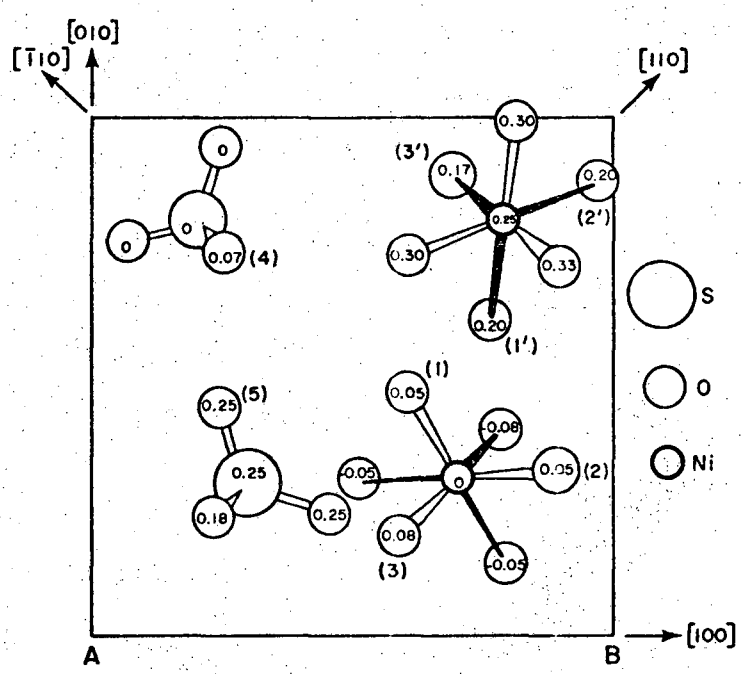

Fig. 5

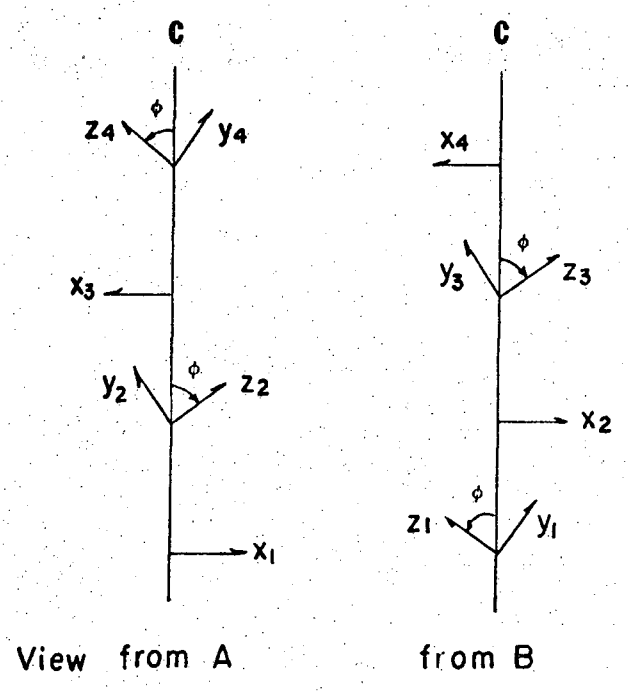

XBL 7012-7309

Fig. 6

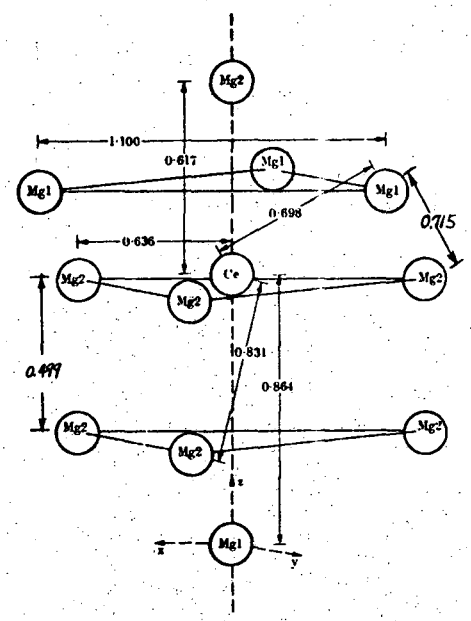

Fig. 7

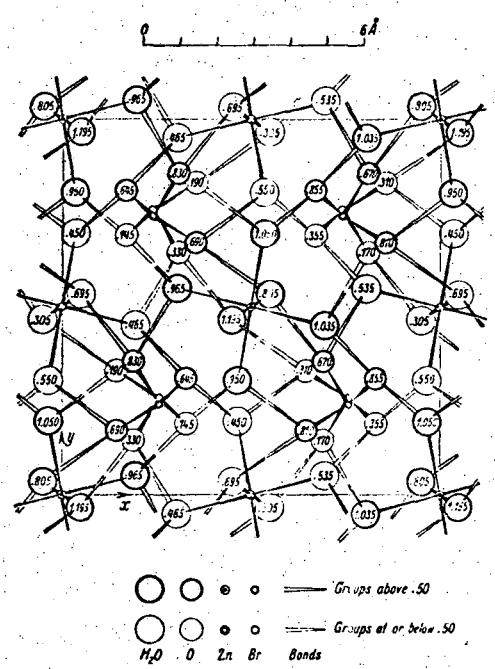

XBL 7012-7291

Fig. 8

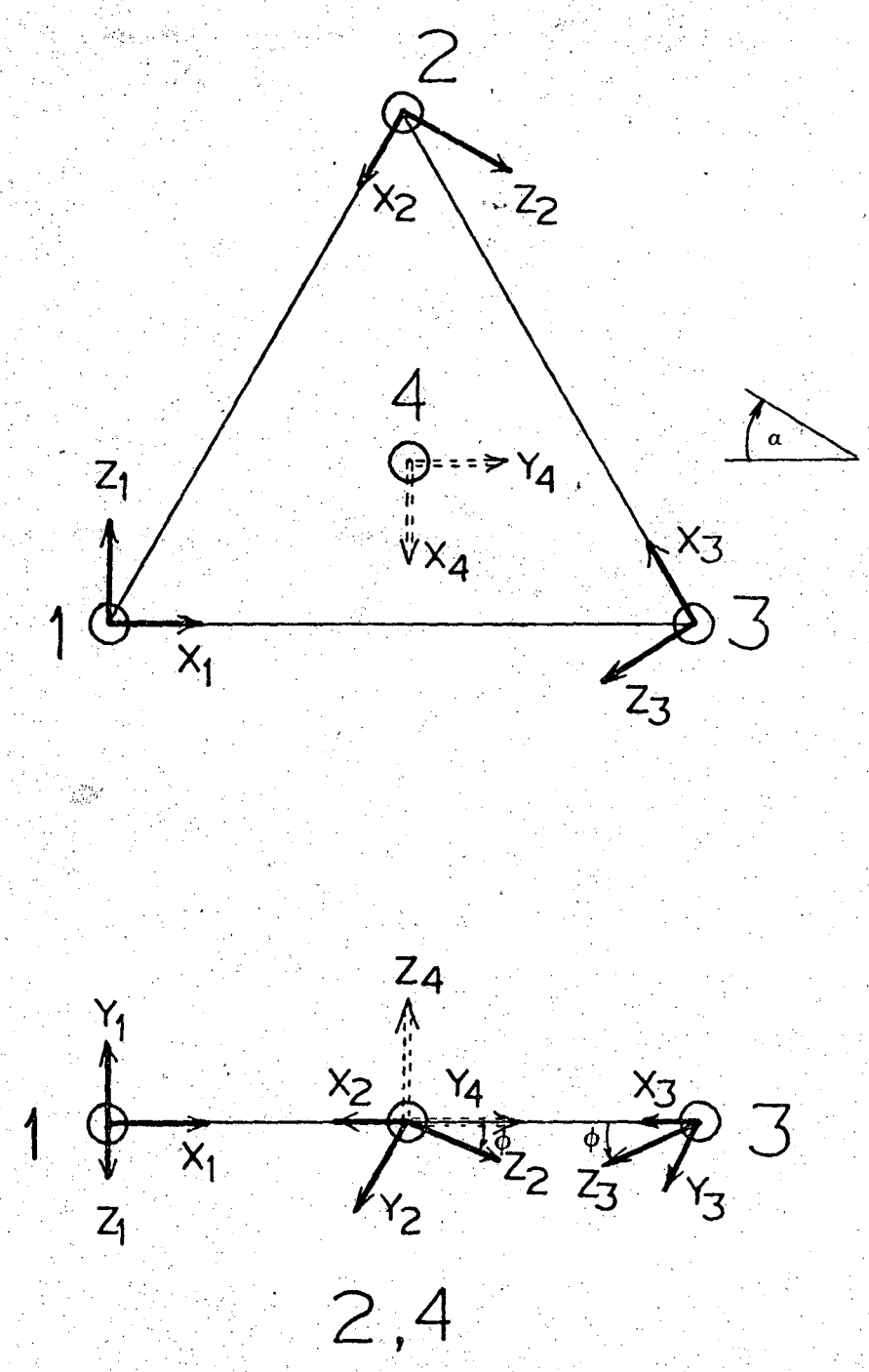

XBL 7012-7296

Fig. 9

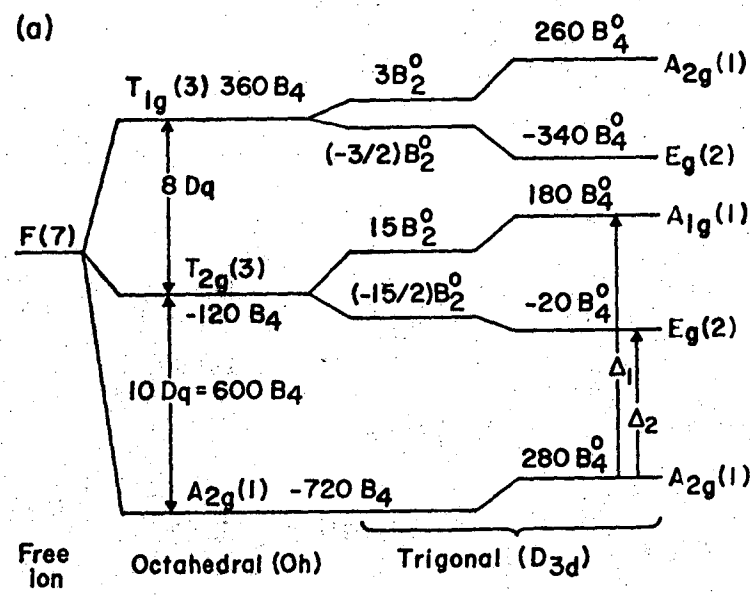

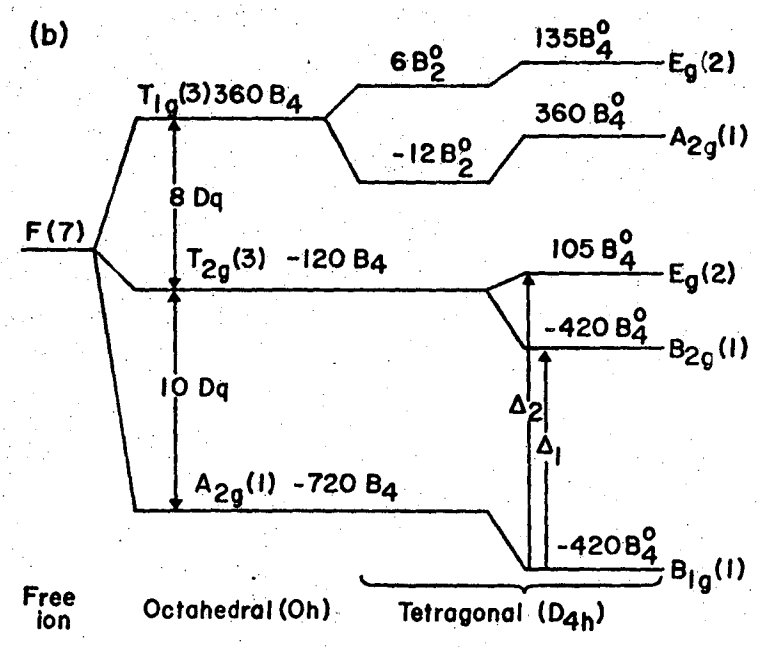

XBL 7012-7308

Fig. 10

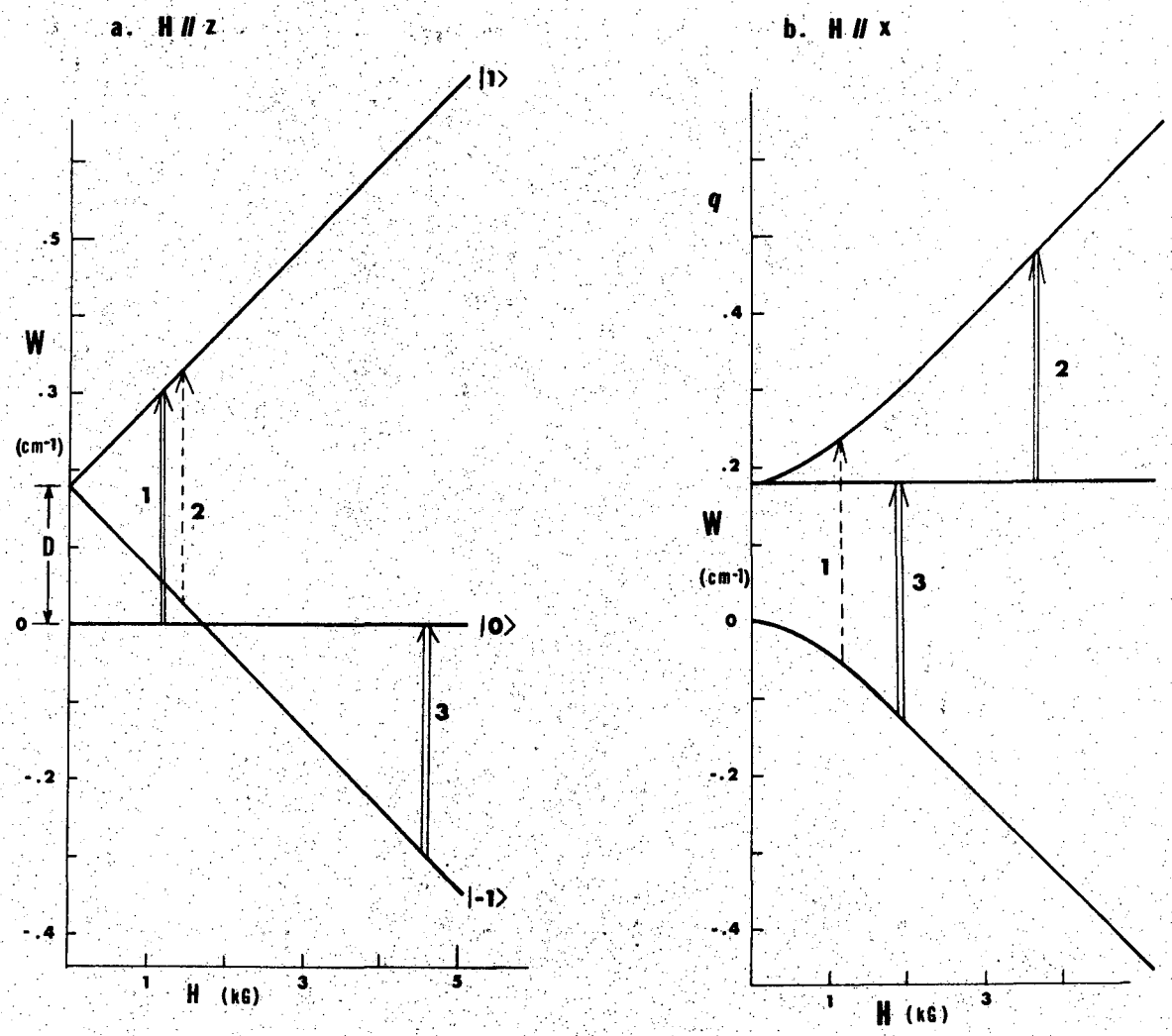

XBL 7012-7315

Fig. 11

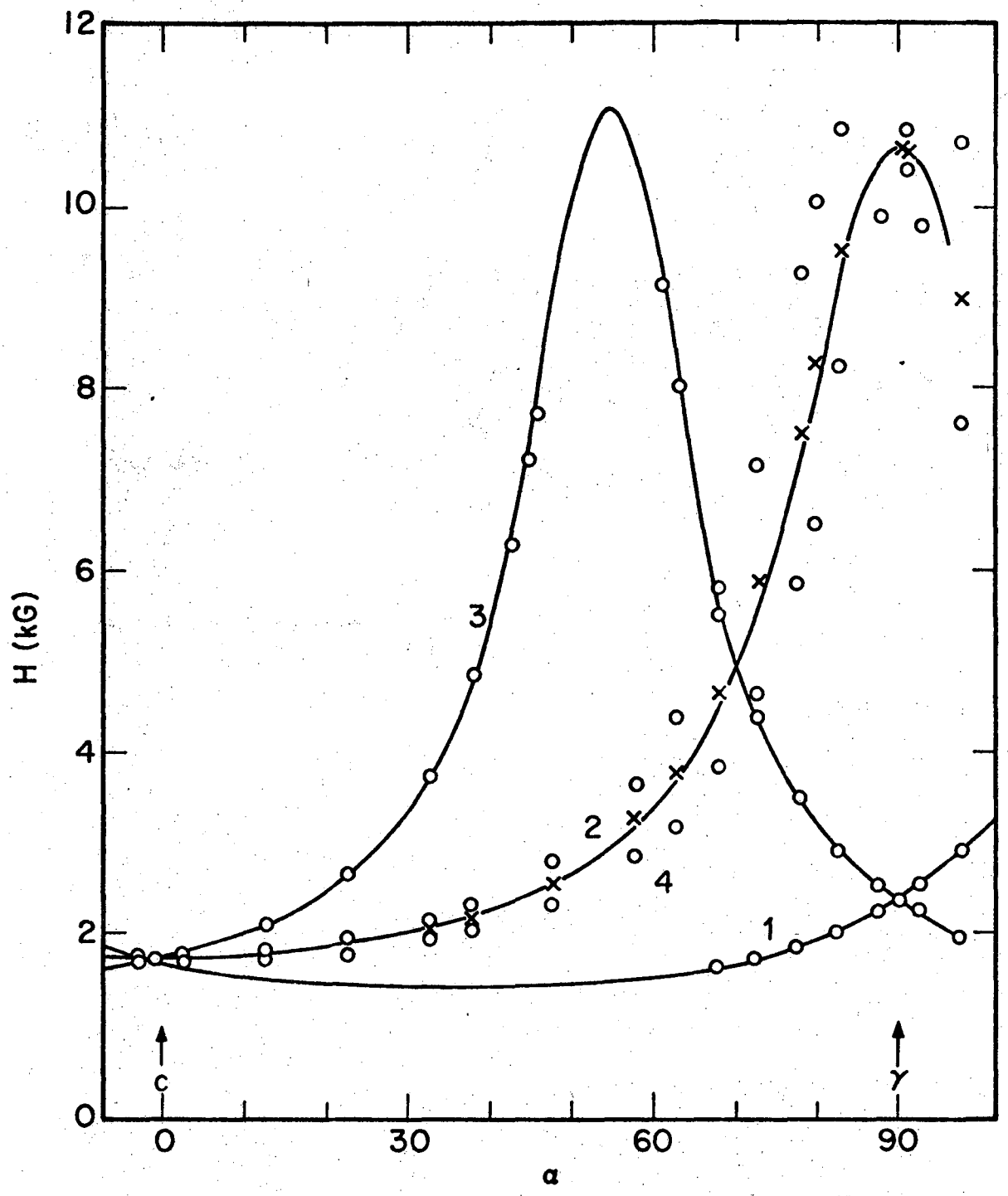

XBL 7012-7313

Fig. 12

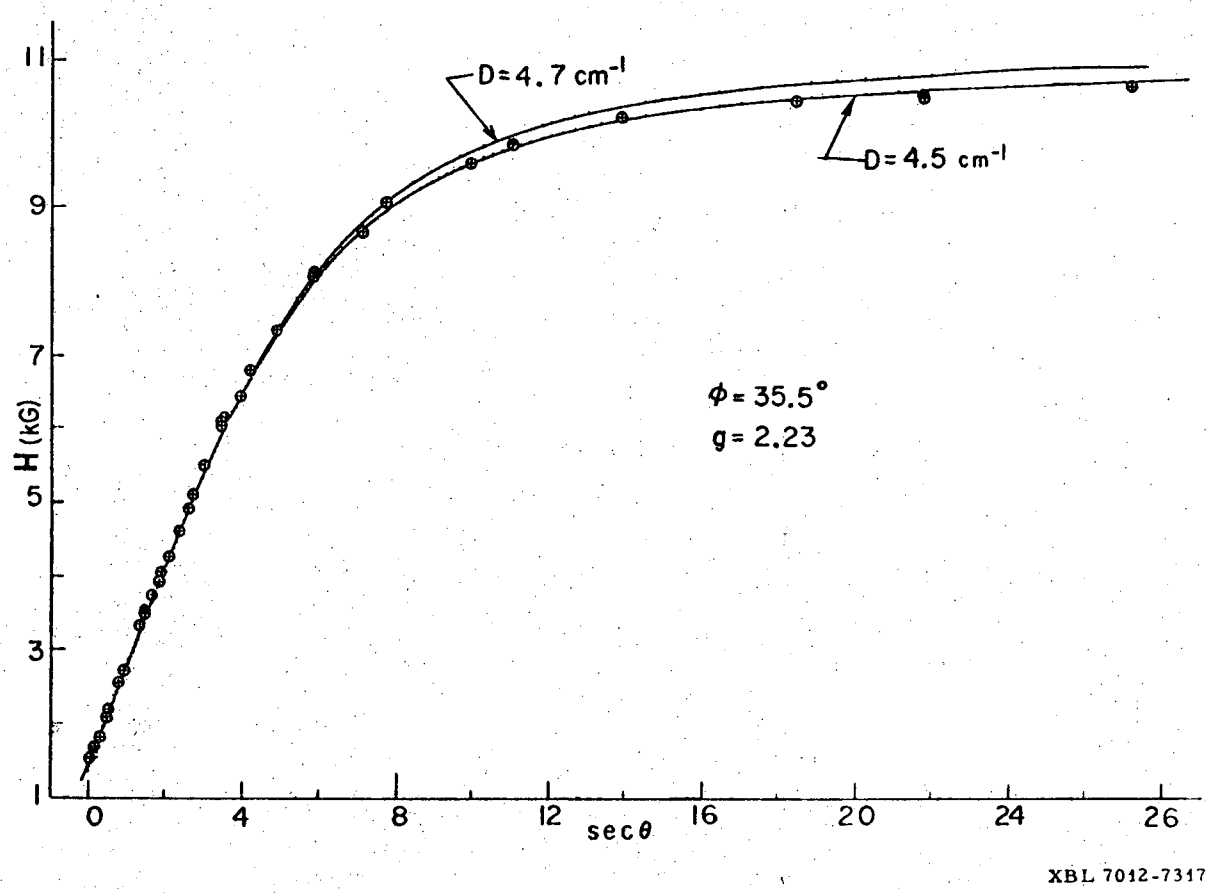
D=4.7 cm⁻¹
D=4.5 cm⁻¹
Φ= 35.5°
g= 2.23
H (kG)
sec θ
11
9
7
5
3
1
0
4
8
12
16
20
24
26
XBL 7012-7317

Fig. 13

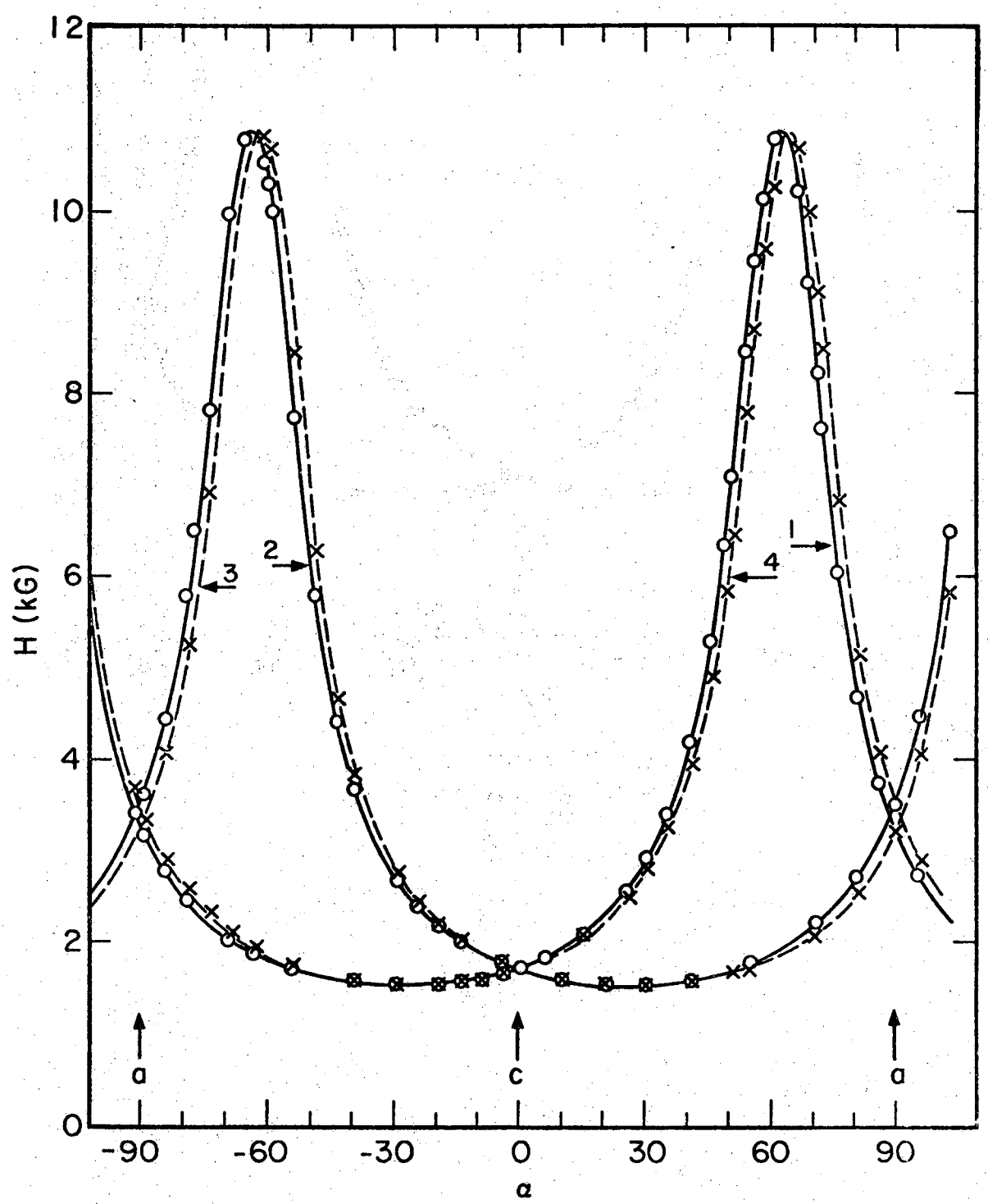

XBL 7012-7303

Fig. 14

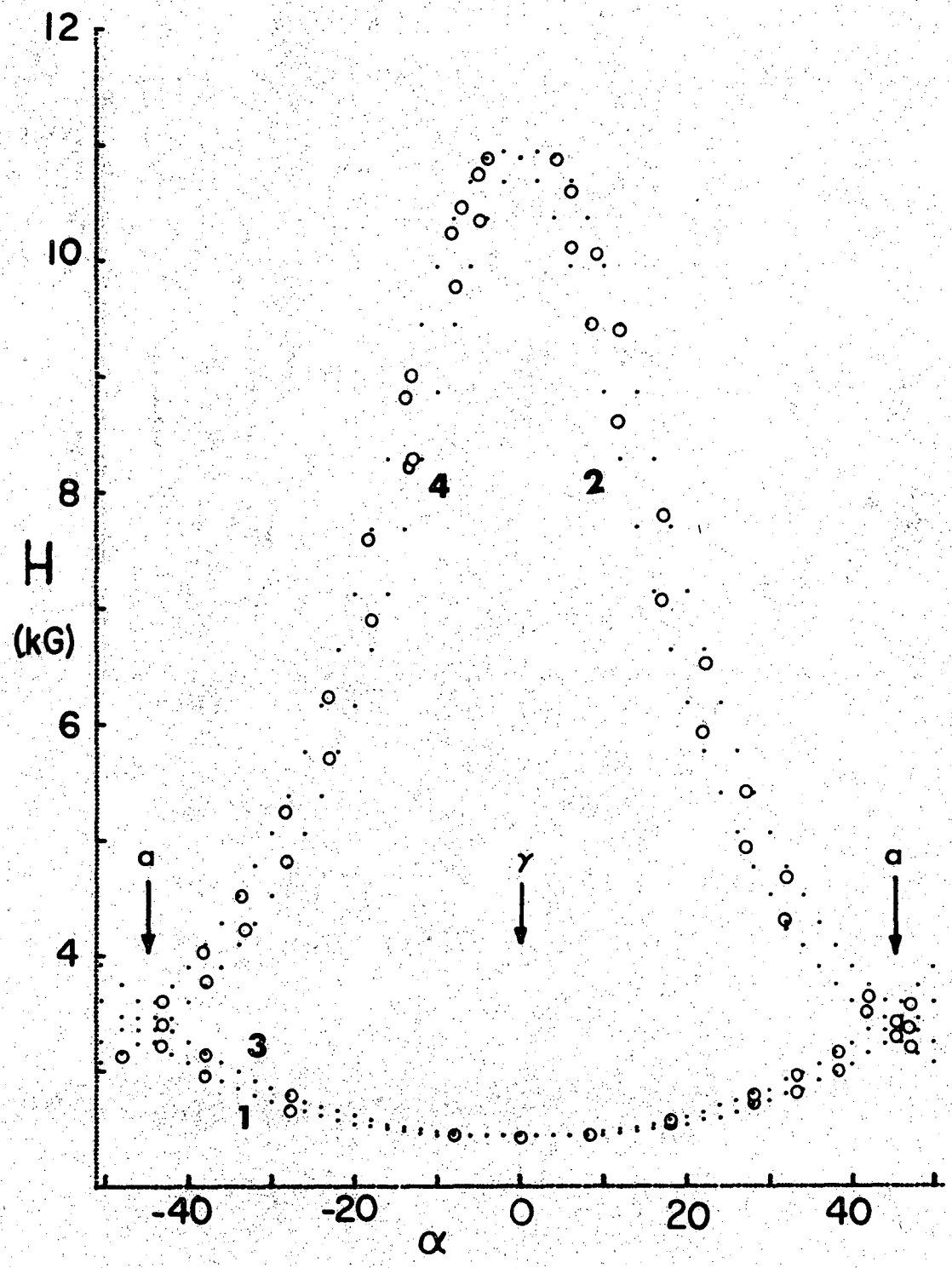

XBL 7012-7292

Fig. 15

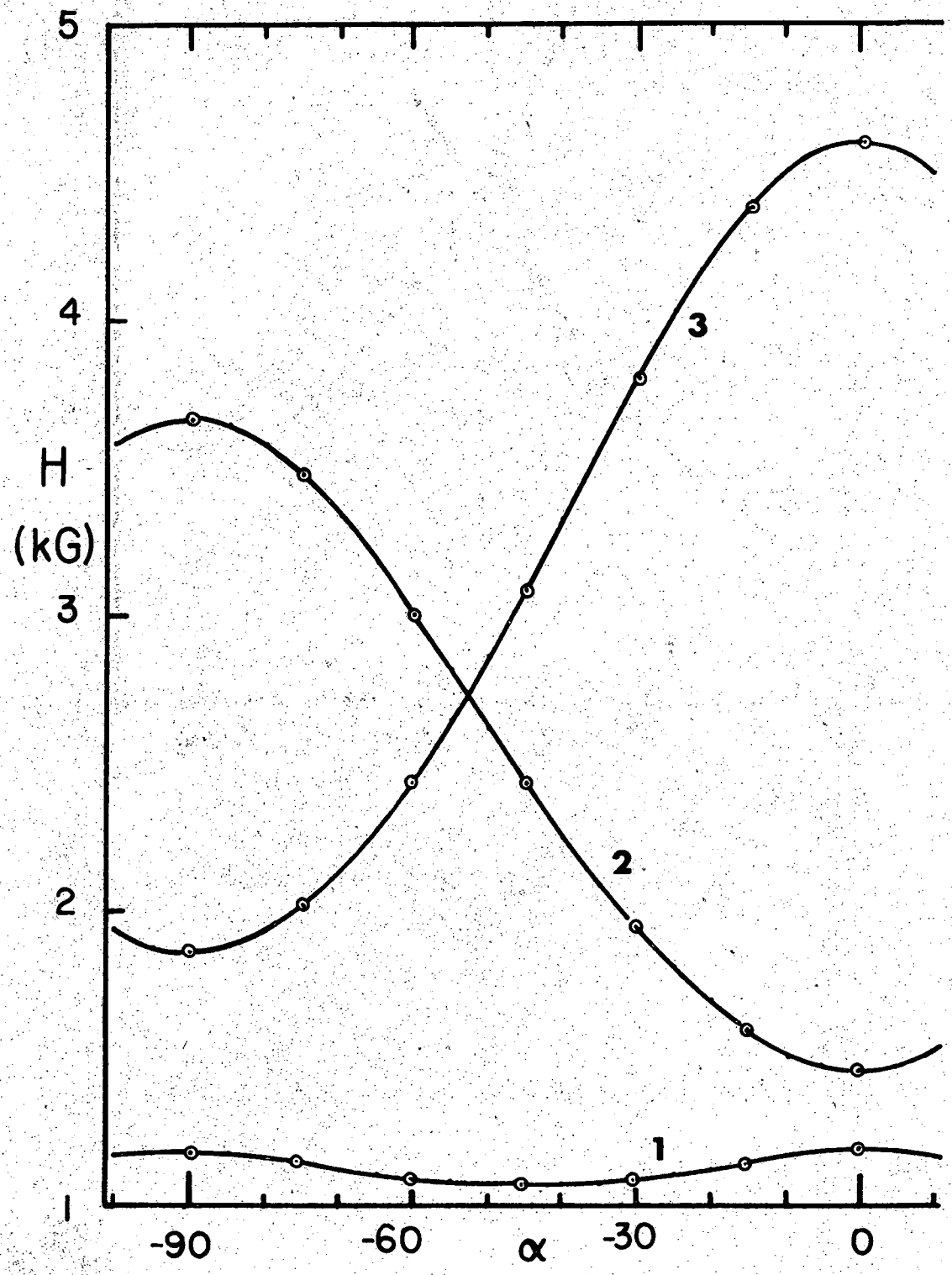

XBL 7012-7297

Fig. 16

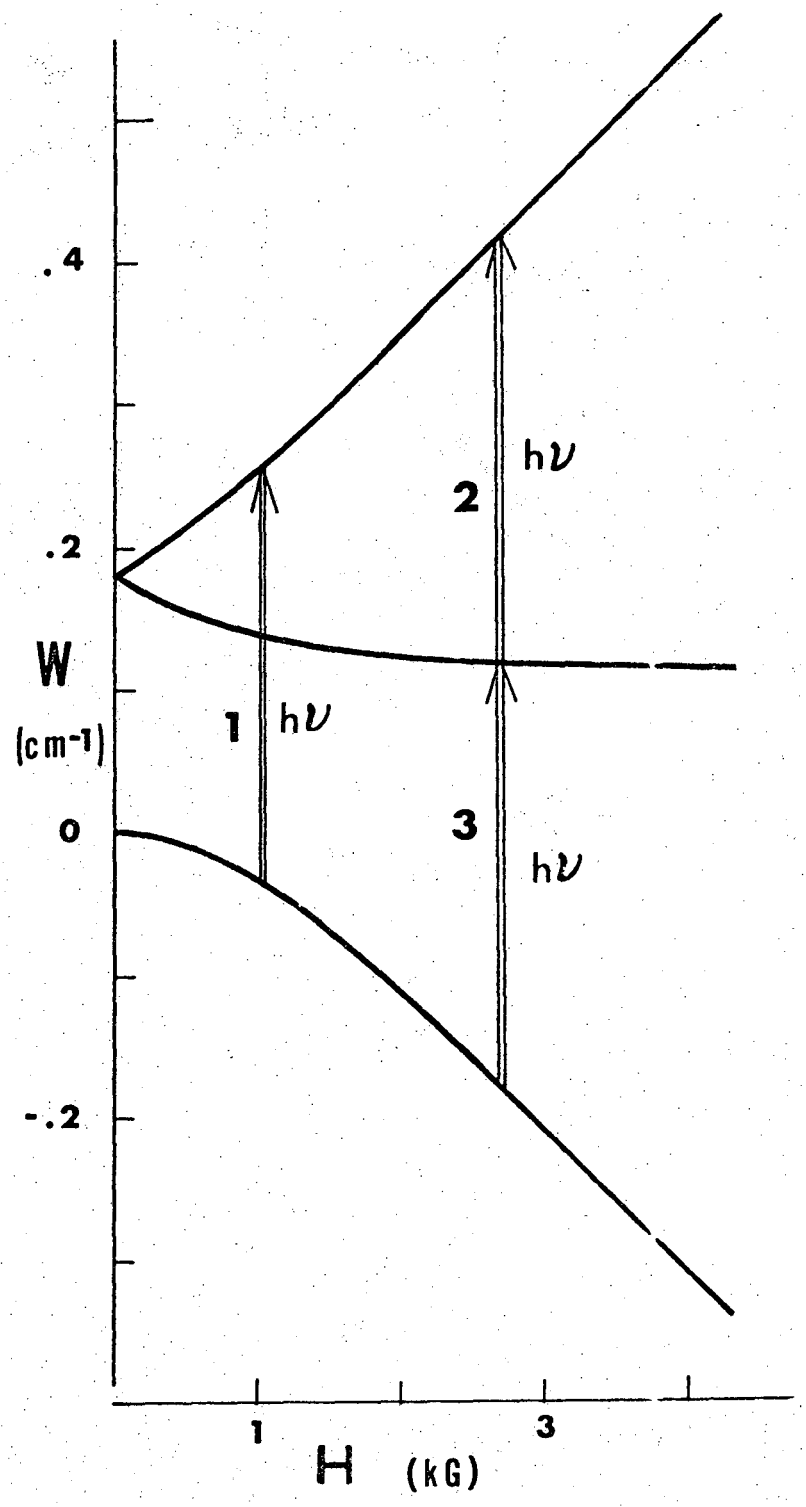

XBL 012-7302

Fig. 17

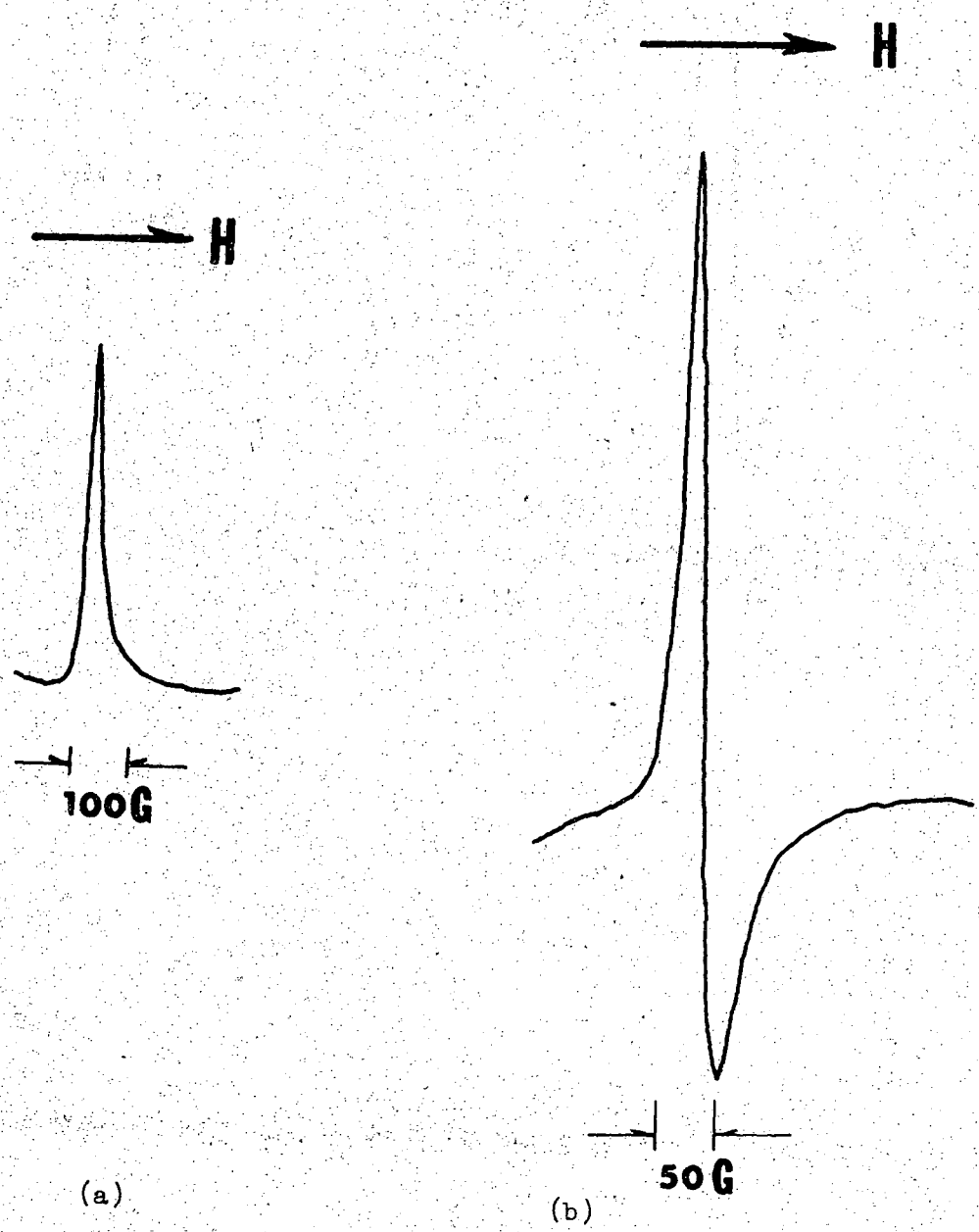

XBL 7012-7295

Fig. 18

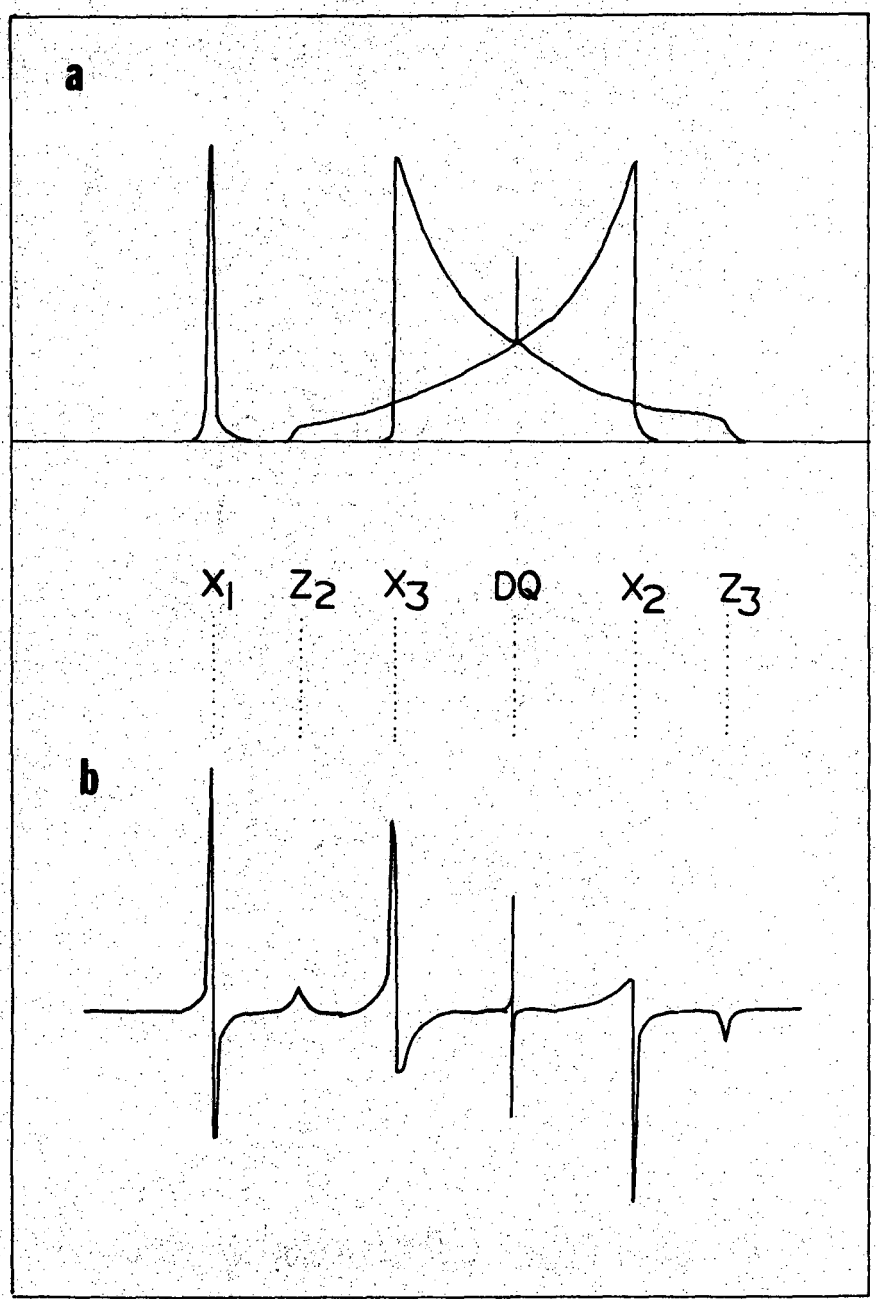

XBL 7012-7312

Fig. 19

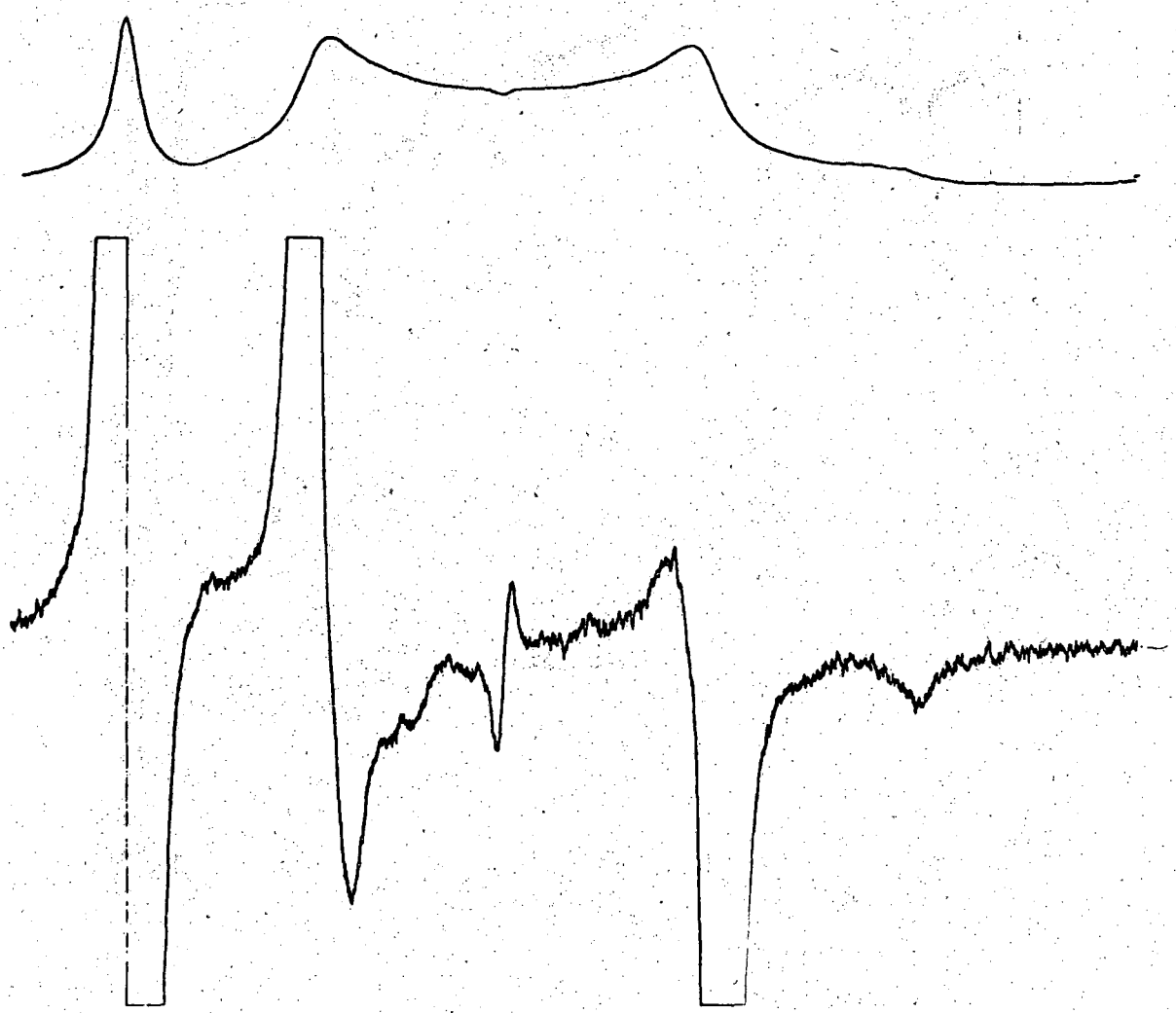

XBL 7012-7319

Fig. 20

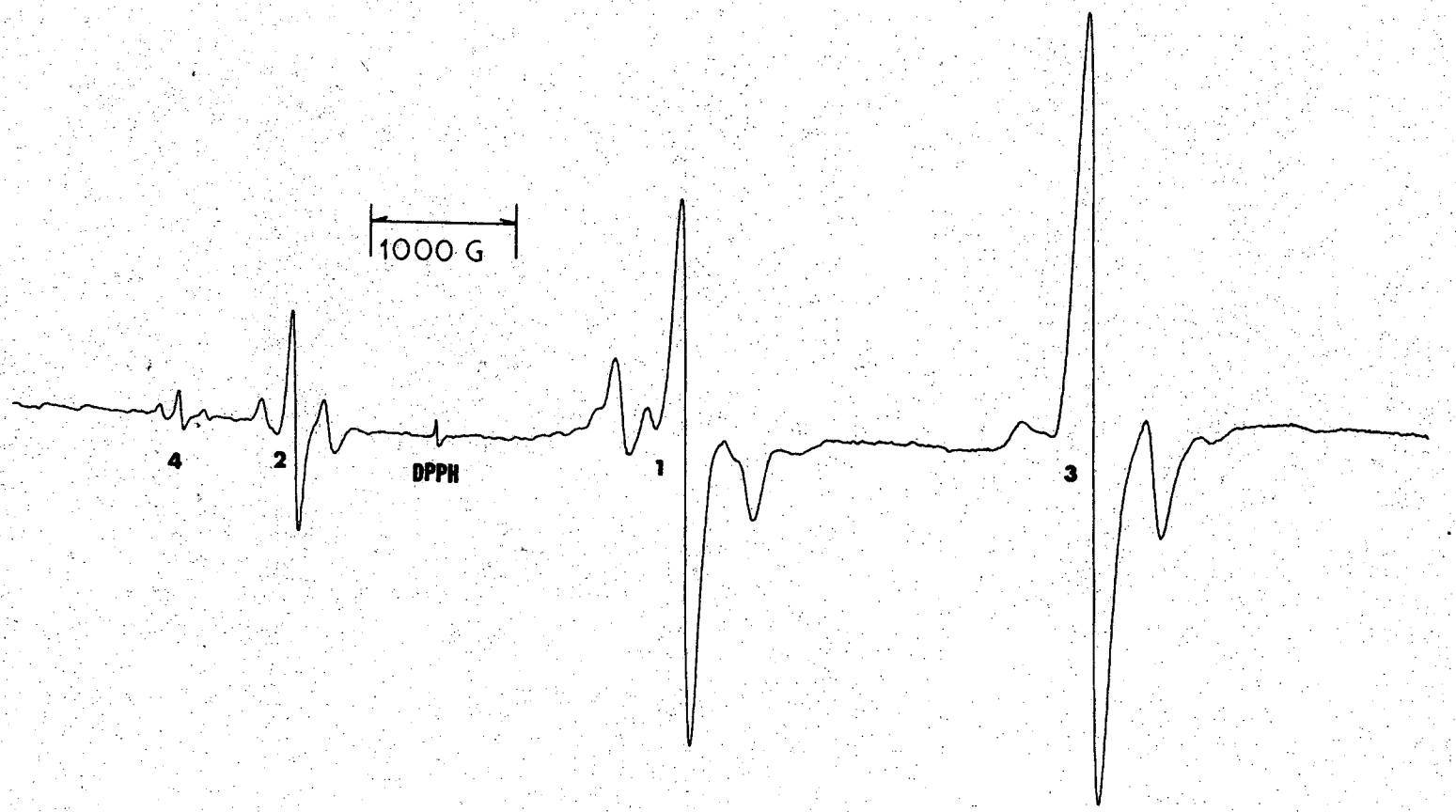

XBL 7012-7314

Fig. 21

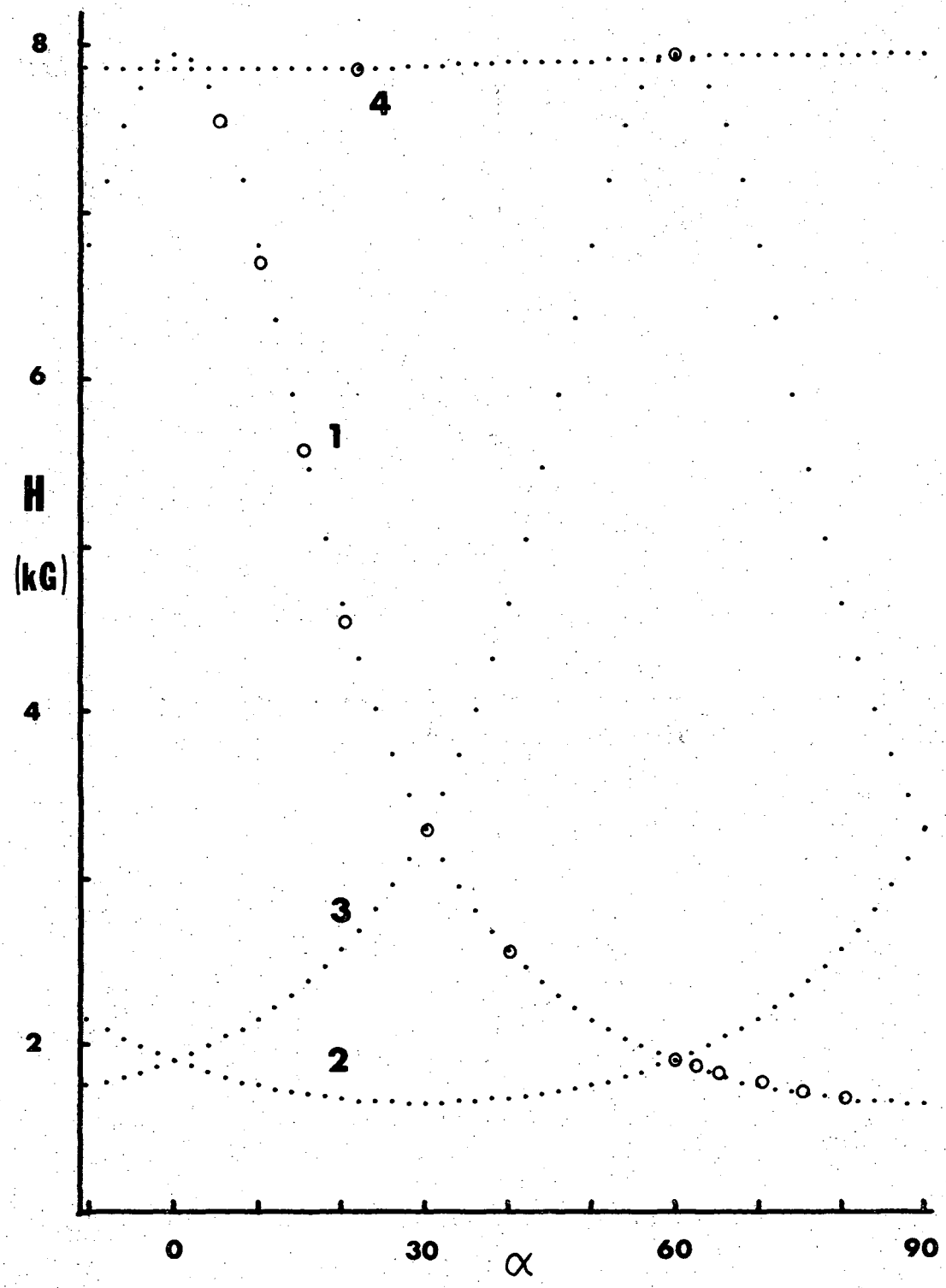

XBL 7012-7299

Fig. 22

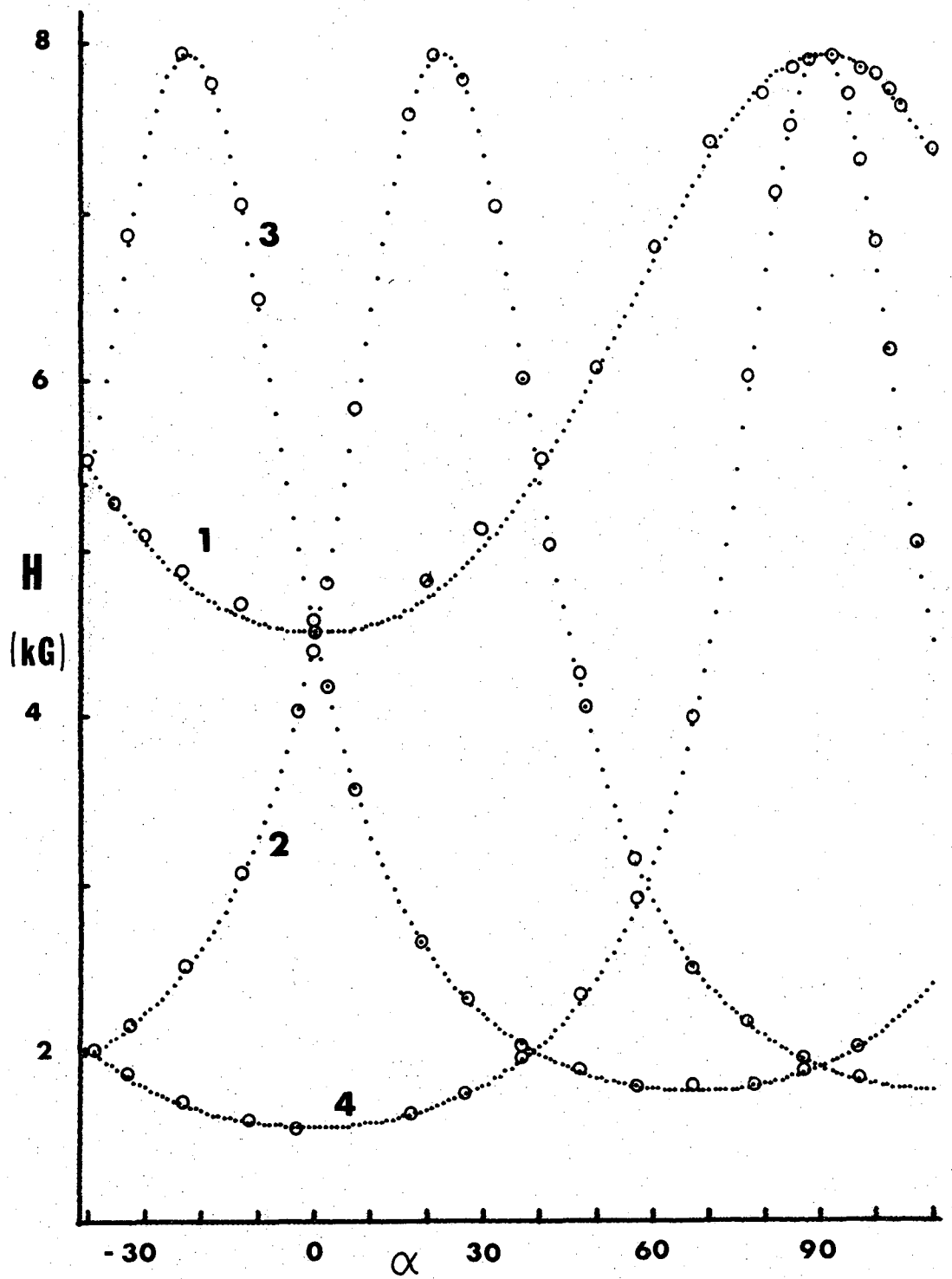

XBL 7012-7301

Fig. 23

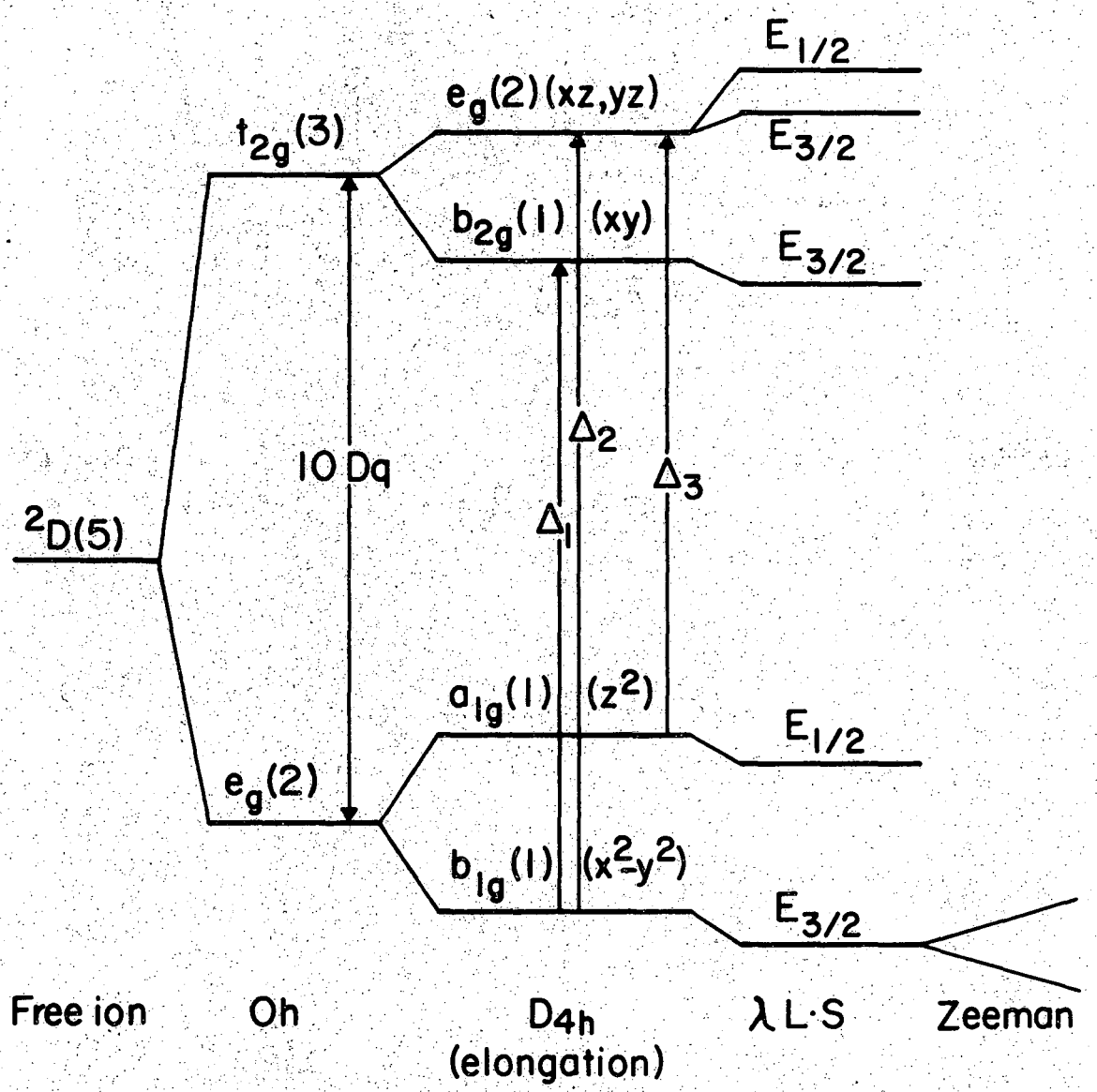

XBL 7012-7311

Fig. 24

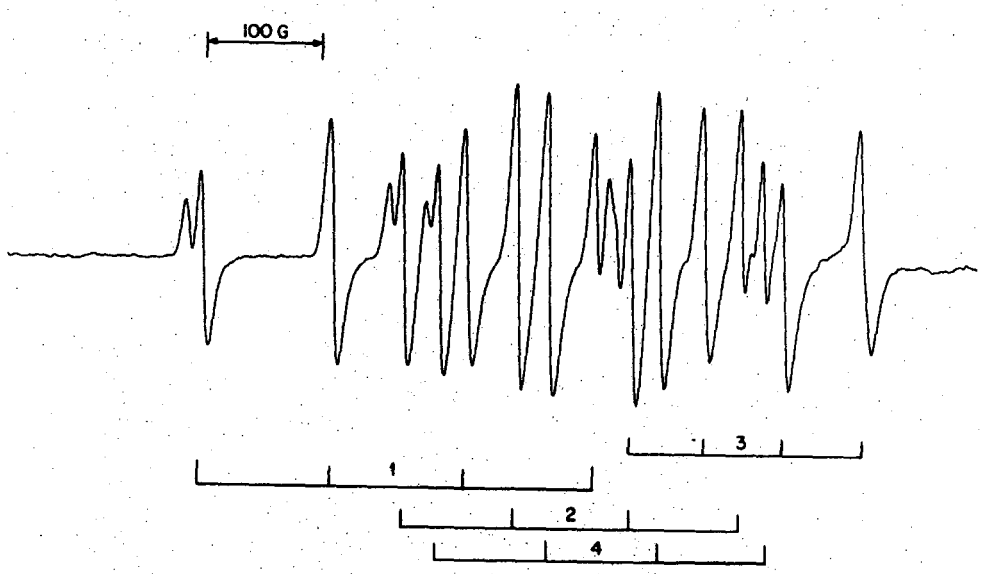

(a)

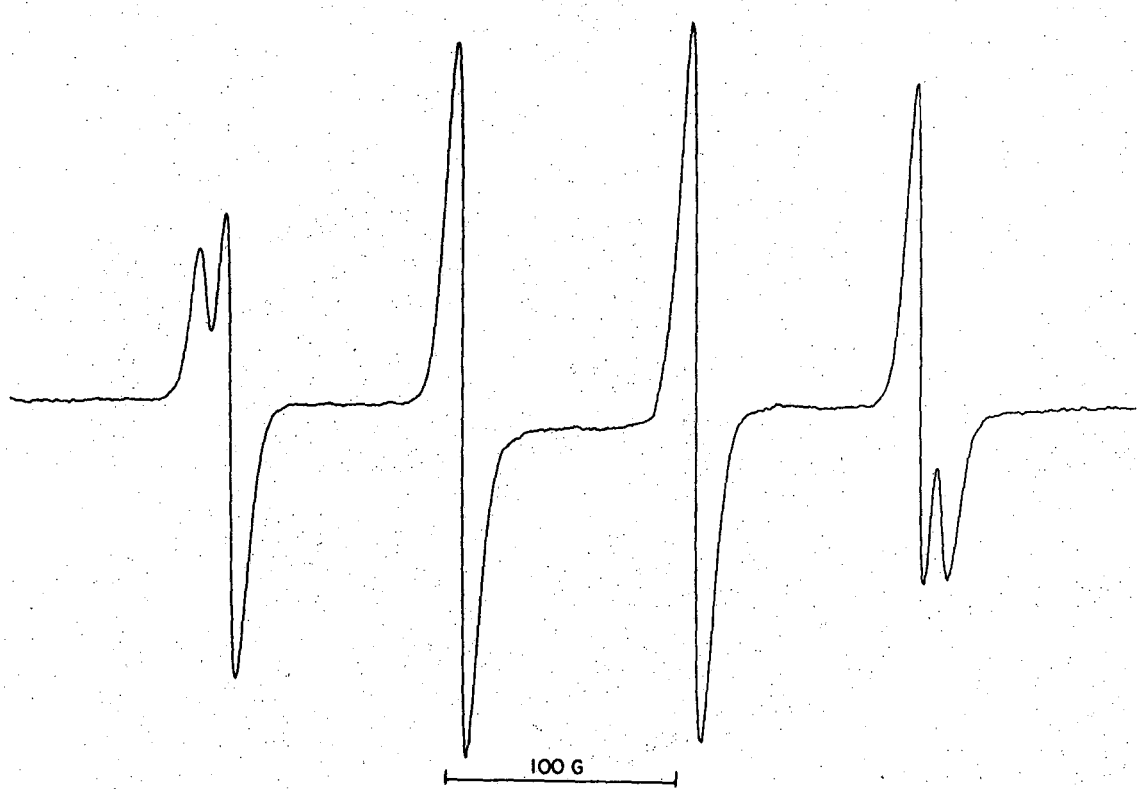

(b)

XBL 7012-7316

Fig. 25

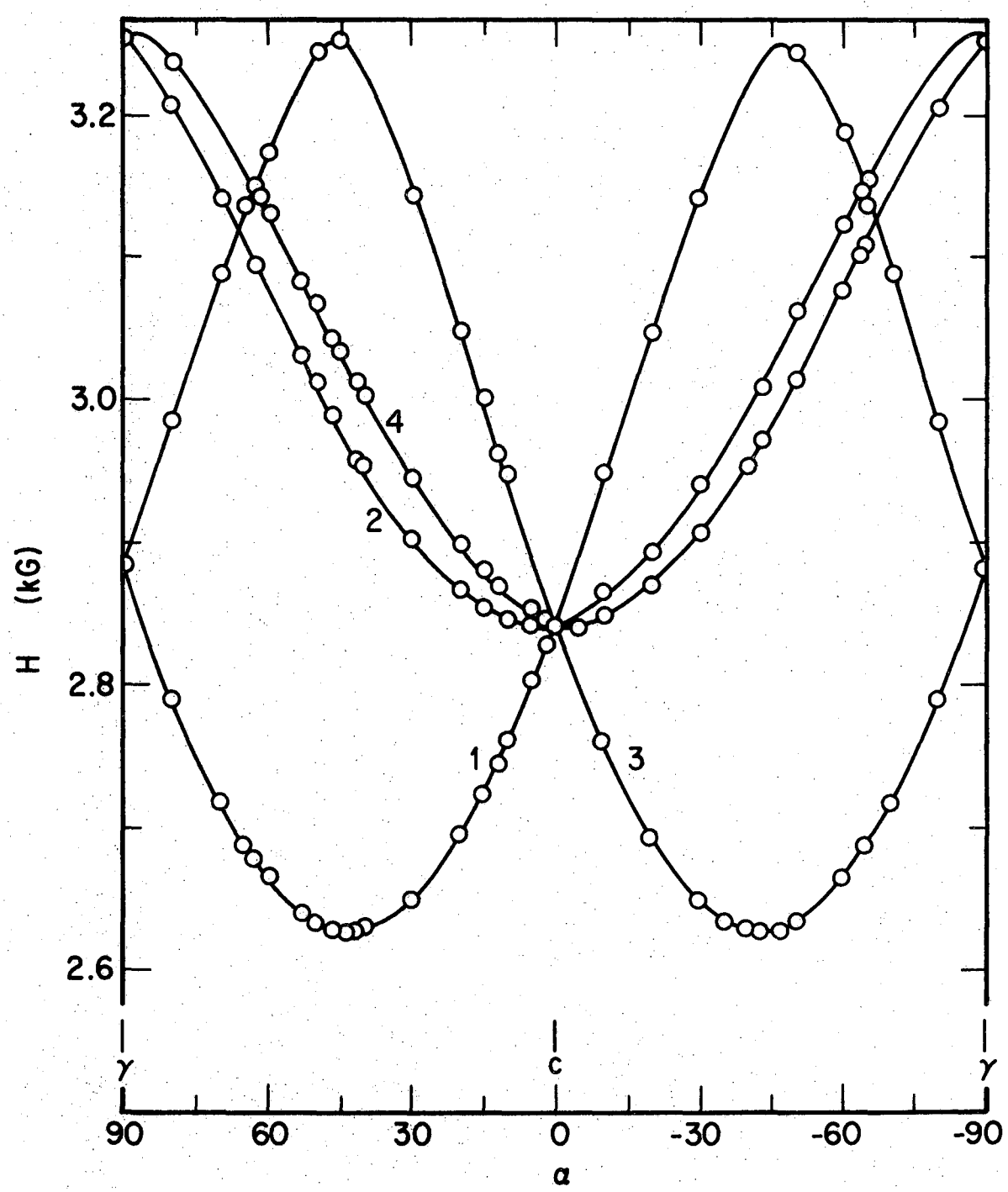

XBL 7012-7298

Fig. 26

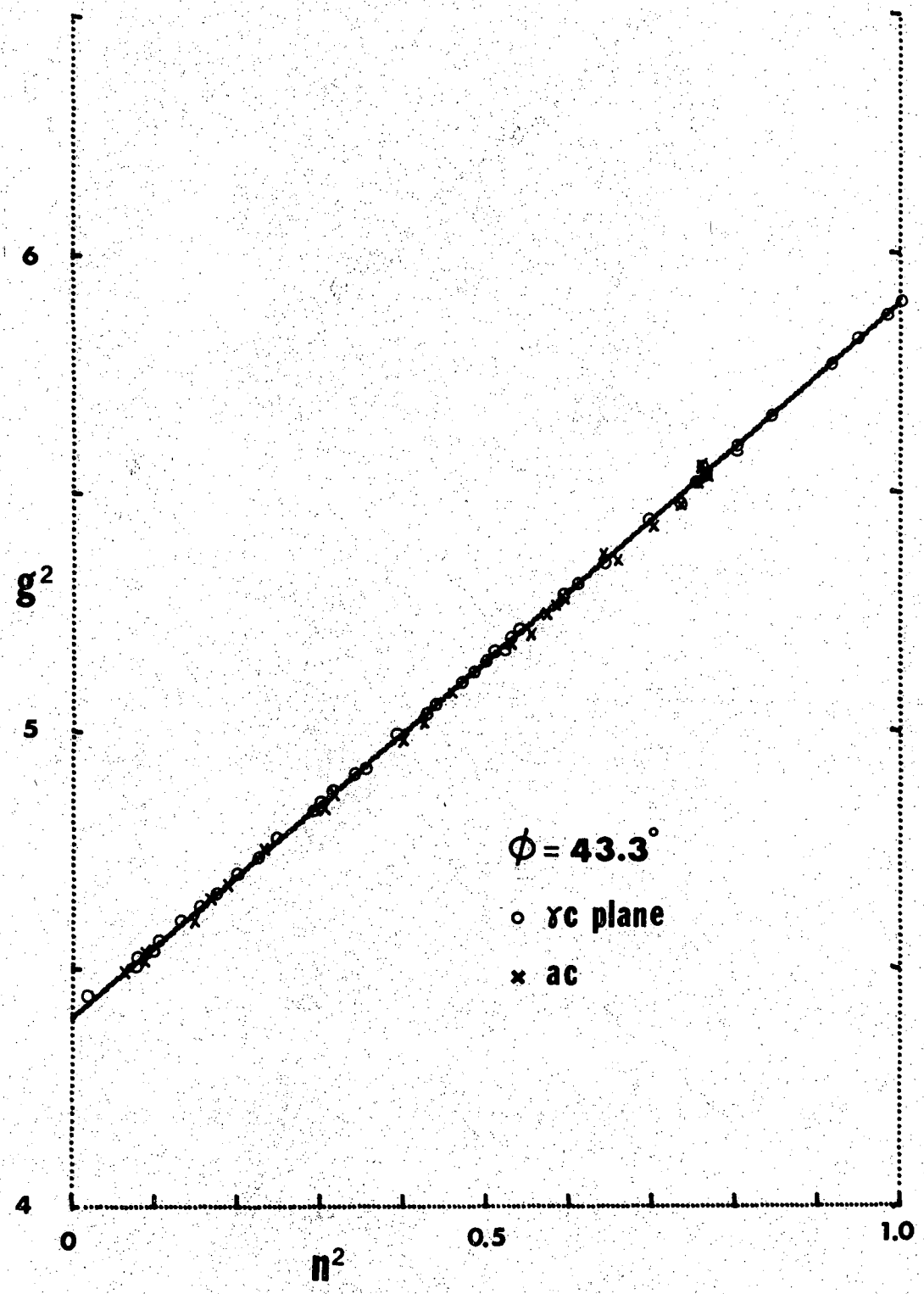

XBL 7012-7318

Fig. 27 a

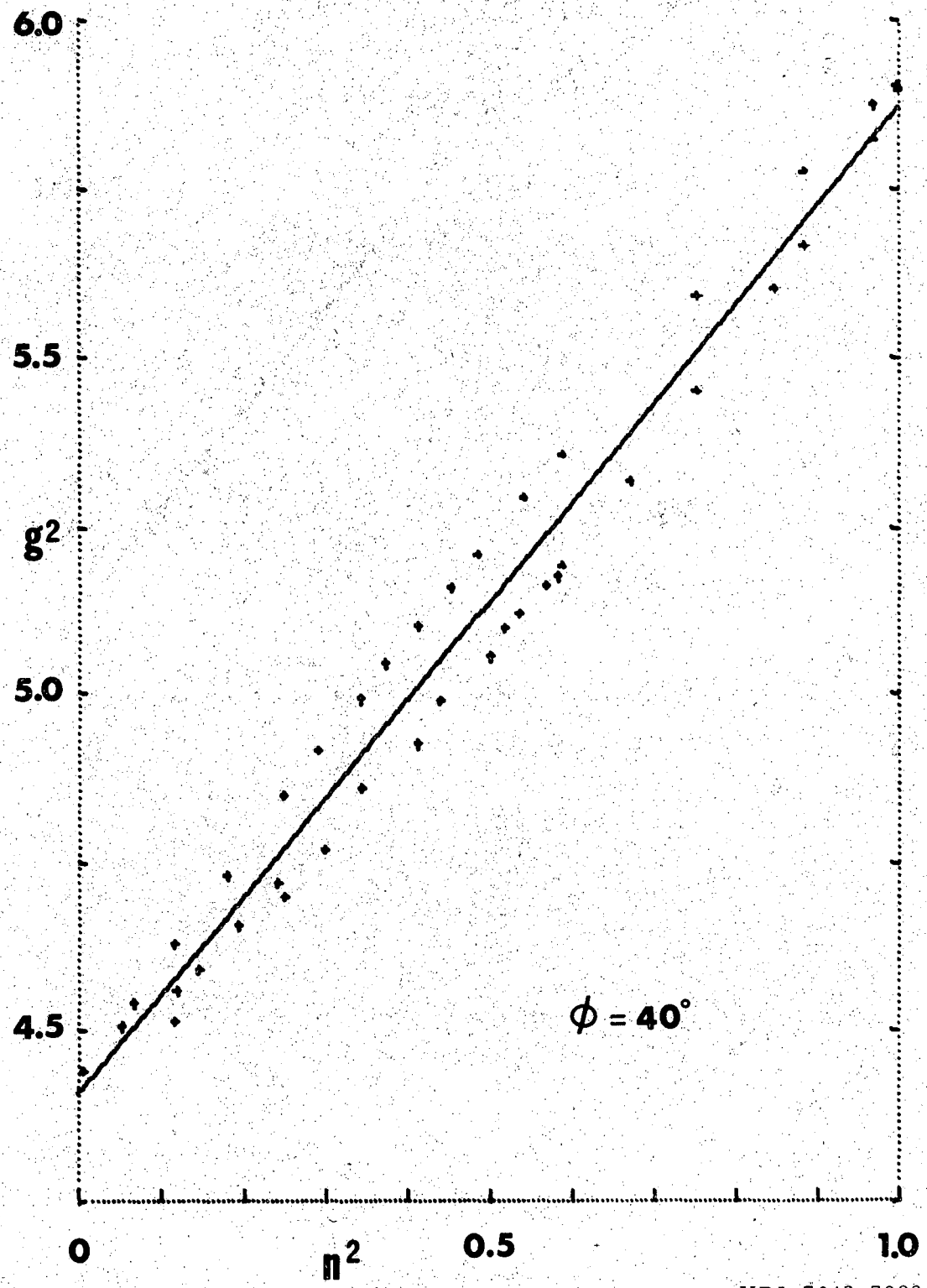

XBL 7012-7383

Fig. 27 b

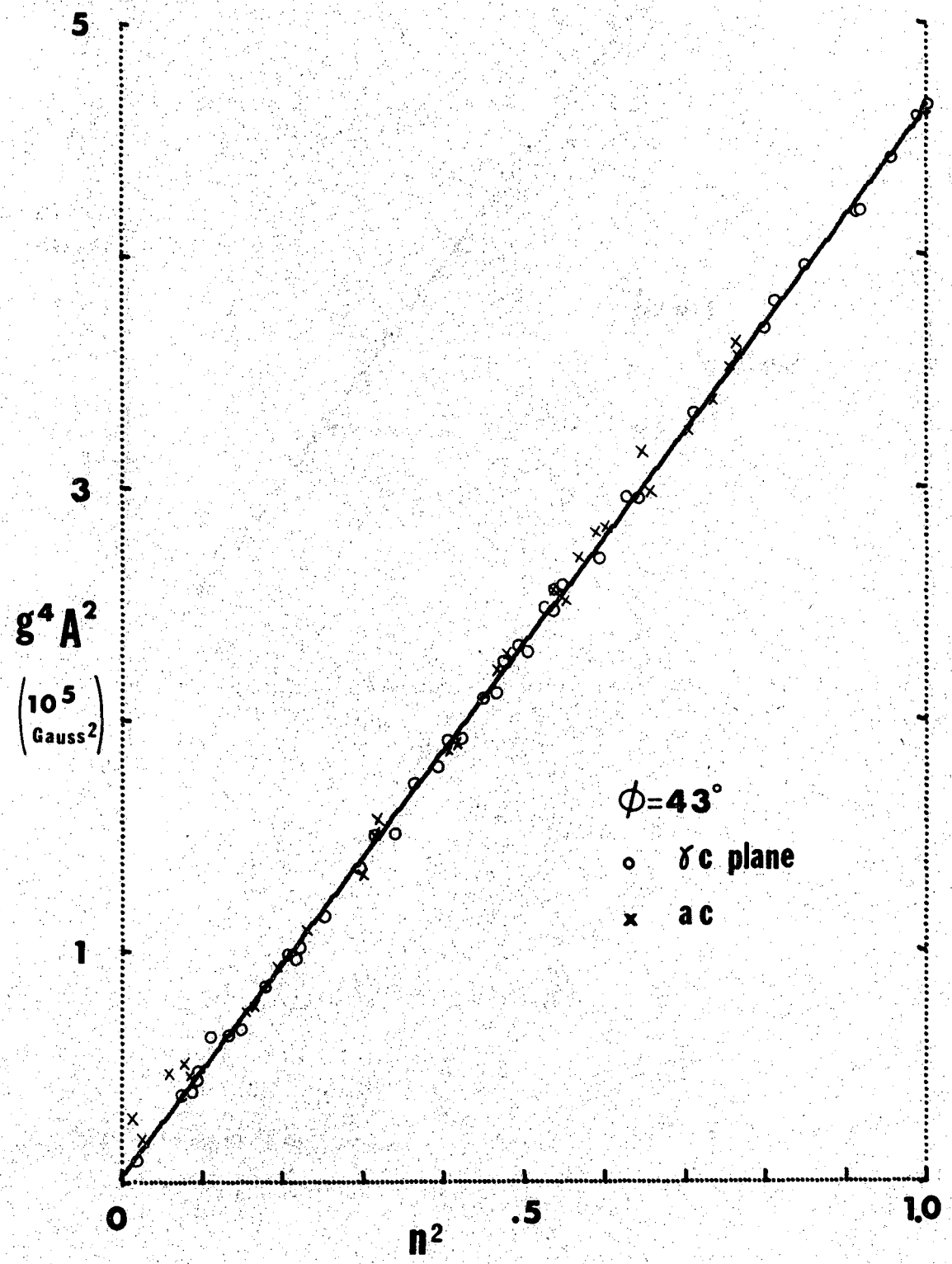

XBL 7012-7300

Fig. 28

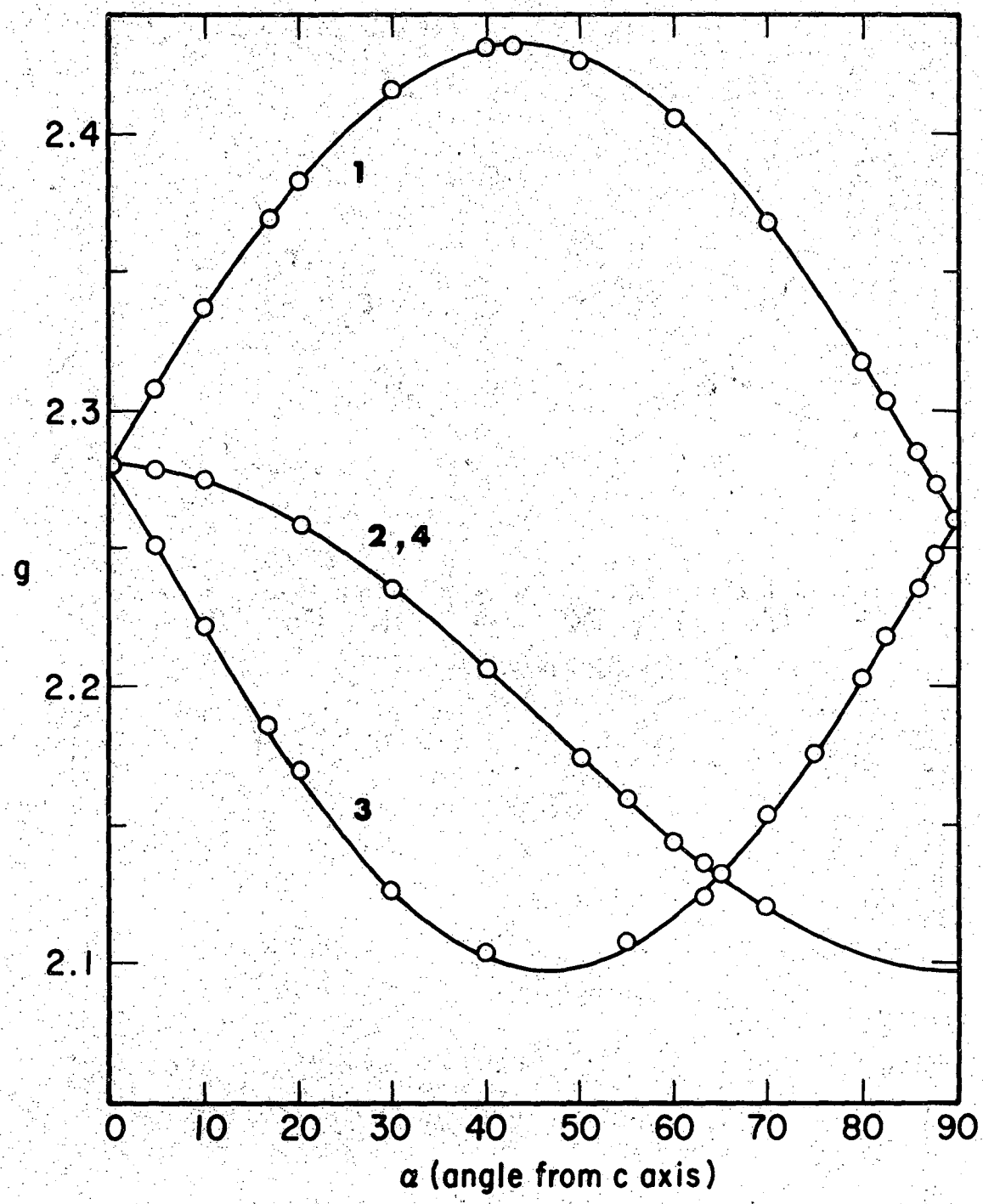

XBL 7012-7289

Fig. 29 a

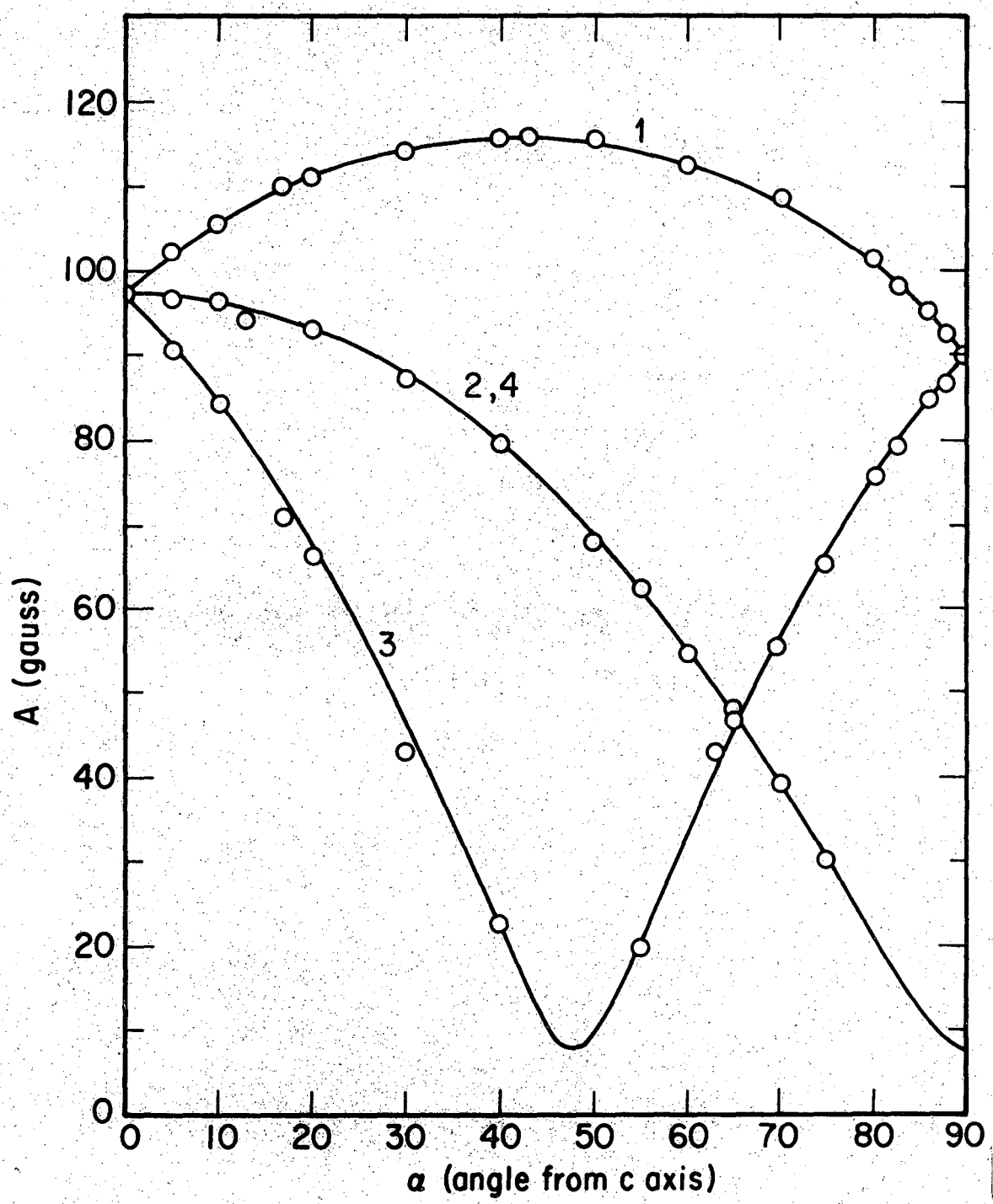

XBL 7012-7304

Fig. 29 b

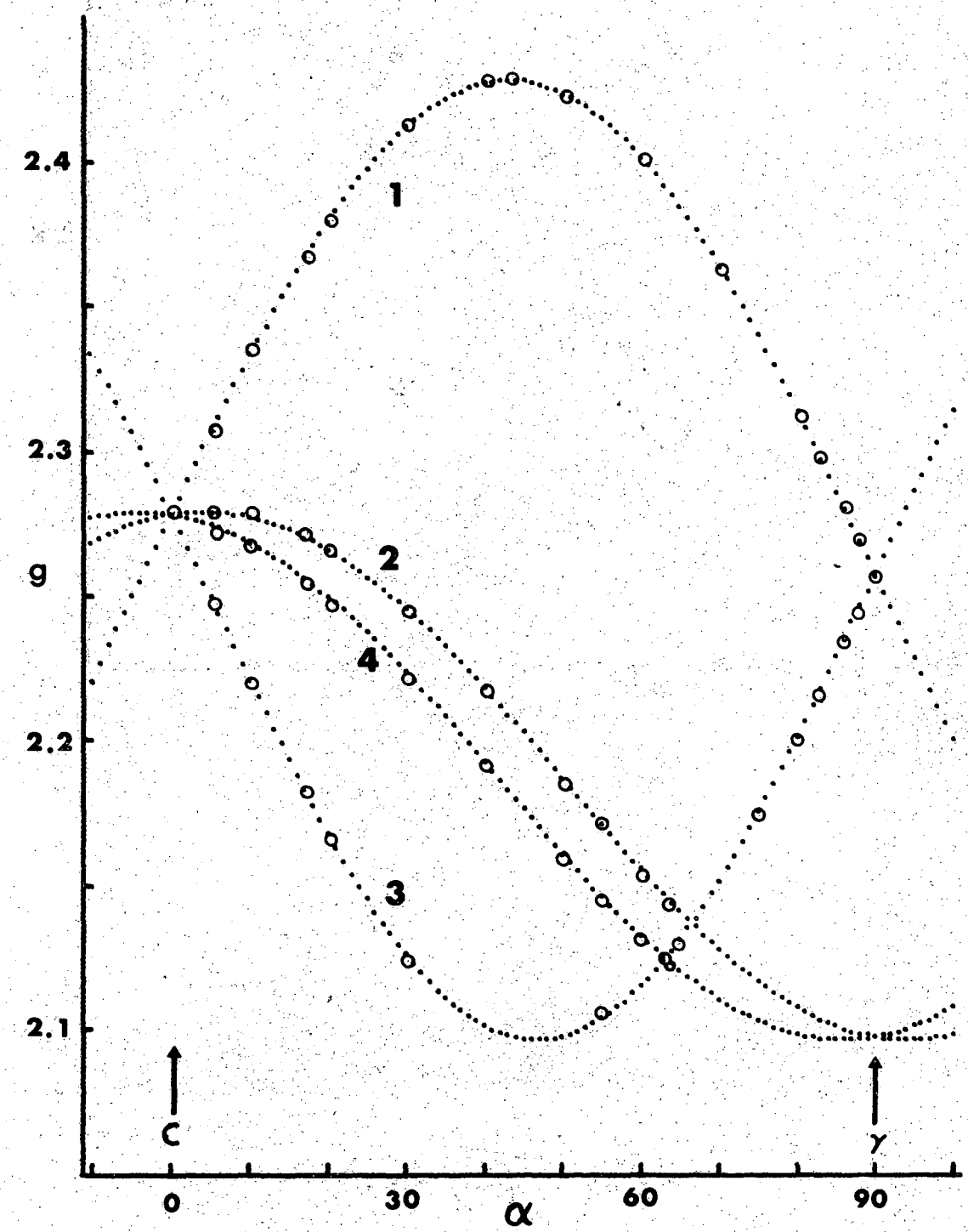

XBL 7012-7306

Fig. 30

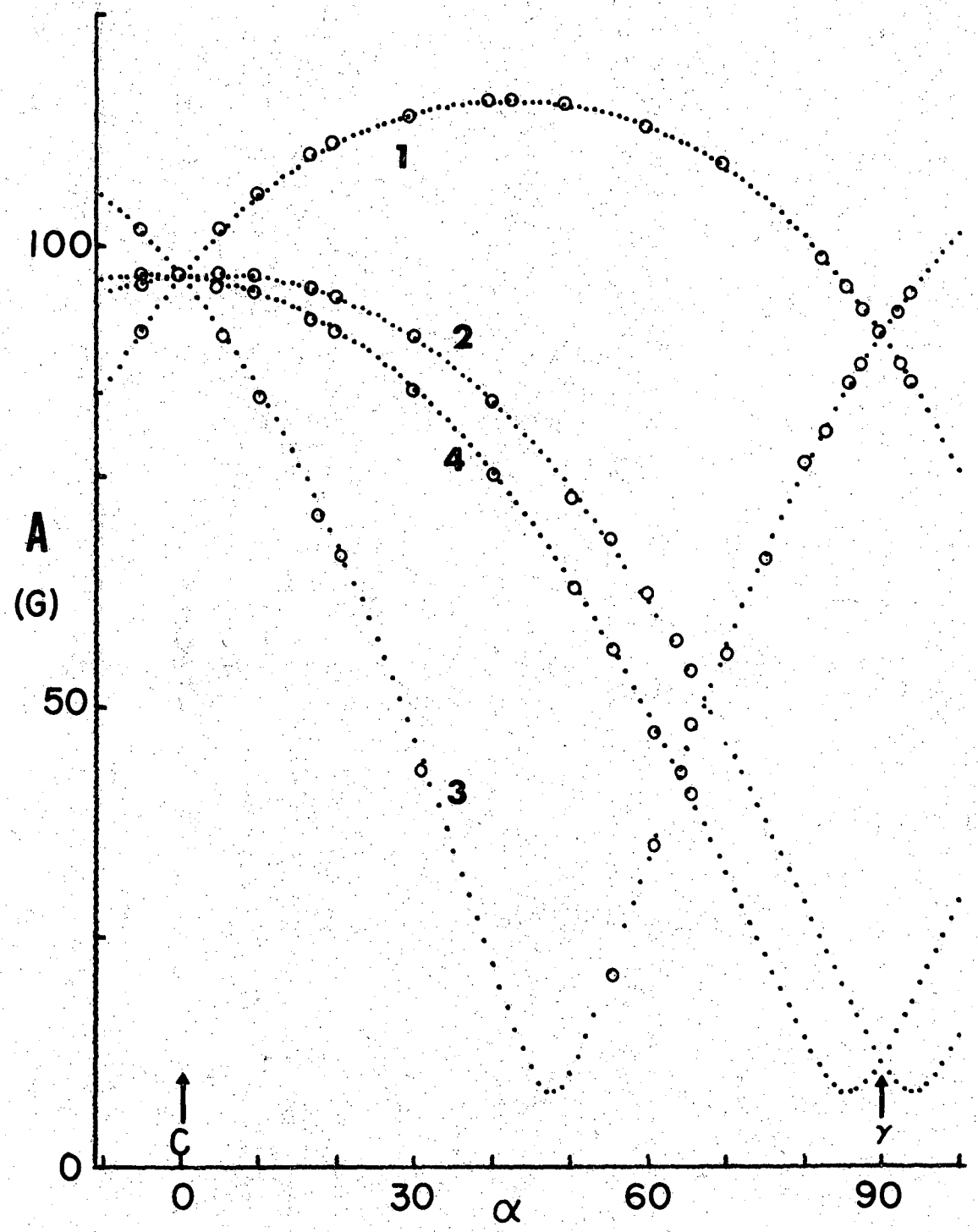

XBL 7012-7293

Fig. 31

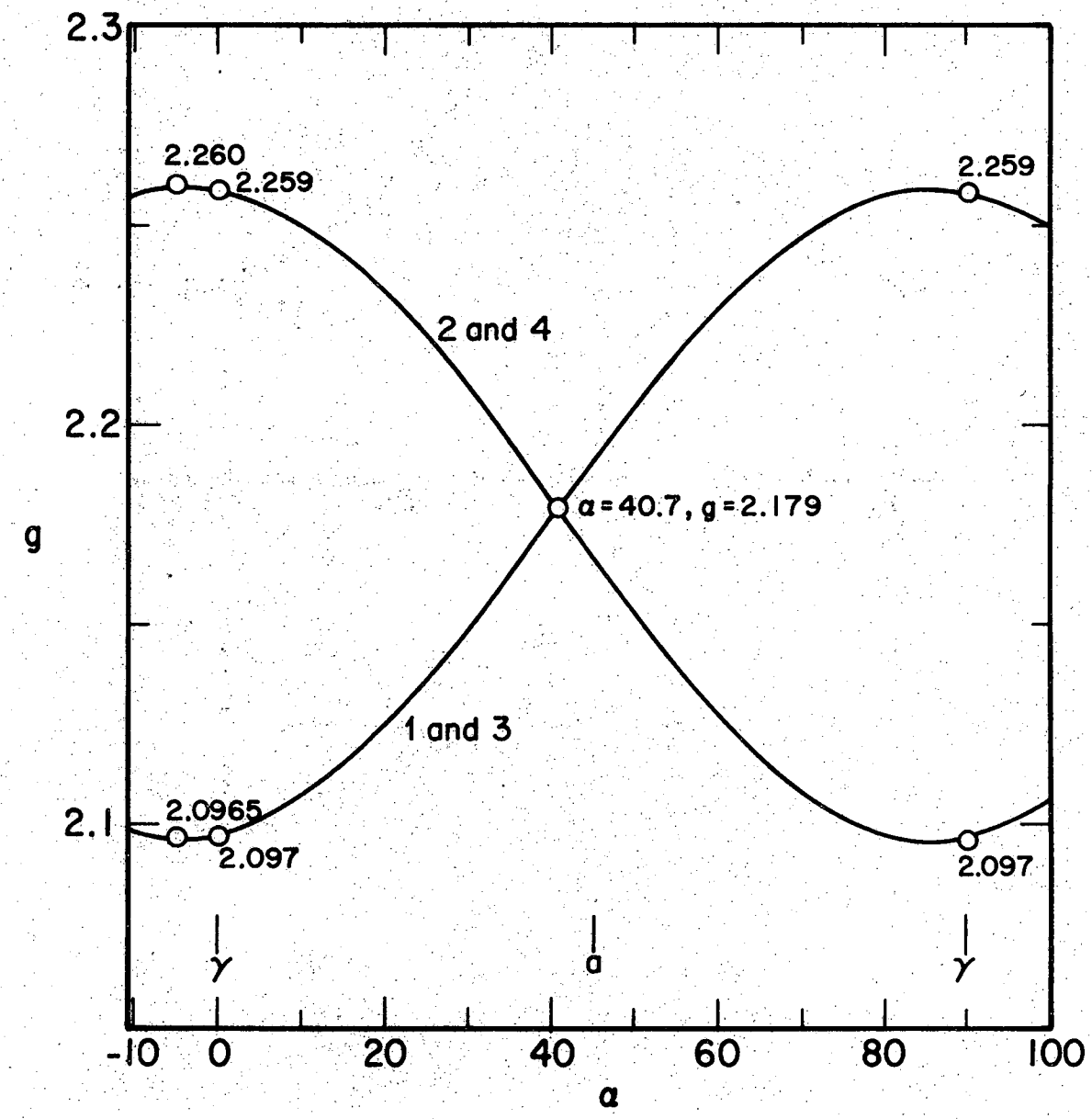

XBL 7012-7305

Fig. 32

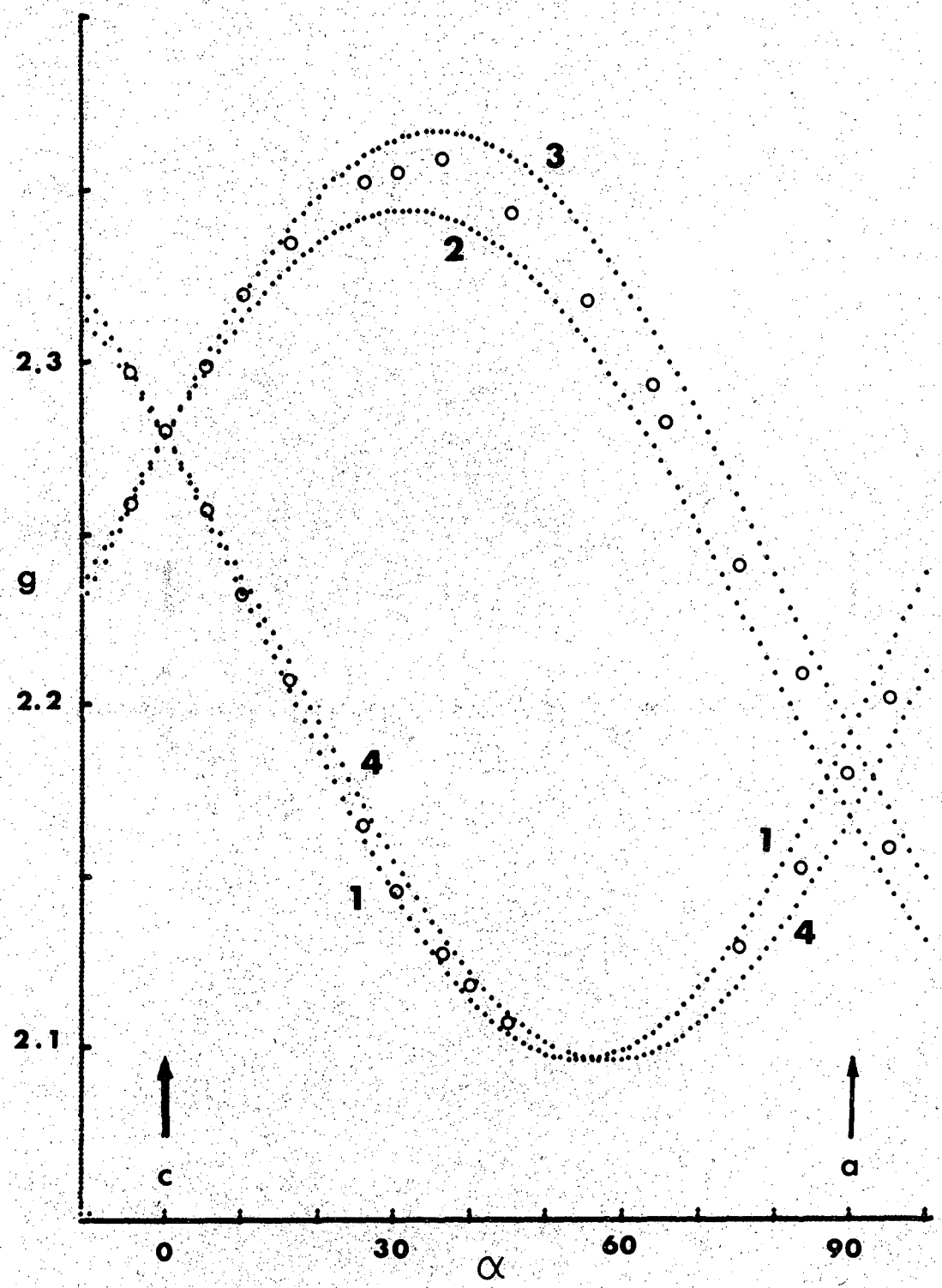

XBL 7012-7307

Fig. 33

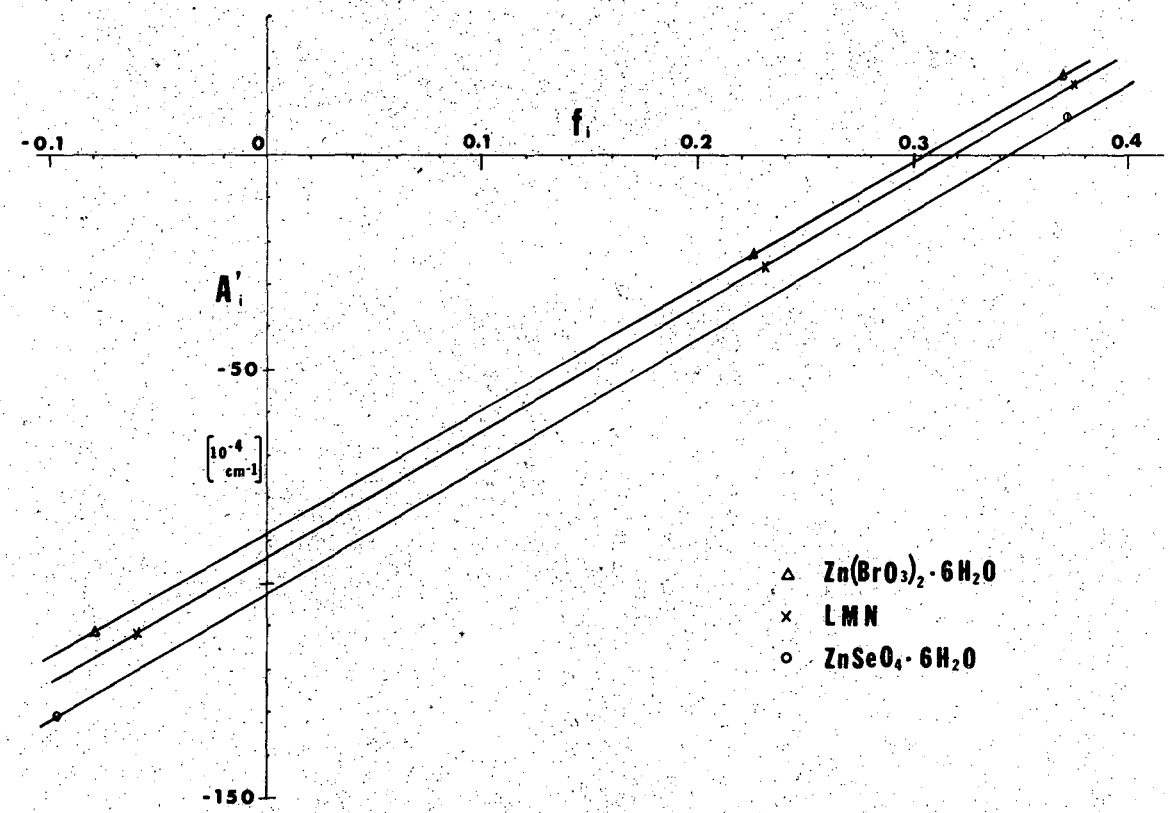

XBL 7012-7385

Fig. 34

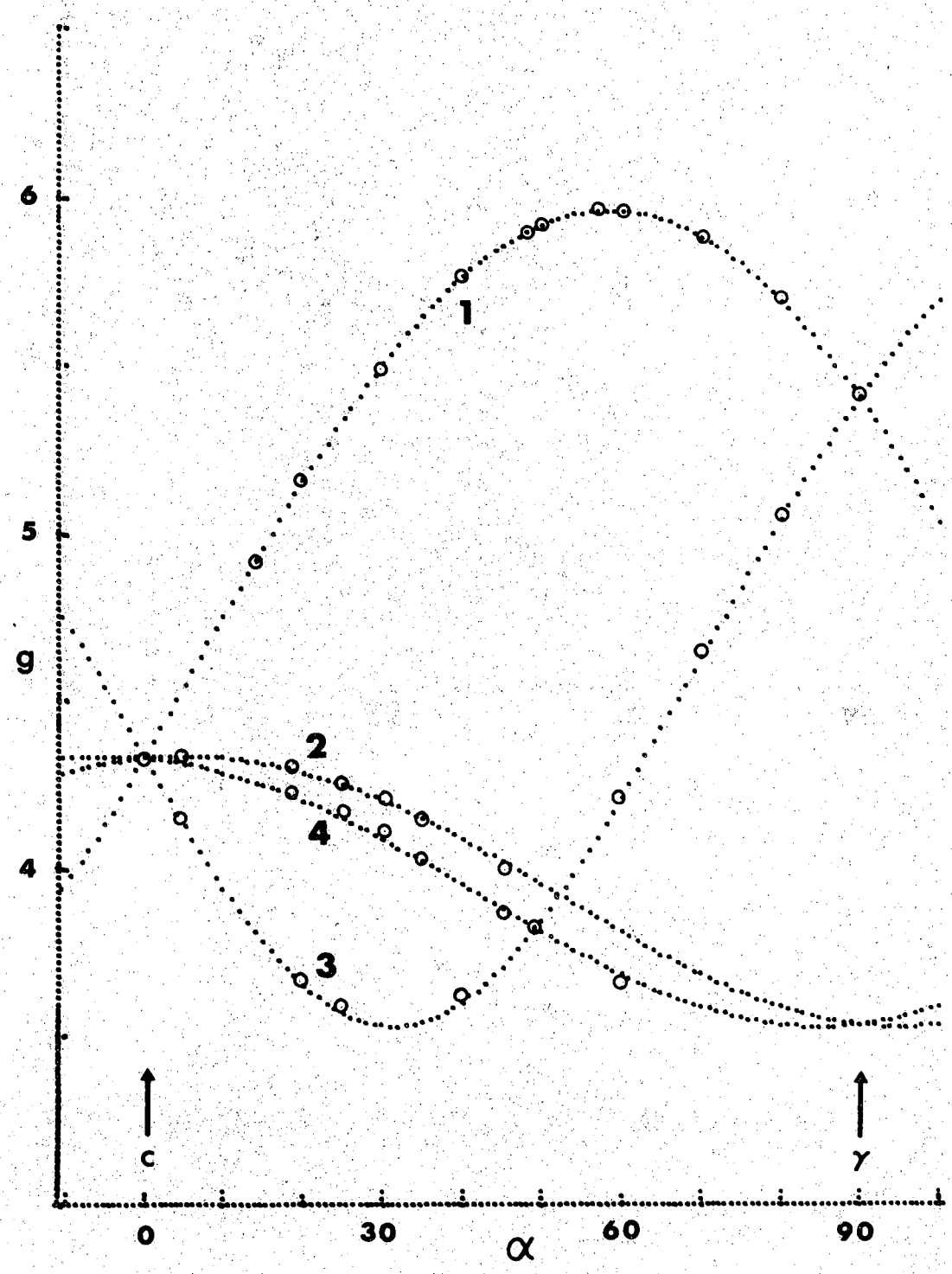

XBL 7012-7290

Fig. 35

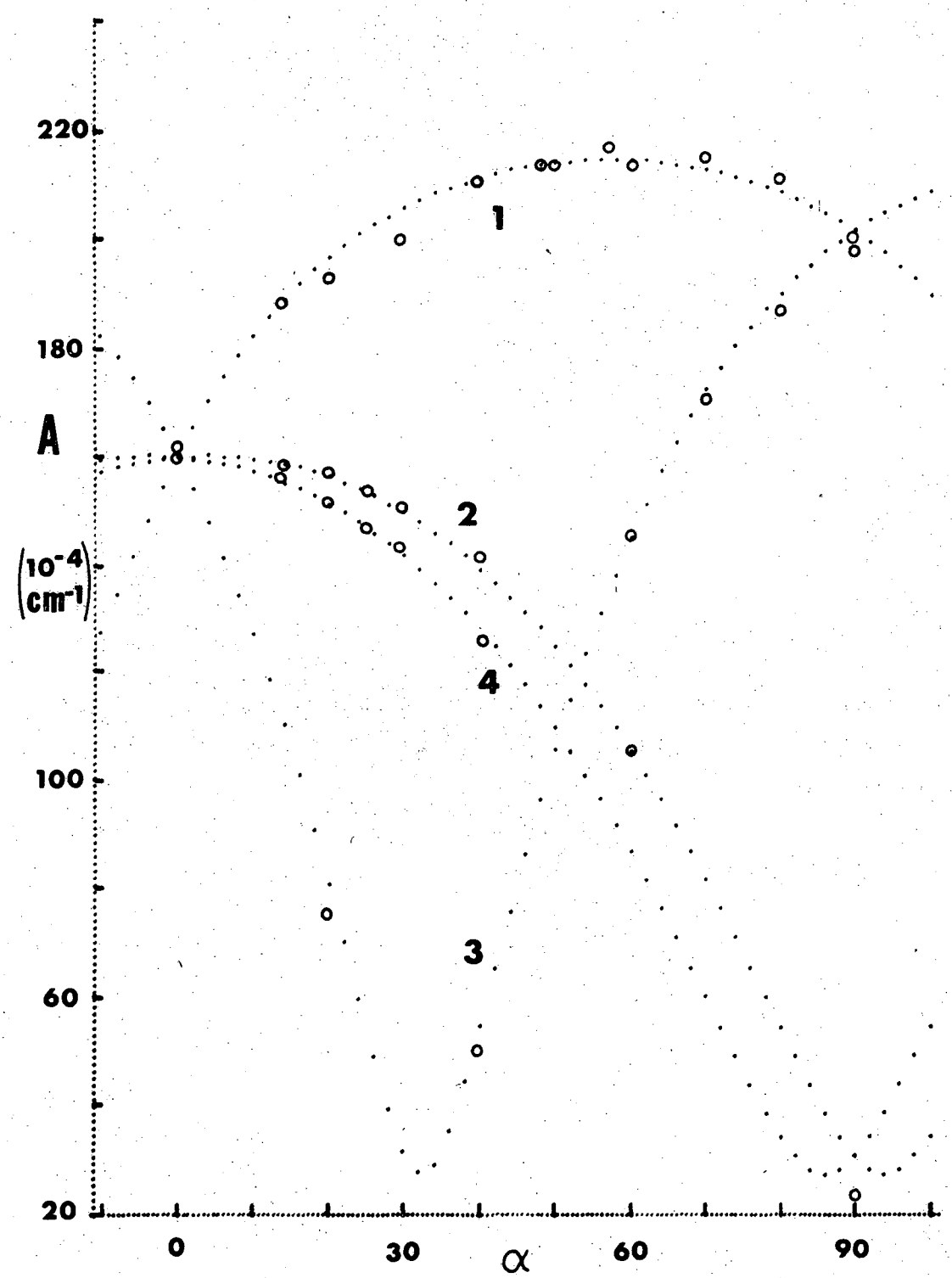

XBL 7012-7408

Fig. 36

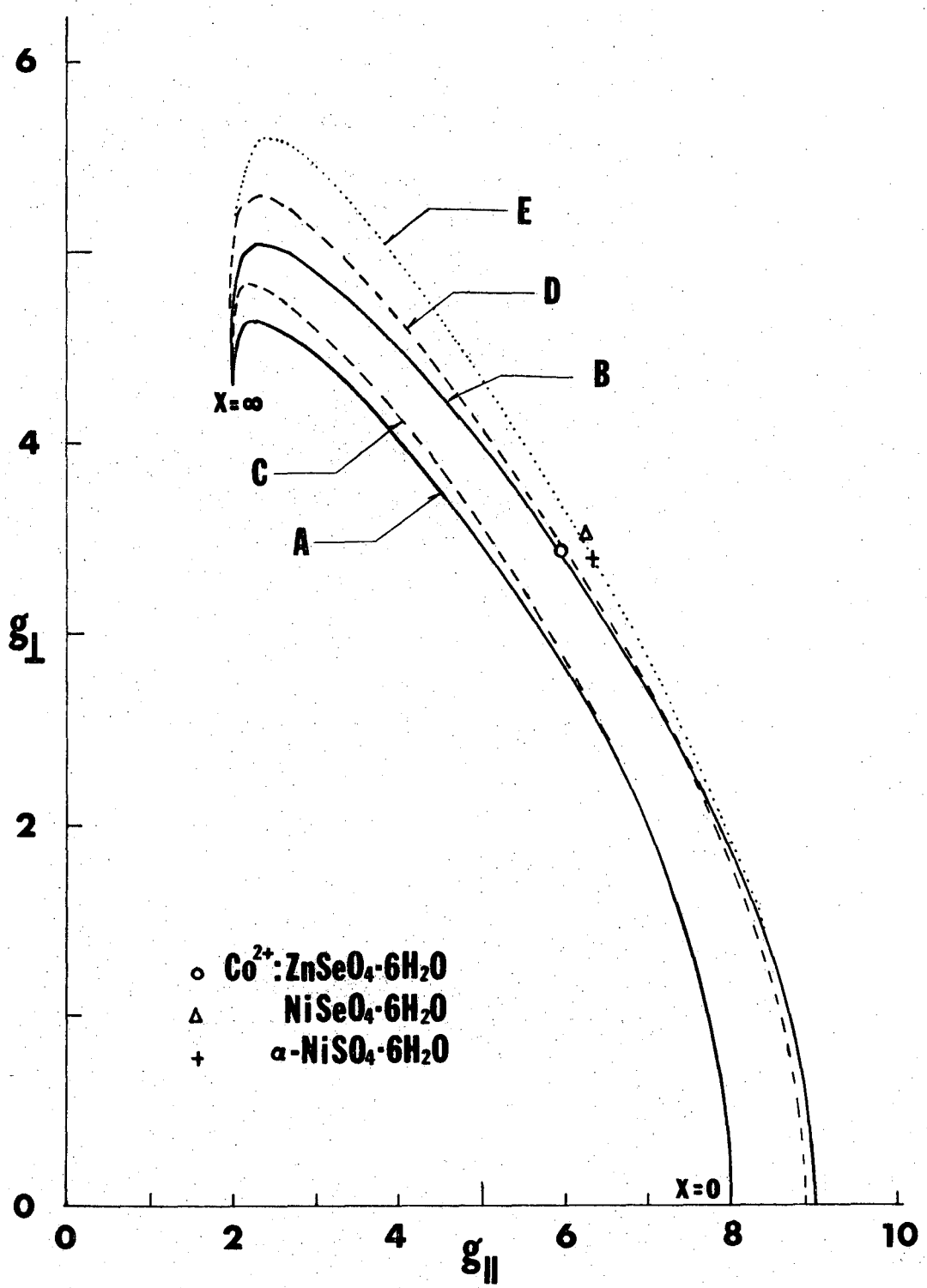

XBL 711-27

Fig. 37

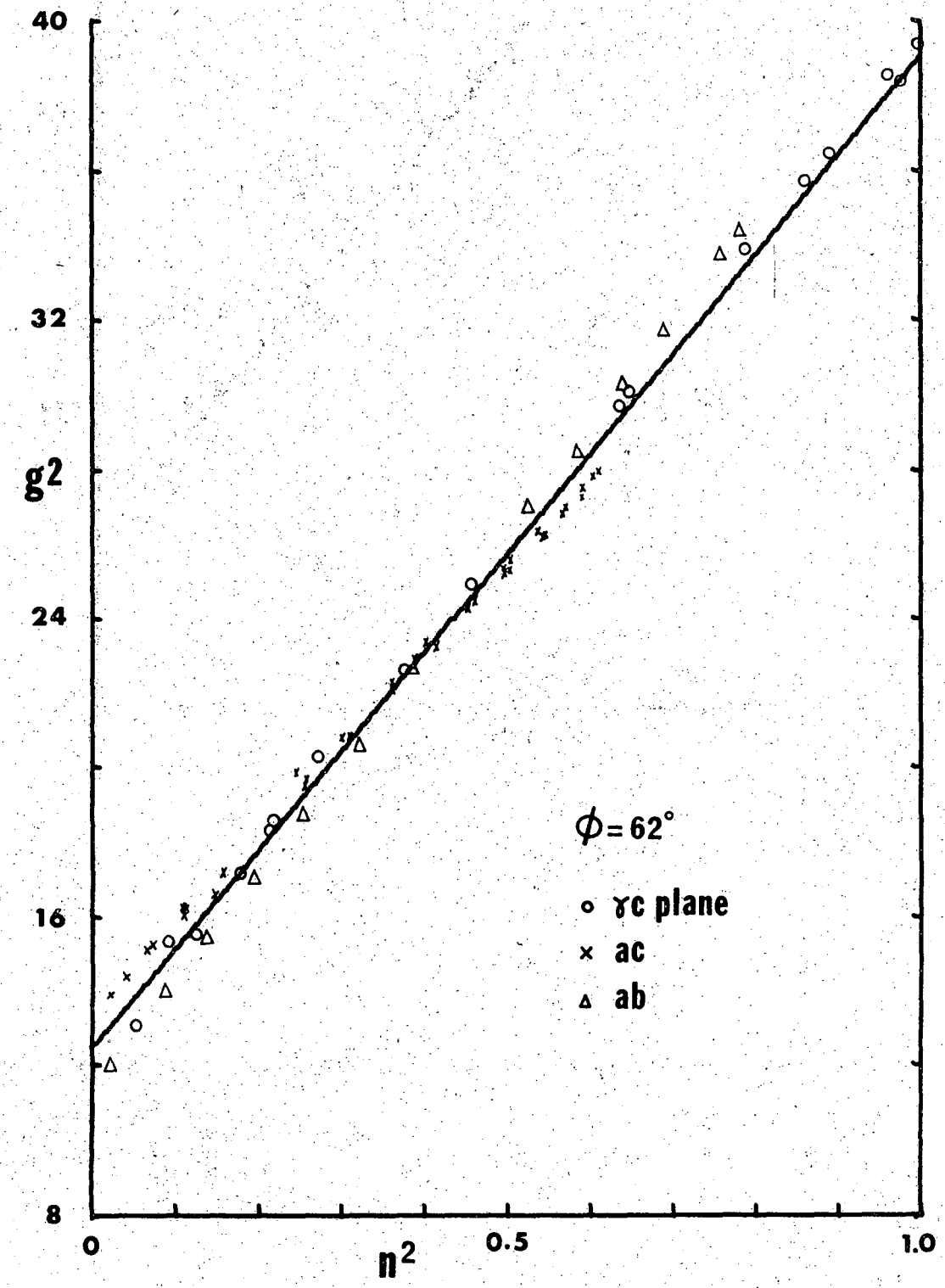

XBL 7012-7378

Fig. 38

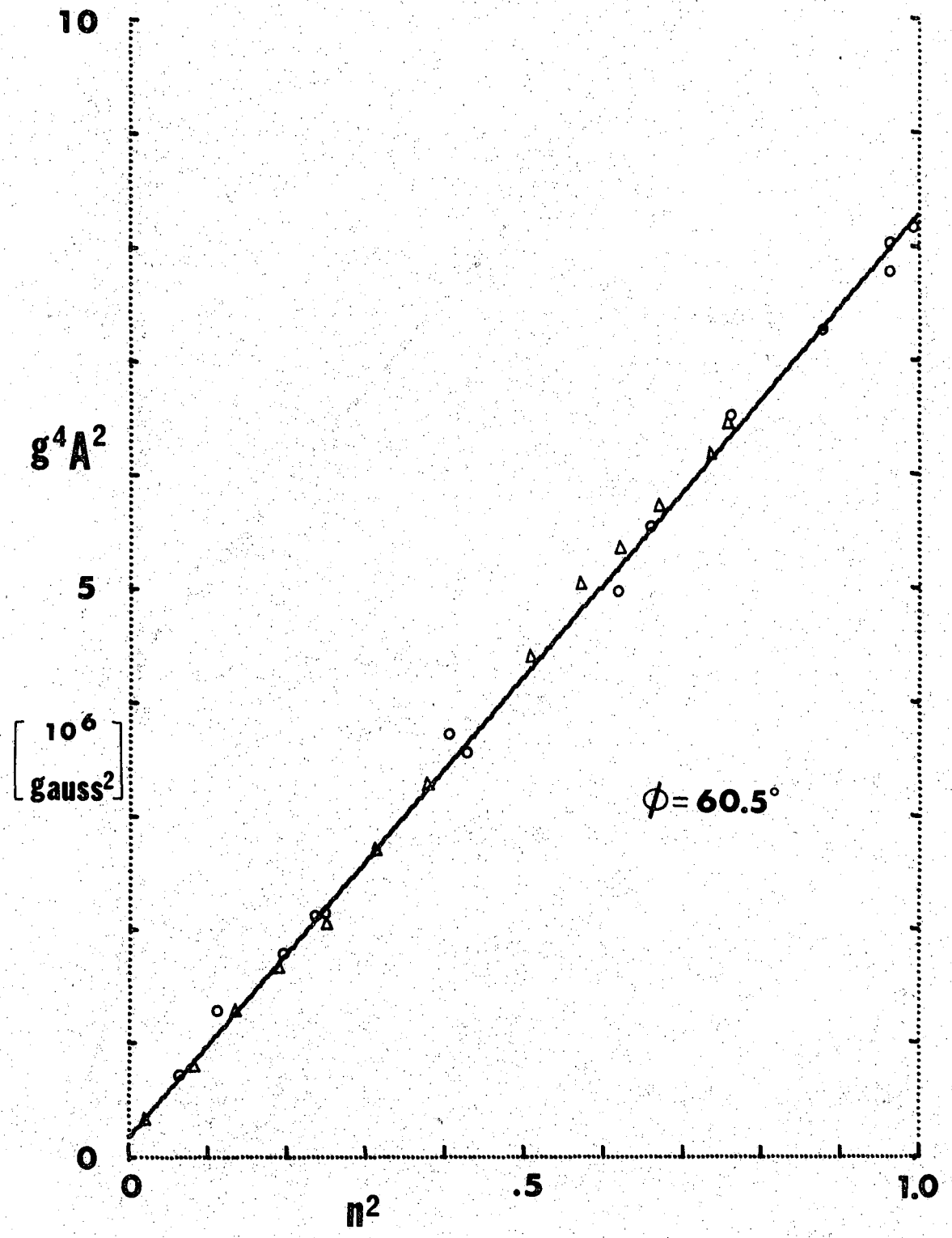

XBL 7012-7380

Fig. 39

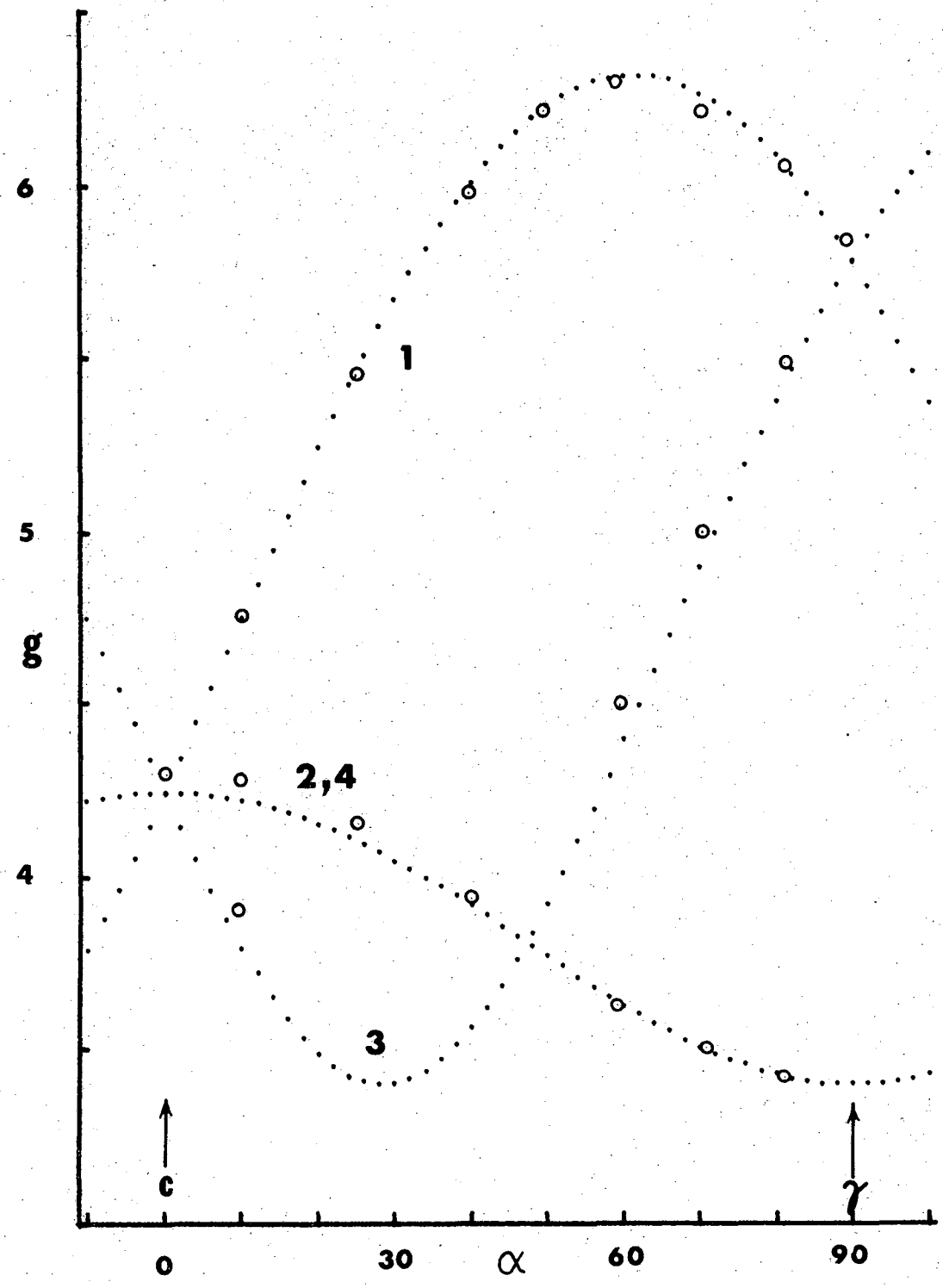

XBL 7012-7377

Fig. 40

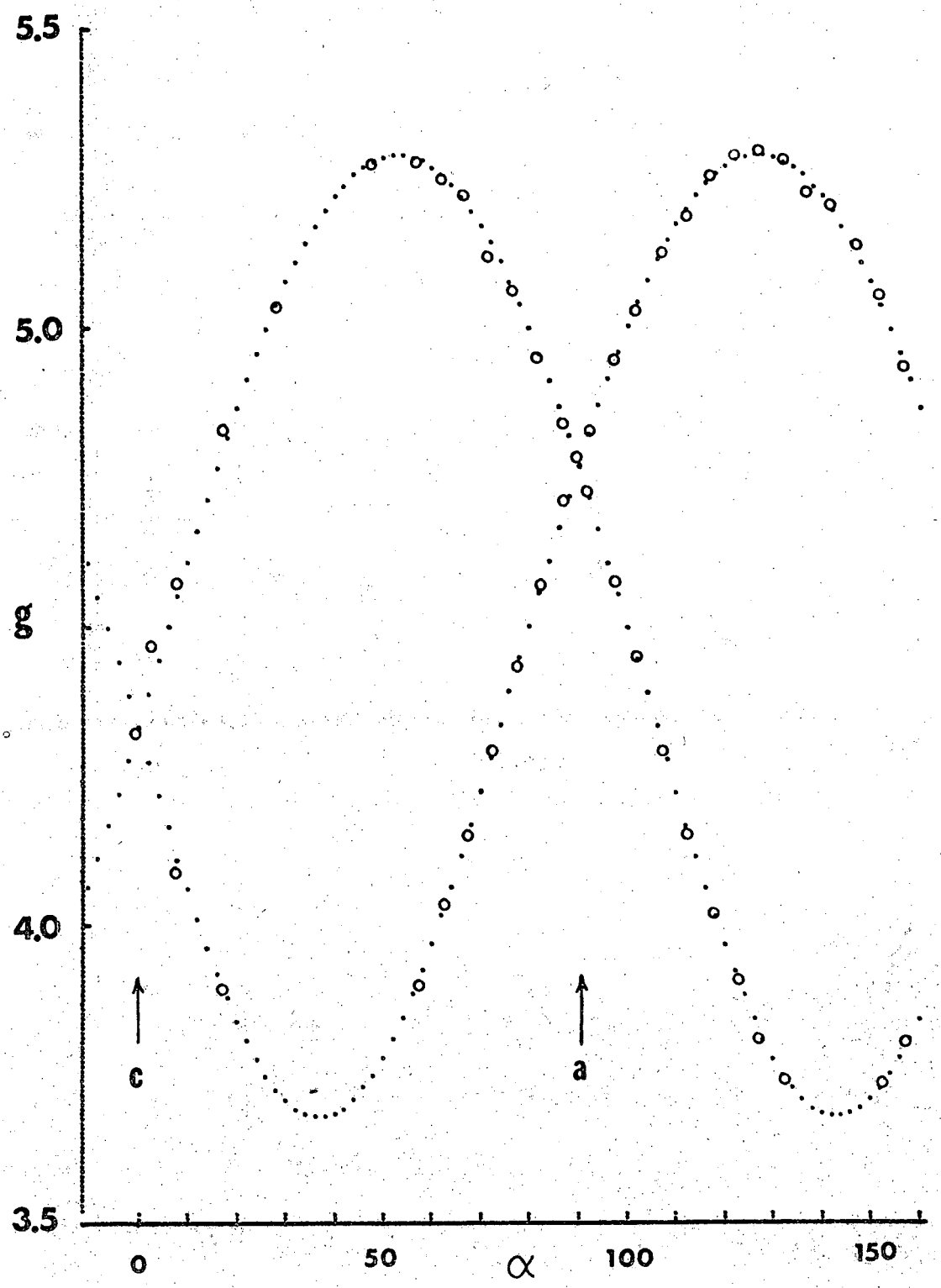

XBL 7012-7384

Fig. 41

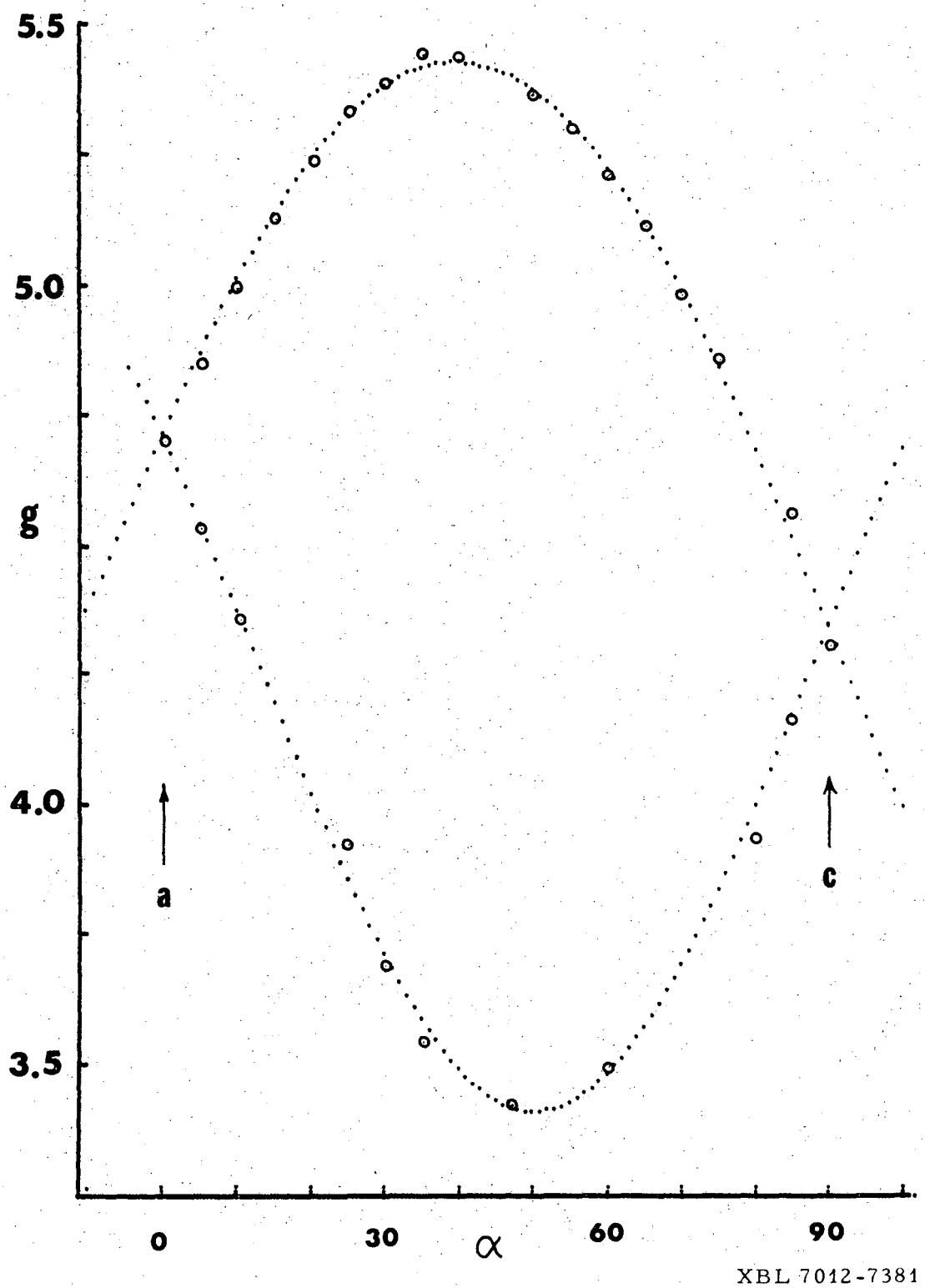

Fig. 42

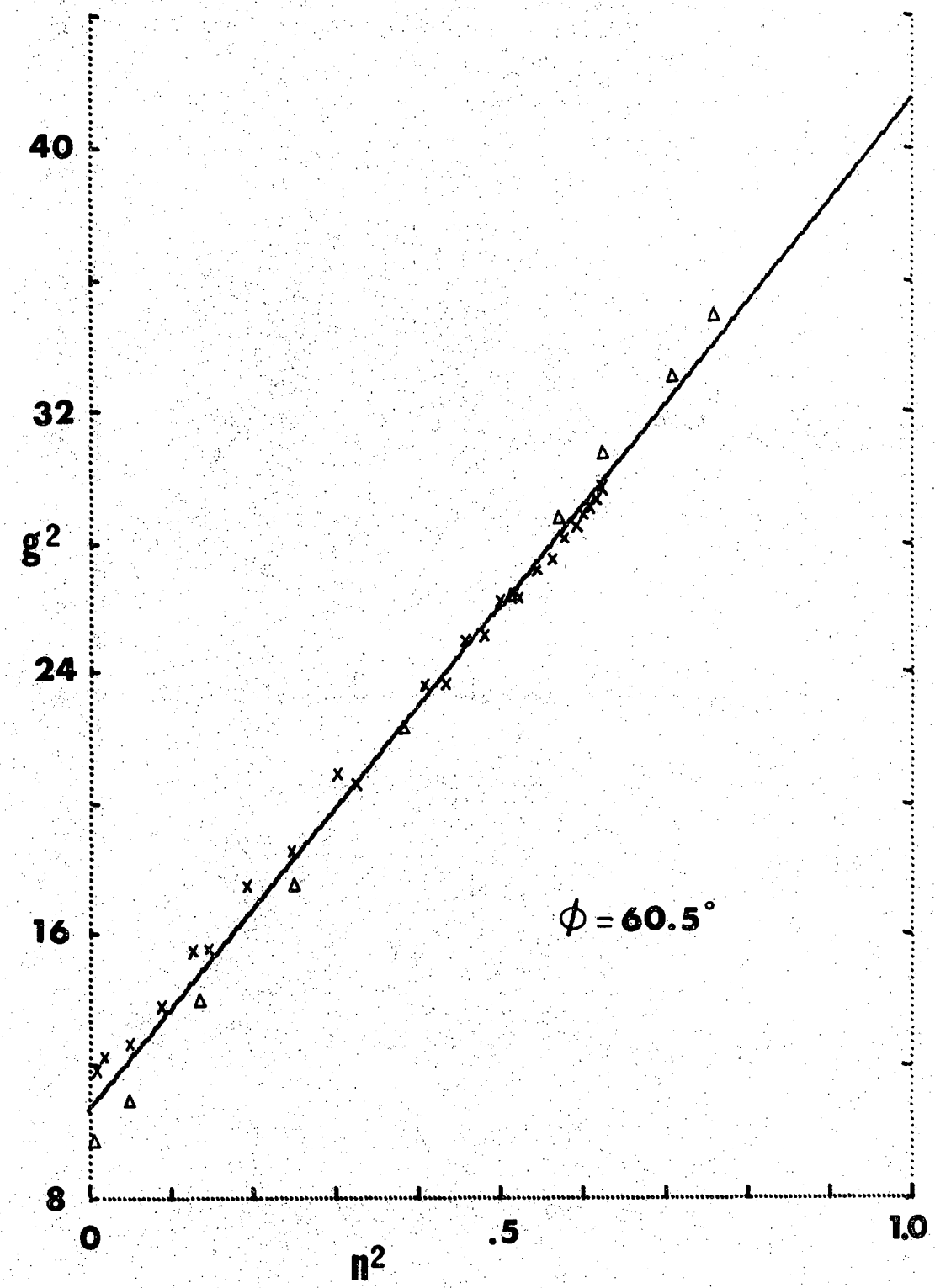

XBL 7012-7379

Fig. 43

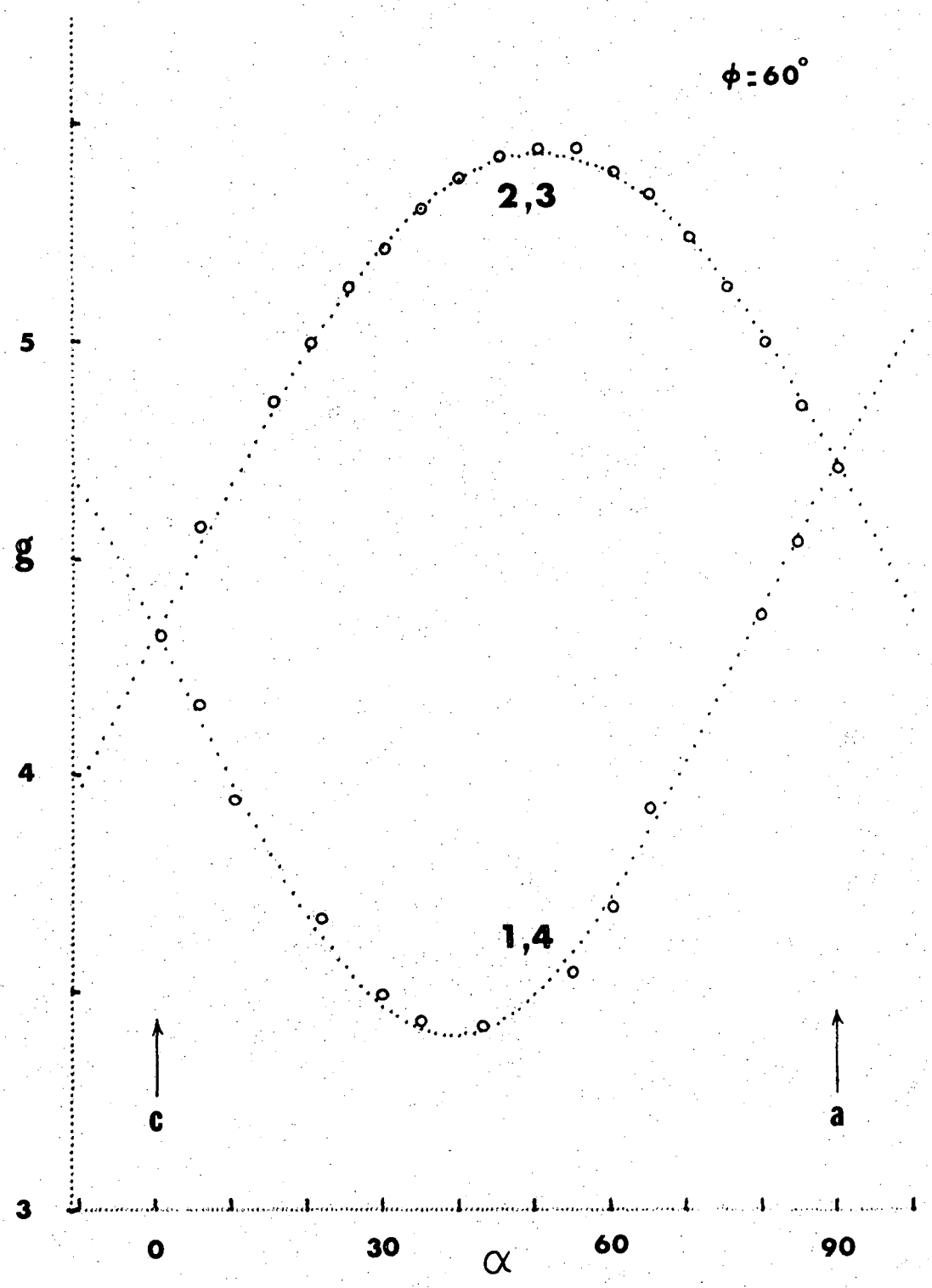

XBL 7012-7406

Fig. 44

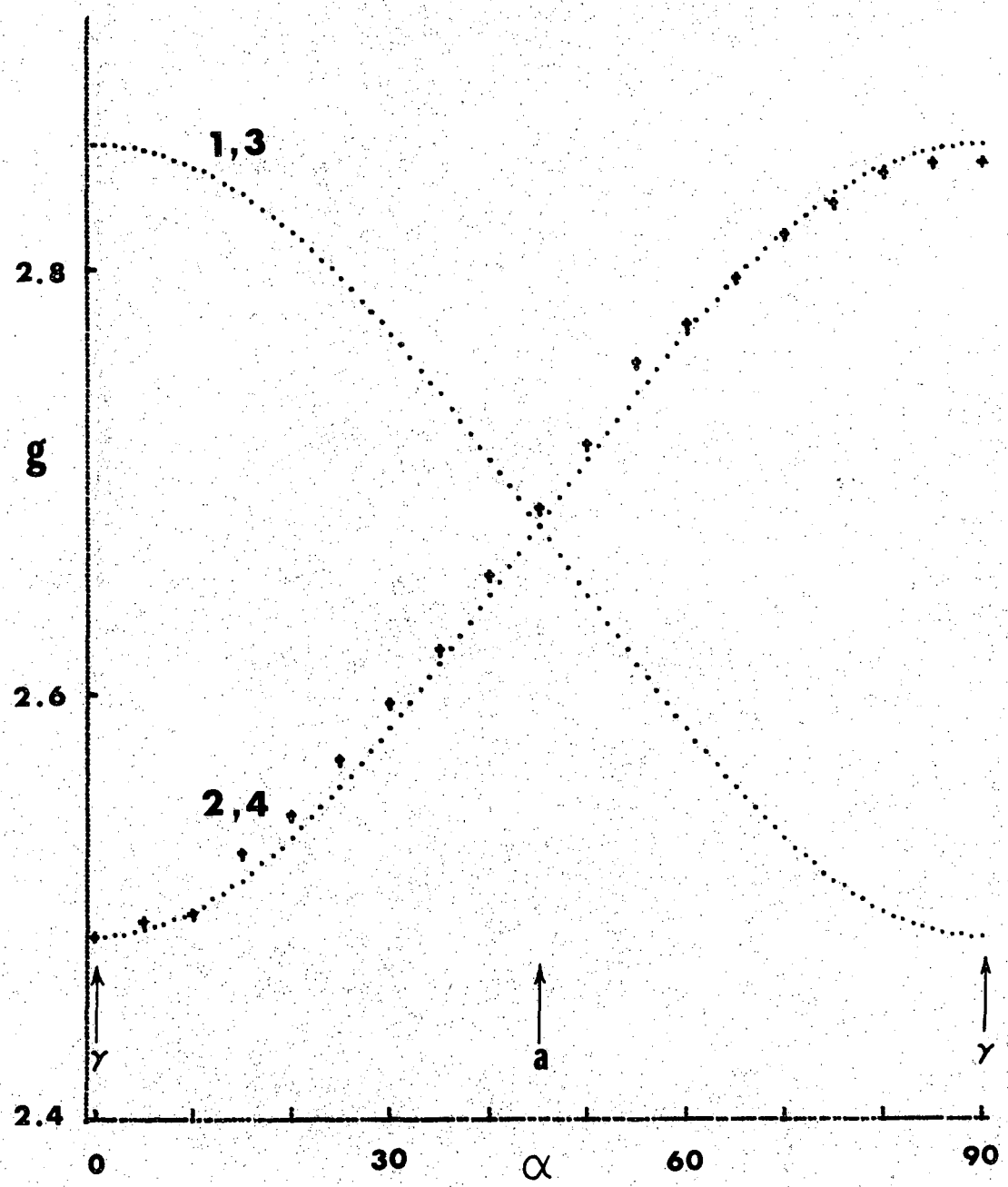

XBL 7012-7407

Fig. 45

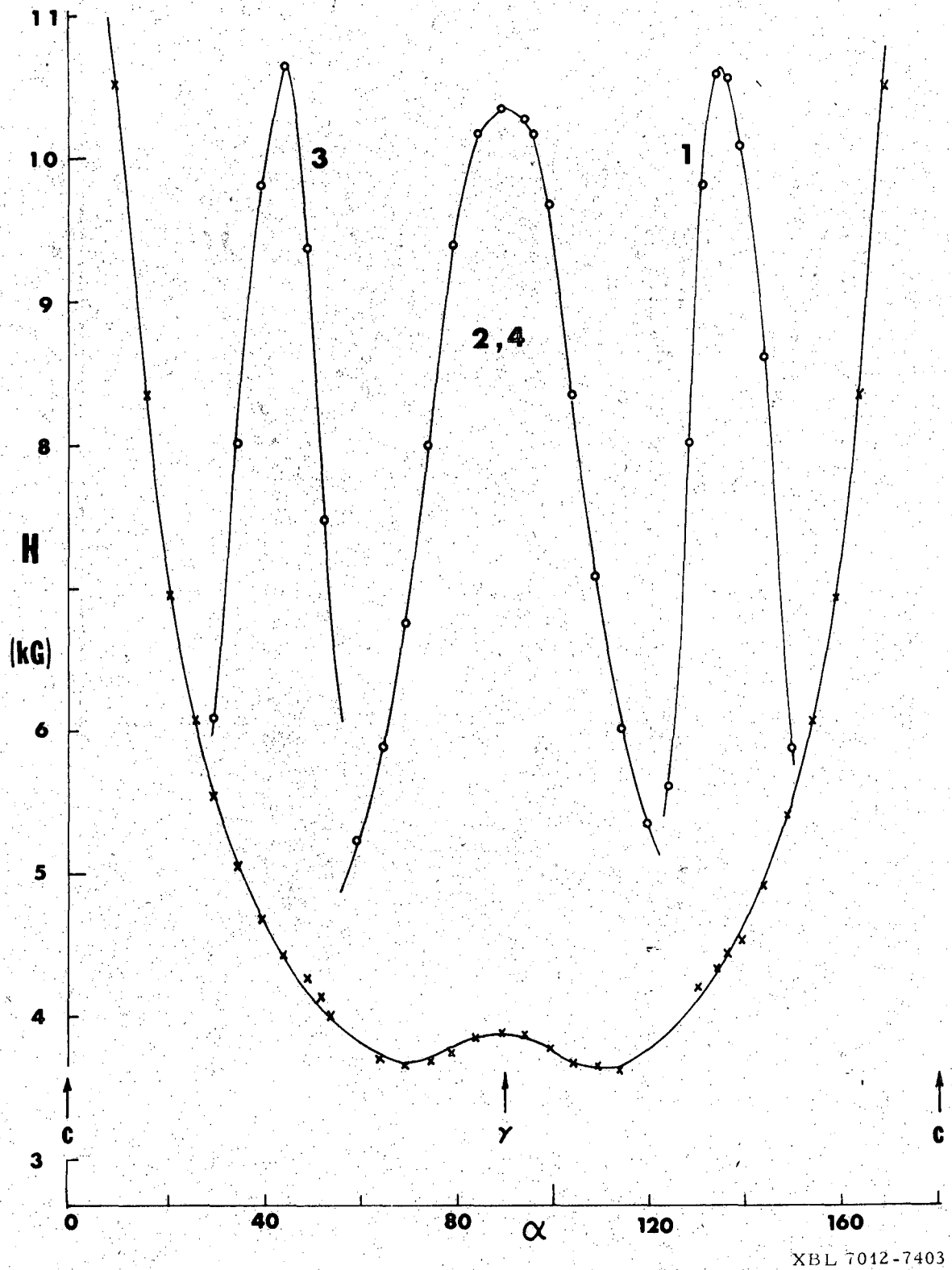

Fig. 46

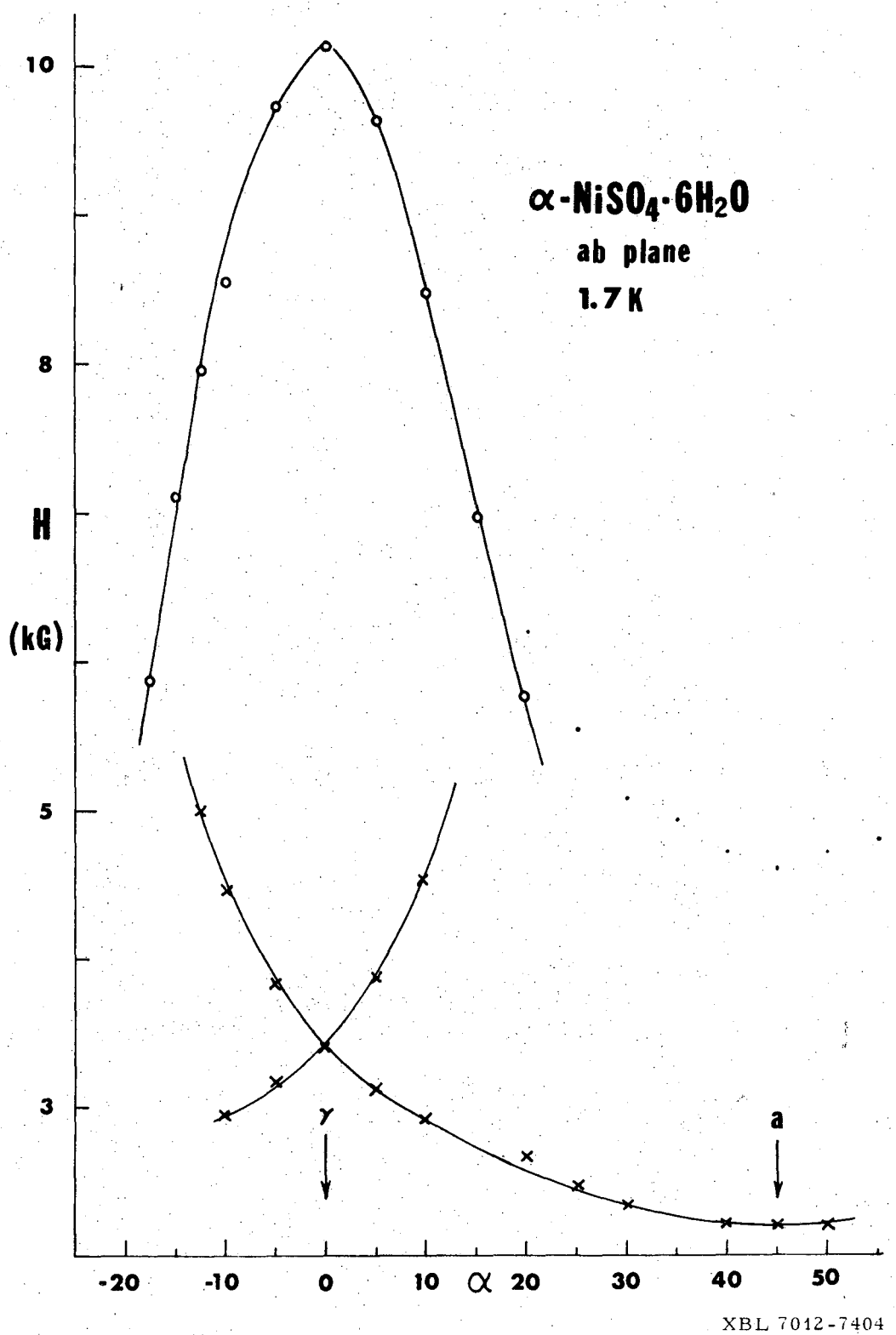
α-NiSO4·6H2O
ab plane
1.7 K
H
(kG)
10
8
5
3
γ
a
-20
-10
0
10
α
20
30
40
50
XBL 7012-7404

Fig. 47

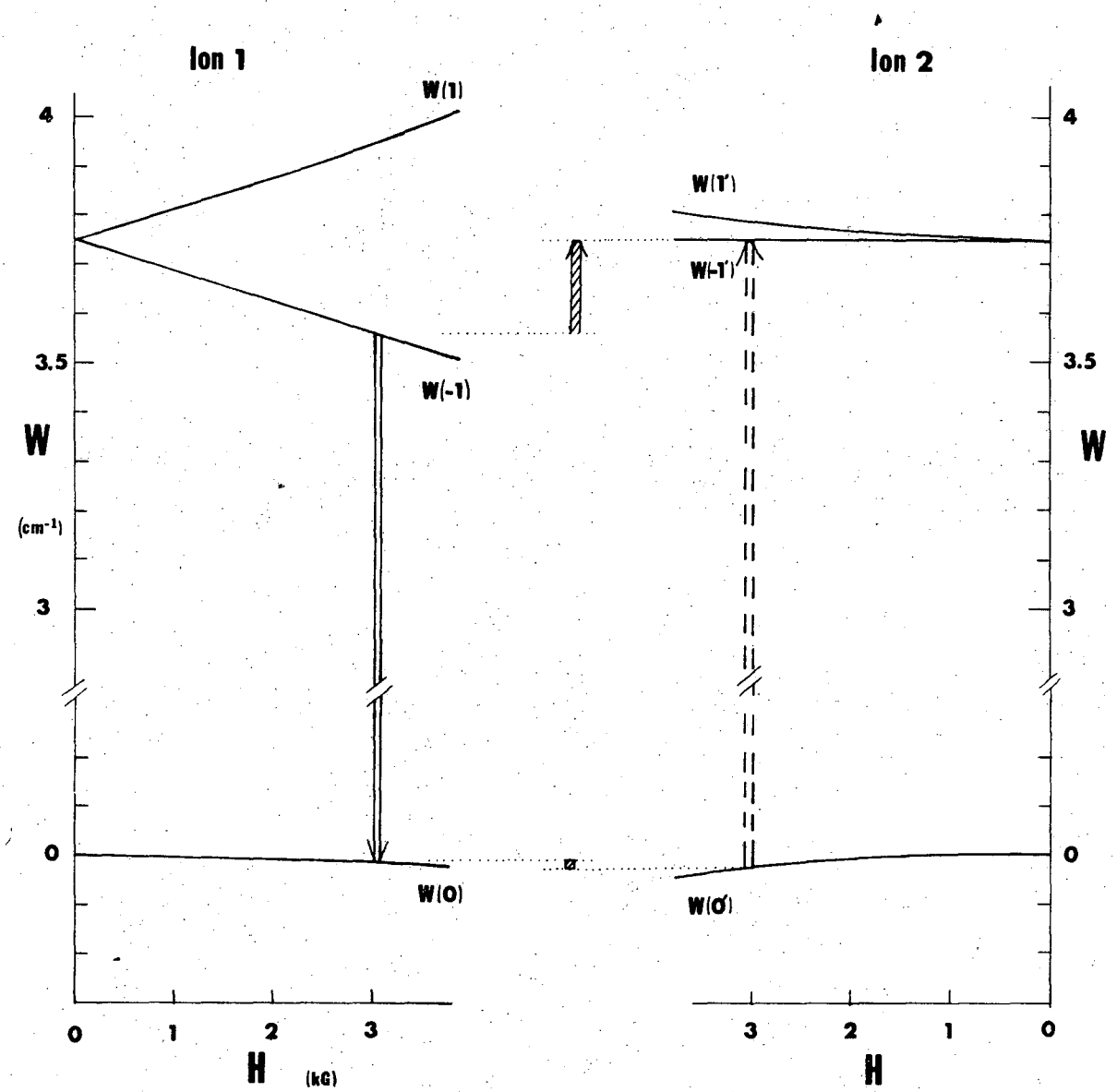

Fig. 48

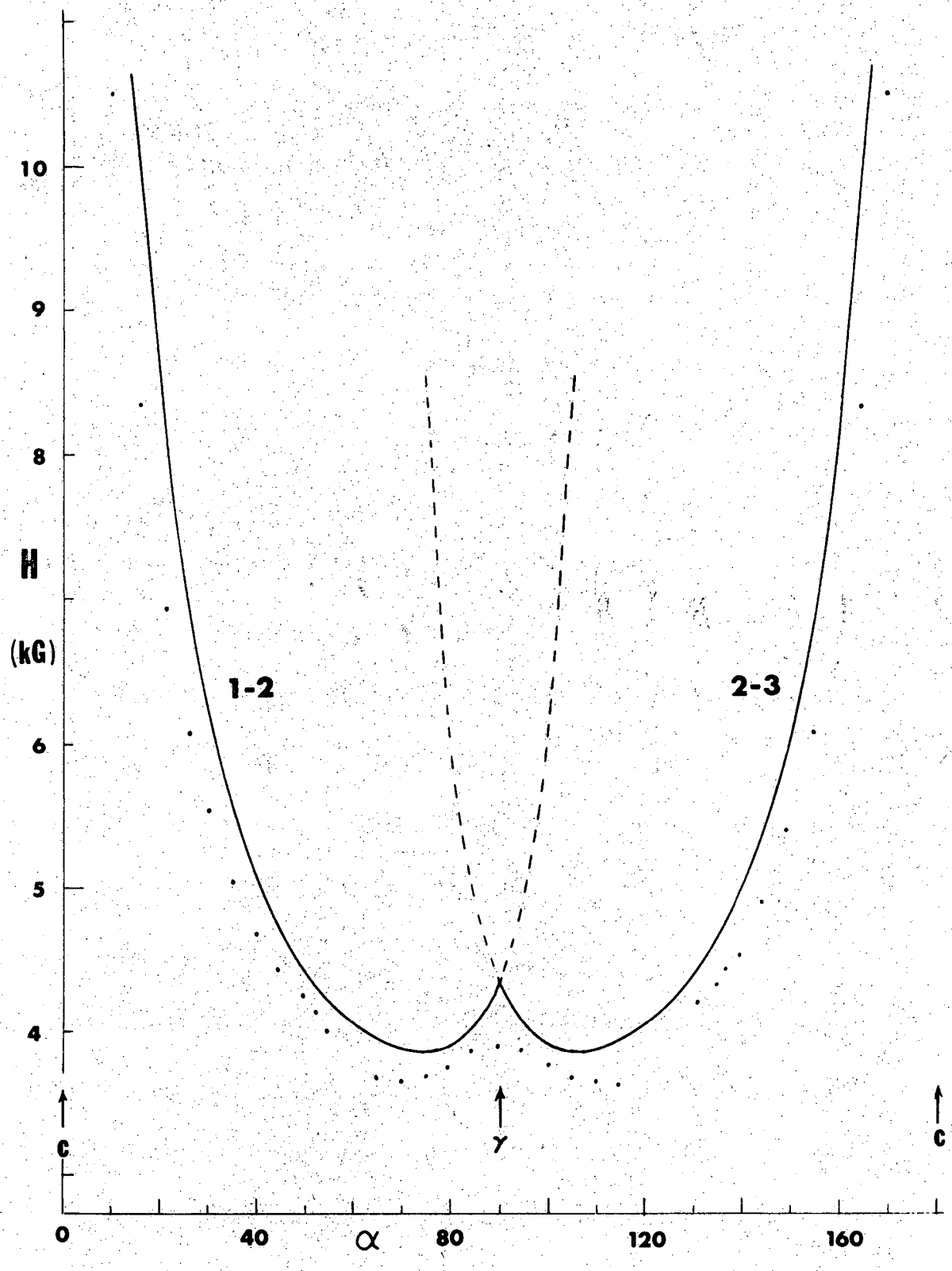

XBL 711-30

Fig. 49

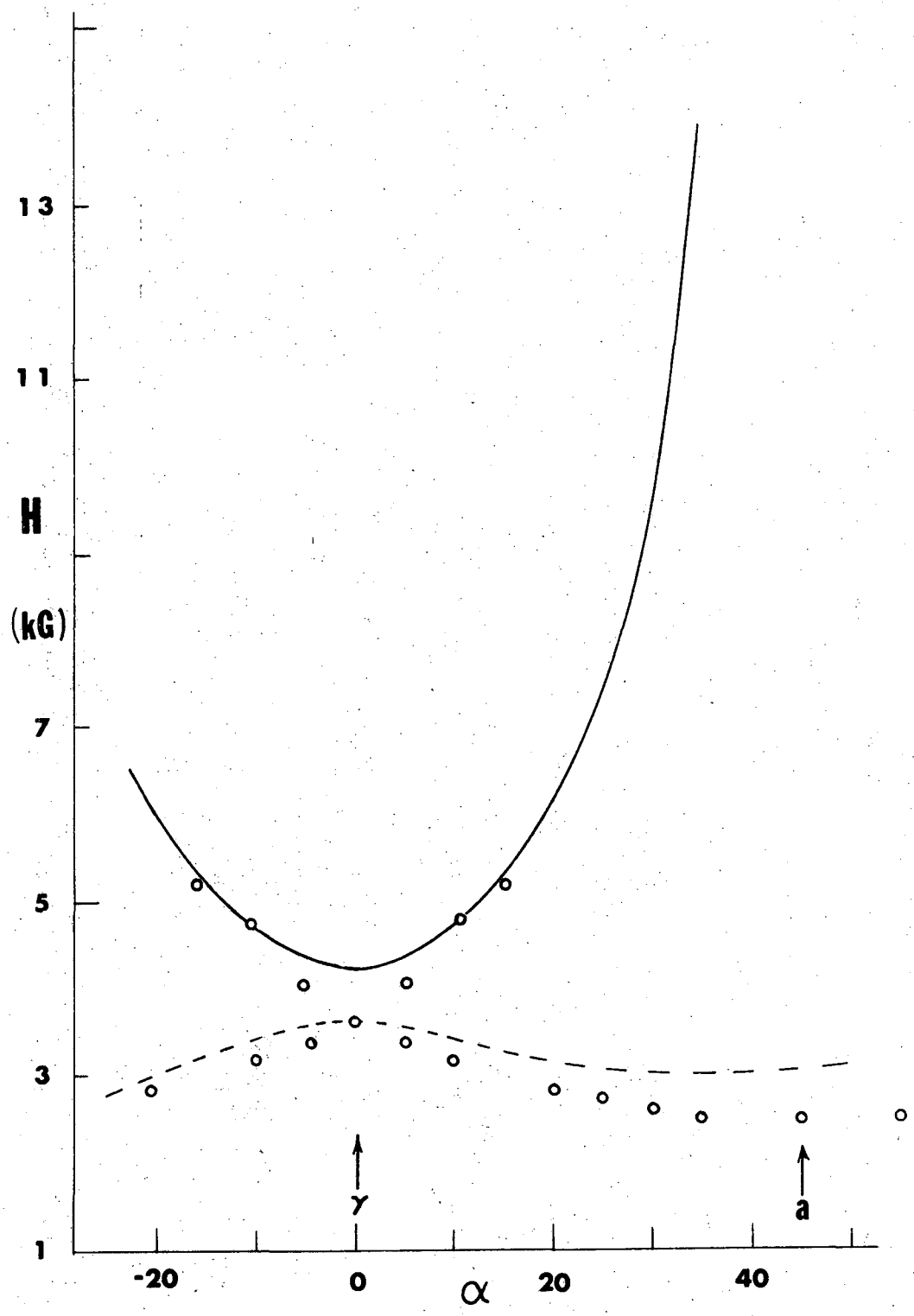

XBL 711-28

Fig. 50

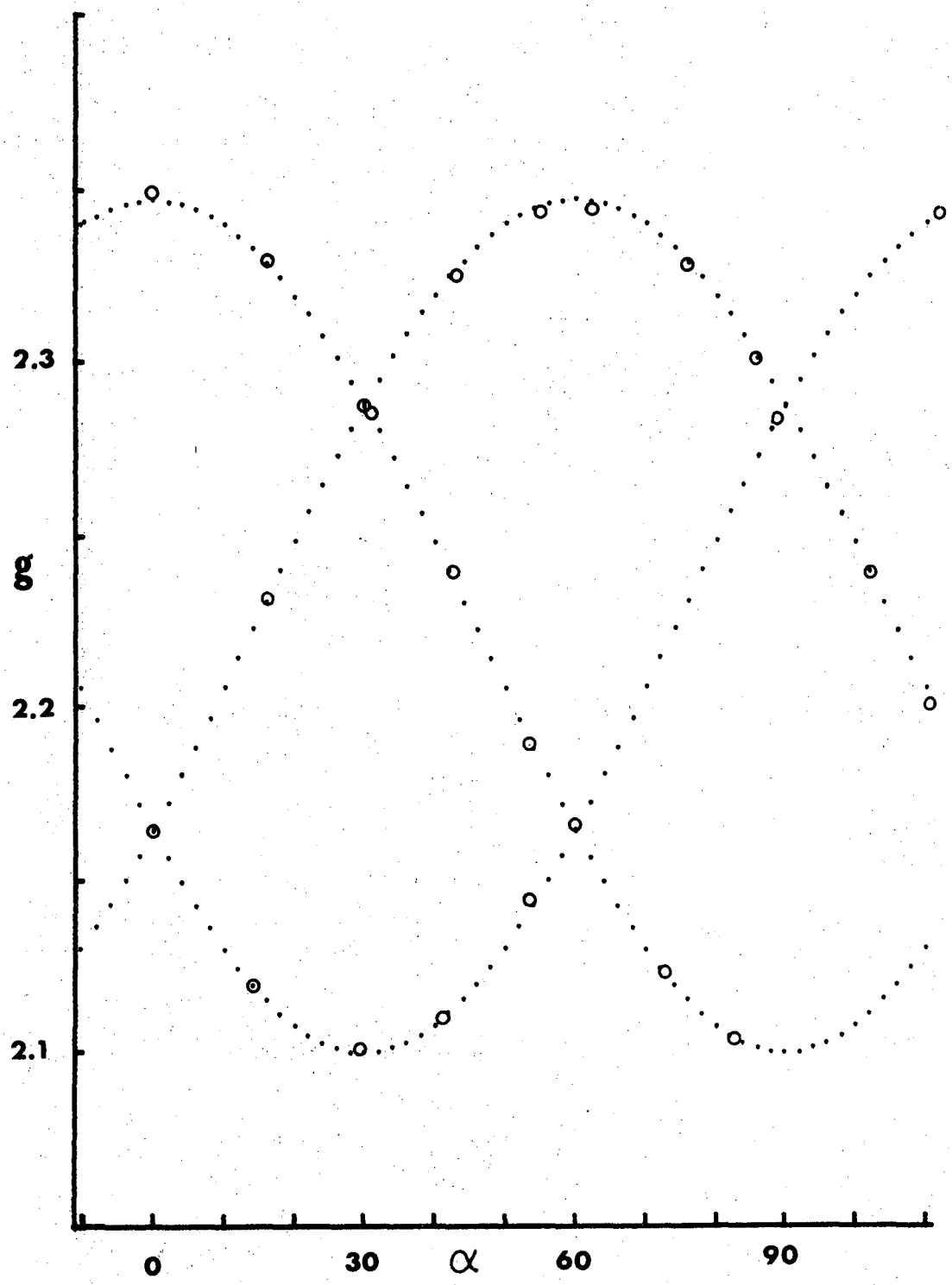

XBL 7012-7382

Fig. 51

LEGAL NOTICE

This report was prepared as an account of work sponsored by the United States Government. Neither the United States nor the United States Atomic Energy Commission, nor any of their employees, nor any of their contractors, subcontractors, or their employees, makes any warranty, express or implied, or assumes any legal liability or responsibility for the accuracy, completeness or usefulness of any information, apparatus, product or process disclosed, or represents that its use would not infringe privately owned rights.

TECHNICAL INFORMATION DIVISION
LAWRENCE RADIATION LABORATORY
UNIVERSITY OF CALIFORNIA
BERKELEY, CALIFORNIA 94720